

Important Notice

This copy may be used only for the purposes of research and private study, and any use of the copy for a purpose other than research or private study may require the authorization of the copyright owner of the work in question. Responsibility regarding questions of copyright that may arise in the use of this copy is assumed by the recipient.

UNIVERSITY OF CALGARY

Improving Reservoir Simulation with
Time-lapse Seismic Surveys

by

John Jianlin Zhang

A DISSERTATION

SUBMITTED TO THE FACULTY OF GRADUATE STUDIES
IN PARTIAL FULFILLMENT OF THE REQUIREMENTS
FOR THE DEGREE OF DOCTOR OF PHILOSOPHY

DEPARTMENT OF GEOSCIENCE
CALGARY, ALBERTA

APRIL, 2010

© John J. Zhang 2010

THE UNIVERSITY OF CALGARY
FACULTY OF GRADUATE STUDIES

The undersigned certify that they have read, and recommended to the Faculty of Graduate Studies for acceptance the thesis entitled "Improving Reservoir Simulation with Time-lapse Seismic Surveys" submitted by John Jianlin Zhang in partial fulfilment of the requirements for the degree of Doctor of Philosophy.

Supervisor, L. R. Bentley, Geoscience, U. of Calgary

Co-Supervisor, A. Settari, Chemical and Petroleum Engineering, U. of Calgary

Co-Supervisor, E. S. Krebs, Geoscience, U. of Calgary

M. Pooladi-Darvish, Chemical and Petroleum Engineering, U. of Calgary

Thomas J. (Tom) Boone, Imperial Oil Resources (external)

Date: Nov. 20, 2009

ABSTRACT

Reservoir simulation is an important tool for field planning and reservoir management, but it depends on input data and assumptions. If these conditions are not known accurately, which is the common case, the predictions from the simulation would be also inaccurate, or even misleading, in application. It is therefore essential to have an independent observation to guide the modelling process.

In this thesis, we use time-lapse seismic data as a constraint on reservoir simulation with the aim of improving the accuracy of reservoir description and simulation results. It appears based on the time-lapse seismic that two groups of shear fractures across the horizontal well bores were generated during the stage of injection and they may have prevailed in the entire recovery process. Through the fluid flow network of both fractures and well bores, steam in a few locations was driven to the bottom of the reservoir and further leaked to the underlying formations, even deep into Devonian carbonates. The break-through into the overlying formations may also have happened, as evidenced by reflection event disturbances. The interpretations suggest a new pattern of fluid flow within (and outside) the reservoir, and they are the crucial information for input data modification and assumption adjustment. Reservoir simulation coupled with geomechanical modeling was run with the interpretations applied, and the results are considerably different compared to those without the time-lapse seismic investigation.

Time-lapse seismic modelling based on the parameters acquired with the updated reservoir simulation indicates that the seismic observables of anomalies (newly created events, amplitude boost and event time delay) are consistent with

those identified in the real time-lapse seismic. This is additional evidence to validate the reservoir simulation.

ACKNOWLEDGEMENTS

This dissertation would not have been made possible without tremendous help and support from my supervisors and their associates, data sponsor, our research group, friends and numerous others. I owe a great debt of gratitude to them, their generosity and kindness. It was their patience and trustworthiness that strengthened my mind in the face of difficulties and frustrations of many kinds encountered in the course of the academic pursuit.

I have been fortunate to have a group of outstanding faculty members sitting in the supervisory committee, who have long been working productively in their respective fields. Larry Bentley taught me geostatistics applications, especially in Kriging's algorithms, and underground fluid flow. His comprehensive knowledge in a wide range of subjects led me forward on the right track. My frequent discussion with Tony Settari was always stimulating and enjoyable. His geomechanical modeling coupled with reservoir simulation enhanced significantly my understanding of fluid movement in reservoirs and its effects on other fronts. His spirits of diligence and persistence have left me a lasting impression. I occasionally asked Ed Krebes questions beyond theoretical geophysics, e.g., the introduction of complex number in mathematics. His insight into geophysics and science fundamentals widened my vision. My curiosity and courage to explore grew correspondingly. I am heartily thankful to them.

The associates of my supervisors have become my academic friends as well. Dale Walters fixed many bugs in the software (GeoSim). He was the second person after Tony Settari I contacted when I got stalled. I sought assistance with parameter settings from Bob Bachman. Mehran Gharibi helped me with the 3-D visualization software. I offer my regards and blessings to them.

An anonymous data sponsor provided me with the necessary seismic data for research. These data were processed well and 4-D signatures extracted from them were striking and compelling. AccuMap granted the university free access to well logs and hydrocarbon production information. I am grateful to them.

The CREWES project awarded the full scholarship to me when I was a full time student. Their technical support has continued all the time since I left campus for industry a few years ago. Rolf Maier was interrupted in countless times to repair my computer and network connection. Kevin Hall and Henry Bland helped in many other ways. Other faculty members, staff and fellow graduate students were also instrumental in my research progress. I extend my appreciation to them.

Sam Sun, who is now engaged in intensive academic work in China, showed me his interests and accomplishments in his company when I planned to organize my proposal. The interaction and his willingness to help led to my decision to choose heavy oil recovery as my topic. Along with him, Howard Lee made efforts to acquire data on my behalf. We exchanged the points of view, and the communications clarified my thought of lines and improved my knowledge in the specific study area. I oblige them from the bottom of my heart.

Finally, it is my pleasure to acknowledge the substantial contributions from my family and other friends over the years. Their names are not mentioned here, but their immerse support and dedication will unforgettably stay in my life.

TABLE OF CONTENTS

TITLE PAGE	I
APPROVAL PAGE	II
ABSTRACT	III
ACKNOWLEDGEMENTS.....	V
TABLE OF CONTENTS	VII
LIST OF TABLES.....	IX
LIST OF FIGURES.....	X
CHAPTER 1 INTRODUCTION.....	23
CHAPTER 2 REGIONAL GEOLOGY BACKGROUND	30
CHAPTER 3 RESERVOIR CHARACTERIZATION.....	37
3.1 Introduction	37
3.2 Reservoir geometry.....	38
3.3 Reservoir structure.....	40
3.4 Population of porosity and permeability of oil sands	45
3.5 Distribution of tight strings	48
3.6 Tight strings picked from 3-D seismic data.....	51
CHAPTER 4 RESERVOIR SIMULATION COUPLED WITH GEOMECHANICAL MODELING.....	58
4.1 Underlying principles	58
4.2 Reservoir model	62
4.3 Geomechanical model	67
4.4 Simulation parameters	69
4.5 Software tool.....	70
4.6 Results and discussion	70
4.7 Problems.....	97
CHAPTER 5 POST-STACK TIME-LAPSE SEISMIC PROCESSING AND INTERPRETATION.....	100
5.1 Introduction	100

5.2 Time-lapse seismic data review	100
5.3 Time-lapse seismic processing fundamentals.....	112
5.4 3D cross correlation algorithms	116
5.5 Time-lapse seismic processing and interpretation.....	119
CHAPTER 6 WAVELET TRANSFORM AND ITS APPLICATION TO TIME-LAPSE SEISMIC PROCESSING AND INTERPRETATION	130
6.1 Introduction	130
6.2 Principles.....	134
6.3 General applications.....	138
6.4 Application to time-lapse seismic.....	142
6.5 Case studies	146
6.6 Interpretation.....	175
CHAPTER 7 IMPROVING RESERVOIR SIMULATION WITH TIME-LAPSE SEISMIC DATA.....	190
7.1 Introduction	190
7.2 Mismatch of reservoir simulation and seismic observables	191
7.3 Design of new parameters	192
7.4 Match of production data	195
7.5 Simulation of fluid flow patterns.....	201
CHAPTER 8 SEISMIC MODELLING	239
8.1 Introduction	239
8.2 Rock physics models	240
8.3 Seismic modelling.....	242
CHAPTER 9 CONCLUSIONS.....	247
REFERENCES.....	249
APPENDIX 1.....	259
APPENDIX 2.....	260

LIST OF TABLES

Table 4. 1 Summary of the timing of steam injection and oil production	71
Table 6. 1 Relation of dominant frequency and max-tuning thickness.....	146

LIST OF FIGURES

Figure 2.1 Geological map of the Western Canada Sedimentary basin.....	31
Figure 2. 2 Index map of atlas subsurface control showing the designated "atlas control wells" and the lines of regional "master" cross-sections.	32
Figure 2. 3 Geological cross section along the line D-D' in Figure 2.2	33
Figure 2. 4 Paleogeography at deposition of the Clearwater formation	35
Figure 3. 1 3-D visualization of the formations and development wells	38
Figure 3. 2 Typical well logs for the Clearwater Formation	39
Figure 3. 3 3-D visualization of the reservoir, development wells and target area	39
Figure 3. 4 3-D visualization of the Clearwater reservoir	40
Figure 3. 5 Histogram of Gamma ray log value (API) from forty-five wells	41
Figure 3. 6 Cores of cap rock and reservoir rock (oil sands).....	42
Figure 3. 7 Cores of reservoir rock (oil sands)	42
Figure 3. 8 Cores of reservoir rock (oil sands)	43
Figure 3. 9 Cores of reservoir rock (oil sands)	43
Figure 3. 10 Cores of reservoir rock (oil sands)	44
Figure 3. 11 Lab report	44
Figure 3. 12 Histogram of porosity measurements of core samples from fifteen wells	45
Figure 3. 13 Cross plot of corrected neutron porosity and corrected density porosity logs.....	47
Figure 3. 14 Histogram of porosity calculations from eleven wells	47
Figure 3. 15 3-D visualization of the porosity distribution of oil sands in the reservoir.....	49
Figure 3. 16 Contour of the number of tight strings per well location.....	50
Figure 3. 17 Variogram model with the number of tight strings per location as the random variable.....	50

Figure 3. 18 3-D visualization of the porosity distribution of the reservoir body	51
Figure 3. 19 3-D seismic surveys and the wells with sonic and density logs.....	52
Figure 3. 20 Synthetic seismic traces, sonic and density logs	54
Figure 3. 21 Seismic traces in the time window of 410-460 ms in crossline 36.....	54
Figure 3. 22 Seismic peak picks (blue lines) in the reservoir window.....	55
Figure 3. 23 Histogram of the number of seismic picks per trace.....	55
Figure 3. 24 Histogram of the number of well log picks per well.....	56
Figure 3. 25 3-D visualization of the porosity distribution of the reservoir body in the area covered by 3-D seismic surveys	56
Figure 3. 26 3-D visualization of the permeability (Kx) distribution of the reservoir body in the area covered by 3-D seismic surveys	57
Figure 4. 1 Time-lapse 3-D seismic survey area (blue) and reservoir simulation area (green)	64
Figure 4. 2 3-D visualization of reservoir simulation grid (43*36*20)	64
Figure 4. 3 3-D visualization of porosity in the seismic area	65
Figure 4. 4 3-D visualization of permeability in I direction in the seismic area ..	66
Figure 4. 5 3-D visualization of permeability in J direction in the seismic area ..	66
Figure 4. 6 3-D visualization of permeability in K direction in the seismic area.	67
Figure 4. 7 3-D visualization of geomechanical modeling (43*36*30)	68
Figure 4. 8 Oil saturation on K-plane on Oct 16, 1997	72
Figure 4. 9 Oil saturation on J-plane on Oct 16, 1997.....	72
Figure 4. 10 Oil saturation on I-plane on Oct 16, 1997.....	73
Figure 4. 11 Gas saturation on K-plane on Oct 16, 1997	73
Figure 4. 12 Gas saturation on J-plane on Oct 16, 1997.....	74
Figure 4. 13 Gas saturation on I-plane on Oct 16, 1997.....	74
Figure 4. 14 Water saturation on K-plane on Oct 16, 1997	75
Figure 4. 15 Water saturation on J-plane on Oct 16, 1997	75
Figure 4. 16 Water saturation on I-plane on Oct 16, 1997	76
Figure 4. 17 Fluid pressure on K-plane on Oct 16, 1997 (unit: KPa)	76

Figure 4. 18 Fluid pressure on J-plane on Oct 16, 1997 (unit: KPa)	77
Figure 4. 19 Fluid pressure on I-plane on Oct 16, 1997 (unit: KPa)	77
Figure 4. 20 Temperature on K-plane on Oct 16, 1997 (unit: Celsius).....	78
Figure 4. 21 Temperature on J-plane on Oct 16, 1997 (unit: Celsius)	78
Figure 4. 22 Temperature on I-plane on Oct 16, 1997 (unit: Celsius)	79
Figure 4. 23 S_x distribution in the middle of the reservoir on Oct 16, 1997 (unit: KPa).....	83
Figure 4. 24 S_x distribution on the top of the reservoir on Oct 16, 1997 (unit: KPa)	83
Figure 4. 25 S_x distribution on the ground on Oct 16, 1997 (unit: KPa)	84
Figure 4. 26 S_y distribution in the middle of the reservoir on Oct 16, 1997 (unit: KPa).....	84
Figure 4. 27 S_y distribution on the top of the reservoir on Oct 16, 1997 (unit: KPa)	85
Figure 4. 28 S_y distribution on the ground on Oct 16, 1997 (unit: KPa)	85
Figure 4. 29 S_z distribution in the middle of the reservoir on Oct 16, 1997 (unit: KPa).....	86
Figure 4. 30 S_z distribution on the top of the reservoir on Oct 16, 1997 (unit: KPa)	86
Figure 4. 31 S_z distribution on the ground on Oct 16, 1997 (unit: KPa)	87
Figure 4. 32 U_x distribution in the middle of the reservoir on Oct 16, 1997 (unit: m).....	87
Figure 4. 33 U_x distribution on the top of the reservoir on Oct 16, 1997 (unit: m).....	88
Figure 4. 34 U_x distribution on the ground on Oct 16, 1997 (unit: m)	88
Figure 4. 35 U_y distribution in the middle of the reservoir on Oct 16, 1997 (unit: m).....	89
Figure 4. 36 U_y distribution on the top of the reservoir on Oct 16, 1997 (unit: m)	89
Figure 4. 37 U_y distribution on the ground on Oct 16, 1997 (unit: m)	90

Figure 4. 38 U_z distribution in the middle of the reservoir on Oct 16, 1997 (unit: m).....	90
Figure 4. 39 U_z distribution on the top of the reservoir on Oct 16, 1997 (unit: m).....	91
Figure 4. 40 U_z distribution on the ground on Oct 16, 1997 (unit: m)	91
Figure 4. 41 Oil saturation on K-plane on Feb 28, 1998	92
Figure 4. 42 Oil saturation on J-plane on Feb 28, 1998.....	92
Figure 4. 43 Oil saturation on I-plane on Feb 28, 1998.....	93
Figure 4. 44 Fluid pressure on K-plane on Feb 28, 1998 (unit: KPa).....	93
Figure 4. 45 Fluid pressure on J-plane on Feb 28, 1998 (unit: KPa)	94
Figure 4. 46 Fluid pressure on I-plane on Feb 28, 1998 (unit: KPa)	94
Figure 4. 47 Gas saturation on K-plane on Feb 28, 1998.....	95
Figure 4. 48 U_z distribution in the middle of the reservoir on Feb 28, 1998 (unit: m).....	95
Figure 4. 49 U_z distribution on the top of the reservoir on Feb 28, 1998 (unit: m)	96
Figure 4. 50 U_z distribution on the ground on Feb 28, 1998 (unit: m)	96
Figure 4. 51 Production history for well 239.....	99
Figure 4. 52 Production history for well 226.....	99
Figure 5. 1 3 D time-lapse seismic survey area and well locations.....	101
Figure 5. 2 Seismic sections of baseline (upper, 1997) and monitor (lower, 1998) surveys.....	102
Figure 5. 3 Amplitude spectra of baseline (left, 1997) and monitor (right, 1998) surveys.....	102
Figure 5. 4 Amplitude anomalies (as indicated by red circles) of 1998 data at 540 ms at five locations. (Note: polarity flipped for striking effect).....	103
Figure 5. 5 No amplitude anomalies of 1997 data at 540 ms at five locations....	103
Figure 5. 6 Map of RMS amplitude anomalies at the window of 10 ms centred at 540ms for 1998 data	104

Figure 5. 7 Cross correlation of the window of 510-560 ms between 1997 data and 1998 data	104
Figure 5. 8 Time sag and trace disturbance below the reservoir for 1998 data..	106
Figure 5. 9 No time sag and trace disturbance below the reservoir zone for 1997 data.....	106
Figure 5. 10 Map of the horizon of Top Devonian for 1998 data, indicating time sags across the wells	107
Figure 5. 11 Amplitude map across the wells along the horizon of Top Devonian for 1998 data.....	107
Figure 5. 12 Cross correlation of the window of 560-605 ms between 1997 data and 1998 data	108
Figure 5. 13 No time sag observed across the wells along the horizon of Top Devonian for 1997 data	108
Figure 5. 14 No Amplitude attenuation zone observed across the wells along the horizon of Top Devonian for 1997 data	109
Figure 5. 15 Seeming trace disturbance below top Devonian for 1998 data.....	109
Figure 5. 16 No trace disturbance for 1997 data	110
Figure 5. 17 Cross correlation of the window of 625-675 ms between 1997 data and 1998 data	110
Figure 5. 18 Apparent trace disturbance above the reservoir for 1998 data.....	111
Figure 5. 19 Original undisturbed section of 1997 data.....	111
Figure 5. 20 Cross correlation of the window of 450-510 ms between 1997 data and 1998 data	112
Figure 5. 21 Difference seismic section without time-lapse processing.....	113
Figure 5. 22 Crossplot (on the window of 300-500ms) of 98 and 97 data without time-lapse processing	113
Figure 5. 23 Band pass filtered seismic sections of baseline (upper, 1997) and monitor (lower, 1998) survey	121

Figure 5. 24	Crossplot (on the window of 300-500ms) of 98 and 97 data with band pass filter applied to both volumes	121
Figure 5. 25	Crossplot (on the window of 300-500ms) of 98 and 97 data with global amplitude scaling further applied to 98 data.....	122
Figure 5. 26	Crossplot (on the window of 300-500ms) of 98 and 97 data with global time and phase shifts further applied to 98 data.....	122
Figure 5. 27	Crossplot (on the window of 300-500ms) of 98 and 97 data with shaping filter further applied to 98 data.....	123
Figure 5. 28	Crossplot (on the window of 300-500ms) of 98 and 97 data with seismic events alignment by way of 3D cross correlation further applied to 98 data.....	124
Figure 5. 29	Redrawing of Figure 5.28 with removal of edge traces	124
Figure 5. 30	Final processed section (Inline45) of the monitor survey	125
Figure 5. 31	Final processed section (Inline 40) of the monitor survey	125
Figure 5. 32	Difference section (Inline 40)	126
Figure 5. 33	Contour map of Inst. amplitude on the window of 560-590ms.....	127
Figure 5. 34	Contour map of Inst. amplitude on the window of 525-560ms.....	128
Figure 5. 35	Contour map of Inst. amplitude on the window of 510-535ms.....	128
Figure 5. 36	Contour map of Inst. amplitude on the window of 615-635ms.....	129
Figure 6. 1	Amplitude spectrum of Ricker wavelet	133
Figure 6. 2	Wavelet time localization	134
Figure 6. 3	Synthetic seismic section (60 hz wavelet)	139
Figure 6. 4	Synthetic seismic section (150 hz wavelet)	140
Figure 6. 5	Wedge model and its synthetic (using 100hz Ricker wavelet)	143
Figure 6. 6	Amplitude cross section along the reflection peaks on the top boundary	143
Figure 6. 7	Wavelet transform of Figure 6.5 at 50 hz dominant frequency	144
Figure 6. 8	Wavelet transform of Figure 6.5 at 90 hz dominant frequency	144
Figure 6. 9	Wavelet transform of Figure 6.5 at 130 hz dominant frequency	145

Figure 6. 10	Wavelet transform of Figure 6.5 at 170 hz dominant frequency	145
Figure 6. 11	Wavelet transform of Figure 6.5 at 310 hz dominant frequency	145
Figure 6. 12	Amplitude map at 540 ms from original data.....	147
Figure 6. 13	Amplitude map at 550 ms from original data.....	148
Figure 6. 14	Amplitude map at 566 ms from original data.....	148
Figure 6. 15	Amplitude map at 573 ms from original data.....	149
Figure 6. 16	Amplitude map at 540 ms from 10hz data	149
Figure 6. 17	Amplitude map at 550 ms from 10hz data	150
Figure 6. 18	Amplitude map at 566 ms from 10hz data	150
Figure 6. 19	Amplitude map at 573 ms from 10hz data	151
Figure 6. 20	Amplitude map at 540 ms from 20hz data	151
Figure 6. 21	Amplitude map at 550 ms from 20hz data	152
Figure 6. 22	Amplitude map at 566 ms from 20hz data	152
Figure 6. 23	Amplitude map at 573 ms from 20hz data	153
Figure 6. 24	Amplitude map at 540 ms from 30hz data	153
Figure 6. 25	Amplitude map at 550 ms from 30hz data	154
Figure 6. 26	Amplitude map at 566 ms from 30hz data	154
Figure 6. 27	Amplitude map at 573 ms from 30hz data	155
Figure 6. 28	Amplitude map at 540 ms from 40hz data	155
Figure 6. 29	Amplitude map at 550 ms from 40hz data	156
Figure 6. 30	Amplitude map at 566 ms from 40hz data	156
Figure 6. 31	Amplitude map at 573 ms from 40hz data	157
Figure 6. 32	Amplitude map at 540 ms from 50hz data	157
Figure 6. 33	Amplitude map at 550 ms from 50hz data	158
Figure 6. 34	Amplitude map at 566 ms from 50hz data	158
Figure 6. 35	Amplitude map at 573 ms from 50hz data	159
Figure 6. 36	Amplitude map at 540 ms from 60hz data	159
Figure 6. 37	Amplitude map at 550 ms from 60hz data	160
Figure 6. 38	A Amplitude map at 566 ms from 60hz data	160

Figure 6. 39	Amplitude map at 573 ms from 60hz data	161
Figure 6. 40	Amplitude map at 540 ms from 70hz data	161
Figure 6. 41	Amplitude map at 550 ms from 70hz data	162
Figure 6. 42	Amplitude map at 566 ms from 70hz data	162
Figure 6. 43	Amplitude map at 573 ms from 70hz data	163
Figure 6. 44	Amplitude map at 540 ms from 80hz data	163
Figure 6. 45	Amplitude map at 550 ms from 80hz data	164
Figure 6. 46	Amplitude map at 566 ms from 80hz data	164
Figure 6. 47	Amplitude map at 573 ms from 80hz data	165
Figure 6. 48	Amplitude map at 540 ms from 90hz data	165
Figure 6. 49	Amplitude map at 550 ms from 90hz data	166
Figure 6. 50	Amplitude map at 566 ms from 90hz data	166
Figure 6. 51	Amplitude map at 573 ms from 90hz data	167
Figure 6. 52	Seismic section of Xline 60 from original data	168
Figure 6. 53	Seismic section of Xline 60 from 20hz data.....	169
Figure 6. 54	Seismic section of Xline 60 from 40hz data.....	169
Figure 6. 55	Seismic section of Xline 60 from 60hz data.....	170
Figure 6. 56	Seismic section of Xline 60 from 80hz data.....	170
Figure 6. 57	Seismic section of Inline 45 from original data	171
Figure 6. 58	Seismic section of Inline 45 from 20hz data.....	171
Figure 6. 59	Seismic section of Inline 45 from 40hz data.....	172
Figure 6. 60	Seismic section of Inline 45 from 60hz data.....	172
Figure 6. 61	Seismic section of Inline 45 from 80hz data.....	173
Figure 6. 62	Seismic section of Inline 56 from original data	173
Figure 6. 63	Seismic section of Inline 56 from 20hz data.....	174
Figure 6. 64	Seismic section of Inline 56 from 40hz data.....	174
Figure 6. 65	Seismic section of Inline 56 from 60hz data.....	175
Figure 6. 66	Seismic section of Inline 56 from 80hz data.....	175
Figure 6. 67	Instantaneous amplitude slice at 544ms cut from the data at 40hz	178

Figure 6. 68	Instantaneous amplitude seismic cross section of Xline 60 at 40hz	179
Figure 6. 69	Cross section of Xline 60 at 40hz for the baseline survey (1997)	179
Figure 6. 70	Instantaneous amplitude seismic cross section of Xline 79 at 40hz	180
Figure 6. 71	Instantaneous amplitude seismic cross section of Inline 12 at 40hz	180
Figure 6. 72	Cross section of Inline 12 at 40hz for the baseline survey (1997) ...	181
Figure 6. 73	Instantaneous amplitude seismic cross section of Inline 24 at 40hz	181
Figure 6. 74	Instantaneous amplitude seismic cross section of Inline 32 at 40hz	182
Figure 6. 75	Instantaneous amplitude seismic cross section of Inline 40 at 40hz	182
Figure 6. 76	Instantaneous amplitude seismic cross section of Inline 50 at 40hz	183
Figure 6. 77	Instantaneous amplitude seismic cross section of Inline 59 at 40hz	183
Figure 6. 78	Cross section of Inline 59 at 40hz	184
Figure 6. 79	Instantaneous amplitude seismic cross section of Inline 67 at 40hz	184
Figure 6. 80	Cross section of Inline 67 at 40hz for the baseline survey (1997) ...	185
Figure 6. 81	Instantaneous amplitude seismic cross section of Inline 74 at 40hz	185
Figure 6. 82	Cross section of Inline 67 at 40hz	186
Figure 6. 83	Instantaneous amplitude seismic cross section of Inline 83 at 40hz	186
Figure 6. 84	Instantaneous amplitude seismic cross section of Inline 90 at 40hz	187
Figure 6. 85	Instantaneous amplitude seismic cross section of Inline 99 at 40hz	187

Figure 6. 86	Instantaneous amplitude slice at 507ms cut from the data at 40hz	188
Figure 6. 87	Instantaneous amplitude slice at 604ms cut from the data at 40hz	188
Figure 6. 88	Instantaneous amplitude slice at 638ms cut from the data at 40hz	189
Figure 7. 1	Conceptual diagram of shear failure in oil sands	193
Figure 7. 2	Two groups of fractures of high permeability	194
Figure 7. 3	Bottom of the reservoir showing downward leaking points	194
Figure 7. 4	Match of cumulative oil production for well 197 (unit: m ³).....	196
Figure 7. 5	Match of cumulative water production for well 197 (unit: m ³).....	197
Figure 7. 6	Match of cumulative oil production for well 205 (unit: m ³).....	197
Figure 7. 7	Match of cumulative water production for well 205 (unit: m ³).....	198
Figure 7. 8	Match of cumulative oil production for well 214 (unit: m ³).....	198
Figure 7. 9	Match of cumulative water production for well 214 (unit: m ³).....	199
Figure 7. 10	Match of cumulative oil production for well 226 (unit: m ³).....	199
Figure 7. 11	Match of cumulative water production for well 226 (unit: m ³).....	200
Figure 7. 12	Match of cumulative oil production for well 239 (unit: m ³).....	200
Figure 7. 13	Match of cumulative water production for well 239 (unit: m ³).....	201
Figure 7. 14	Map of reservoir pressure (KPa) at the end of Feb. 1998.....	202
Figure 7. 15	Map of reservoir pressure (KPa) at the end of Feb. 1998.....	202
Figure 7. 16	Oil saturation on K-plane on Oct 16, 1997	203
Figure 7. 17	Oil saturation on reservoir bottom on Oct 16, 1997	203
Figure 7. 18	Oil saturation on I-plane on Oct 16, 1997.....	204
Figure 7. 19	Oil saturation on I-plane on Oct 16, 1997.....	204
Figure 7. 20	Oil saturation on J-plane on Oct 16, 1997.....	205
Figure 7. 21	Oil saturation on J-plane on Oct 16, 1997.....	205
Figure 7. 22	Water saturation on K-plane on Oct 16, 1997	206
Figure 7. 23	Water saturation on reservoir bottom on Oct 16, 1997	206
Figure 7. 24	Water saturation on I-plane on Oct 16, 1997	207
Figure 7. 25	Water saturation on I-plane on Oct 16, 1997	207
Figure 7. 26	Water saturation on J-plane on Oct 16, 1997	208

Figure 7. 27	Water saturation on J-plane on Oct 16, 1997	208
Figure 7. 28	Fluid pressure on K-plane on Oct 16, 1997	209
Figure 7. 29	Fluid pressure on I-plane on Oct 16, 1997.....	209
Figure 7. 30	Fluid pressure on J-plane on Oct 16, 1997.....	210
Figure 7. 31	Temperature on K-plane on Oct 16, 1997.....	210
Figure 7. 32	Temperature on I-plane on Oct 16, 1997	211
Figure 7. 33	Temperature on J-plane on Oct 16, 1997	211
Figure 7. 34	Sx distribution in the middle of the reservoir on Oct 16, 1997.....	212
Figure 7. 35	Sx distribution on the top of the reservoir on Oct 16, 1997	213
Figure 7. 36	Sy distribution in the middle of the reservoir on Oct 16, 1997	213
Figure 7. 37	Sy distribution on the top of the reservoir on Oct 16, 1997	214
Figure 7. 38	Sz distribution in the middle of the reservoir on Oct 16, 1997.....	214
Figure 7. 39	Sz distribution on the top of the reservoir on Oct 16, 1997	215
Figure 7. 40	Ux distribution in the middle of the reservoir on Oct 16, 1997	215
Figure 7. 41	Ux distribution on the top of the reservoir on Oct 16, 1997	216
Figure 7. 42	Ux distribution on the ground on Oct 16, 1997.....	216
Figure 7. 43	Uy distribution in the middle of the reservoir on Oct 16, 1997	217
Figure 7. 44	Uy distribution on the top of the reservoir on Oct 16, 1997	217
Figure 7. 45	Uy distribution on the ground on Oct 16, 1997.....	218
Figure 7. 46	Uz distribution in the middle of the reservoir on Oct 16, 1997.....	218
Figure 7. 47	Uz distribution on the top of the reservoir on Oct 16, 1997	219
Figure 7. 48	Uz distribution on the ground on Oct 16, 1997	219
Figure 7. 49	Oil saturation in the middle of the reservoir on Feb 28, 1998	220
Figure 7. 50	Oil saturation on the bottom of the reservoir on Feb 28, 1998	221
Figure 7. 51	Oil saturation on I-plane on Feb 28, 1998.....	221
Figure 7. 52	Oil saturation on I-plane on Feb 28, 1998.....	222
Figure 7. 53	Oil saturation on J-plane on Feb 28, 1998.....	222
Figure 7. 54	Oil saturation on J-plane on Feb 28, 1998.....	223
Figure 7. 55	Water saturation in the middle of the reservoir on Feb 28, 1998....	223

Figure 7. 56	Water saturation on the bottom of the reservoir on Feb 28, 1998...	224
Figure 7. 57	Water saturation on I-plane on Feb 28, 1998	224
Figure 7. 58	Water saturation on I-plane on Feb 28, 1998	225
Figure 7. 59	Water saturation on J-plane on Feb 28, 1998	225
Figure 7. 60	Water saturation on J-plane on Feb 28, 1998	226
Figure 7. 61	Gas saturation in the middle of the reservoir on Feb 28, 1998.....	226
Figure 7. 62	Gas saturation on I-plane on Feb 28, 1998	227
Figure 7. 63	Gas saturation on J-plane on Feb 28, 1998	227
Figure 7. 64	Fluid pressure in the middle of the reservoir on Feb. 28, 1998.....	228
Figure 7. 65	Fluid pressure on I planes on Feb. 28, 2008	228
Figure 7. 66	Fluid pressure on J planes on Feb. 28, 2008	229
Figure 7. 67	Temperature in the middle of the reservoir on Feb. 28, 1998	229
Figure 7. 68	Temperature on I planes on Feb. 28, 1998.....	230
Figure 7. 69	Temperature on J planes on Feb. 28, 1998.....	230
Figure 7. 70	Sx distribution in the middle of the reservoir on Feb 28, 1998	231
Figure 7. 71	Sx distribution on the top of the reservoir on Feb 28,1998	232
Figure 7. 72	Sy distribution in the middle of the reservoir on Feb 28, 1998	232
Figure 7. 73	Sy distribution on the top of the reservoir on Feb 28, 1998.....	233
Figure 7. 74	Sz distribution in the middle of the reservoir on Feb 28, 1998	233
Figure 7. 75	Sz distribution on the top of the reservoir on Feb 28, 1998	234
Figure 7. 76	Ux distribution in the middle of the reservoir on Feb 28, 1998	234
Figure 7. 77	Ux distribution on the top of the reservoir on Feb 28, 1998	235
Figure 7. 78	Ux distribution on the ground on Feb 28, 1998.....	235
Figure 7. 79	Uy distribution in the middle of the reservoir on Feb 28, 1998	236
Figure 7. 80	Uy distribution on the top of the reservoir on Feb 28, 1998	236
Figure 7. 81	Uy distribution on the ground on Feb 28, 1998.....	237
Figure 7. 82	Uz distribution in the middle of the reservoir on Feb 28, 1998	237
Figure 7. 83	Uz distribution on the top of the reservoir on Feb 28, 1998	238
Figure 7. 84	Uz distribution on the ground on Feb 28, 1998.....	238

Figure 8. 1	Cross section of the synthetic baseline seismic along well 226.....	243
Figure 8. 2	Cross section of the synthetic monitor seismic along well 226.....	243
Figure 8. 3	Time map of the top Devonian sliced from the synthetic monitor survey (1998).....	244
Figure 8. 4	Cross correlation coefficient between the synthetic baseline and monitor surveys on the window of 400-500ms.....	245
Figure 8. 5	Cross correlation time shift between the synthetic baseline and monitor surveys on the window of 400-500ms.....	245
Figure 8. 6	RMS amplitude map sliced from the synthetic difference volume on the window of 430-450ms	246

CHAPTER 1 INTRODUCTION

Time-lapse seismic surveys refer to the acquiring of seismic data repeatedly over a period of time at the same location in an attempt to find changes in the reservoir throughout the entire life of recovery. This idea is not new, and it has evolved from the development of exploration seismology. At the early stage of seismic exploration, low signal/noise ratio limited its use only to structural imaging. It only tried to locate reservoir traps or target zones by measuring the time for the seismic waves, which were reflections generated from underground interfaces between geological formations with different acoustic properties, to take to arrive at the surface recorders. This method of structural imaging has ever since brought remarkable discoveries and it remains today the primary goal of exploration seismology. In the early 1970's, the oil industry recognized that a hydrocarbon accumulation sometimes changed the reflectivity enough to allow its direct detection (bright spot) and mapping, and therefore they invested heavily to have more accurate recording, processing and interpretation of amplitude information (after Sheriff and Geldart, 1995). Over this period of time, numerous field examples and theoretical models were proposed to tie seismic to the presence of hydrocarbon, and the seismic indicators expanded to include frequency and velocity etc.. Pan and de Bremaecker (1970) provided a methodology to predict pore-fluid saturations and porosity based on rock physics and seismic inversion. Then, geophysicists started to truly believe that it was practically possible to extract from seismic data more information about rock properties such as fluid contents, porosity and lithology etc..

The idea of using successive seismic surveys to image the underground fluid flow and other changes as the reservoir was developed became a logical

extension of the above techniques of seismic detection of pore fluids and other rock properties. In 1979, Britton et al. (1982) shot four seismic survey lines over the Street Ranch Pilot area and found that seismic response that was indicated by the reflection disturbance was strong enough to delineate the steam invaded region in the reservoir. Encouraged by this successful seismic imaging of a steam flood, Stanford University Rock Physics Lab conducted a systematic lab study of the effect of the heated heavy oil or tar sands on wave propagation. The conclusion of their study was that the heating of the heavy oil or tar sands had very large effects on the measured P and S-velocities and amplitudes (Nur et al.,1984), which implied that the seismic data might provide a powerful tool for the mapping of the temperature and thermal fronts.

The first detailed study of time-lapse seismic surveys was published in Geophysics in 1987. Greaves and Fulp (1987) shot the 3-D seismic surveys over a pilot in-situ combustion project area three times in a one-year period with the same acquisition parameters. They processed these data with the same processing parameters with aim to map the extent and directions of in-situ combustion propagation in time. A comparison of the reflection strengths on the top of the reservoir from the preburn, midburn and postburn seismic surveys revealed a bright spot, which was a result of the increased gas saturation from the combustion and injection along the top of the reservoir. A dim spot on the strong reflection from the limestone zone below the reservoir represented the wave energy attenuation across the burned zone and indicated the actual swept region. Instead of directly using seismic amplitudes as before, Vedanti and Sen (2009) inverted pre-stack time-lapse seismic data for elastic attributes to track the thermal front of in-situ combustion away from the injection wells. The images appeared better and more accurate.

One of the most successful examples of seismic monitoring of steam injection is from the Duri field, Sumatra, Indonesia, where a series of 3-D seismic surveys were shot a few months apart, starting from the steam injection and covered the entire project area (Jenkinns et al., 1997; Waite and Sigit, 1997). The time thickness for the reservoir on the seismic section changed with the steam injection progression and it was employed to track the pressure front at first and then the expansion of the steam chamber later. The time pull-up or push-down on the bottom of the reservoir was chiefly caused by the dissolution of gas into oil or the existence of the injected steam.

The Gullfaks oil field in the Norwegian North Sea supplies 20% of Norway's production (Jack, 1997). Repeat saturation well logs revealed considerable velocity changes, which resulted from the upward movement of the oil-water contact (Jack, 1997). Sonneland et al. (1997) tied, at well locations, the seismic attributes to three classes of reservoirs (, i.e., oil-filled, gas-filled and water-filled), and applied the discrimination principle to the areas without well control. This study successfully located the bypassed oil pockets. Similarly, Johnston (1997) identified the acoustic impedance changes due to water influx and pressure decline in the North Sea Fulmar field, and used time-lapse seismic inversion for the acoustic impedance changes, which may suggest areas of bypassed oil. There are plenty of other successful examples in this area to monitor the fluid movement using time-lapse seismic (Gabriels et al., 1999; Hubans et al., 2003; Kloosterman et al., 2003; Koster et al., 2000; Waal et al., 2003; and so on). These seismic interpretations have been useful in identifying oil/gas-water contact movement, displacement efficiency and sealing capabilities.

CO₂ or miscible gas flood in carbonate reservoirs may cause more velocity changes than expected from the Gassmann's equation (Hirsche et al., 1997) and it

may be feasible to conduct seismic monitoring in many reservoir types. CSM (1997) worked on the 3-C and 4-D seismic project at the Vacuum oil field, New Mexico, and found visible anomalies in amplitude difference and in variations in shear anisotropy, which were interpreted as a CO₂ miscible bank. Spetzler et al. (2008) employed cross-well seismic tomography for travelttime delay computation and found a time-lapse velocity anomaly on the order of -18 percent within the porous sandstone flooded by CO₂. In Weyburn Field, Saskatchewan, time-lapse images illustrate that fracture zones served as conduits for injected CO₂ and intervention was necessary to improve recovery efficiency (Davis, 2005).

On the other hand, the conventional method of predicting the reservoir changes during the course of development is accomplished by using reservoir simulation, a computer solution to the mathematical equations describing the fundamental laws that govern fluid motions in porous media. This is a valuable tool for reservoir engineers who need to plan the field development and conduct reservoir management. It can answer many questions (such as well arrangement, well completion, reservoir pressure maintenance, fluid production and recovery enhancement) encountered throughout the whole life of hydrocarbon recovery (after Aziz and Settari, 1979). However, successful reservoir simulation requires an accurate estimation of reservoir physical properties in space and time (in particular, permeability), which can be difficult to ascertain because of limited amounts of available information and complexities of fluid-rock interaction. Matching the reservoir simulation predictions with the historical performance by adjusting the parameters of the reservoir model may provide a practical means of validating. But the outcome is often not unique since data is sparse and local (after Waal et al., 2003). With large amounts of historical data, history matching becomes a formidable task that may be rendered difficult or even intractable. We

remain unclear about how properties are distributed and how fluids migrate within the reservoir.

It is evident that reservoir simulation needs to be constrained by independent direct observations in order for us to have a significant amount of confidence in employing it for reservoir management. Observation wells can be drilled for verification, but they are sparsely located and their drilling and operation prove too costly. Successful examples of using time-lapse seismic surveys to detect changes in pore fluids and other reservoir properties as described early in this chapter definitely open a new avenue to improving reservoir simulation. Gosselin et al. (2004) and Huang et al. (1997 and 1998) incorporated time-lapse seismic differences into the objective function of history production matching. In addition to fitting the recovery performance, reservoir simulation results, which were converted to synthetic time-lapse seismic differences, also needed to match the real time-lapse seismic differences, as it was illustrated with an example from the Gulf of Mexico (Huang et al., 1997 and 1998). The computational algorithm for mismatch optimization was further improved to relieve highly intensive computation using seismic attribute zonation (Huang et al., 2001). However, the great disadvantage of this treatment on the part of seismic is that it deals with sheer mathematical differences, which can mislead due to challenging repeatability (after Eastwood et al., 1998; Huang et al., 1999) and shortcomings of rock physics models (such as how the elastic moduli and velocities are related to lithology, pore fluids, porosity, pressure and temperature etc.), without accurate interpretation of the fluid flow pattern within the reservoir and beyond, which is a dominant and controlling factor for reservoir simulation and also key to generation of time-lapse seismic differences. Walker et al. (2006) noticed seismic images of water-oil contact movements during production and tried to re-create the same pictures with reservoir

simulation. Scorer et al. (2005) identified the independent water front advancements for turbidite bodies with time-lapse seismic, and used the results to assign a proper model of permeability in the reservoir model. As a result, history matching was substantially enhanced so that they were more confident to forecast future performance and detect possible infill drilling locations (after Scorer et al., 2005). Chadwick et al. (2005) marked with bright reflections the plume formed by CO₂ injection in the aquifer and further estimated the CO₂ saturation distribution based on observed reflectivity and velocity pushdown. The resultant reservoir simulation that matched well the time-lapse seismic response provided an acceptable description of CO₂ movement.

The thesis furthers the previous work with a novel approach to unravelling the fluid flow pattern, which serves as a framework fundamental to reservoir simulation and subsequent history matching. The synthetic time-lapse seismic derived from significantly enhanced reservoir simulation matches the real seismic data, and the validation gains more confidence for the reservoir engineer, who can then use the model to take whatever measures possible to remedy operational problems and increase recovery efficiency.

The thesis illustrates the methodology with a practical case of the heavy oil reservoir under steam injection, which was covered by time-lapse seismic surveys to monitor the production performance. The thesis begins with the integration of all available data (geology, well logs, core samples and seismic) for a reservoir characterization model, which appears incomplete and imperfect. Reservoir simulation coupled with geomechanical modelling is performed to find the spatial distribution of the reservoir conditions (saturation, pressure and temperature) and also the patterns of stress, strain and displacements with recovery progression within the reservoir and beyond. Then, time-lapse seismic

data are processed and interpreted (both conventional and nonconventional) to identify the fluid flow pattern and potential pathways of leakage to the overlying and underlying formations. A comparison of simulated scenarios and seismic observations reveals the serious problems of the initial reservoir simulation model, indicating the need for an overhaul of the reservoir description and assumptions. Being reconstructed and production history matched, the simulation is re-run with results that visualize the fluid migration as closely as the seismic indicated. Using rock physics models, the corresponding spatial distribution of elastic moduli, density and velocities are calculated with the recovery progression. Finally, time-lapse seismic modelling is carried out to simulate the time-lapse seismic responses. A close fit between the synthetic and real seismic increases further the confidence in the reservoir simulation results, which may then offer valuable advice for engineering actions.

CHAPTER 2 REGIONAL GEOLOGY BACKGROUND

The Western Canada sedimentary basin is divided into two primary stages of tectonic evolution, i.e., a generally passive continental margin terrace stage that existed from the Paleozoic to the early-middle Jurassic with up to 20 km thickness of carbonates dominated sediments resting on pre-Cambrian crystalline basement, and a late Jurassic to early Eocene foreland basin stage with most clastic rocks, which resulted from, to its southwest, the oblique collision of the westward-moving North American plate with the foreign plates and the subsequent overload of northeastward detached, displaced, compressed and stacked sedimentary layers. They are in angularly unconformable contact (Figure 2.3). The total thickness of the sediments tapers from a maximum just east of the foothill front to a zero-edge in the northeast along the Canadian shield (see Figures 2.1 and 2.3).

In the first stage, the basin underwent three cycles of transgression and regression with the main external source of sediments derived from northeast. Earliest inundation occurred in Cambrian until a significant sea level drop in early Ordovician. Sediments included clastics at the east edge westward to carbonates at the shelf to shale at the deep sea. In the end, a marine deposition was restricted to the continental margin. The second transgression from late Ordovician to Silurian led to a lengthy phase of carbonate sedimentation. The third transgression in Devonian spread deep into the continental terrace and formed a reef-dominated shale basin with a broad carbonate-evaporate marginal shelf. Starting from early Carboniferous, the sea level dropped, and to Triassic, the continental terrace was under erosion with some continental sedimentation, marking the demise of this stage of tectonic evolution.

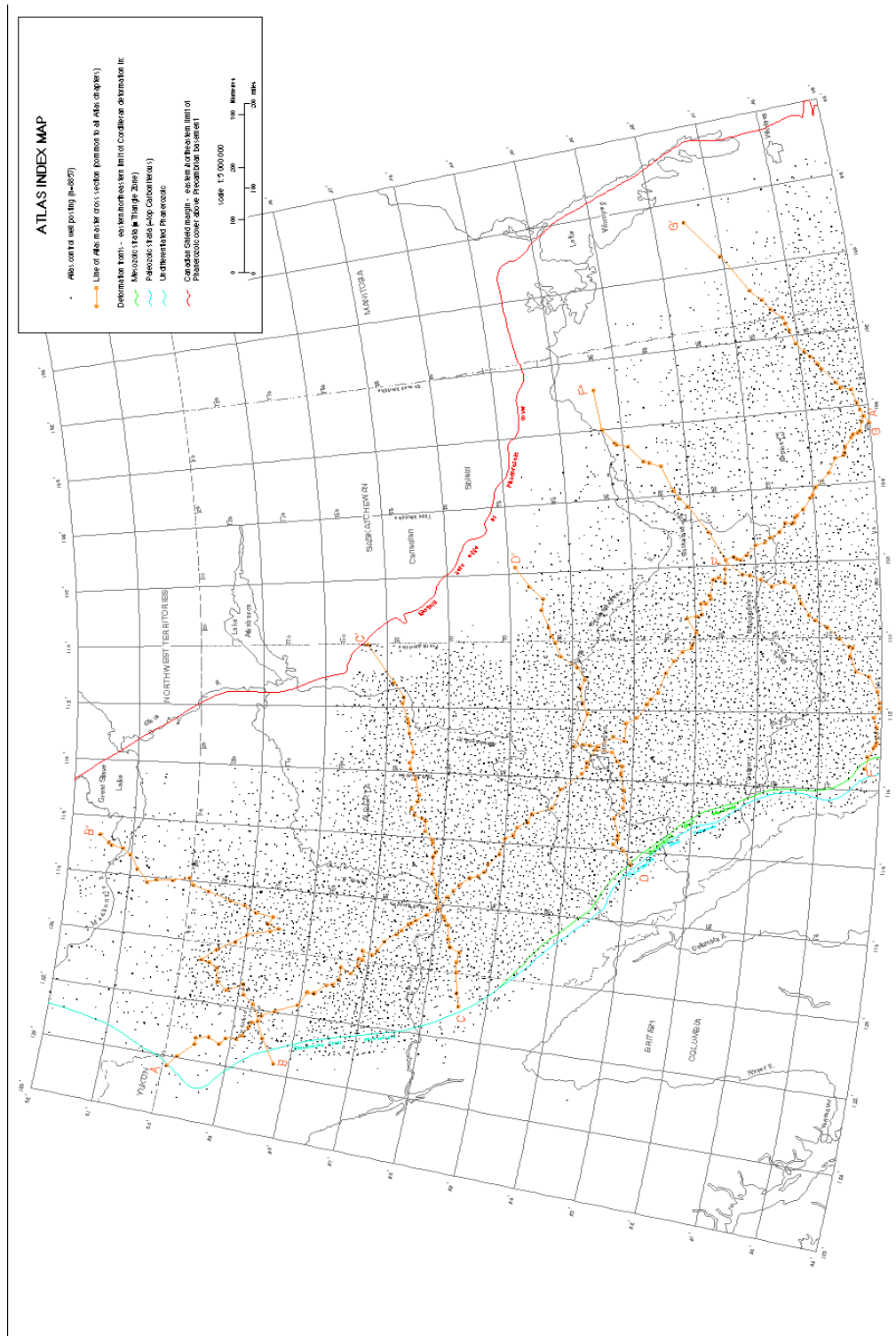


Figure 2. 2 Index map of atlas subsurface control showing the designated "atlas control wells" and the lines of regional "master" cross-sections.

(http://www.ags.gov.ab.ca/publications/wcsb_atlas/A_CH01/ch_01.html)

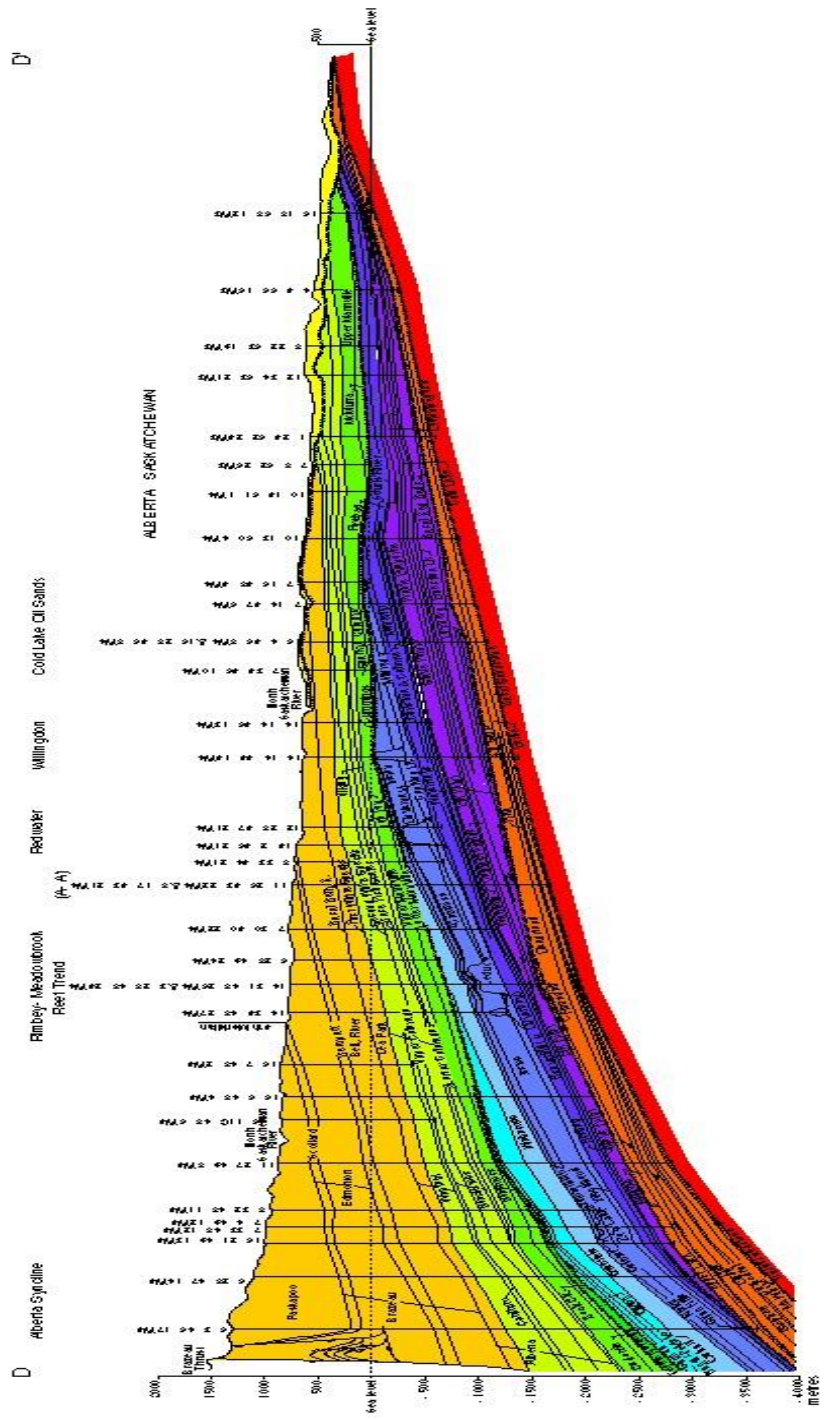


Figure 2.3 Geological cross section along the line D-D' in Figure 2.2 (http://www.ags.gov.ab.ca/publications/ATLAS_WWW/A_CH03/FG03_04L.s.html).

In the second stage, in response to the multi-phase collision of the craton with the foreign plates, there developed five corresponding depositional cycles each representing strata bounded by major unconformities or lithologic changes (after Cant and Stockmal, 1989). The lowermost cycle of the foreland basin succession contains the Fernie-Kootenary group from late Jurassic to earliest Cretaceous as a result of the collision and accretion of the Intermontane belt (foreign plate) located in Canadian Cordilleran (after Leckie and Smith, 1992). The foreland basin was narrow and elongate, the source of sediments came from the uplifted thrust and stacked zones, and, Omineca belt (the suture between the Intermontane belt and the craton). Lithofacies started from marine and ended in continental clastics with the thickness of 2.7 km in the foothills. Afterwards, there was the 12 Ma hiatus of widespread extension, which suggests a significant period of tectonic quiescence (Cant and Stockmal, 1989). Then the collision and subsidence renewed and the second cycle of the Mannville group was deposited on the irregularly eroded surface. The general topography of this phase was tilted toward the northwest, where a deep sea long persisted, and it was complicated by a series of regional highs. At the beginning of this cycle, continental sediments predominated, including alluvial fans and fluvial facies with the drainage system and channels toward the northwest. Subsequently, flooding from north occurred and the transgression continued southward across Alberta. At its maximum, eastern British Columbia, Alberta and Saskatchewan were inundated, leaving only isolated highs. Thick clastic sediments prograded northward across the foreland basin, forming extensive flood plain and stacked shoreline sandstones and conglomerates (Leckie and Smith, 1992), as shown in Figure 2.4. In the end, sea water retreated and most areas were subject to erosion. After a short while of uplift (Cant and Stockmal, 1989), the third cycle of the Colorado group developed corresponding to a long period of global sea level rise. It contained three sub-order sequences of transgression and regression.

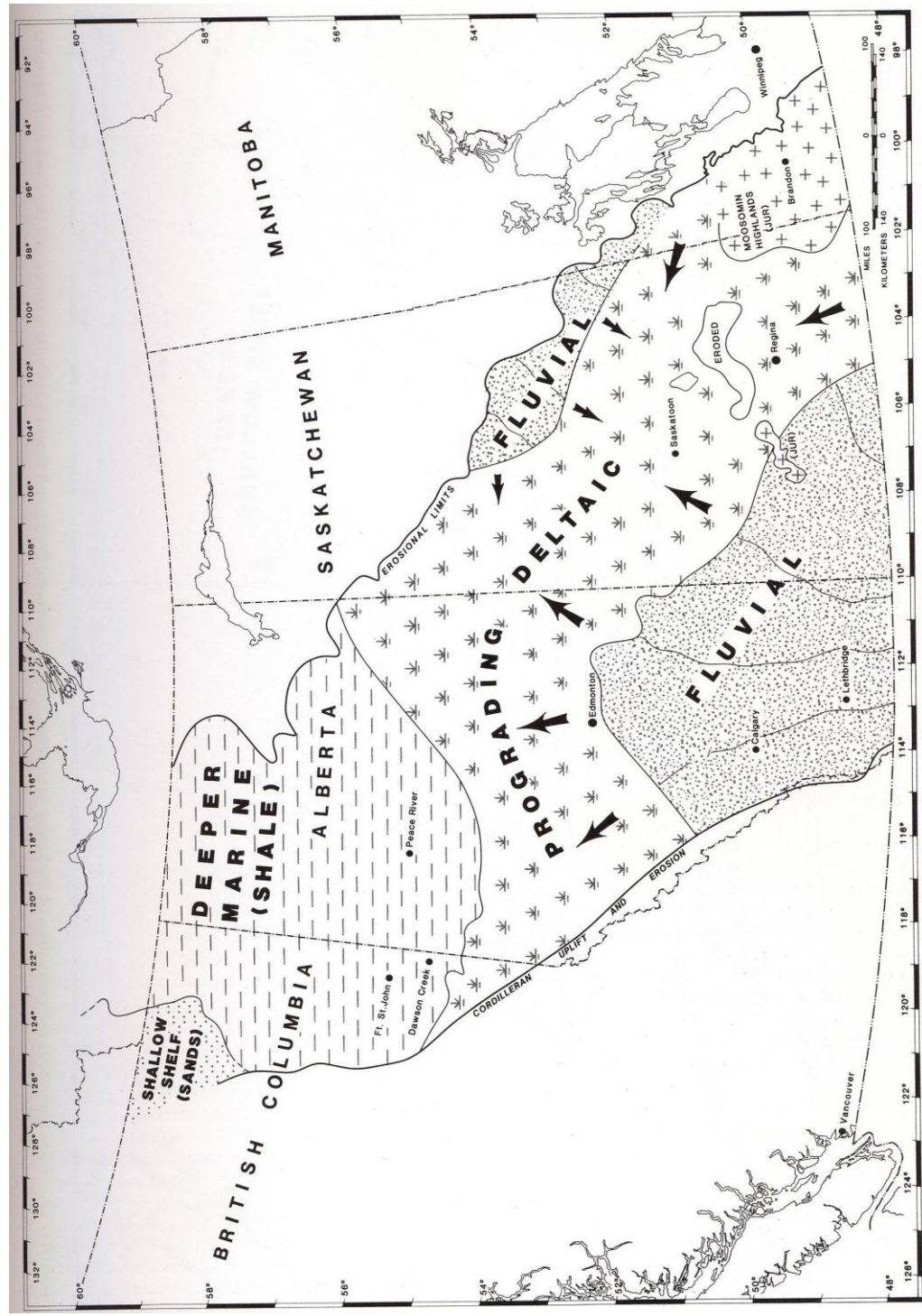


Figure 2. 4 Paleogeography at deposition of the Clearwater formation (Leckie and Smith, 1992).

In late Cretaceous to early Eocene, the renewed collision and subsidence generated the fourth cycle of sedimentation dominated by nonmarine clastic detritus. The top of this cycle represents a wide-range of erosion and it marks the end of the foreland basin. The sediments on this unconformity are unconsolidated, incised-valley fill sands and gravels on isolated locations in Tertiary and a wide cover of glacier drifts in Quaternary. This sequence may be collectively called the fifth cycle of sedimentation.

During the two stages of basin development as outlined above, there are at least nine sources rocks spanning in age from Ordovician to the third cycle of the foreland basin. They have been thermally mature in the deeply-buried western half of Alberta. When other essential conditions (migration, trap and caprock) were satisfied, hydrocarbon accumulations had happened within or away from them. In the former case, conventional oil reserves were formed. In the latter case, hydrocarbon migrated updip for a long distance along the pathways like the unconformity between Paleozoic and Cretaceous. Due to meteoric water infiltration, biodegradation occurred and oil was degraded to the heavy oil and bitumen. Peace River, Athabasca and Cold Lake are three examples of these super oil charges and later degradation.

CHAPTER 3 RESERVOIR CHARACTERIZATION

3.1 Introduction

The study area is located in the Western Canada Sedimentary Basin and the target zone is the lower-Cretaceous Clearwater reservoir of oil sands buried in a depth of approximately 410 to 470 meter (Figures 3.1 and 3.2). As shown in Figure 2.4, the Clearwater formation was deposited in a prograding deltaic environment during the middle of the second depositional cycle of the foreland basin stage (Leckie and Smith, 1992) and sea water from north invaded the area regularly. Reservoir sands contain feldspar, volcanic fragments, quartz and chert etc. predominantly in channel fills facies.

Since 1986 the oil company has produced heavy oil using CSS (cyclic steam stimulation) in this area. Recently they drilled five horizontal wells into the middle of the Clearwater reservoir in an untapped patch (Figures 3.1 and 4.1) in an attempt to enhance recovery efficiency. CSS recovery processes started late in 1997 and have since continued to the present. To forecast thermal fronts and fluid flow with recovery progression in the aid of development plans and reservoir management, reservoir simulation is conventionally employed to find the distribution of saturation, pressure and temperature with time. In this chapter, a reservoir characterization model (that is a necessary input to reservoir simulation) will be established from well logs, core observations and measurements, 3-D seismic data and other sources of information.

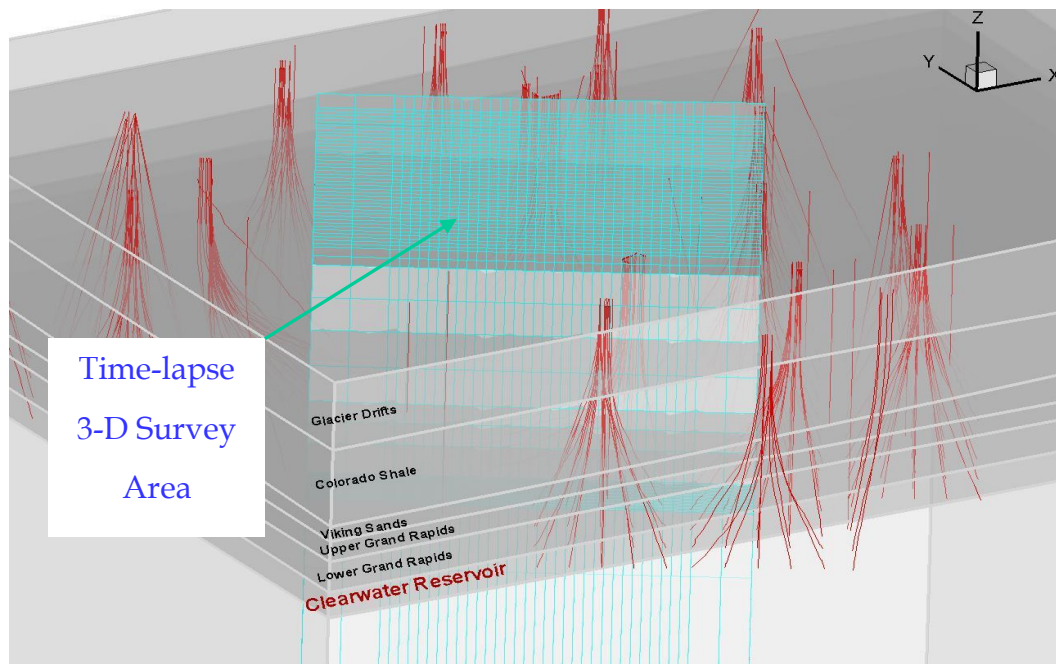


Figure 3.1 3-D visualization of the formations and development wells
(x points to east and y to north, the same below)

3.2 Reservoir geometry

The Clearwater formations bounded on bottom by the McMurray formation and on top by the Grand Rapids formation. It belongs to the upper Mannville group. A shale layer of a few meters on the top serves as the caprock to seal the reservoir. The oil saturated sands in the reservoir are identified in well logs by low Gamma ray, low SP potential, and high electrical resistivity. Figure 3.2 shows a typical set of well log curves. From shale to oil sands, SP, Gamma ray and resistivity logs undergo a substantial change, while sonic, neutron porosity and density logs do not alter significantly. This presents a disadvantage of being difficult to seismically delineate the reservoir geometry. We picked the tops and the bottoms of the reservoir on all available well logs (available wells indicated in Figure 3.1) in this region and fitted a second-order polynomial surface to the top

and bottom boundaries. The misfit between the actual value and the one computed from trend analysis is on the average of 4.7 meters. Figures 3.3 and 3.4 visualize in three-dimension the reservoir geometry.

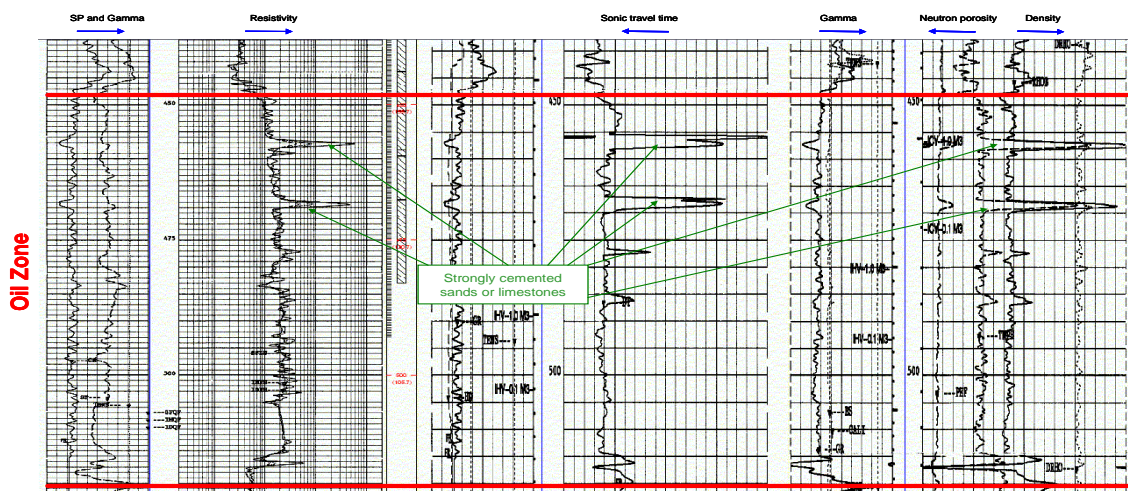


Figure 3. 2 Typical well logs for the Clearwater Formation

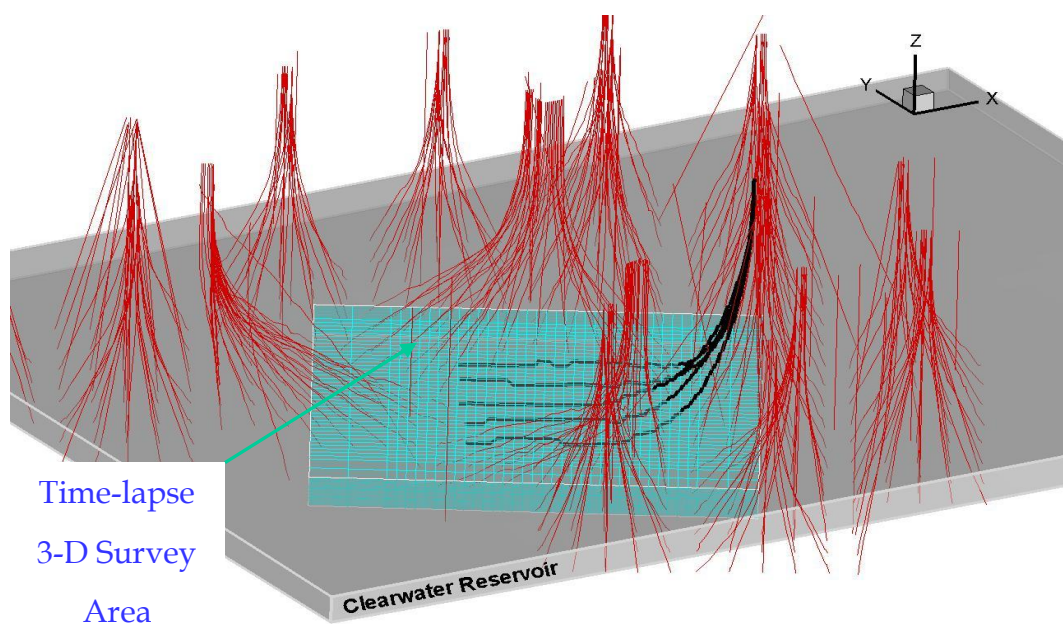


Figure 3. 3 3-D visualization of the reservoir, development wells and target area

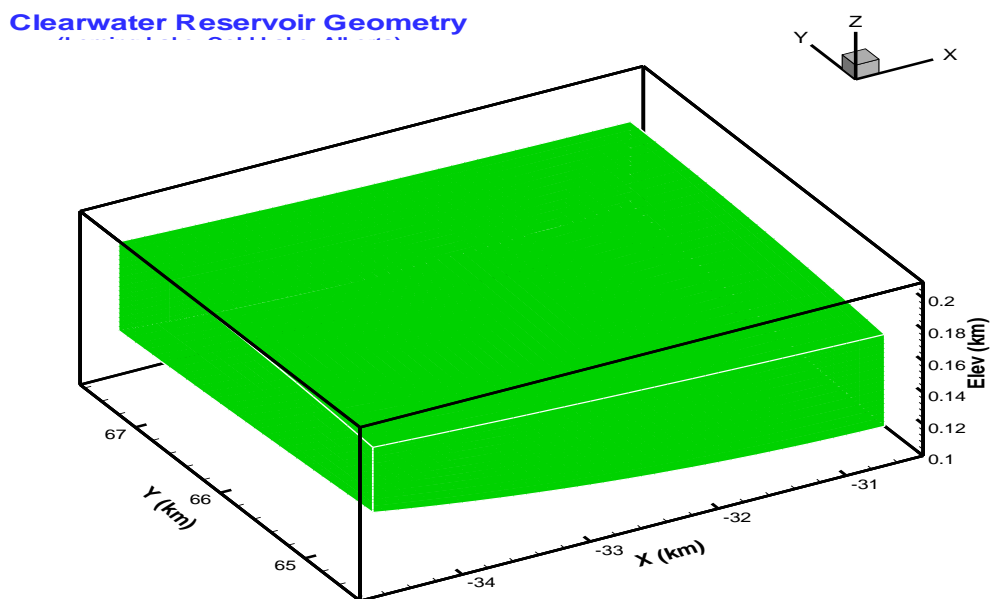


Figure 3. 4 3-D visualization of the Clearwater reservoir

3.3 Reservoir structure

From all available well logs in this region we found that the well log curves of Gamma ray and Spontaneous Potential take almost constant low values from the top to the bottom of the reservoir (see Figure 3.2). As indicated in Figure 3.5, the values of Gamma ray logs from forty-five wells center predominantly between 40-60 API units. The core samples as exhibited in Figures 3.6-3.10 do not bear any shale interbeds within the reservoir. It is inferred that shale interbeds as significant barriers to the across-bed fluid flow may not occur in this specific case.

On the other hand, we can identify aberrant values of high electrical resistivity, high sonic velocity, high density and low porosity from well log curves such as in Figure 3.2. From lap reports (Figure 3.11) and core observations

(Figures 3.6-3.10), these spikes represent limy sands or limestones (called tight rocks or strings). These calcite cements probably precipitated at the early stage of burial due to mixing of marine and meteoric waters (Potocki and Hutcheon, 1992). The dissolution and albitization of feldspar grains and volcanic materials may have provided another source of Ca^{2+} (Surdam and Boles, 1979). The cementation may favor locations with nucleating materials such as clay (Hall et al., 2004).

There are cores from fifteen wells sampled continuously from the top to the bottom of the reservoir. Porosity measurements of these core samples (total of 2343 measurements) demonstrate statistically a bimodal distribution. An overwhelming number of porosities are between 30% and 40% (oil sands), and a few take a very low value or zero (tight strings), as shown in Figure 3.12. It can then be assumed that the reservoir body is composed predominantly of oil sands with randomly dispersed tight strings.

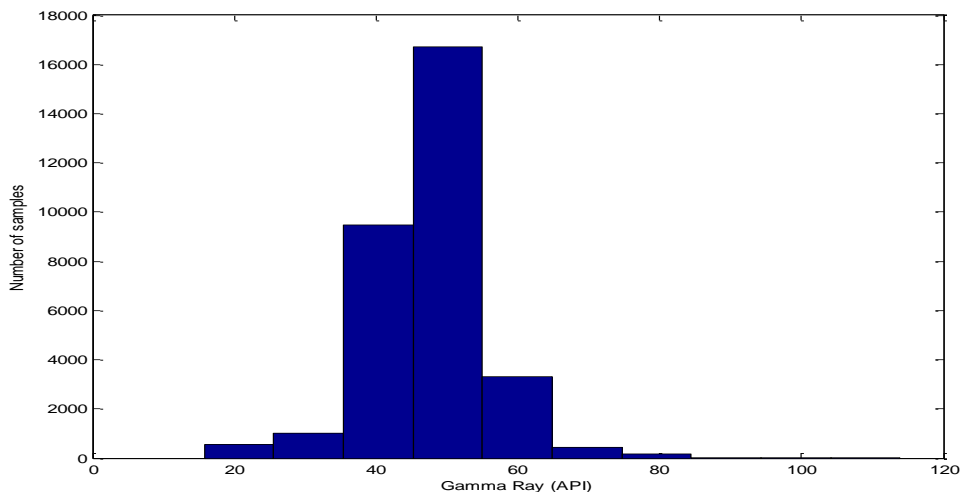


Figure 3. 5 Histogram of Gamma ray log value (API) from forty-five wells



Figure 3.6 Cores of cap rock and reservoir rock (oil sands)

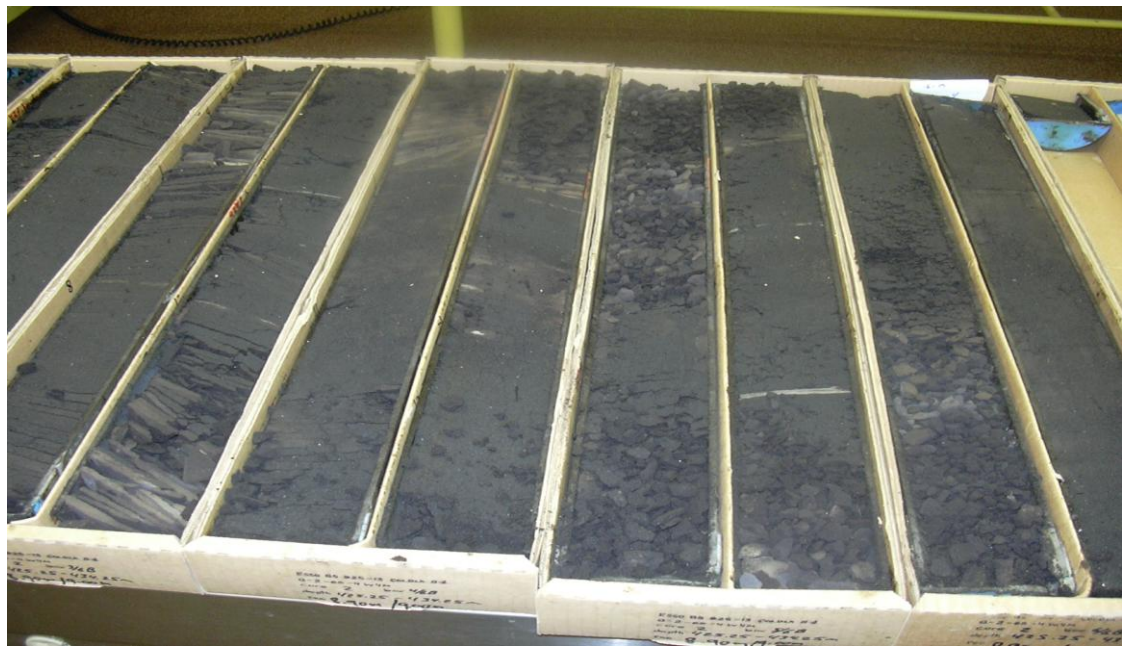


Figure 3.7 Cores of reservoir rock (oil sands)

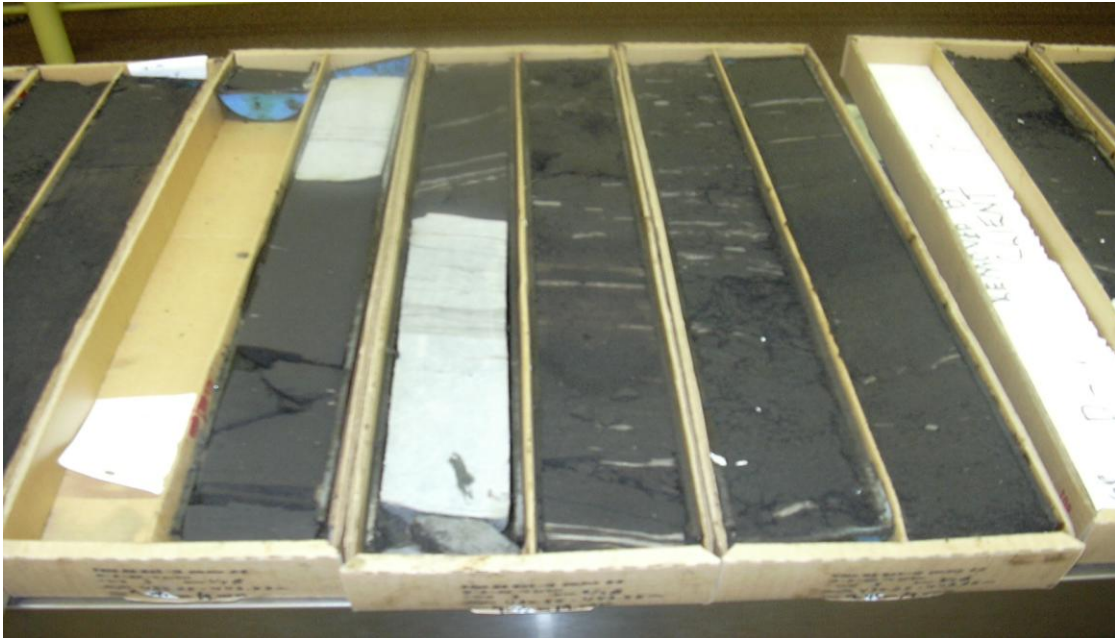


Figure 3. 8 Cores of reservoir rock (oil sands)

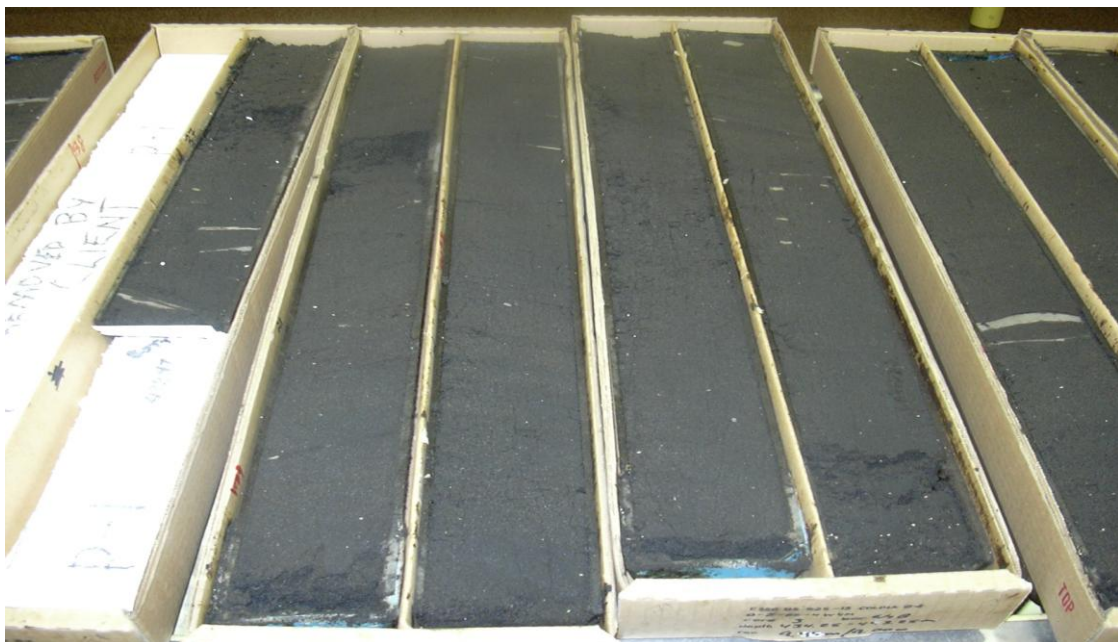


Figure 3. 9 Cores of reservoir rock (oil sands)

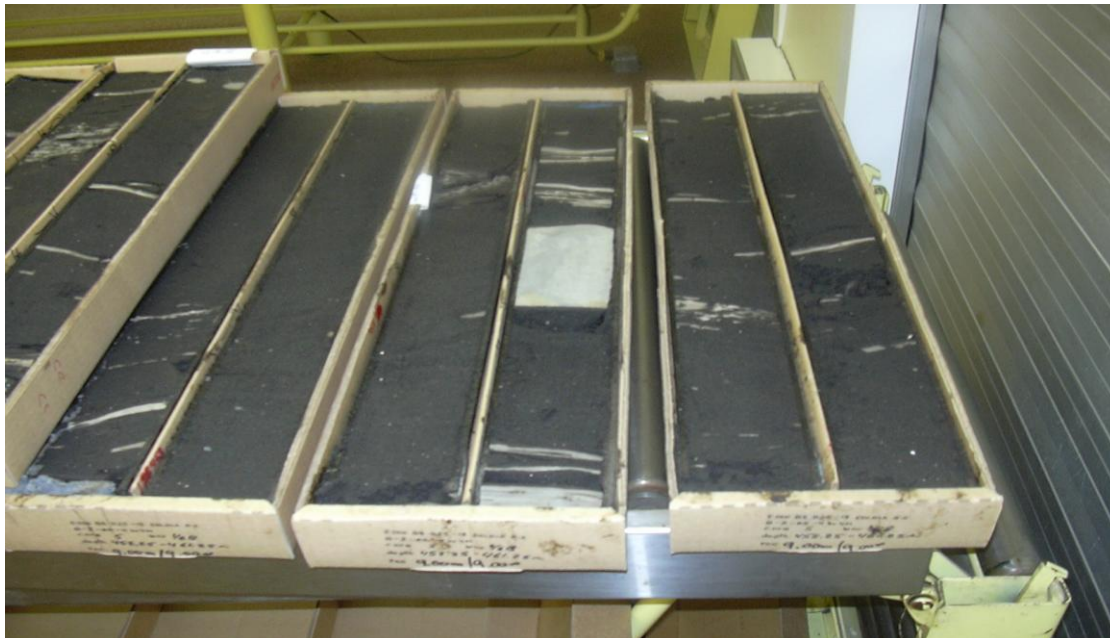


Figure 3.10 Cores of reservoir rock (oil sands)

Lithology											
B	C	D	E	F	G	H	I	J	K	L	M
Sample Ba	Thickness	Sample Forms	Sample To	Porosity	KMax (mD)	Lithology	RSat	Oil RRSat	Wtr f	Bulk Dens	K90 (mD)
725.71	0.39	CLRWTSD	725.32	0	0	SS VF SHY LMY	0	0	0	0	0
726.12	0.41	CLRWTSD	725.71	0.357	0	SS VF F SSHY	0.776	0.224	0	0	0
726.67	0.55	CLRWTSD	726.12	0.361	0	SS VF F SSHY	0.674	0.326	0	0	0
726.82	0.15	CLRWTSD	726.67	0	0	SS VF SSHY LMY	0	0	0	0	0
727.35	0.53	CLRWTSD	726.82	0.362	0	SS VF F SSHY	0.776	0.224	0	0	0
727.89	0.54	CLRWTSD	727.35	0.339	0	SS VF F SSHY	0.726	0.274	0	0	0
728.38	0.49	CLRWTSD	727.89	0.353	0	SS VF F	0.718	0.282	0	0	0
728.88	0.5	CLRWTSD	728.38	0.35	0	SS VF F SSHY	0.71	0.29	0	0	0
729.38	0.5	CLRWTSD	728.88	0.346	0	SS VF F SSHY	0.741	0.259	0	0	0
729.89	0.51	CLRWTSD	729.38	0.346	0	SS VF F SSHY	0.712	0.288	0	0	0
730.39	0.5	CLRWTSD	729.89	0.349	0	SS VF F SSHY	0.726	0.274	0	0	0
730.87	0.48	CLRWTSD	730.39	0.361	0	SS VF F SSHY	0.684	0.316	0	0	0
731.39	0.52	CLRWTSD	730.87	0.351	0	SS VF F	0.684	0.316	0	0	0
731.88	0.49	CLRWTSD	731.39	0.348	0	SS VF F	0.691	0.309	0	0	0
732.48	0.6	CLRWTSD	731.88	0.335	0	SS VF F SSHY	0.651	0.349	0	0	0
732.85	0.37	CLRWTSD	732.48	0	0	SS VF SSHY LMY	0	0	0	0	0
733.37	0.37	CLRWTSD	733	0	0	SS VF SSHY LMY	0	0	0	0	0
733.79	0.42	CLRWTSD	733.37	0.333	0	SS VF F SSHY	0.462	0.538	0	0	0
733.98	0.19	CLRWTSD	733.79	0	0	SS VF SHY LMY	0	0	0	0	0
734.23	0.25	CLRWTSD	733.98	0.333	0	SS VF F SSHY	0.349	0.651	0	0	0
734.28	0.05	CLRWTSD	734.23	0	0	SS VF SHY LMY	0	0	0	0	0
734.38	0.1	CLRWTSD	734.28	0.333	0	AST SS VF F SSHY	0.349	0.651	0	0	0
734.88	0.5	CLRWTSD	734.38	0.351	0	SS VF F SSHY	0.642	0.358	0	0	0
735.38	0.5	CLRWTSD	734.88	0.361	0	SS VF F SSHY	0.736	0.264	0	0	0
735.89	0.51	CLRWTSD	735.38	0.337	0	SS VF F SSHY	0.564	0.436	0	0	0
736.39	0.5	CLRWTSD	735.89	0.353	0	SS VF F SSHY	0.766	0.234	0	0	0
736.89	0.5	CLRWTSD	736.39	0.353	0	SS VF F SSHY	0.75	0.25	0	0	0
737.4	0.51	CLRWTSD	736.89	0.347	0	SS VF F SLTST INCL	0.714	0.286	0	0	0
737.9	0.5	CLRWTSD	737.4	0.355	0	SS VF F SSHY	0.755	0.245	0	0	0
738.4	0.5	CLRWTSD	737.9	0.373	0	SS VF F SSHY SLTST INCL	0.745	0.255	0	0	0
738.9	0.5	CLRWTSD	738.4	0.376	0	SS VF F SLTST INCL	0.789	0.211	0	0	0

Figure 3.11 Lab report

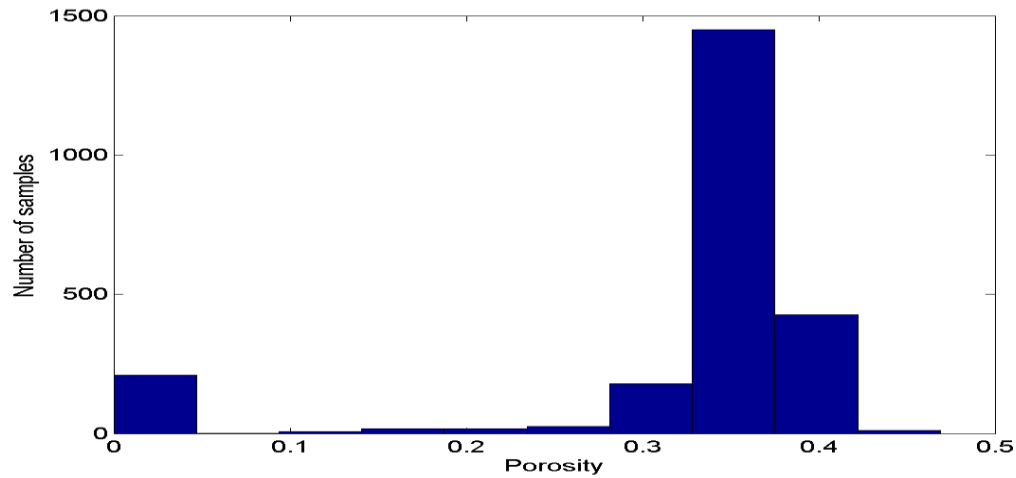


Figure 3. 12 Histogram of porosity measurements of core samples from fifteen wells

3.4 Population of porosity and permeability of oil sands

To populate porosity in oil sands accurately, more information is needed. In addition to porosity measurements from fifteen wells, we generated data from eleven wells with well logs, from which porosity was calculated. The following details the procedure.

The principle of deriving porosity from neutron porosity log and density porosity log is based on the following equations (Serra, 1986):

$$\phi_N = \phi \phi_{N-p} + V_{sh} \phi_{N-sh} + (1-\phi-V_{sh}) \phi_{N-s} \quad 3.1$$

$$\phi_D = \phi \phi_{D-p} + V_{sh} \phi_{D-sh} + (1-\phi-V_{sh}) \phi_{D-s} \quad 3.2$$

where ϕ_N , ϕ_{N-p} , ϕ_{N-sh} and ϕ_{N-s} are neutron porosity log values for fluid-saturated sands, pore fluids, shale and solid grains respectively; ϕ_D , ϕ_{D-p} , ϕ_{D-sh} and ϕ_{D-s} are

density porosity log values for fluid-saturated sands, pore fluids, shale and solid grains respectively; ϕ is the unknown porosity we want to solve; V_{sh} is the volume fraction of shale content. For clean wet sands or sandstones, $\phi_{N-p} = \phi_{D-p} = 1$, $V_{sh}=0$, $\phi_{N-s} = \phi_{D-s} = 0$. Equations 3.1 and 3.2 are simplified as $\phi_N = \phi_D = \phi$. The cross plot of ϕ computed from equation 3.1 (called corrected neutron porosity) and ϕ computed from equation 3.2 (called corrected density porosity) is the same as that of ϕ_N and ϕ_D , which is a straight line $y=x$. In this area, however, sands are filled with both heavy oil and water and contain clay and limy cements. We need to make a calculation of the unknown porosity (ϕ) both from raw neutron porosity log and raw density porosity log, and then plot the pair of values to see if the points are scattered along the straight line $y=x$. If yes, the calculation is suitable. Otherwise, we must go back and re-select the parameters for calculation. The parameters in equations 3.1 and 3.2 are set in the following way. Neutron porosity and density porosity log values for a mixture of heavy oil and water (ϕ_{N-p} and ϕ_{D-p}) are nearly one. The volume shale content (V_{sh}) was computed from $V_{sh} = (G - G_{min}) / (G_{max} - G_{min})$, where G is Gamma ray units, G_{min} and G_{max} are the minimum and maximum Gamma ray units, respectively. Generally, G_{min} and G_{max} take the values of pure sands and pure shale, respectively. ϕ_{N-sh} and ϕ_{D-sh} are ϕ_N and ϕ_D at $G=G_{max}$. Neutron porosity log values for solid grains (ϕ_{N-s}) are zero, but density porosity log values for solid grains (ϕ_{D-s}) may be some value since grains include partly calcite cements.

Figure 3.13 displays the cross plot of corrected neutron and density porosities from one well. The points scatter roughly along the straight line, $y=x$. Figure 3.14 is the histogram of porosity calculations from eleven wells, which is very similar to Figure 3.12. Most data fall within the range of 30% to 40%. The main difference is that it has no zero values because neutron and density

porosity logs unlike core measurements can detect the disconnected pores in tight strings.

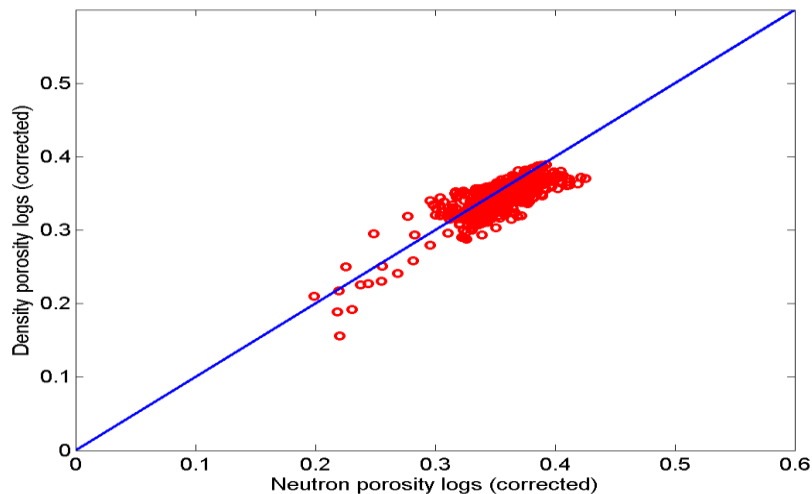


Figure 3. 13 Cross plot of corrected neutron porosity and corrected density porosity logs

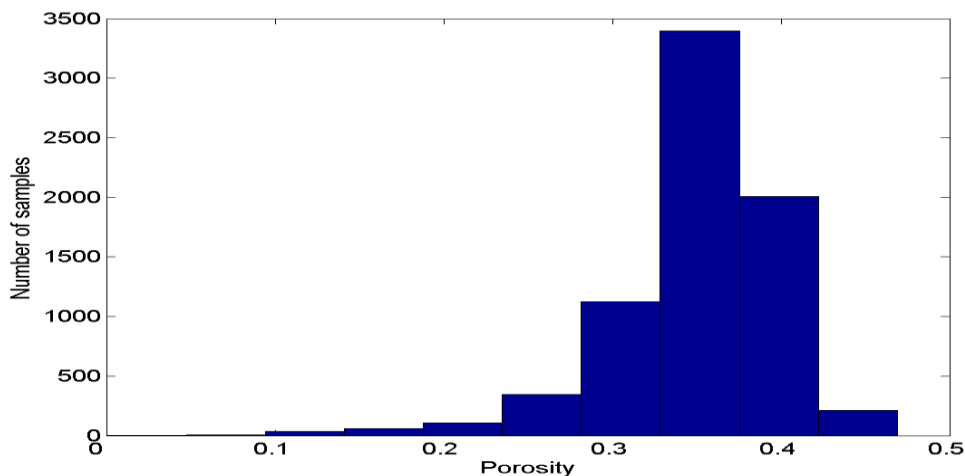


Figure 3. 14 Histogram of porosity calculations from eleven wells

With porosity measurements and porosity calculations for these wells, we can use the inverse distance weight method to interpolate or extrapolate porosity

of oil sands at locations without well control. Figure 3.15 is the result of this operation, where the contour colour denotes porosity and the red lines represent wells with either porosity measurements or porosity calculations.

To populate permeability in oil sands appears to be intractable since data are scant and no relationship between porosity and permeability can be found from core measurements. We assume in the thesis $K_x=K_y=2000$ md and $K_z=650$ md.

3.5 Distribution of tight strings

After the population of porosity and permeability of oil sands was carried out as described above, the following task is to find the spatial distribution of tight strings and put them into the reservoir body. As indicated in Figure 3.2, tight strings in the Clearwater reservoir are identified in wells and are characterized in well logs by spikes of high resistivity, low sonic travel time, low neutron porosity and high density. We picked as tight strings the spikes of high resistivity in the oil zone for 250 wells, 27 of which were verified by sonic, neutron porosity and density logs. The number of these spikes seems to change randomly from well location to well location without any preferential directions, which may imply the stationarity of this variable (number of tight strings), as seen in Figure 3.16.

Based on the well log picks of the spikes from 250 wells, a model variogram for the number of these spikes per well location was constructed using standard geostatistical procedures (Isaaks, 1989; Olivier, 2003) and is shown in Figure 3.17. The mathematical form for the model variogram is:

$$\gamma(h) = \gamma_0 + \gamma_1 [1 - \exp(-3h/2)] \quad 3.3$$

where $\gamma(h)$ is variogram, h is distance (km); γ_0 is 1.3; γ_1 is 0.7. From equation 3.3, the number of tight strings for all locations in the reservoir x y plane was estimated from these 250 wells using universal Kriging. Once the number of these tight strings was populated in the reservoir x y plane, they were placed along the vertical section at each x y location on the assumption that placements are random since we do not observe from well logs any horizontal connection for these spikes. As exhibited in Figure 3.18, the irregularly distributed tight strings were placed back into the reservoir body using the above geostatistical model. The porosity and permeability of tight strings are set to be zero in sharp contrast to those of oil sands. The shaded area around each patch of tight strings is a transition between tight strings and oil sands interpolated by the software.

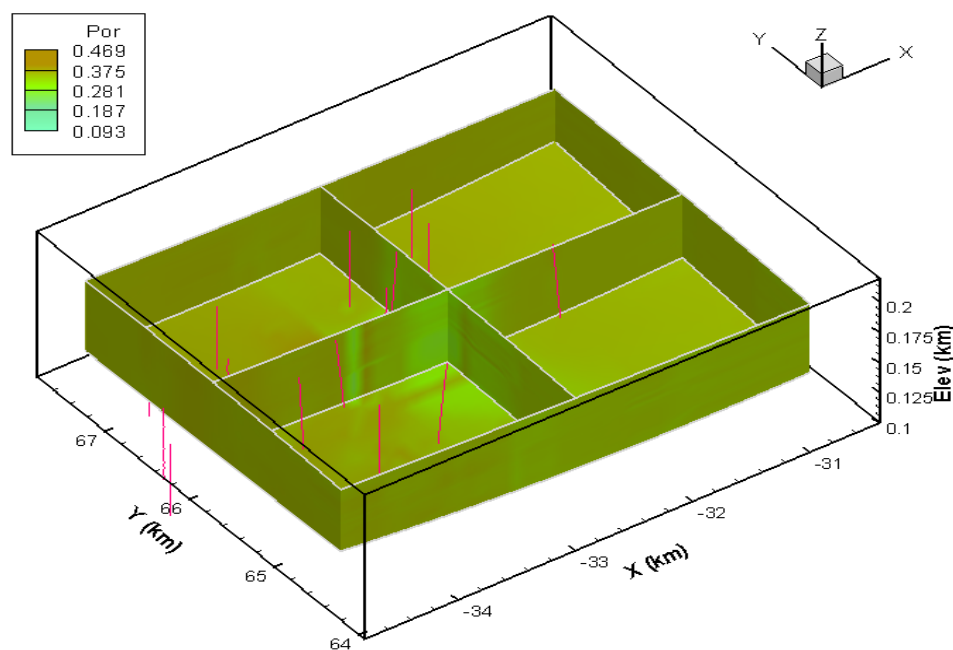


Figure 3. 15 3-D visualization of the porosity distribution of oil sands in the reservoir

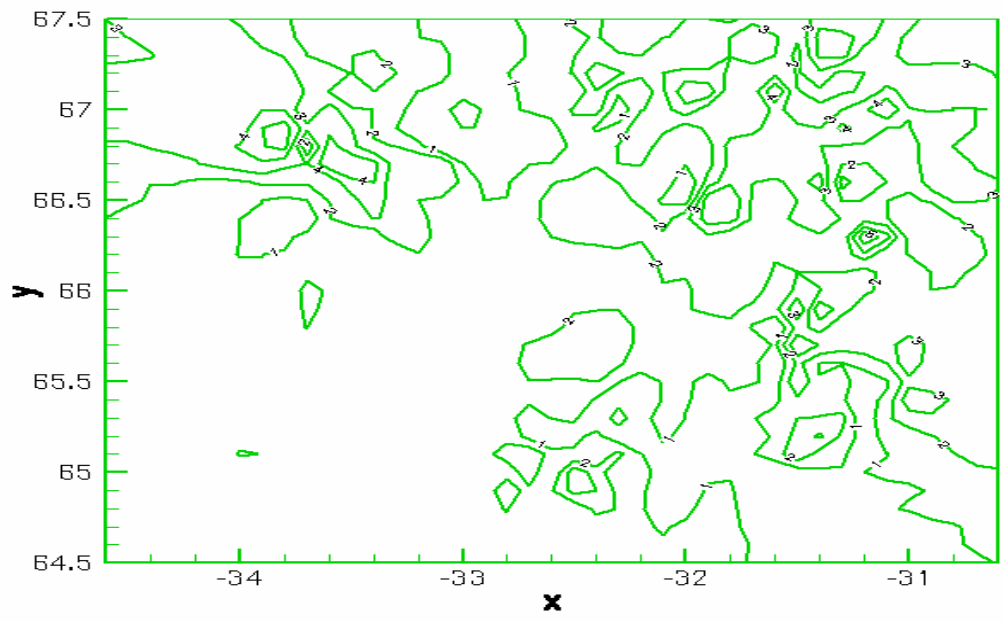


Figure 3. 16 Contour of the number of tight strings per well location (based on the counts of tight strings on well locations)

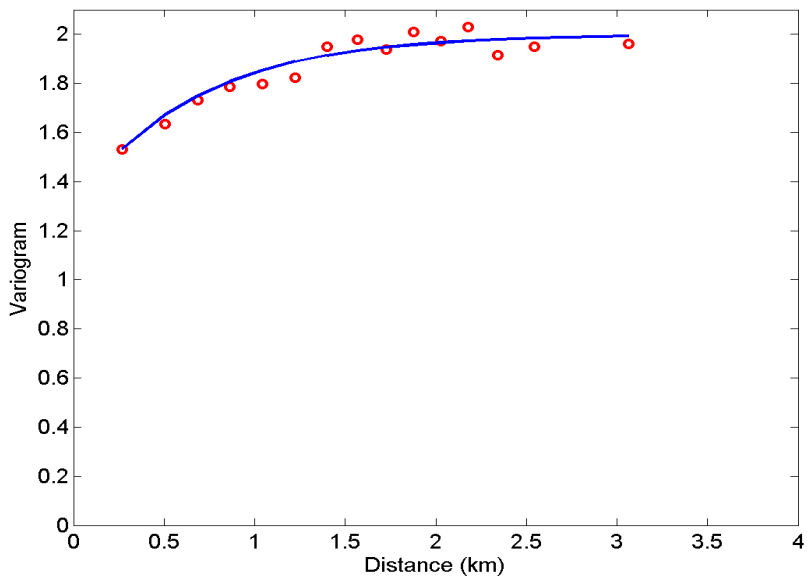


Figure 3. 17 Variogram model with the number of tight strings per location as the random variable

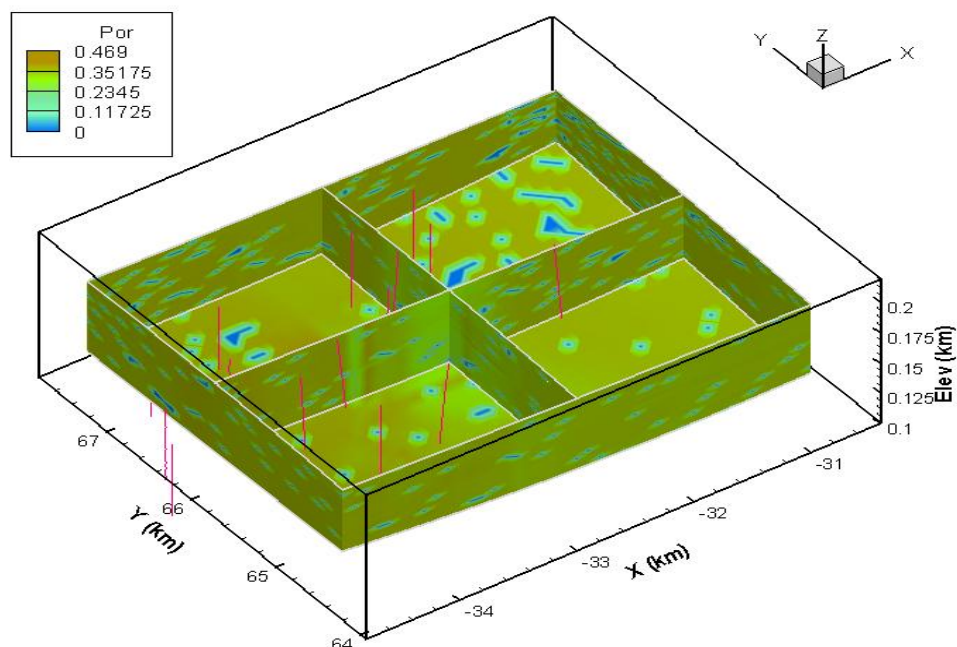


Figure 3. 18 3-D visualization of the porosity distribution of the reservoir body

3.6 Tight strings picked from 3-D seismic data

A simple reservoir characterization model has been established above from integration of all available core samples and well logs in this region using geostatistical methodology. If no other information becomes available, the section of the model drilled by the five horizontal wells can serve as an input for reservoir simulation. To monitor thermal fronts and fluid flow, the oil company shot 3-D baseline and monitor line seismic surveys to cover the area drilled by the five horizontal wells, as demonstrated in Figures 3.1 and 4.1. This section deals with picks of tight strings from these 3-D seismic surveys.

In this seismic-covered area, there are a few wells (Figure 3.19) with sonic and density logs. The synthetic seismogram (Figure 3.20) for one well indicates that it is feasible to use seismic data to pick these tight strings. The wavelet we

employed for synthetics is the Ricker wavelet with the dominant frequency of 80 Hz, which represents the dominant frequency of 3-D seismic data. As seen, the synthetic seismic has almost the same vertical resolution as well logs to pick these tight strings. Moreover, an important advantage for seismic picks is that they have far better horizontal resolution. Wells are at least 100 meter apart, while 3-D seismic here has a bin size of 10 m by 10m.

The reservoir top on the seismic section was found to be located around 410 ms. The bottom is not penetrated by the wells and can be estimated to be $410\text{ms} + 60\text{m (thickness)} / 2300\text{m/s (velocity)} * 1000 * 2(\text{two-way travel time}) = 460\text{ms}$. The time window between 410ms - 460 ms, as shown in Figure 3.21, is then defined as the reservoir zone and any seismic attributes extracted from the zone can be interpreted for reservoir properties. On trace displays, the time window for the reservoir looks between 510 ms-560 ms since the seismic

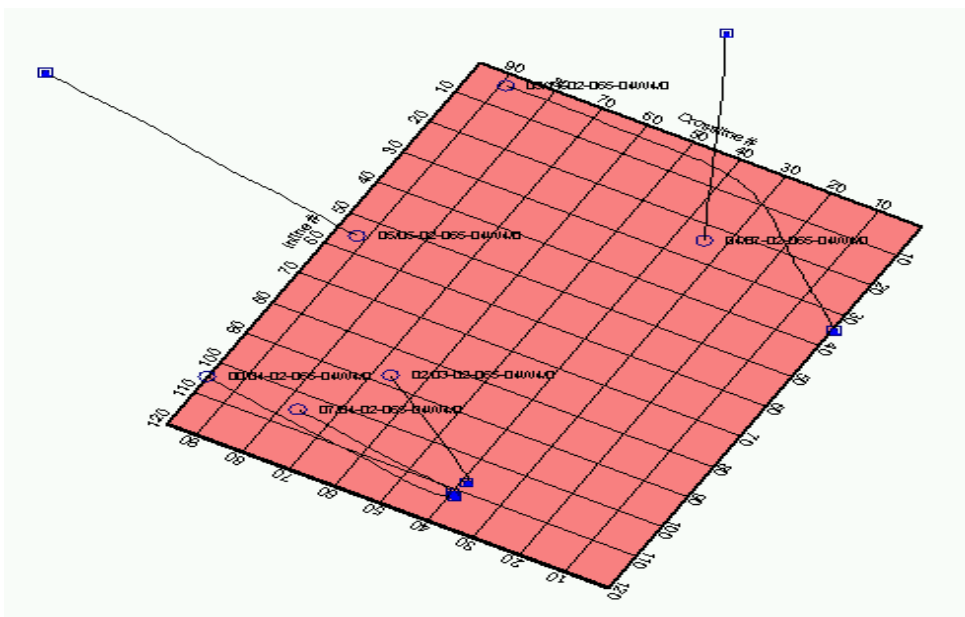


Figure 3. 19 3-D seismic surveys and the wells with sonic and density logs
(blue square: well head; open circle: bottom hole)

traces were bulk shifted by 100ms downward by the processor. We picked the peaks for each trace of the 3-D seismic data volume, as done in Figure 3.22, and assumed that they were seismic responses of tight strings. The minimum value set for the peak to be picked appears to be arbitrary, which would make seismic picks less meaningful. We imposed a constraint and stipulated that this value was such that the number of seismic picks for each trace in the seismic-covered area (Figure 3.23) and the number of well log picks for each well in the region (Figure 3.24) have similar statistical parameters such as minimum, maximum, mean, and similar histograms. As demonstrated in these two figures, the minimum, maximum and mean values are almost the same, and the shape of the histograms is roughly close. To the first order approximation, seismic picks may truly locate the positions of tight strings in the reservoir zone.

Similar to placing the tight strings picked from well logs into the oil sands body we did previously, the tight strings picked from the 3-D seismic volume were put into the sand body, whose porosity was computed by the inverse distance method from data points and whose permeability was assumed to be constant. It is seen from Figure 3.25 and Figure 3.26 that tight strings are scattered over the sand body, showing lateral continuity in some places and random distribution in other places. It is noted that the result in Figure 3.18 can be regarded as a realization with only a certain amount of confidence.

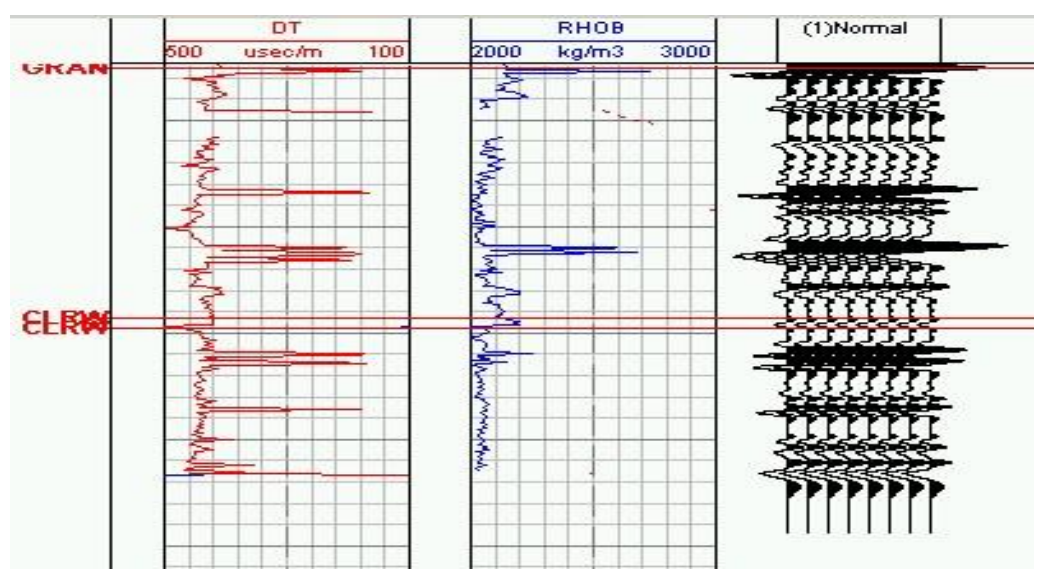


Figure 3. 20 Synthetic seismic traces, sonic and density logs

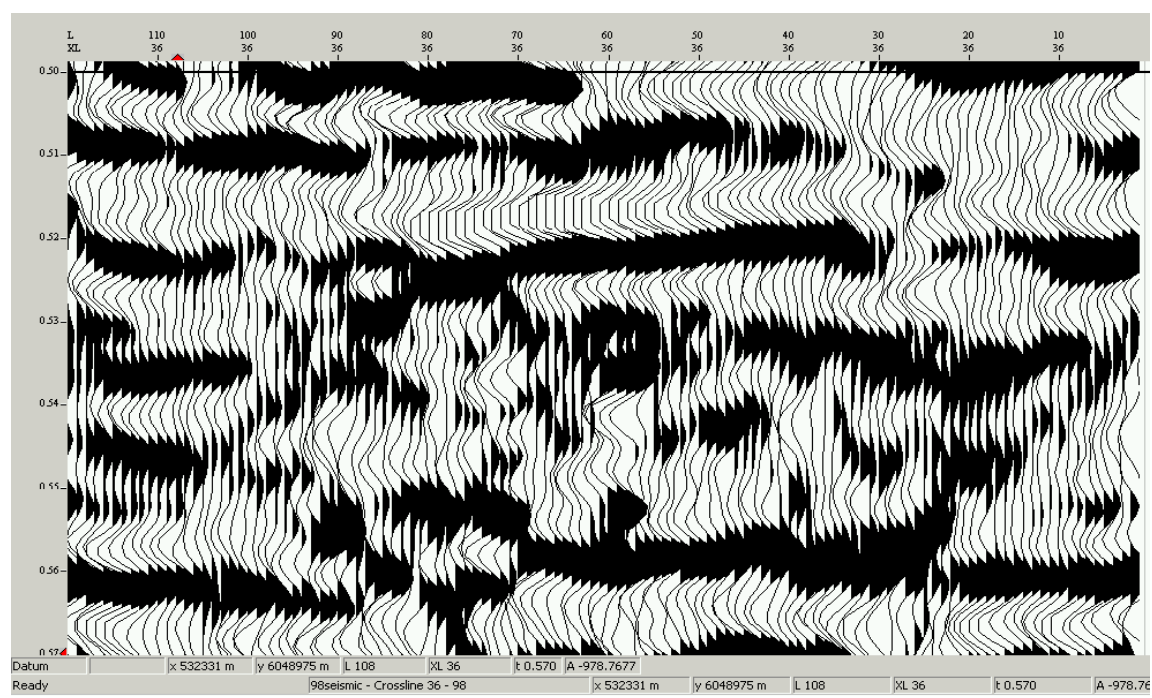


Figure 3. 21 Seismic traces in the time window of 410-460 ms in crossline 36 (time displays 510-560 ms due to a bulk time shift of 100 ms downward)

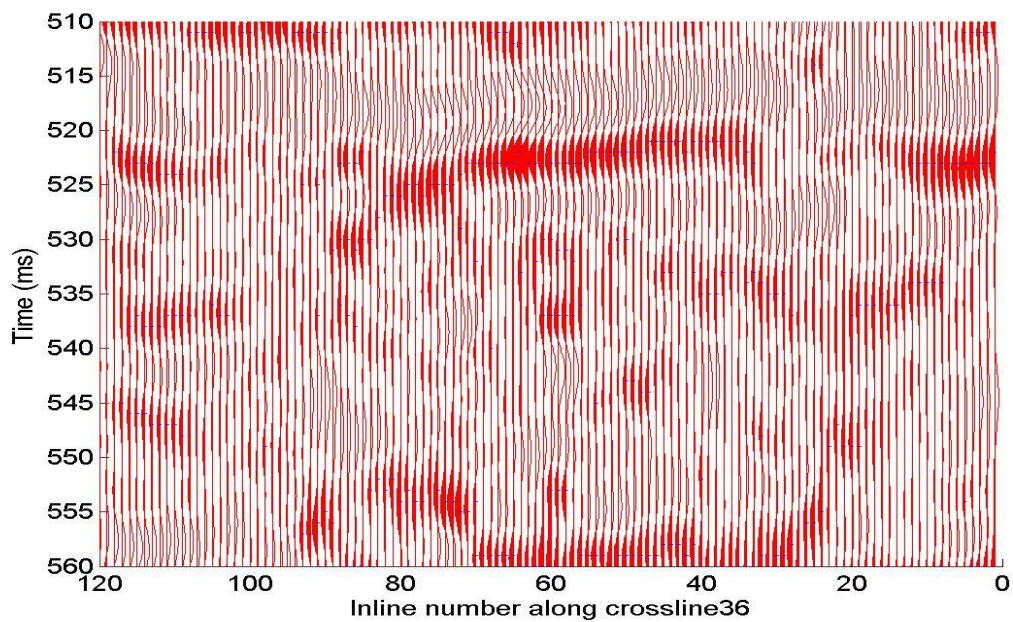


Figure 3. 22 Seismic peak picks (blue lines) in the reservoir window

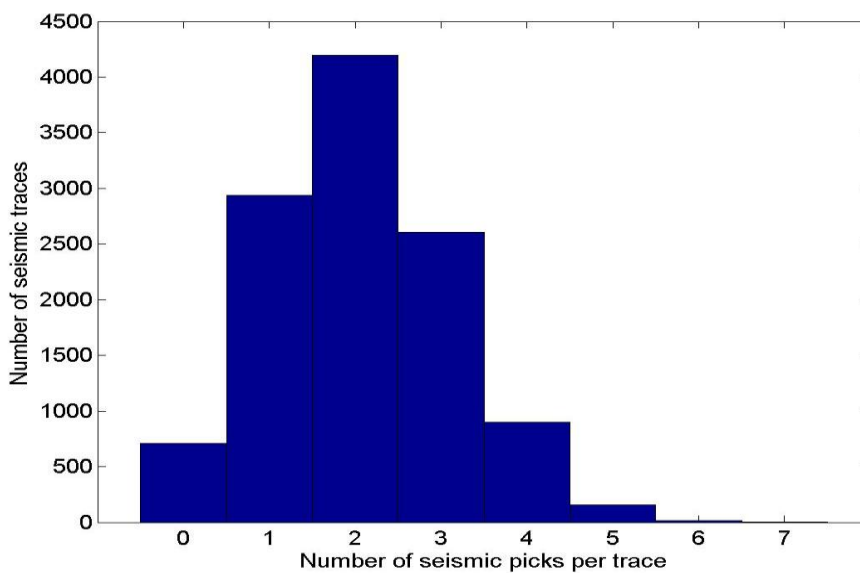


Figure 3. 23 Histogram of the number of seismic picks per trace

Mean=2.05, Min=0, Max=7, STD=1.09

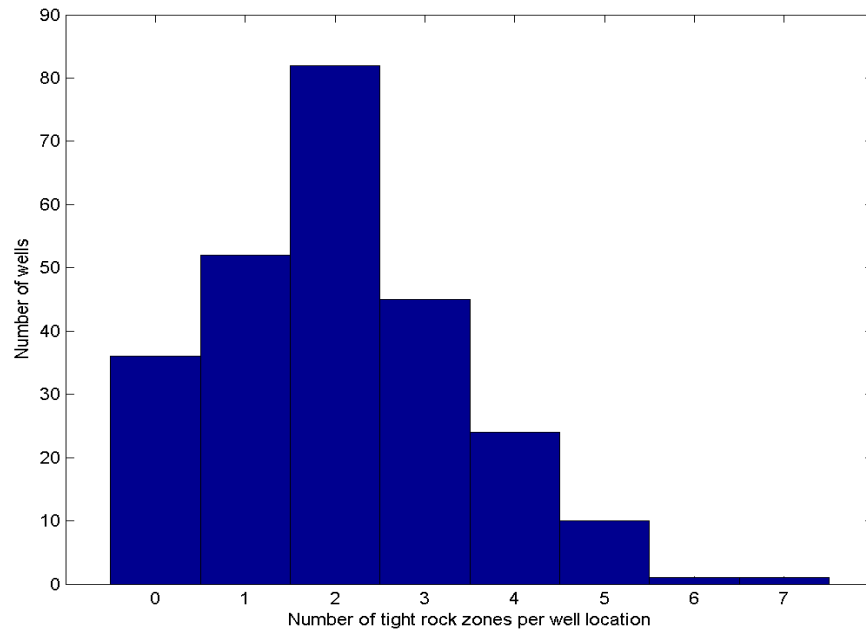


Figure 3. 24 Histogram of the number of well log picks per well

Mean=2.03, Min=0, Max=7, STD=1.37

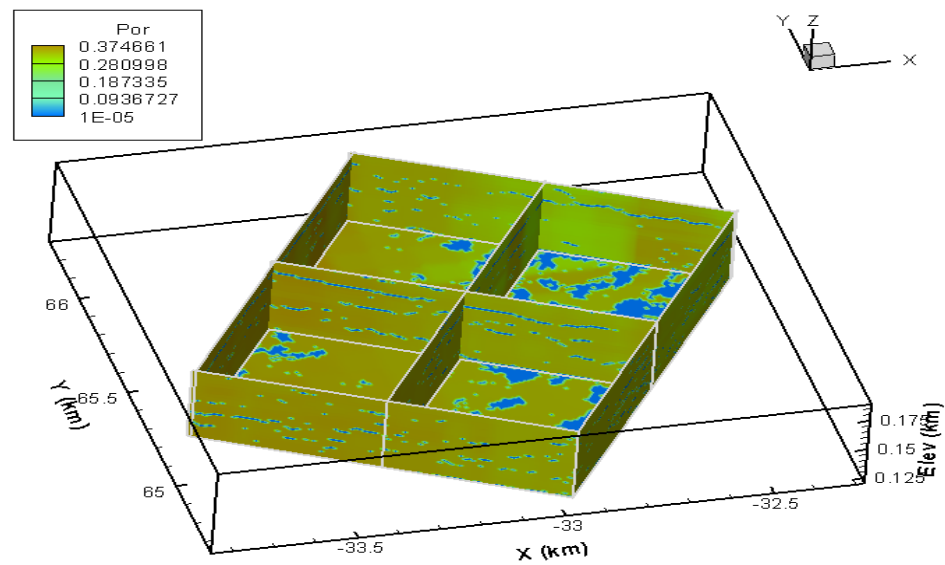


Figure 3. 25 3-D visualization of the porosity distribution of the reservoir body in the area covered by 3-D seismic surveys

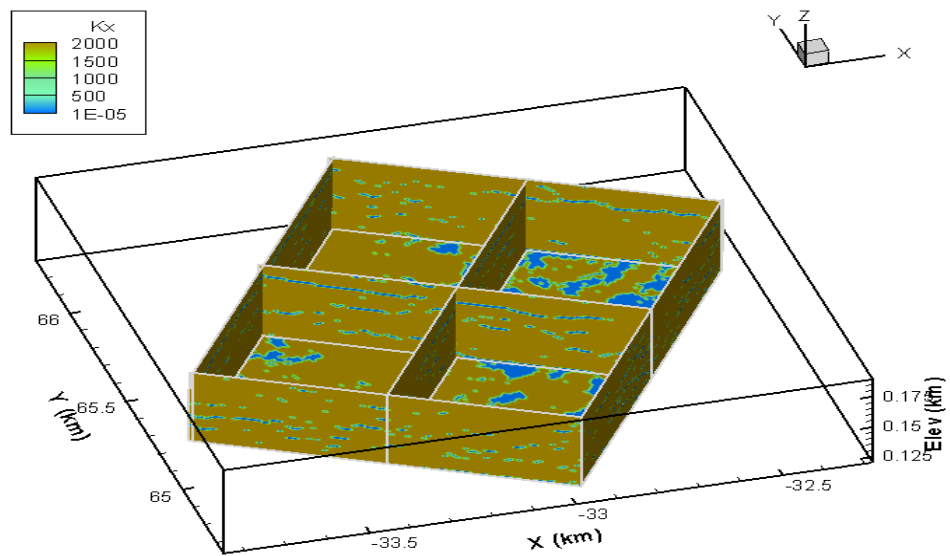


Figure 3. 26 3-D visualization of the permeability (K_x) distribution of the reservoir body in the area covered by 3-D seismic surveys

CHAPTER 4 RESERVOIR SIMULATION COUPLED WITH GEOMECHANICAL MODELING

4.1 Underlying principles

Fluid injection and/or production from a reservoir disturb the static equilibrium of pore fluids and solid framework. A natural tendency to reach a new balance initiates fluid flow and deformation. During the dynamic process the law of conservation holds for the whole affected area and it is fundamental to the subsequent undertaking and work flow. Equation 4.1 is the mathematical formula for fluid conservation.

$$-\oint_s \rho_f \phi v_f \cdot ds = \frac{\partial}{\partial t} \left(\int_v \rho_f \phi dv \right) + Q_f \quad 4.1$$

where ρ_f is the fluid density, ϕ is the porosity, v_f is the fluid velocity vector, s is the area, t is the time, v is the volume, and Q_f is the disturbance (rate of fluid injection or production) leading to fluid pressure changes and fluid movement within the reservoir, which in turns causes changes of effective stress and deforms the solid framework. Similarly the conservation of grain solid mass is applicable, as shown in equation 4.2.

$$-\oint_s \rho_s (1 - \phi) v_s \cdot ds = \frac{\partial}{\partial t} \left[\int_v \rho_s (1 - \phi) dv \right] + Q_s \quad 4.2$$

where ρ_s is the solid density, v_s is the solid velocity vector, and Q_s is the rate of solid mass moving into or out of the volume. The conservation of momentum for

both fluid and grain solid are expressed in a vector form in equation 4.3, which can also be derived from the Newton second law.

$$\oint_{\mathbf{s}} \mathbf{S} \cdot \mathbf{ds} + \int_{\mathbf{v}} [\rho_s(1-\phi) + \rho_f\phi] \mathbf{g} d\mathbf{v} = \frac{\partial}{\partial t} \left\{ \int_{\mathbf{v}} [\rho_s(1-\phi)\mathbf{v}_s + \rho_f\phi\mathbf{v}_f] d\mathbf{v} \right\} \quad 4.3$$

\mathbf{S} is the stress vector and \mathbf{g} is the gravity acceleration vector. A secondary outcome of fluid flow and deformation is energy transfer in the media, which is also satisfied with energy conservation as seen in equation 4.4.

$$-\oint_{\mathbf{s}} [\rho_f\phi\mathbf{v}_f H_f + \rho_s(1-\phi)\mathbf{v}_s H_s + C_T \nabla T] \cdot \mathbf{ds} = \frac{\partial}{\partial t} \left\{ \int_{\mathbf{v}} [\rho_f U_f \phi + \rho_s U_s (1-\phi)] d\mathbf{v} \right\} + Q_{\text{heat}} \quad 4.4$$

where H_f is the fluid enthalpy, H_s is the solid enthalpy, C_T is the thermal conductivity, T is the temperature, U_f is the fluid internal energy, U_s is the solid internal energy, and Q_{heat} the heat flux. Applying the Green-Gauss theorem and removing the integral over the representative volume \mathbf{v} , which is arbitrary, we obtain the following equations 4.5-4.8.

$$-\nabla \cdot (\rho_f \phi \mathbf{v}_f) = \frac{\partial}{\partial t} (\rho_f \phi) + Q_f \quad 4.5$$

$$-\nabla \cdot [\rho_s (1-\phi) \mathbf{v}_s] = \frac{\partial}{\partial t} [\rho_s (1-\phi)] + Q_s \quad 4.6$$

$$\nabla \cdot \mathbf{S} + [(1-\phi)\rho_s + \phi\rho_f] \mathbf{g} = \frac{\partial}{\partial t} [\rho_s (1-\phi)\mathbf{v}_s + \rho_f\phi\mathbf{v}_f] \quad 4.7$$

$$-\nabla \cdot [\rho_f\phi\mathbf{v}_f H_f + \rho_s(1-\phi)\mathbf{v}_s H_s + C_T \nabla T] = \frac{\partial}{\partial t} [\rho_f U_f \phi + \rho_s U_s (1-\phi)] + Q_{\text{heat}} \quad 4.8$$

The fluid velocity v_f is related to Darcy velocity v in a form of $v=(v_f-v_s)\phi$ and equation 4.5 for single-phase fluid flow can be further reformulated as:

$$-\nabla \bullet [\rho_f (k/\mu_f)(\nabla P - \rho_f g) + \rho_f \phi v_s] = \frac{\partial}{\partial t} (\rho_f \phi) + Q_f \quad 4.9$$

where k is the permeability, μ_f is the viscosity and P is the pressure. For a multi-component multi-phase system, the equation is decomposed into a number of equations with each corresponding to one of these components.

Considering that the time scales in days during hydrocarbon recovery is gigantic when compared with the magnitude of displacements in millimeters or smaller, v_s is rendered negligibly small. For practical simplification, all the terms multiplied by v_s can be dropped out. Likewise equation (4.6) may be insignificant and could be removed from the group of equations. In addition, v_f is typically around 10 m/day and $\partial v_f / \partial t$ is much smaller. To the first-order approximation, the term related to v_f on the right-hand side in equation (4.7) can be omitted. Then a final set of equations results as follows:

$$-\nabla \bullet [\rho_f (k/\mu_f)(\nabla P - \rho_f g)] = \frac{\partial}{\partial t} (\rho_f \phi) + Q_f \quad 4.10$$

$$-\nabla \bullet [\rho_f (k/\mu_f)\nabla P H_f + C_T \nabla T] = \frac{\partial}{\partial t} [\rho_f U_f \phi + \rho_s U_s (1 - \phi)] + Q_{\text{heat}} \quad 4.11$$

$$\nabla \bullet \mathbf{S} + [\rho_s (1 - \phi) + \rho_f \phi] \mathbf{g} = 0 \quad 4.12$$

Total stress \mathbf{S} (stress convention is that compressive stress is positive) is resolved into the sum of fluid pressure and effective stress, which relates to the displacements through the constitutive equation. As a result, equation (4.12) has

two unknowns (pressure and displacement vector). All together, equations (4.10), (4.11) and (4.12) have three unknowns and the solution is unique.

A numerical solution to equations (4.10) and (4.11) is traditionally called reservoir simulation, which finds fluid pressure, temperature (and saturations if it is a multi-phase flow). There are many commercial software packages for this purpose such as STARTS, EXOTHERM, TETRED, ECLIPSE, VIP, GEOSIM etc., which can handle multi-phase multi-component fluid flow and heat transfer.

A setback of traditional reservoir simulation is that porosity and permeability are assumed to be constant or are artificially treated as a function of fluid pressure. For well consolidated rocks, this treatment may not generate substantial errors. For unconsolidated sands, however, deformation is significant especially when fractures are opened. Porosity and permeability changes with recovery progression need to be charted with accuracy in order to have results accurately computed from reservoir simulation. On the other hand, the stress field disturbed by production and/or injection needs to be computed for engineering purposes within the reservoir and in the surrounding areas, which may undergo significant stress changes and deformation. The upheaval in some areas after steam injection appears to result from considerable expansion far beyond the production zone. The geomechanical modeling is therefore necessary to couple with traditional reservoir simulation.

Reservoir simulation and geomechanical modeling can be fully coupled, i.e., equations (4.10), (4.11) and (4.12) to be solved simultaneously for the unknowns, but we rarely do that. Reservoir simulation and geomechanical modeling have been highly developed separately in the last decades. It is cost effective to make full use of these ready-made modeling components instead of

spending long time in re-programming numerical solutions to the difficult non-linear problem. The commonly used method is iteration or partial coupling between the two independent applications. If iterated to full convergence, it solves the problem as rigorously as a fully coupled (simultaneous) solution (Settari, 1998). The link is fluid pressure and porosity and permeability. The pressure computed from reservoir simulation in a time step passes as an input to geomemechanical modeling, which computes stresses, strains and displacements. The new porosity and permeability computed from strains input into reservoir simulation, which re-computes the pressure and other unknowns. This process is repeated until a good convergence is found.

4.2 Reservoir model

A reservoir characterization model defines the geometry and physical properties of the reservoir, which are the input for reservoir simulation. The last chapter has detailed this model developed from core measurements, well logs and three-dimensional seismic data. This section discusses boundary conditions, gridding and how to scale up the physical properties from the small scale acquired from seismic data to the coarser grid used for reservoir simulation.

Three-D seismic surveys over an area shown in Figure 4.1 were repeatedly shot in March 1997, February 1998 and February 1999 etc. in an attempt to monitor the five horizontal wells for cyclic steam stimulation and production. Steam injection started in September 1997 and the seismic survey of 1997 is then viewed as the baseline. The adjacent deviated wells in the survey area were also injected and produced at the same period and at much earlier times as well. Even though they may have affected the 3-D survey area to some degree, their

interaction is neglected for simplicity. Since the simulator boundaries require no-flow boundary, the area for reservoir simulation was extended on three sides beyond the seismic survey area, as shown in Figures 4.1 & 4.2.

The three-D seismic surveys cover an area of 1200 m * 960 m with 120*96 stacked traces. The bin size is 10 m * 10 m. The reservoir zone extends vertically for 50 m from 410 ms to 460 ms, sampled at an interval of 1 ms. If this grid was retained for reservoir simulation, the total number of blocks would exceed half a million, a time-consuming daunting task at current conditions of computing power. In practical sense, a coarser grid is required. By experiment, a grid of 40*32*20 was selected for the area with seismic data and then an additional, coarser grid beyond that was arranged, as seen in Figure 4.2. This is a tradeoff between horizontal and vertical resolution.

Horizontally, each reservoir simulation cell contains nine seismic traces. Vertically, 50 time samples correspond to 20 cells and it appears difficult to do averaging over each cell. It is noted from the last chapter that the most important thing acquired from the seismic section is locations of peaks, which indicate the existence of tight rocks assumed to be of zero porosity and zero permeability and suggested to be thick around 2 meters by well logs and core measurements. We re-sampled the time window of 50 ms at an interval of 0.5 ms. The new total number of samples is 100 and each sample represents 0.6 meter. Each tight rock peak and the two immediately adjacent samples are assumed to be the tight rock. So each peak corresponds to 1.8 meters of tight rock.

Now each reservoir simulation cell contains 3*3*5 seismic sub-cells. Upscaling can be done to find its porosity and permeability. The porosity is simply an arithmetic average of 45 seismic sub-cells. Permeability, however, is

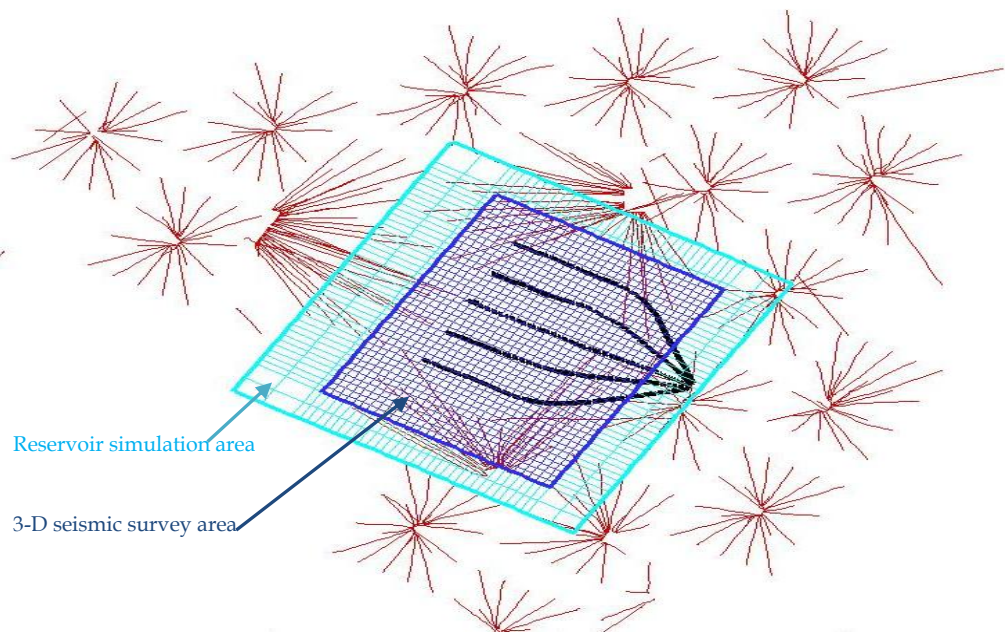


Figure 4. 1 Time-lapse 3-D seismic survey area (blue) and reservoir simulation area (green)

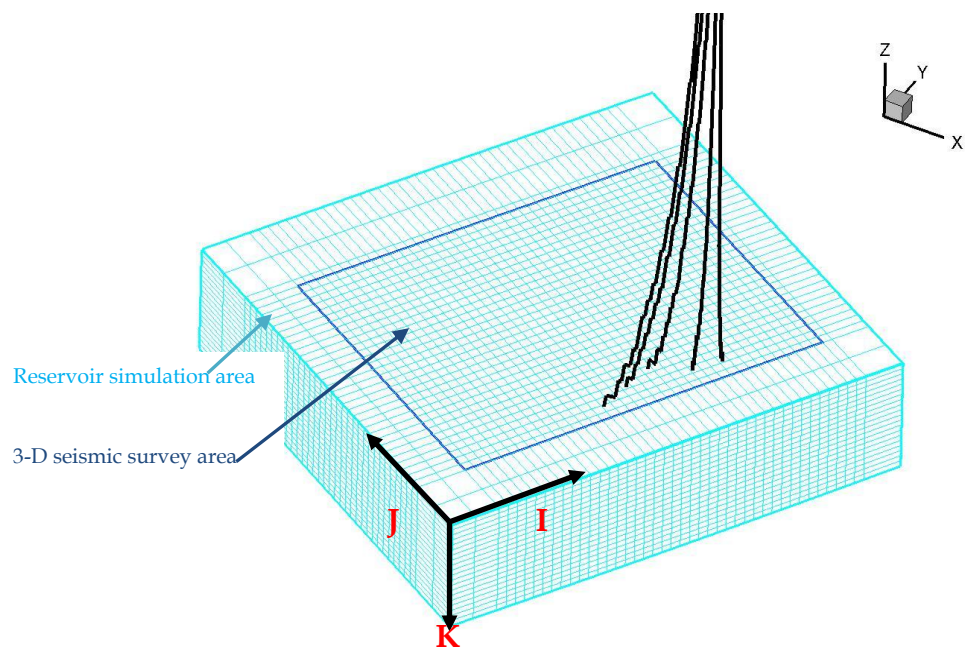


Figure 4. 2 3-D visualization of reservoir simulation grid (43*36*20)

(Note: $I=1,43$; $J=1,36$; $K=1,20$. The XYZ on right up corner is the real coordinates) more complicated. We assume that oil sands have a horizontal and vertical permeability of 2000 md and 650 md, respectively. The permeability for tight rocks is zero. The averaging methodology is as follows: averaging first along z direction for each of nine vertical columns of sub-cells, arithmetic for K_x and K_y and harmonic for K_z . Second along y direction for each of three rows, arithmetic for K_x and K_z and harmonic for K_y . Finally along x direction to average the last remaining sub-cells, harmonic for K_x and arithmetic for K_y and K_z . The final result is demonstrated in Figures 4.3-4.6.

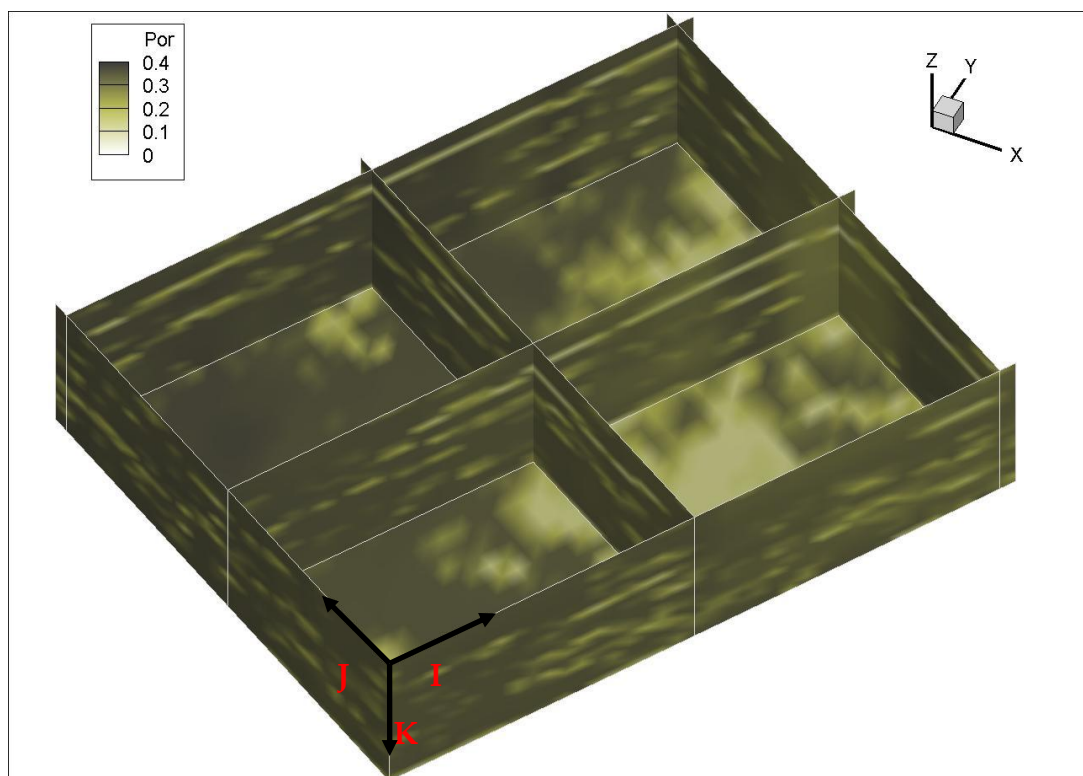


Figure 4. 3 3-D visualization of porosity in the seismic area

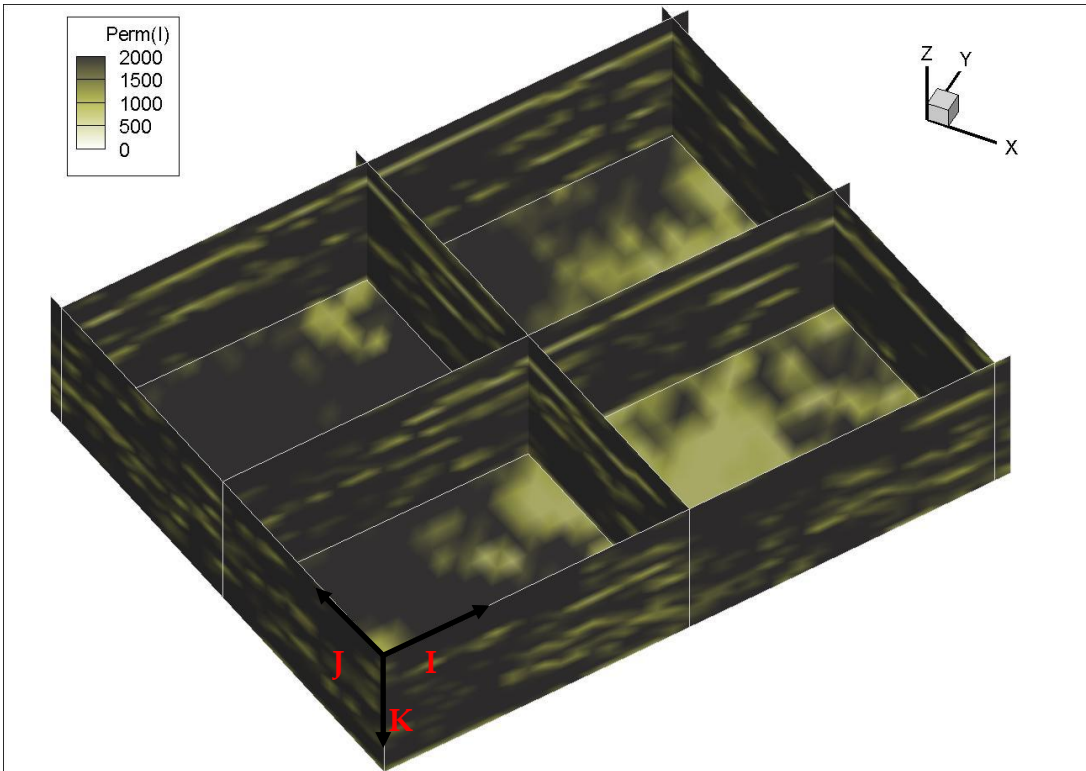


Figure 4. 4 3-D visualization of permeability in I direction in the seismic area

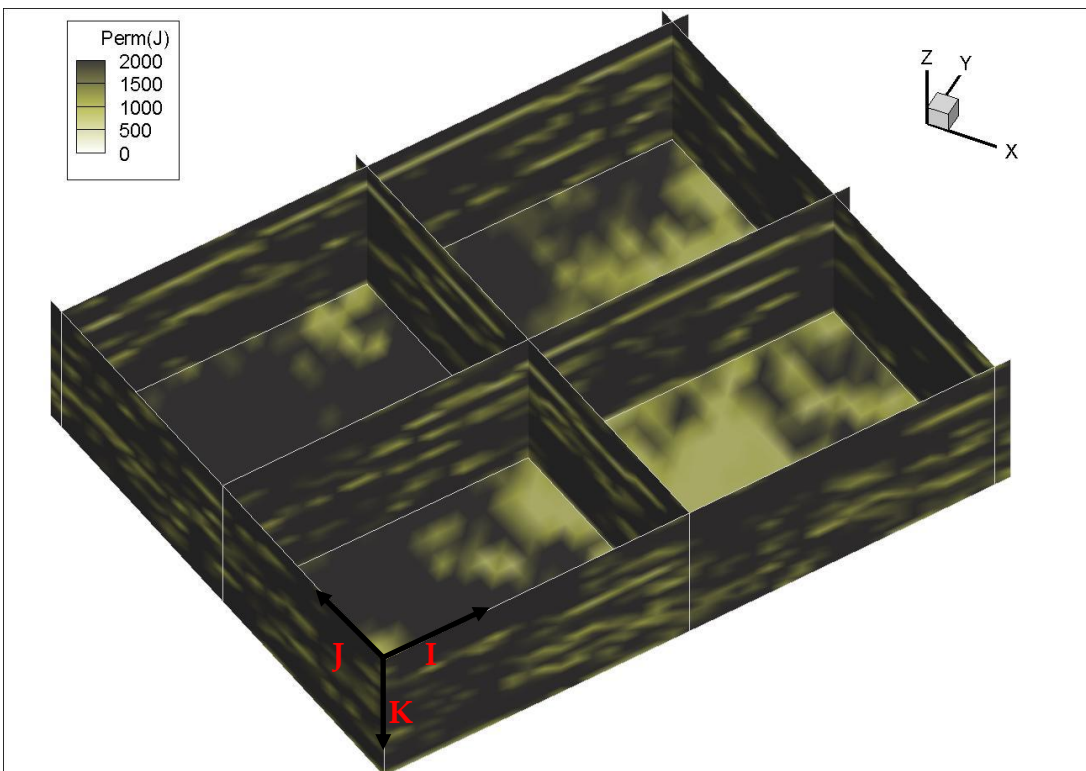


Figure 4. 5 3-D visualization of permeability in J direction in the seismic area

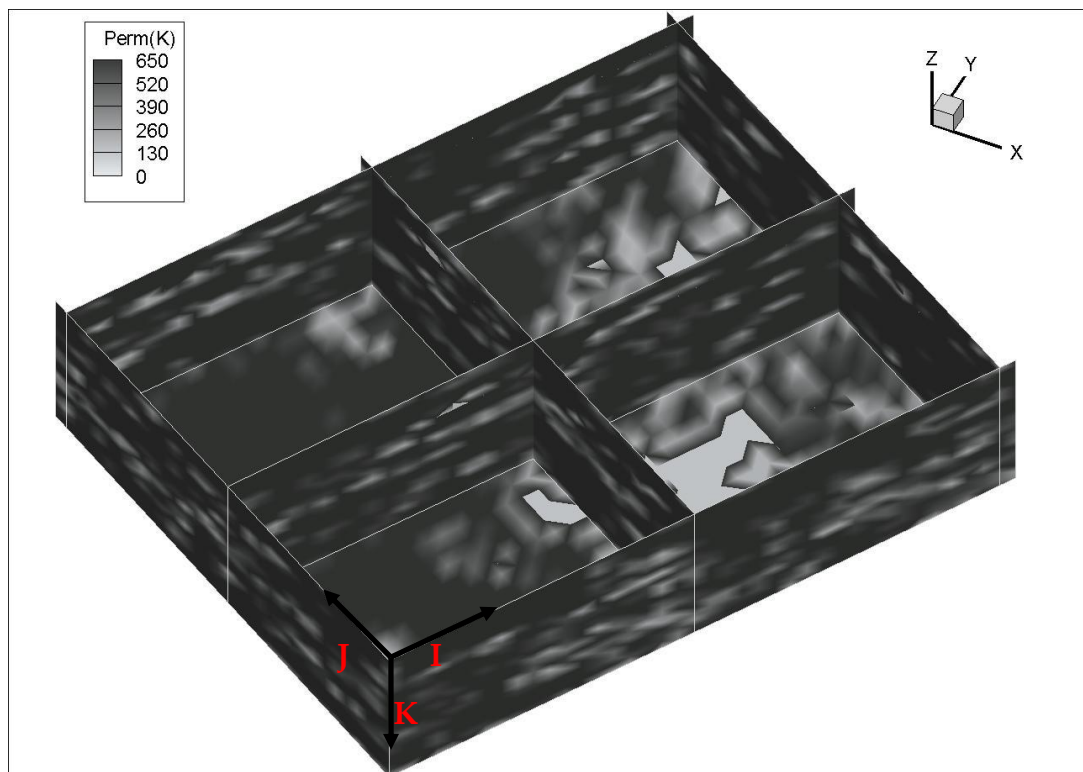


Figure 4. 6 3-D visualization of permeability in K direction in the seismic area

4.3 Geomechanical model

One purpose for geomechanical modelling is to find changes in stress and strain far beyond wells and the reservoir. The geomechanical model is set to include the reservoir and surrounding formations. Restricted by computer memory and speed, the number of blocks outside of the reservoir must be limited. We chose a number of important seismic reflections above the reservoir as block boundaries (upwards, Clearwater, Lower GrandRapids, GrandRapids, Colnyss-Viking, Colorado Shale, Glacier Drift) and extended the model to the surface. The blocks below the reservoir extend downward over one thousand meters. The lateral boundary geometry is taken to be the same as defined in reservoir simulation and the boundary condition is also viewed as no displacement. The entire grid for the geomechanical model is seen in Figure 4.7.

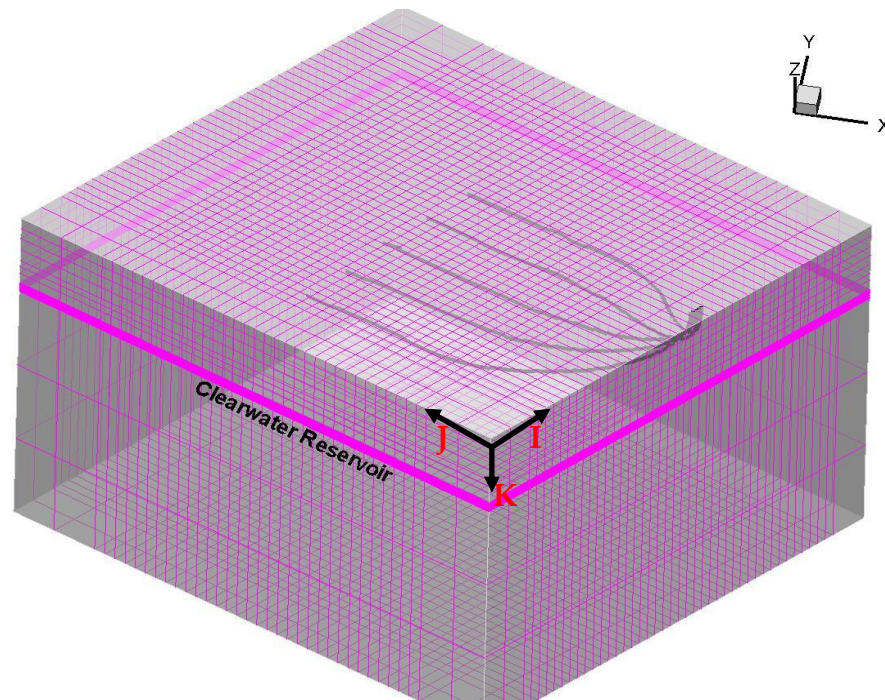


Figure 4. 7 3-D visualization of geomechanical modeling (43*36*30)

The static moduli for geomechanical modeling are often acquired from extensive lab testing and modeling, which are limited to a few samples from target zones. Despite the validity of these values at coring locations, a large area is left without data. Interpolation and extrapolation from a few points to wide other areas is often not reliable. On the other hand, well logs and seismic data are abundant and dynamic moduli can be calculated from them and used to populate the whole area. The key is how to convert dynamic moduli, which measure stress-strain relationship at low strain amplitude and at a short period of time, to static moduli, which describe full long-term stress-strain. The dynamic and static moduli are different because materials are elastic for the former and undergo partially irrecoverable deformation for the latter. In this study, we blocked sonic and density logs according to the vertical grid of the geomechanical model and computed the dynamic moduli. An empirical

relationship between dynamic Young's modulus and static Young's modulus was applied to calculate the static moduli. The equation is $E_s = a E_d^b$ ($a=0.097$ and $b=1.485$, Wang and Nur, 2000). E_s is the static Young's modulus and E_d is the dynamic Young's modulus. Most values were found to be close to those obtained from lab testing (Walters and Settari, 2002).

4.4 Simulation parameters

In addition to porosity, permeability, relative permeability (see Appendix 2) and static moduli, many other parameters also need to be defined. We used the mode of Light Oil to simulate cyclic steam injection into the Clearwater formation in this area. The mode is a three-component and three-phase formulation. The three components are water, light oil and heavy oil and the three phases are water, gas and oil. Depending on pressure and temperature, light oil could be in gas phase or in oil phase or in both. Similarly water was allowed to exist in both gas phase and water phase. But heavy oil is not allowed to vaporize. The three-phase relative permeability was computed from two relative permeability tables for a water-oil system and a liquid-gas system using a modification of Stone's II equation (Settari and Walters, 2000). Other rock physical properties were provided by Taurus Reservoir Solution.

Settari and Raisbeck (1981) measured the vertical and horizontal stresses at a number of depths in poorly consolidated sands in this region. They found the vertical stress gradient was 21.3 kPa/m and the horizontal stress gradient was 20.0 kPa/m. Considering the strike of regional structures in the direction of NW-SE, the stress gradient perpendicular to it is added with a small increment to 20.6 kPa/m. These numbers were used as input for simulation. The initial

distribution of stress implies that vertical fractures may be opened if steam is injected. However, the local stress fields can be different, and stress changes in time, and fractures of other directions may be initiated too.

4.5 Software tool

The coupled reservoir simulation-geomechanical modeling was performed with GEOSIM, a software package produced by Taurus Reservoir Solution. GEOSIM is a modular software system combining a 3-D, 3-phase thermal reservoir simulation with a general 3-D finite element stress-strain simulation (Settari and Walters, 2000). TERASIM-THERM models the flow of oil, steam, water and non condensing (NC) gas in an oil reservoir with heat transfer in the reservoir and over/under-burden. Steam injection and production can be modelled under thermal conditions. FEM3D analyses coupled poro- and thermo-elasticity for stresses and deformations. As mentioned previously, the two components are partially coupled or iterated until convergence.

4.6 Results and discussion

The time-lapse seismic surveys were conducted to monitor the steam chamber and the distribution of pressure, temperature and saturation for five horizontal wells. The influence from other adjacent wells probably needs to be accounted for, but their effect has been neglected in this study.

Steam injection started in early September, 1997, (as estimated from the monthly productions and operation hours available in AccuMap,) for two of the western horizontal wells (Wells 239 and 226; see Table 4.1). It lasted more than

one month to mid-October, and was followed by production in late October for Well 239 and then by full production in November and December for both wells. The well (Well 214) in the middle was on injection from late September to most days in November, and was closed in December. The other two wells on the east side (Wells 205 and 197) were injected from mid-October to a few days beyond mid-November, and were shut in for December. All wells were on full production from January to the end of February 1998. At the latter time, the first monitor seismic survey was shot. Our simulation started from September at the beginning of injection and continued to the end of February, 1998.

Table 4. 1 Summary of the timing of steam injection and oil production

	Sept., 1997	Oct., 1997	Nov., 1997	Dec., 1997	Jan., 1998	Feb., 1998
Well 239*	INJ	INJ & PROD	PROD	PROD	PROD	PROD
Well 226	INJ	INJ	PROD	PROD	PROD	PROD
Well 214	INJ	INJ	INJ	SHUT-IN	PROD	PROD
Well 205		INJ	INJ	SHUT-IN	PROD	PROD
Well 197		INJ	INJ	SHUT-IN	PROD	PROD

* internal well number

Figures 4.8-10 show the 3-D distribution of oil saturation after one month injection for three wells. The saturation decreases away from the well bores faster in the xy plane than in the vertical plane, which is a result of the tendency of fluid vertical movement and maybe vertically opened fractures. The zone of abnormally low oil saturation due to steam displacement can be associated with the steam chamber (either existing or already collapsed into a water zone). As indicated in Figures 4.11-13, steam existed only in Well 214, which experienced high pressure and temperature (Figures 4.17-22) in that time accounted for by later operation of injection. Yet the steam condensed to hot water in two other

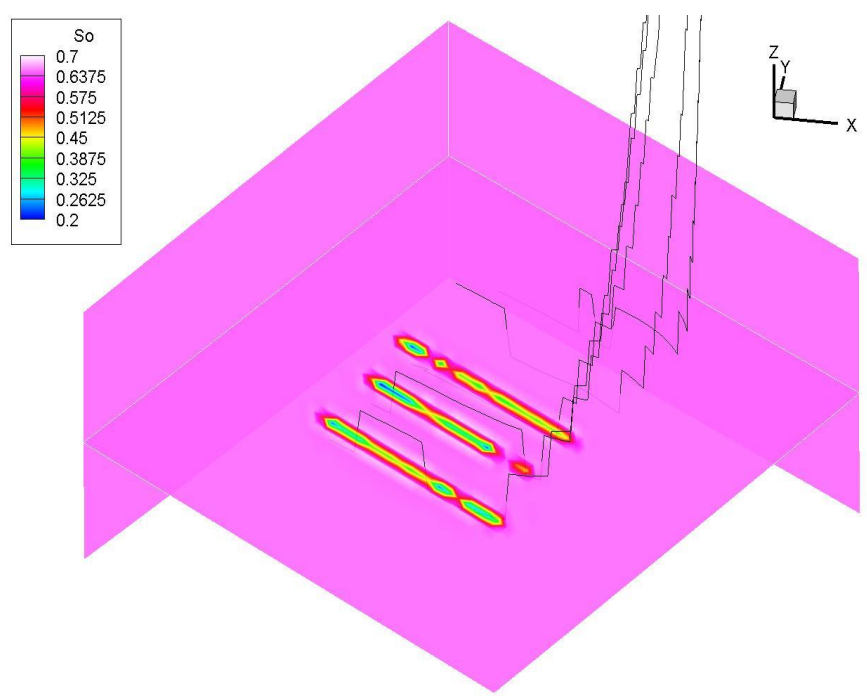


Figure 4. 8 Oil saturation on K-plane on Oct 16, 1997

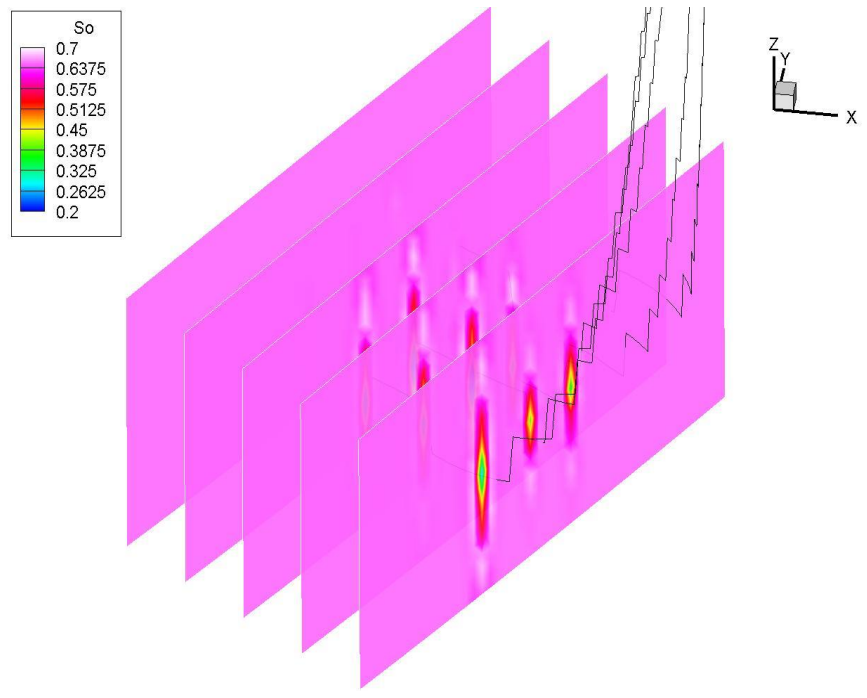


Figure 4. 9 Oil saturation on J-plane on Oct 16, 1997

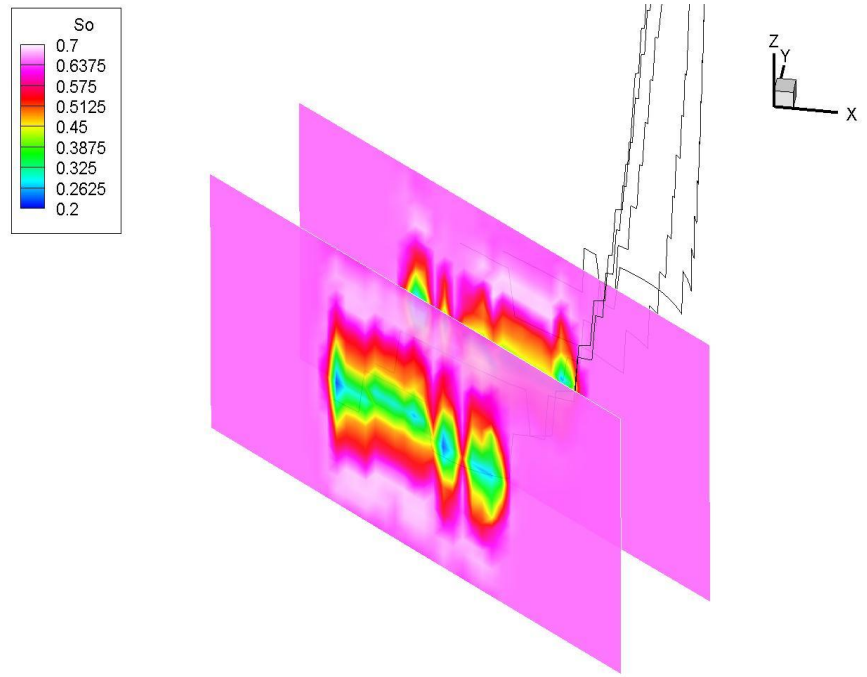


Figure 4. 10 Oil saturation on I-plane on Oct 16, 1997

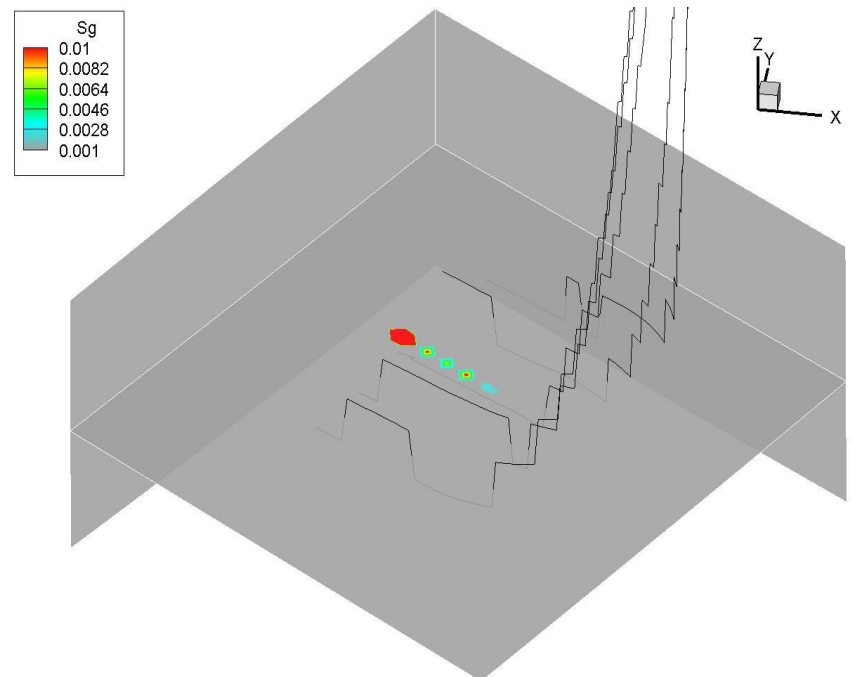


Figure 4. 11 Gas saturation on K-plane on Oct 16, 1997

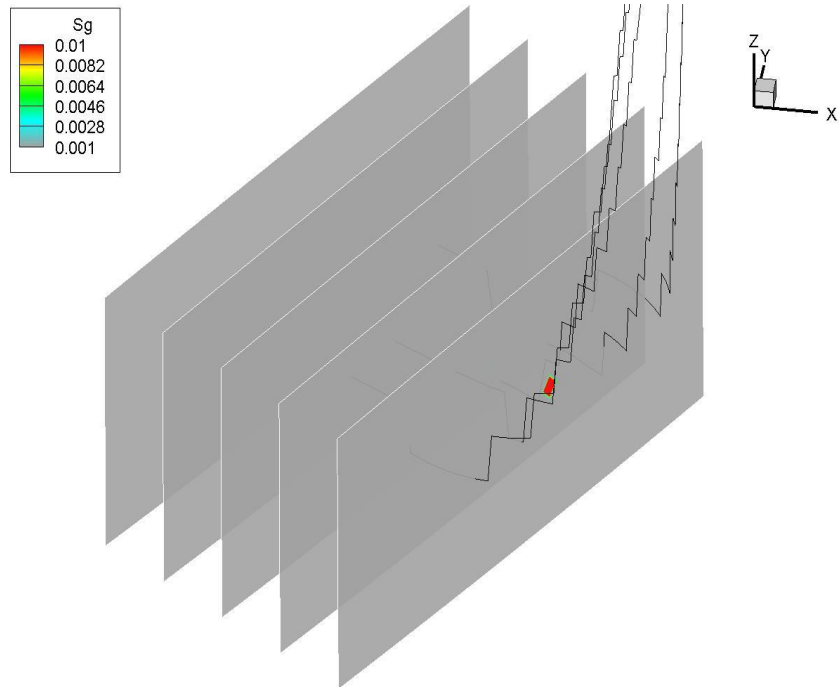


Figure 4. 12 Gas saturation on J-plane on Oct 16, 1997

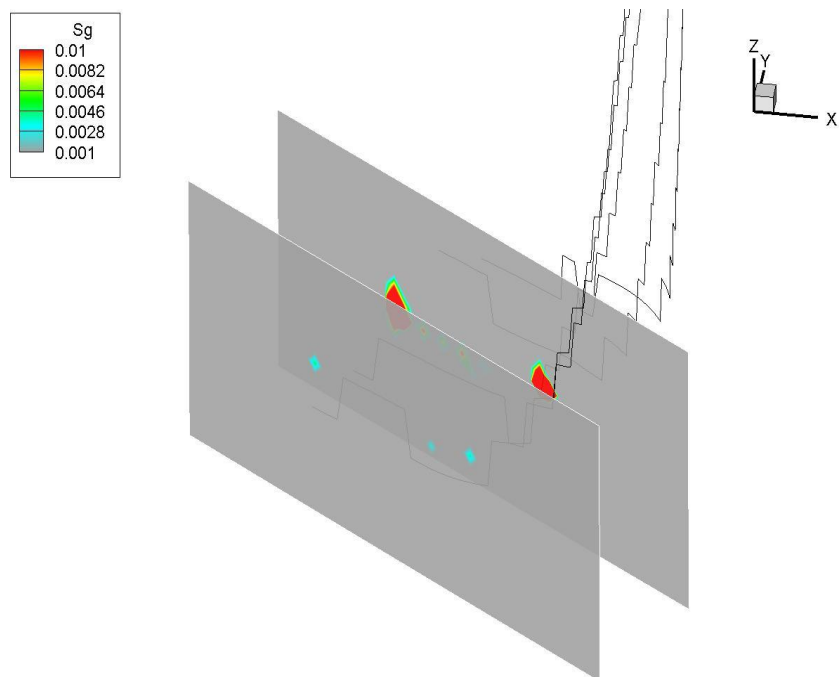


Figure 4. 13 Gas saturation on I-plane on Oct 16, 1997

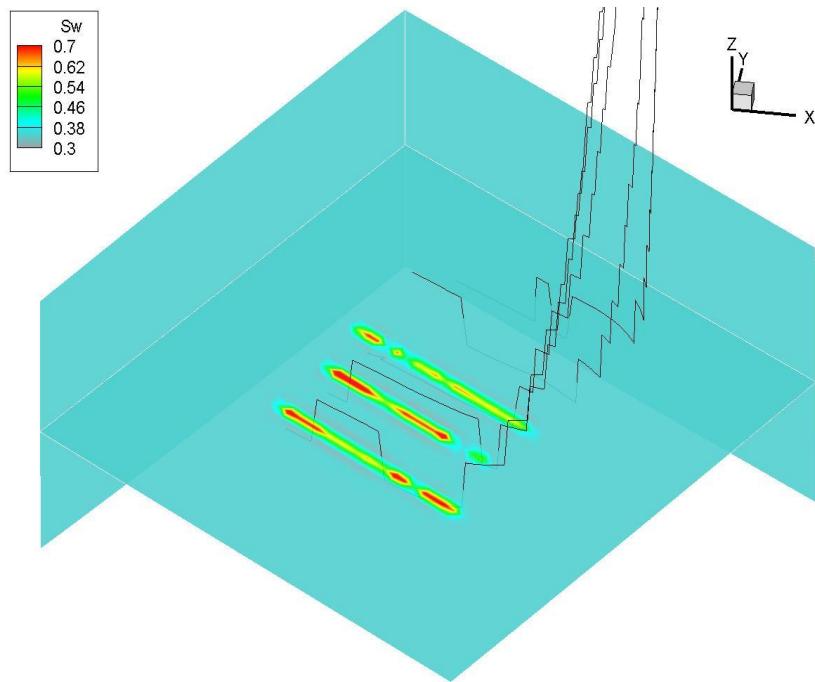


Figure 4. 14 Water saturation on K-plane on Oct 16, 1997

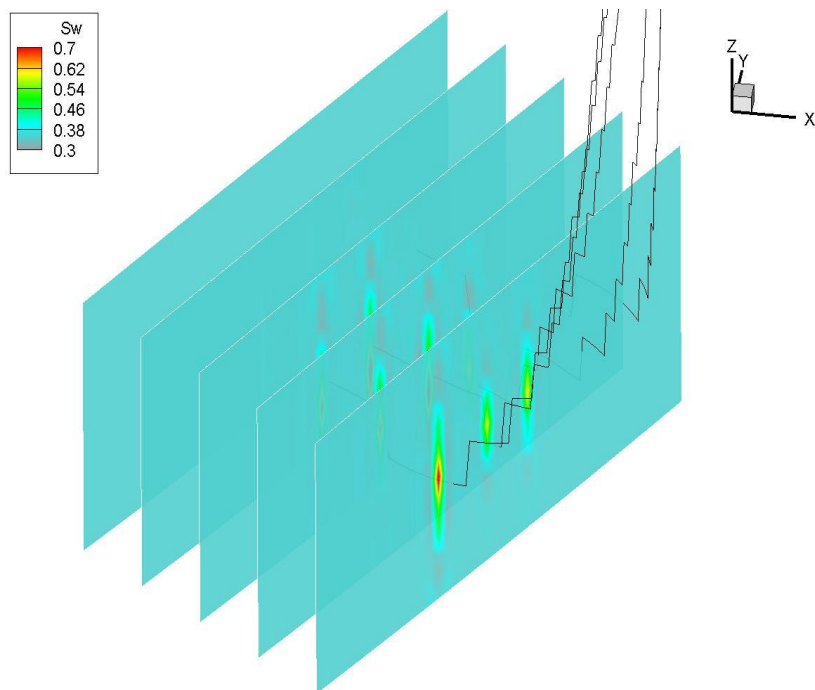


Figure 4. 15 Water saturation on J-plane on Oct 16, 1997

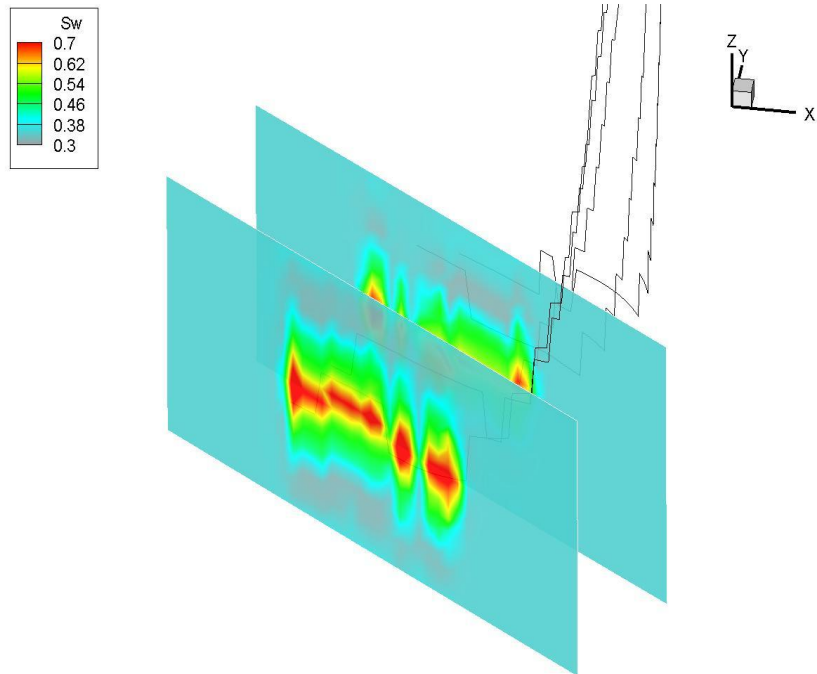


Figure 4. 16 Water saturation on I-plane on Oct 16, 1997

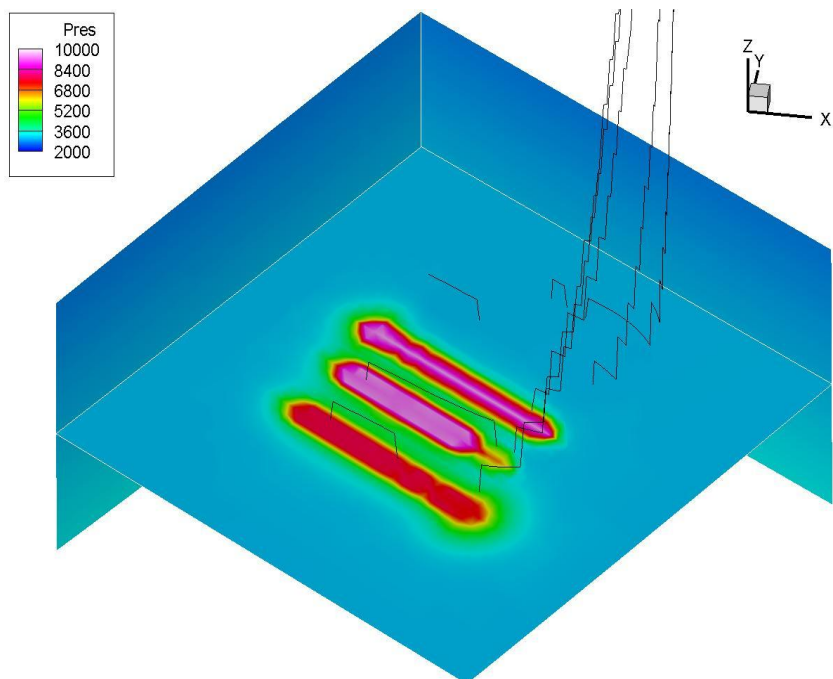


Figure 4. 17 Fluid pressure on K-plane on Oct 16, 1997 (unit: KPa)

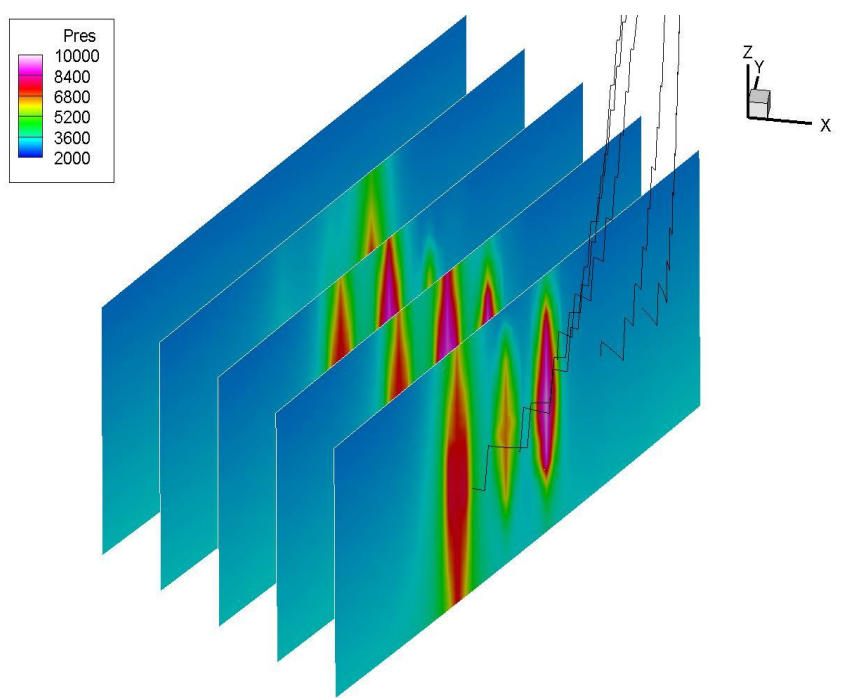


Figure 4. 18 Fluid pressure on J-plane on Oct 16, 1997 (unit: KPa)

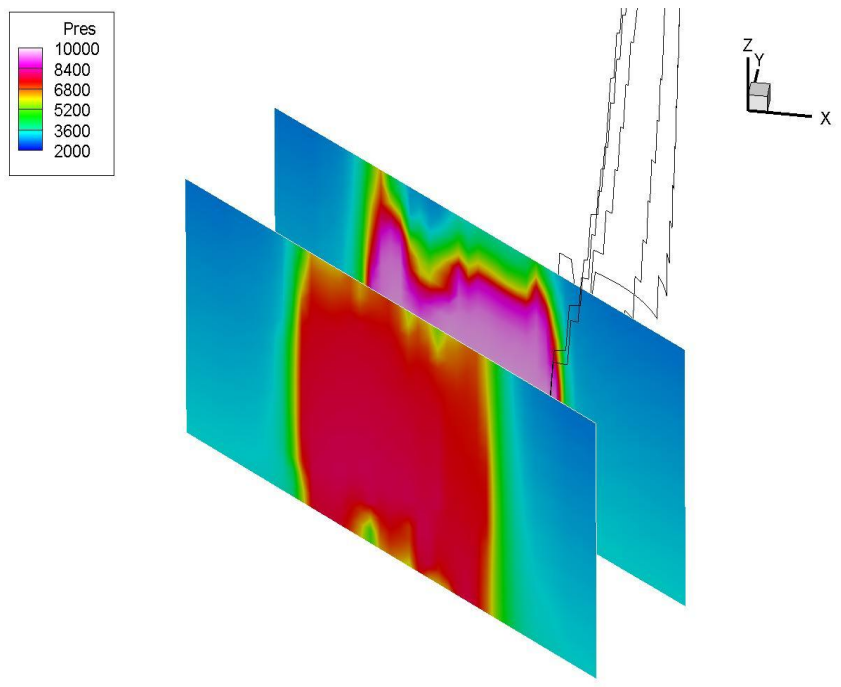


Figure 4. 19 Fluid pressure on I-plane on Oct 16, 1997 (unit: KPa)

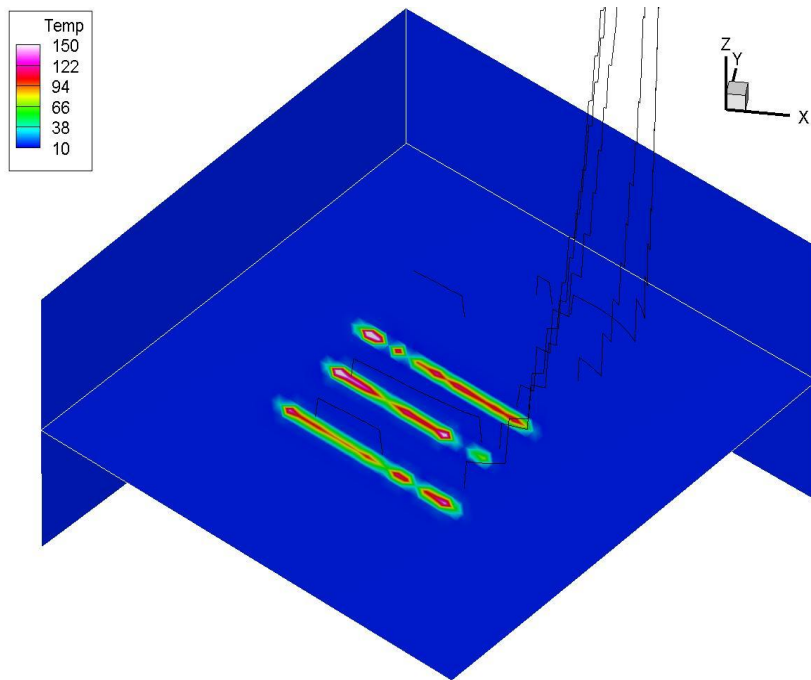


Figure 4. 20 Temperature on K-plane on Oct 16, 1997 (unit: Celsius)

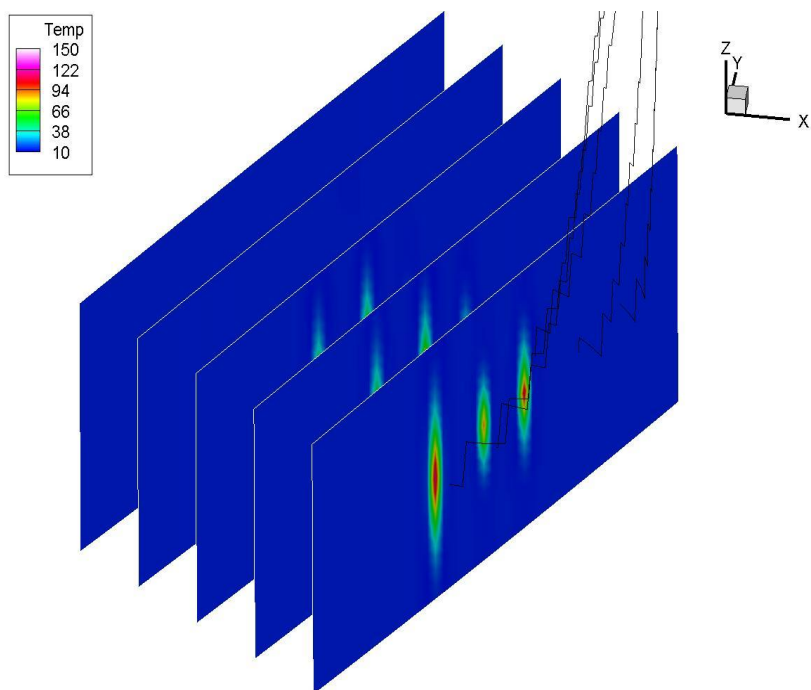


Figure 4. 21 Temperature on J-plane on Oct 16, 1997 (unit: Celsius)

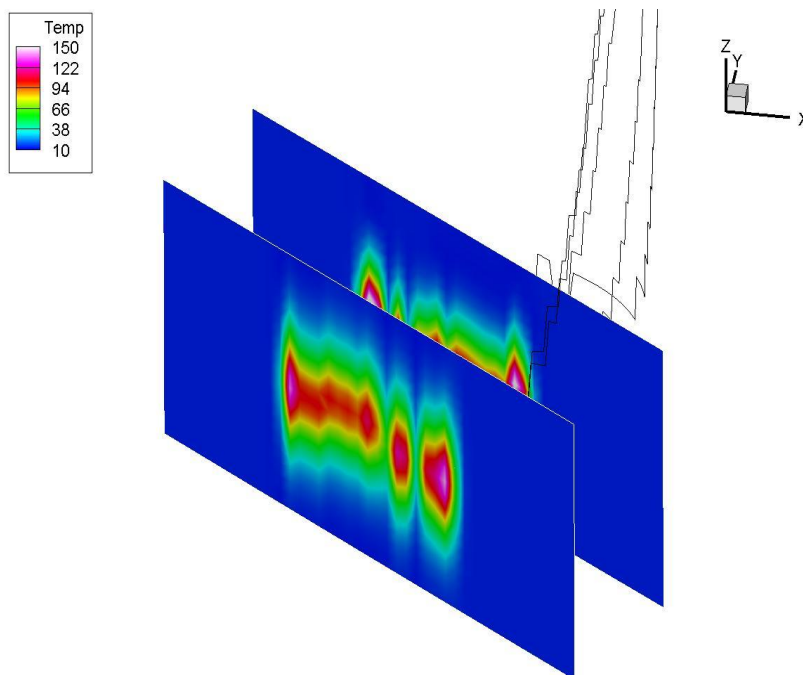


Figure 4. 22 Temperature on I-plane on Oct 16, 1997 (unit: Celsius)

wells. The distribution of water saturation (Figures 4.14-16) displays a similar scenario except for the reverse order of saturation changes. The temperature front seems consistent with the saturation distribution in Figures 4.20-22, which arose from heat transfer dominated by fluid convection in the early stage of injection. The fluid pressure affected wider areas than saturations and temperature, and it formed a unified high-pressure regime in Figures 4.17-19. As a result, three zones are distinguished: steam chamber, anomalies of saturation and temperature, and pressure front. These three zones would have different velocities and densities and would respond differently to seismic waves.

Geomechanical modeling serves two purposes, as mentioned previously. One is to couple stress and strain changes in the reservoir with reservoir

simulation for more accurate results. The other is to find stress, strain and displacements in the reservoir and in areas far beyond. These parameters are very important in well planning and drilling, surface facility arrangement, reservoir development etc.. Since the areas and depth ranges disturbed in the stress-strain field by injection and production are by far larger, they may have collective seismic responses better than those due directly to changes within the reservoir. Kenter et al. (2004) found that time shift in overburden formations due to hydrocarbon recovery can be an order of magnitude larger than changes found in the reservoir.

Figure 4.23 is the effective stress S_x (in the direction of I index, not X in real coordinates, the same below; See Figure 4.2) in the middle of the reservoir. Its pattern is consistent with that of fluid pressure in Figure 4.17 except the reverse order of changes. Along well 214 in the centre, S_x is small and even locally negative, implying the potential existence of vertical fractures. S_x may have been negative in the past for two other wells. On the top of the reservoir, well locations are still discernable in Figure 4.24. Further close to the ground, S_x anomalies become very small and also can't differentiate individual wells in Figure 4.25.

Effective stresses S_y and S_z have a similar character to S_x , as shown in Figures 4.26-31.

Displacements are another important rock mechanical parameter. In Figures 4.32-34, U_x (in the direction of I index, not X in real coordinates, the same below) is oriented in zones along the well direction with a pattern of negative-zero-positive. It is mostly negative in the western part, and becomes predominantly positive eastwards. More interestingly, the magnitude of U_x

increases from the middle to the top of the reservoir, and then decreases to small values (1-2 cm) when close to the ground. U_y anomalies in Figures 4.35-37 concentrate on two ends of the wells, it is positive in north and negative in south. Likewise, U_y culminates on the top of the reservoir and decreases shallower or deeper away from that point. U_z in Figures 4.38-40 is appreciably larger than U_x and U_y , especially on the top of the reservoir (up to 15 cm). The pattern of displacement maximization on the top of the reservoir seems against our intuition that would suggest that lowering $S_{x,y,z}$ more results in more expansion and displacement $U_{x,y,z}$. However, this is not necessarily true. Lowering S_z , for example, greatly leads to large strain ($\partial U_z / \partial Z$), which does not necessarily mean large displacement (U_z). The real displacement U_z needs detailed calculation, as we did before.

Above the reservoir, it looks reasonable that U_z is larger above the wells and smaller away from them.

At the end of February 1998, the first monitor seismic survey was shot in an attempt to capture changes in reservoir conditions. At that time, wells 239 and 226 were already on production for 4-5 months and others were producing almost for two months. Oil would flow into well bores from surrounding areas. As a result, anomalies of low oil saturation and high water saturation around wellbores would shrink, as in Figures 4.41-43. Pressure would drop down (Figures 4.44-46). Gas (CH_4 and CO_2) would ex-solve from the heated heavy oil. As in Figure 4.47, gas occurs only in well 239, where there was sufficient pressure decline due to longest production.

The stress and strain would respond correspondingly. For instance, the vertical displacement U_z decreases and becomes indistinguishable among five

wells in spite of remaining positive in the middle and on the top of the reservoir in Figures 4.48-49. Close to the surface U_z is slightly bigger than on Oct. 16, 1997 (Figures 4.50 and 4.40). The pattern of stress and strain changes represents their delayed and smooth responses to changes in reservoir conditions.

In summary, the simulation provides us with a full set of reservoir and geomechanical parameters in space and time, which describe numerically and precisely what really happens within the reservoir and beyond. The parameters are crucial in decision making with regard to surface facility arrangement, well planning and drilling, reservoir development design and management etc.. As discussed above, simulation results appear largely apprehensible. Yet the magnitudes of these changes are impossible to obtain accurately by thinking or reasoning or simple computation on paper by any experienced and intelligent reservoir engineers or mathematicians. There are some effects that can't be figured out by mental calculation. For example, U_x and U_y between wells are difficult to guess the sign and magnitude. The more vertical displacements on the top of the reservoir than in the middle stand in direct opposition to our intuition, which is unfortunately false. Therefore, simulation can improve our understanding and may lead to new discoveries. It appears that computer modelling is not only worthwhile but also essential.

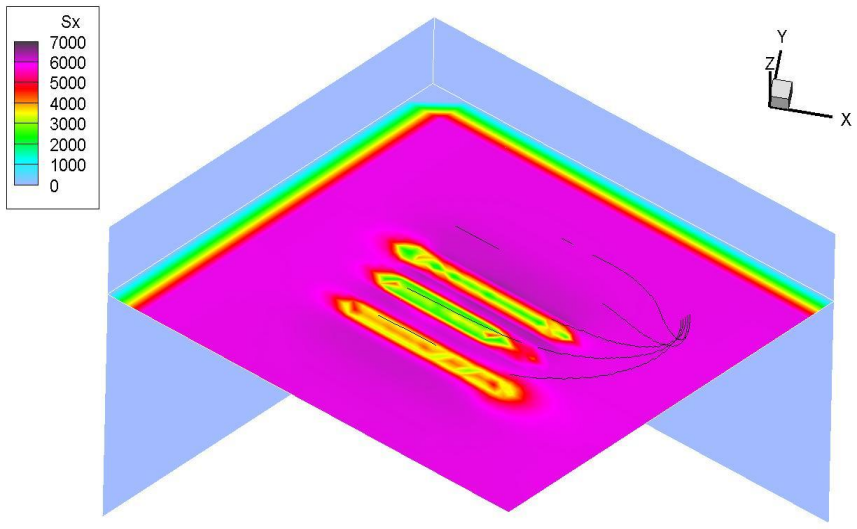


Figure 4. 23 S_x distribution in the middle of the reservoir on Oct 16, 1997 (unit: KPa)

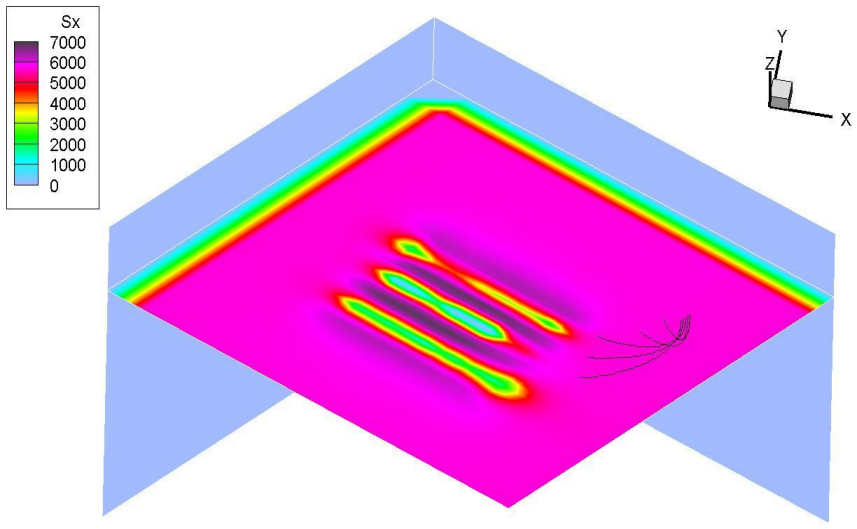


Figure 4. 24 S_x distribution on the top of the reservoir on Oct 16, 1997 (unit: KPa)

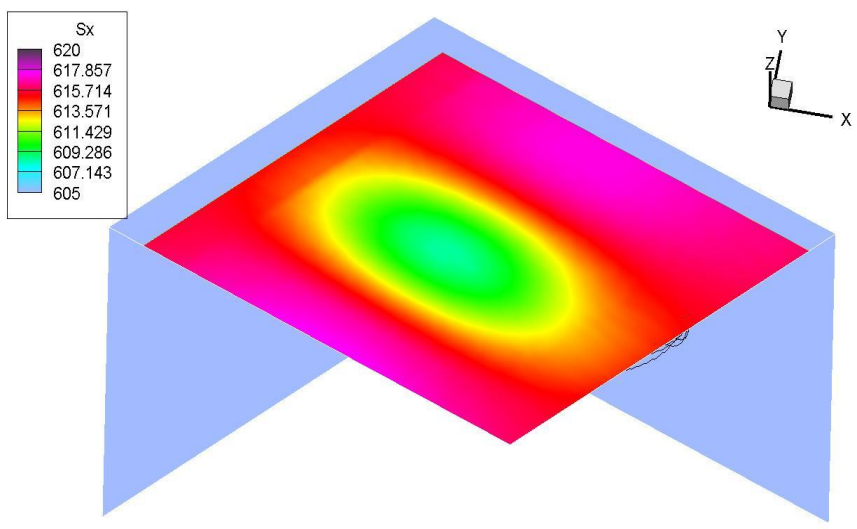


Figure 4. 25 S_x distribution on the ground on Oct 16, 1997 (unit: KPa)

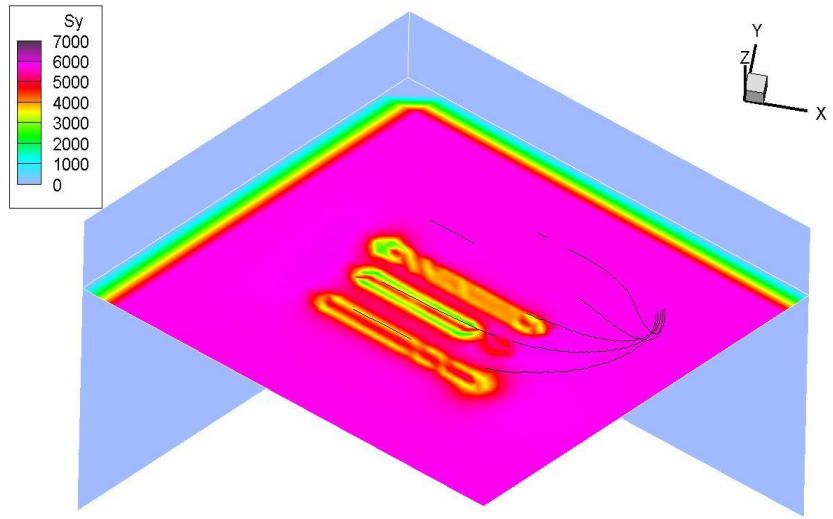


Figure 4. 26 S_y distribution in the middle of the reservoir on Oct 16, 1997 (unit: KPa)

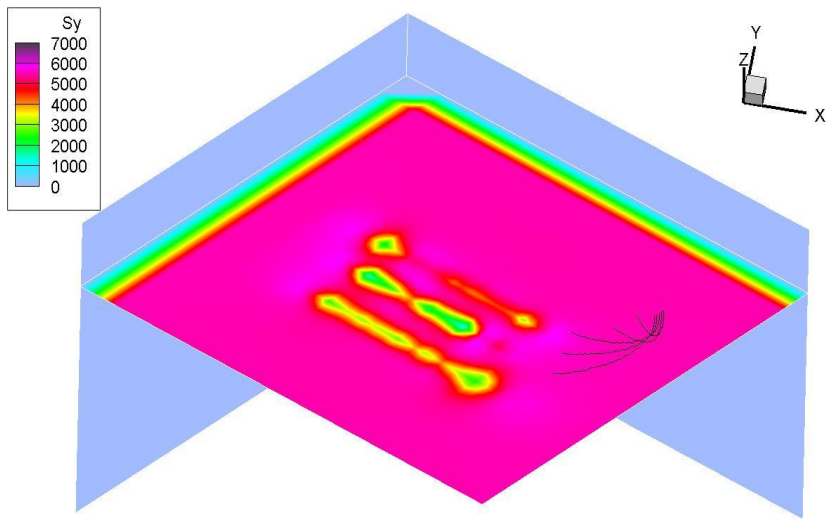


Figure 4. 27 S_y distribution on the top of the reservoir on Oct 16, 1997 (unit: KPa)

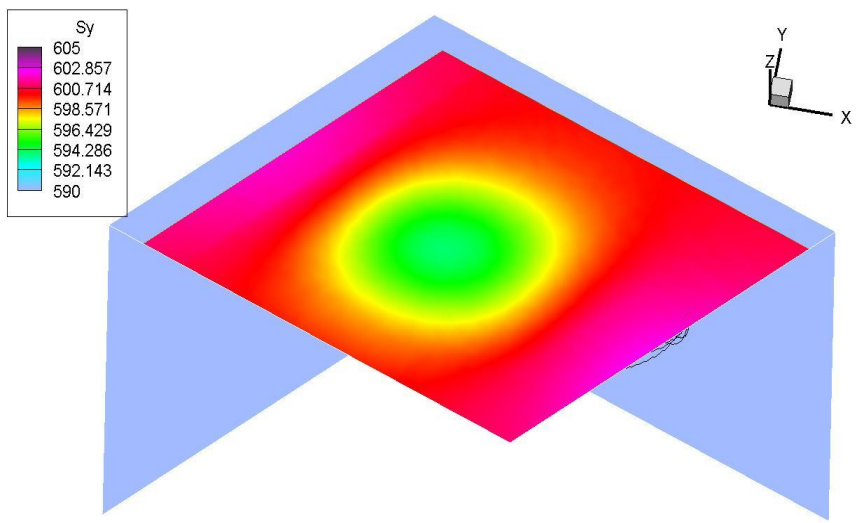


Figure 4. 28 S_y distribution on the ground on Oct 16, 1997 (unit: KPa)

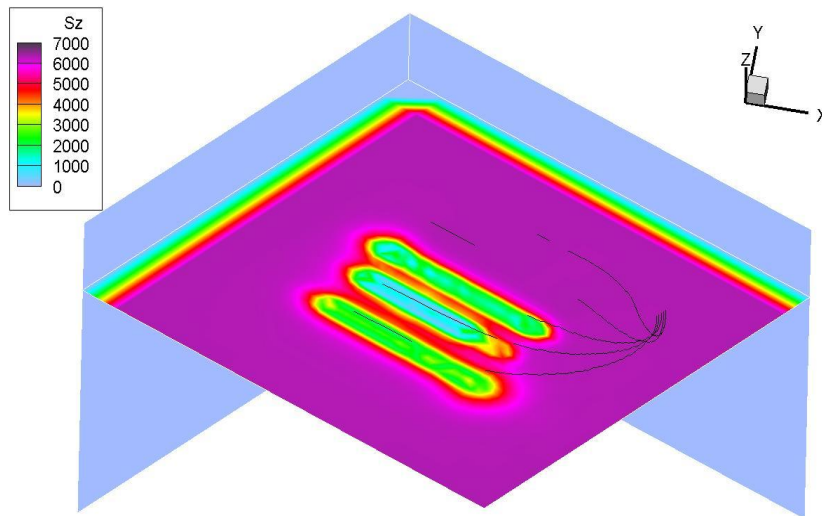


Figure 4. 29 S_z distribution in the middle of the reservoir on Oct 16, 1997 (unit: KPa)

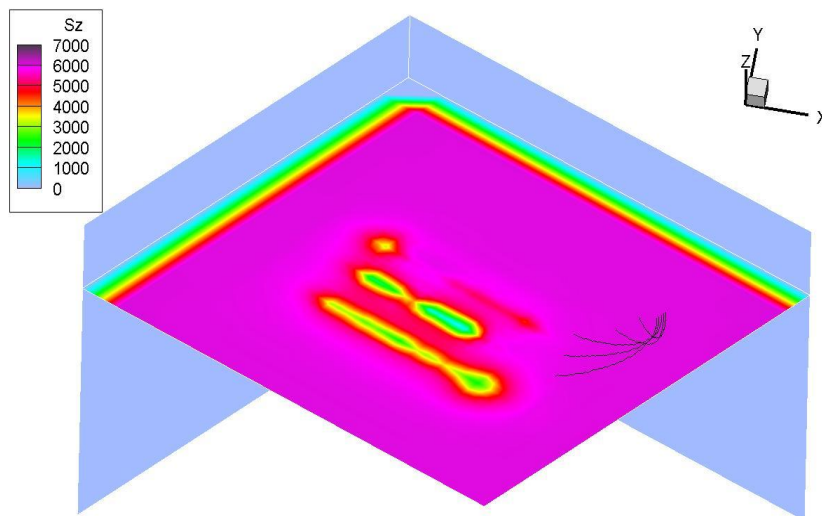


Figure 4. 30 S_z distribution on the top of the reservoir on Oct 16, 1997 (unit: KPa)

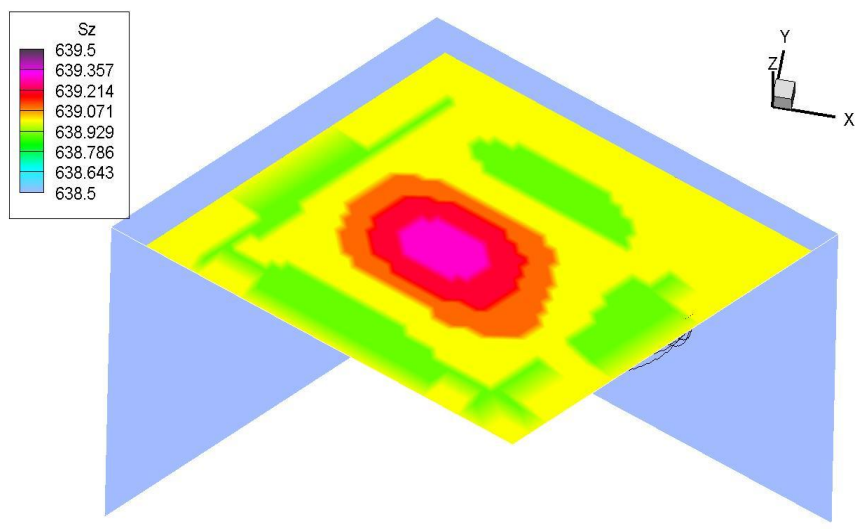


Figure 4. 31 S_z distribution on the ground on Oct 16, 1997 (unit: KPa)

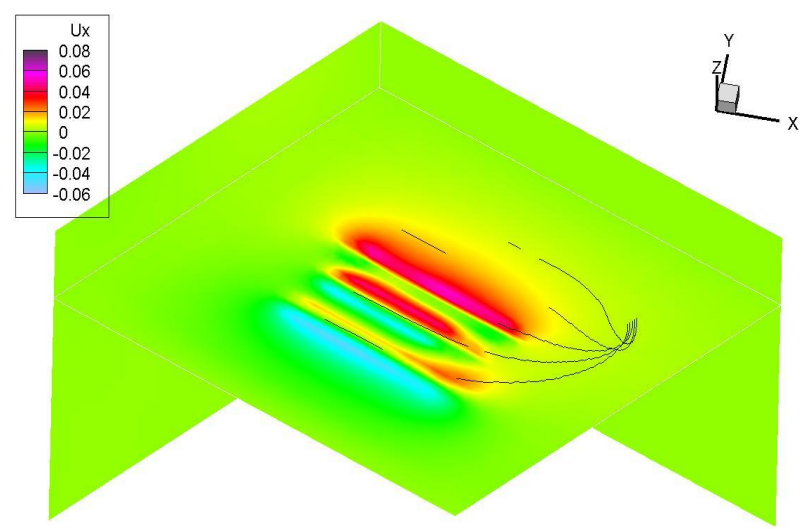


Figure 4. 32 U_x distribution in the middle of the reservoir on Oct 16, 1997 (unit: m)

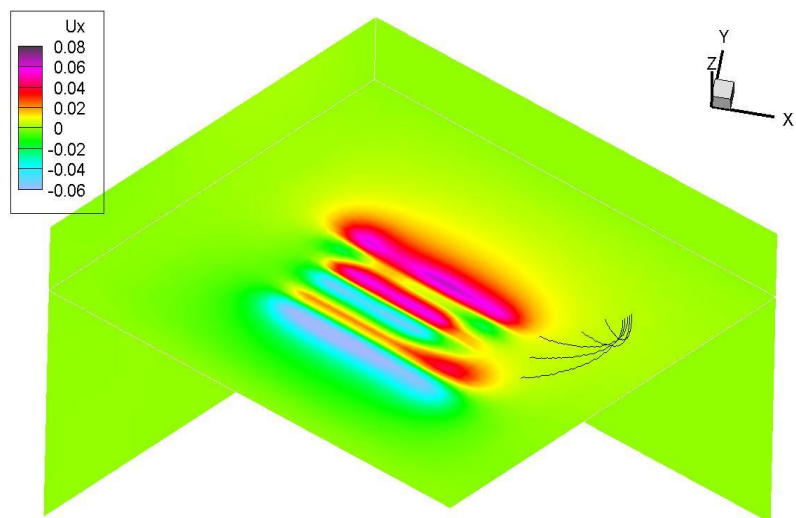


Figure 4. 33 U_x distribution on the top of the reservoir on Oct 16, 1997 (unit: m)

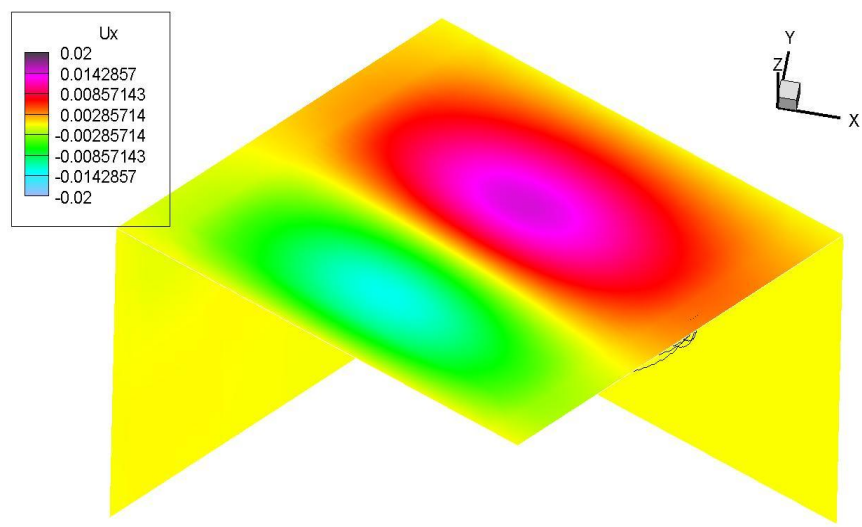


Figure 4. 34 U_x distribution on the ground on Oct 16, 1997 (unit: m)

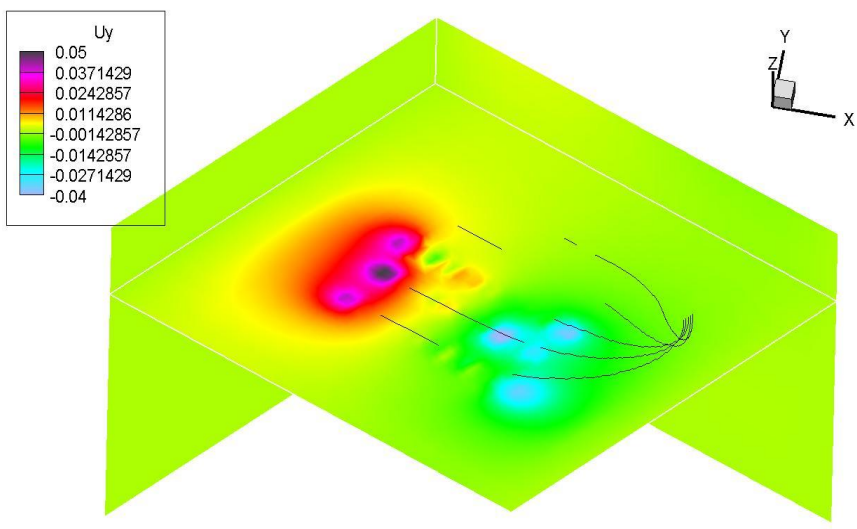


Figure 4. 35 U_y distribution in the middle of the reservoir on Oct 16, 1997 (unit: m)

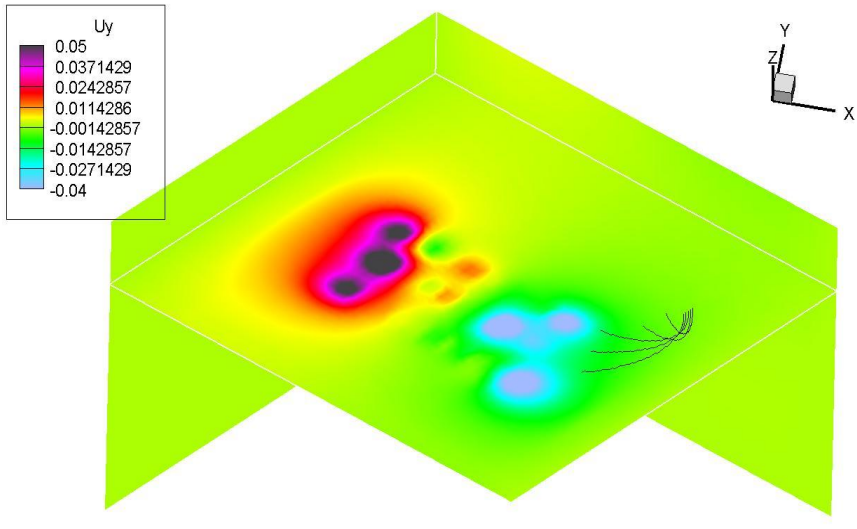


Figure 4. 36 U_y distribution on the top of the reservoir on Oct 16, 1997 (unit: m)

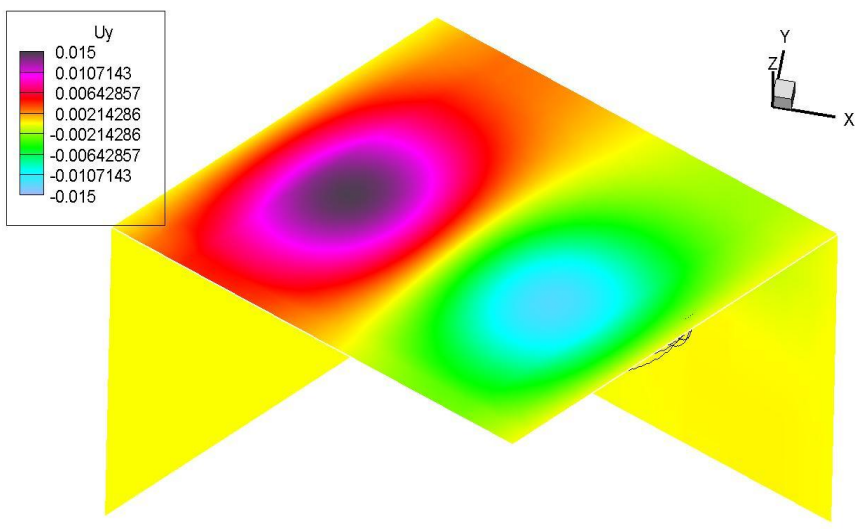


Figure 4. 37 U_y distribution on the ground on Oct 16, 1997 (unit: m)

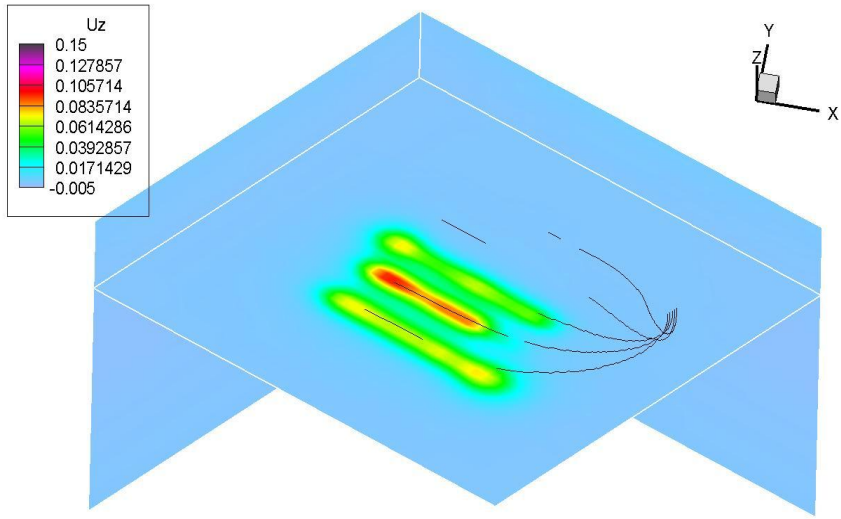


Figure 4. 38 U_z distribution in the middle of the reservoir on Oct 16, 1997 (unit: m)

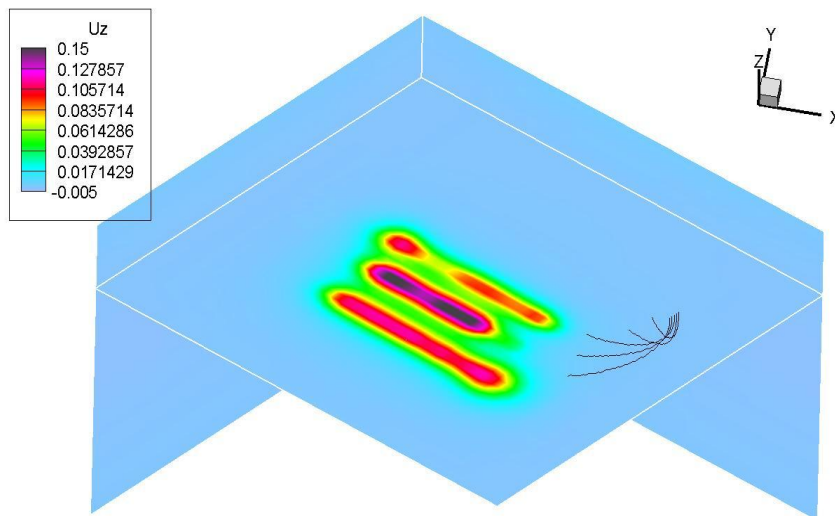


Figure 4. 39 U_z distribution on the top of the reservoir on Oct 16, 1997 (unit: m)

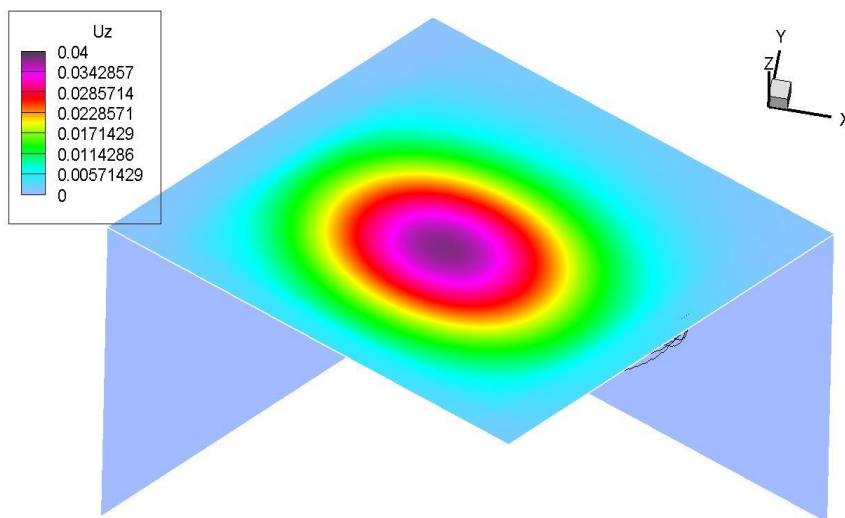


Figure 4. 40 U_z distribution on the ground on Oct 16, 1997 (unit: m)

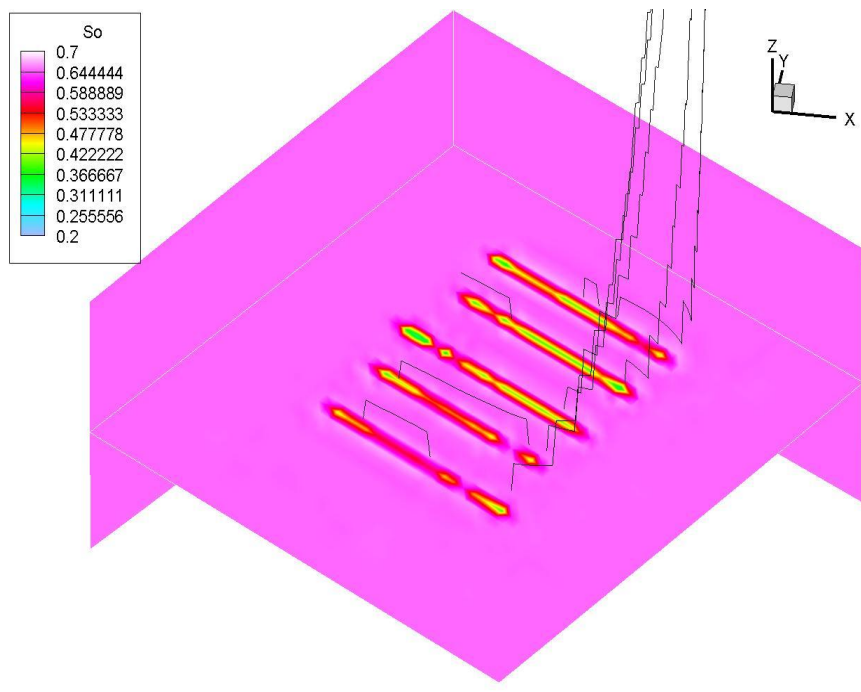


Figure 4. 41 Oil saturation on K-plane on Feb 28, 1998

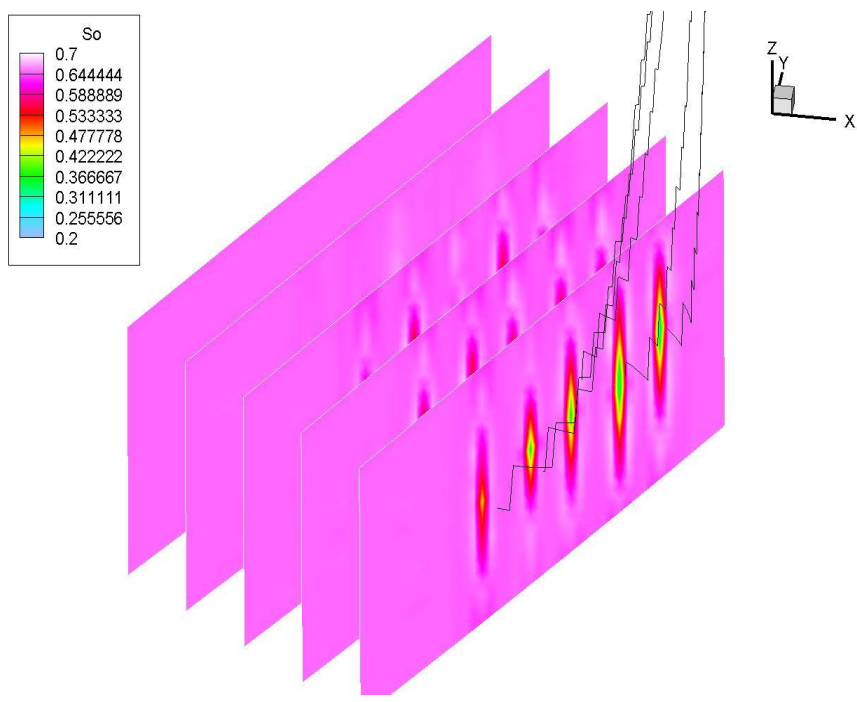


Figure 4. 42 Oil saturation on J-plane on Feb 28, 1998

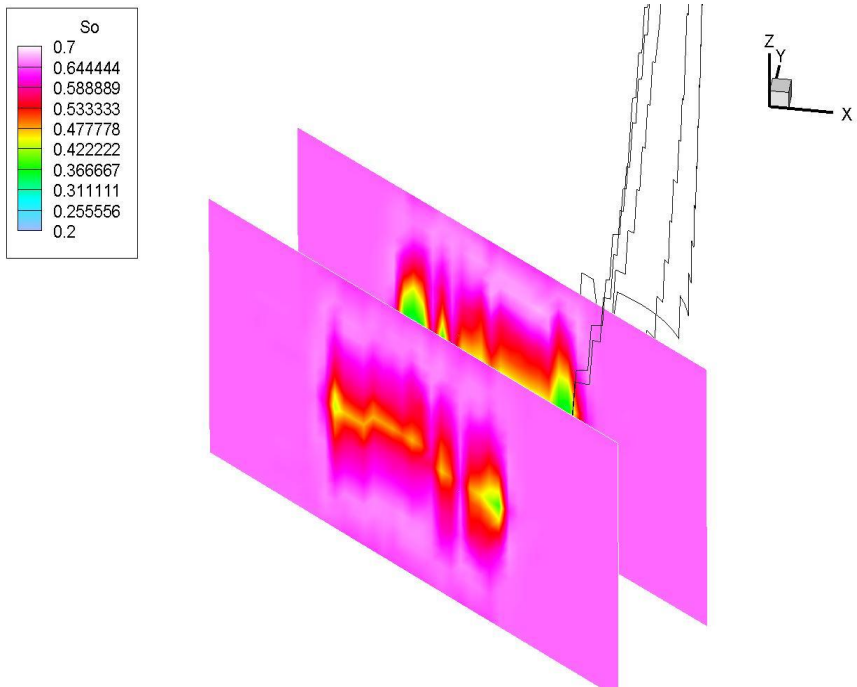


Figure 4. 43 Oil saturation on I-plane on Feb 28, 1998

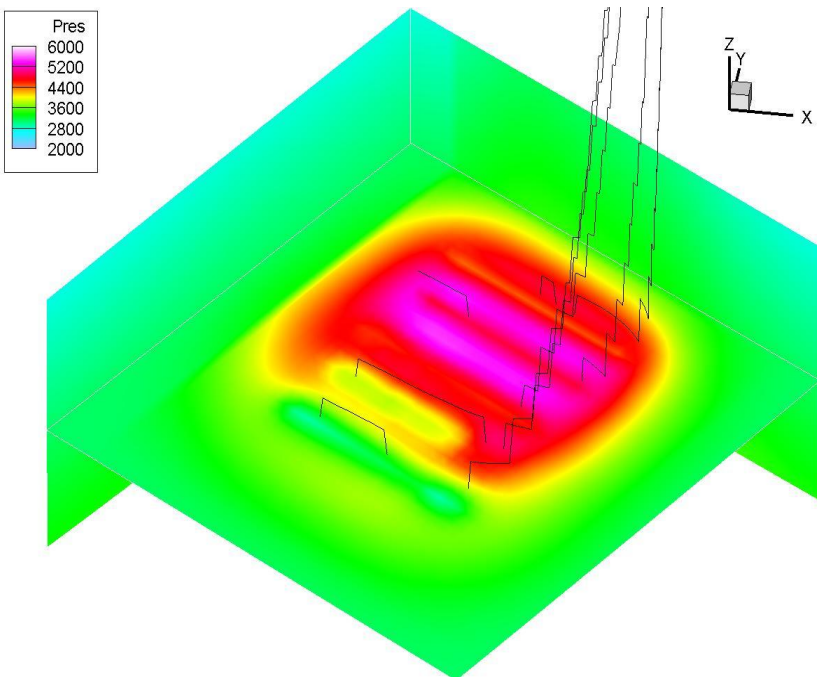


Figure 4. 44 Fluid pressure on K-plane on Feb 28, 1998 (unit: KPa)

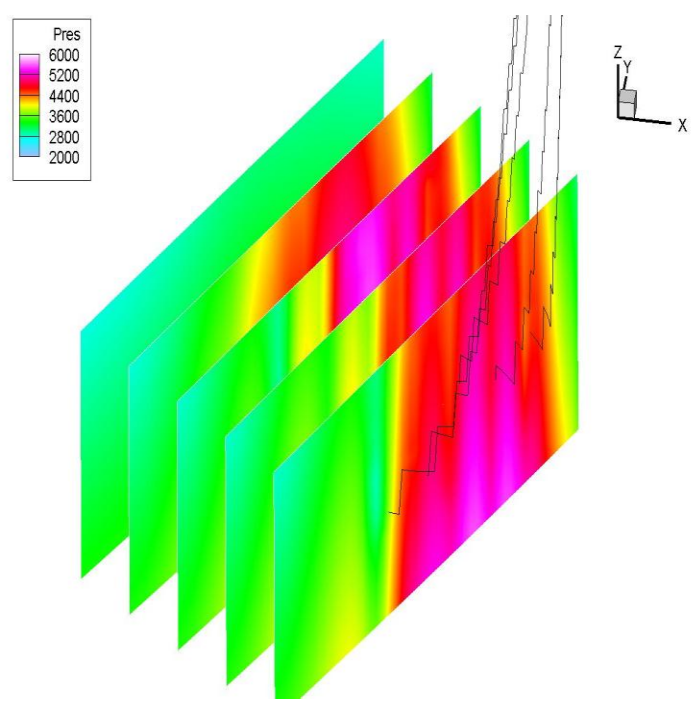


Figure 4. 45 Fluid pressure on J-plane on Feb 28, 1998 (unit: KPa)

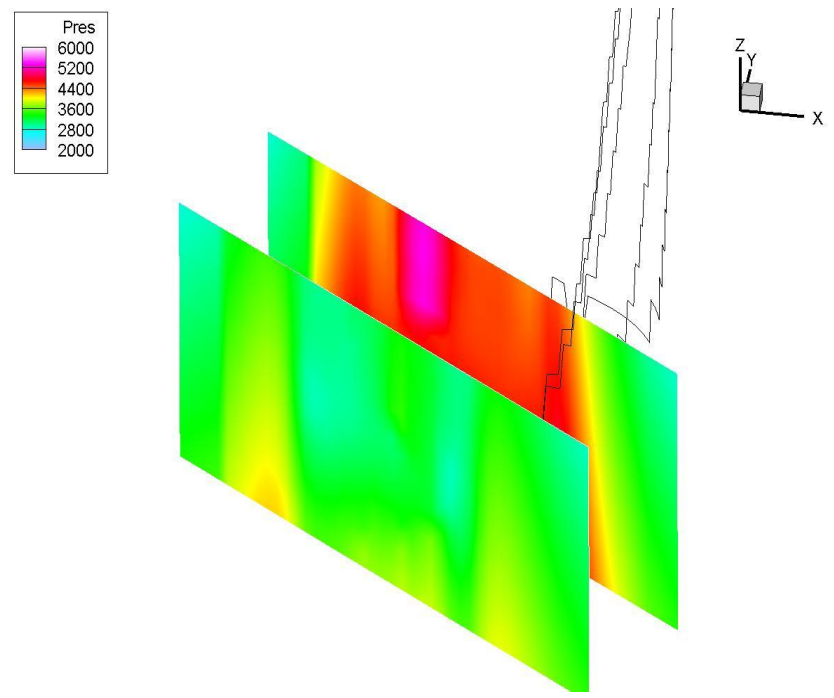


Figure 4. 46 Fluid pressure on I-plane on Feb 28, 1998 (unit: KPa)

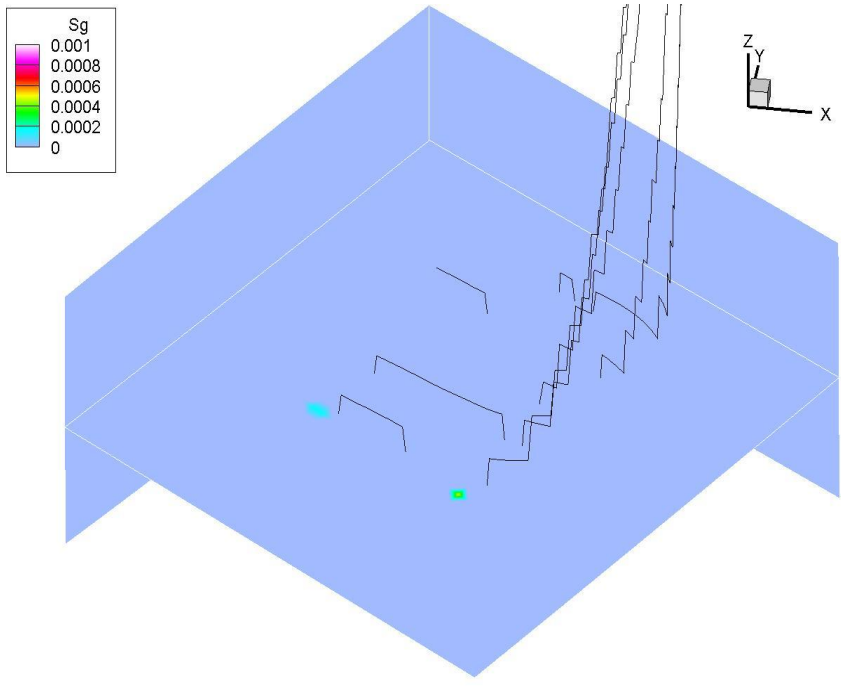


Figure 4. 47 Gas saturation on K-plane on Feb 28, 1998

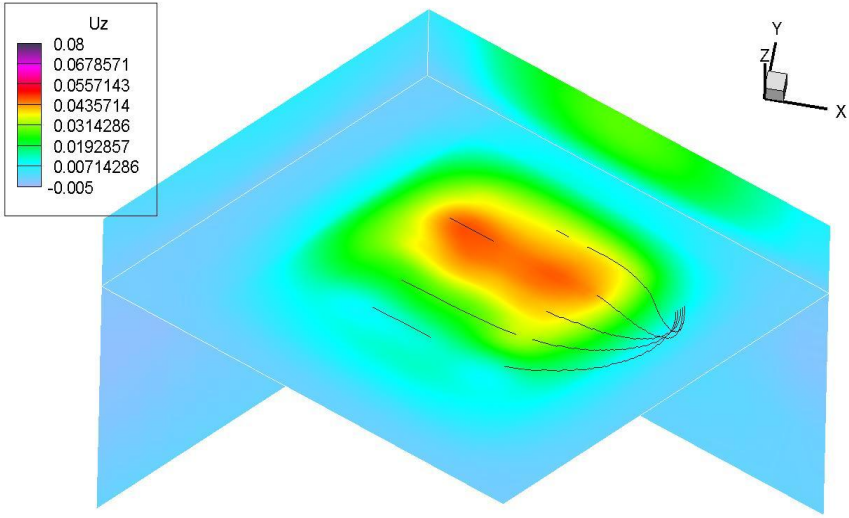


Figure 4. 48 U_z distribution in the middle of the reservoir on Feb 28, 1998 (unit: m)

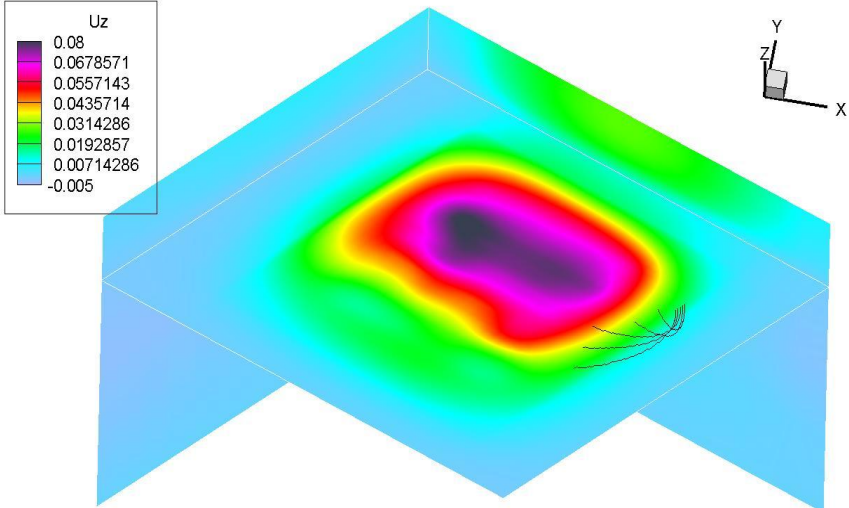


Figure 4. 49 U_z distribution on the top of the reservoir on Feb 28, 1998 (unit: m)

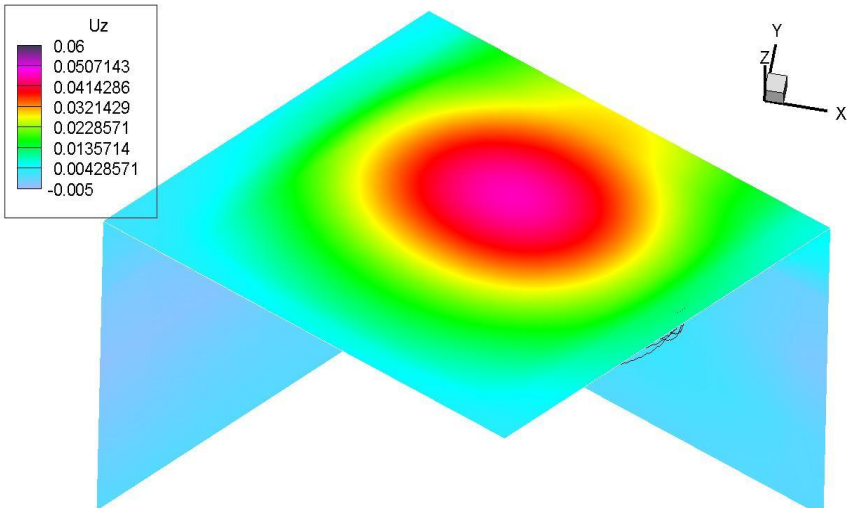


Figure 4. 50 U_z distribution on the ground on Feb 28, 1998 (unit: m)

4.7 Problems

In computer modelling, there are assumptions that must be maintained for the outcome to be close to reality. One of the most important parameters in reservoir simulation is the permeability, whose spatial and temporal evolution with recovery progression controls the flow pattern and its subsequent pressure and temperature fronts, then stress and strain fields.

In the previous chapter, a model of permeability was developed using many different kinds of data resources. In the course of injection and production, vertical hydraulic fractures are assumed to open when effective stress becomes negative (extensional). The flow is also limited within the reservoir body. However, these inputs may not be true. The initial permeability distribution and its anisotropy may not be accurate enough to affect the flow direction in the beginning. In the recovery process, shear failures in addition to tensile fractures may have happened and their interactions are unknown. The breakthrough of fluid movement into overlying/underlying formations may have taken place. Horizontally the fluids may have flowed outside of the simulation area along unknown fractures and adjacent wells may have caused interferences.

A significant implication is that the wells may have communicated with each other in terms of fluid flow, as evidenced by large water cuts and small oil productions for wells 239 and 226 in November (1997) while the rest of wells were under steam injection, followed by declining water outputs and strongly boosted oil rates in December (1997) while the rest of wells were shut in (see Table 4.1 and Figures 4.51 & 4.52). This is in sharp contrast with the independent flow systems predicted by the simulation. There are many other problems, which can invalidate the simulation too. For instance, the initial conditions of fluid

pressure affect the timing and intensity of fracturing. Thermodynamic parameters determine the partition of gas and liquid. These data are quite often in error.

The reality underground, therefore, remains to a large extent a mystery. History matching may help to some degree, but parameter adjustments are arbitrary or empirical. A good match does not necessarily verify the results.

Now that there are many uncertainties, simulation results are always viewed with cautious, even doubtful, eyes. For meaningful and useful simulation, it is necessary to have an independent source validate them.

Surface seismic surveys offer an objective observation of what is really going in the reservoir and surrounding areas. The discipline is called time-lapse or 4D seismic, which compares in different ways the baseline and monitor survey for changes, which may represent the flow path, or pressure, or temperature front. Another unconventional one is wavelet transform that unravels anomalies in the reservoir by using the monitor survey only. In the next two chapters, the direct measurements of the reservoir with seismic data will be deal with before any further meaningful work on reservoir simulation can proceed.

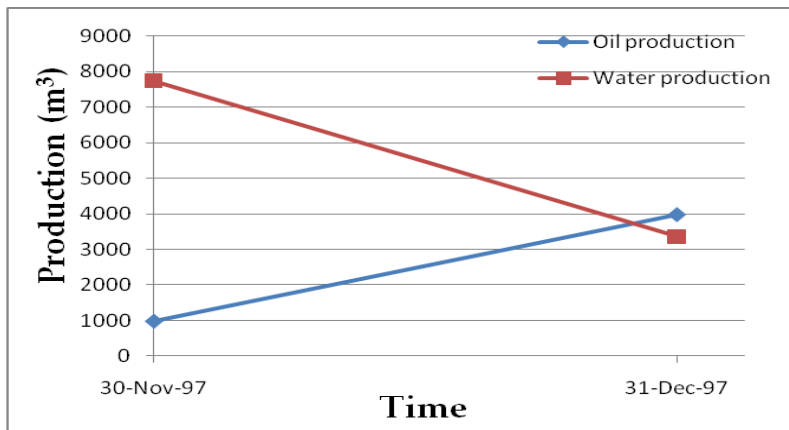


Figure 4. 51 Production history for well 239

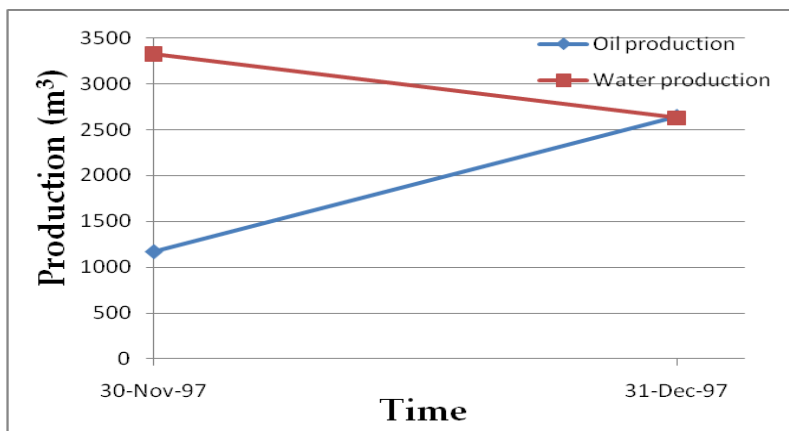


Figure 4. 52 Production history for well 226

CHAPTER 5 POST-STACK TIME-LAPSE SEISMIC PROCESSING AND INTERPRETATION

5.1 Introduction

There are two approaches to unmasking seismic changes caused by reservoir recovery. Conventionally, we compare the baseline survey and the monitor survey in a number of different ways to extract the amount of seismic changes in space. For example, time thickness bound by two definite horizons is an attribute whose changes can indicate velocity changes. Again, trace-by-trace cross correlation can find where trace disturbances occur. The most direct and also widely used attribute is amplitude difference whose magnitude can be used to express the spatial variation of changes. The second approach called an unconventional one is to employ the monitor survey only, a self spatial comparison. It is highly effective if the geology is fairly stable.

Considering that the time-lapse seismic refers traditionally to the conventional one, this chapter deals mainly with cross-equalization post-stack processing and selected attributes and interpretation. The unconventional one will be detailed in the next chapter called Wavelet Transform and its Application to Time-lapse Seismic.

5.2 Time-lapse seismic data review

The oil company drilled five horizontal wells in this area (Figures 3.1 and 5.1), in an attempt to enhance recovery efficiency. To monitor the performance of

these wells, two 3-D seismic surveys (Figure 5.1) were shot prior to steam injection and after oil production, respectively. The procedure of data acquisition and processing was designed for time-lapse seismic repeatability with efforts to minimize any artificial differences, as evidenced by the post-stack seismic sections for the baseline line (1997) and the first monitor line (1998), which look visually similar and comparable (time shift by 100ms down was applied by the processor) (Figure 5.2). The bandwidth and amplitude spectra for the entire seismic traces or for windows of varying time length also demonstrate a resemblance between these two surveys (Figure 5.3).

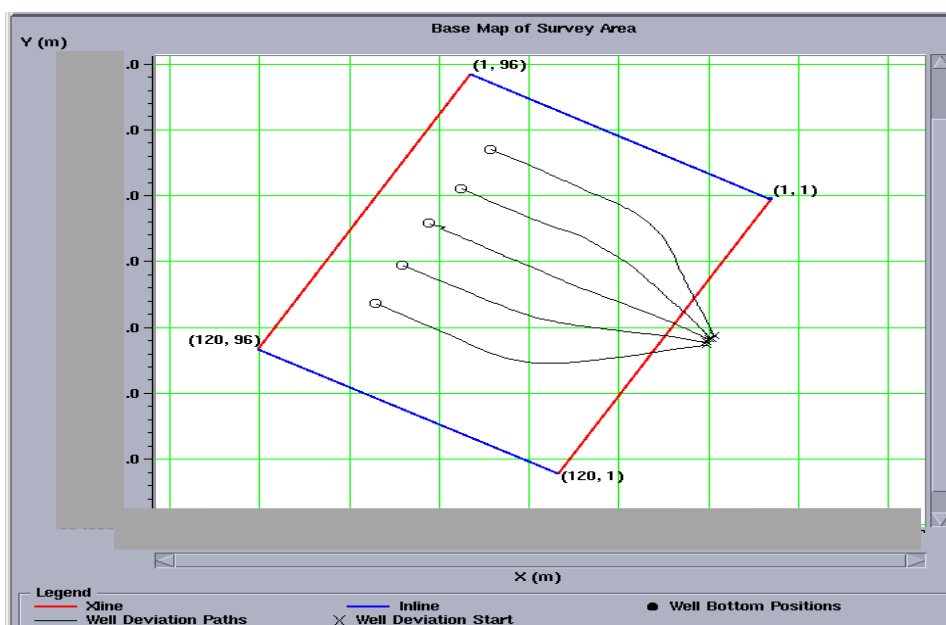


Figure 5.1 3 D time-lapse seismic survey area and well locations

It was seen without detailed cross equalization that the recovery in the reservoir (510-560 ms) has engendered consistent amplitude anomalies at 540 ms at five drilling locations on the monitor survey (Figure 5.4). The anomalies, however, do not occur in the baseline survey (Figure 5.5). RMS amplitude map sliced at the window of 10 ms centred at 540 ms shows the conformance of these

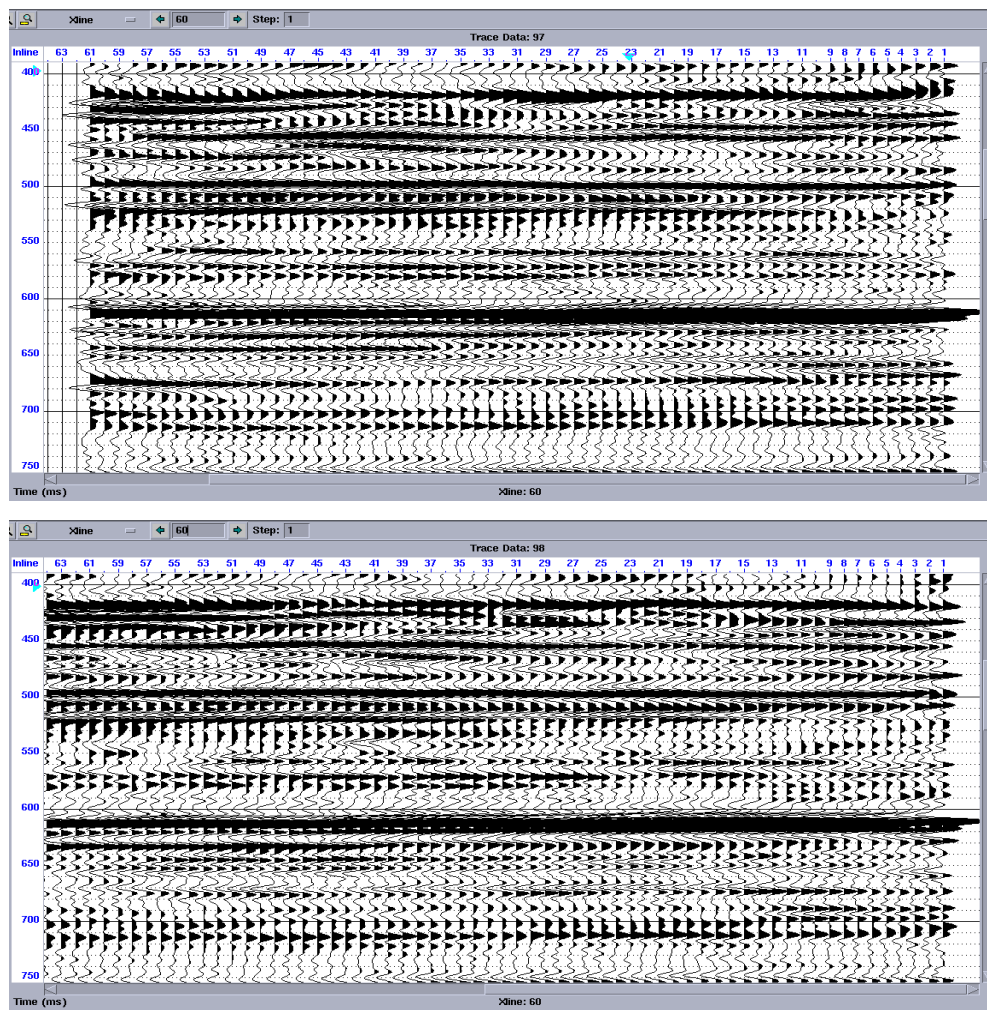


Figure 5. 2 Seismic sections of baseline (upper, 1997) and monitor (lower, 1998) surveys

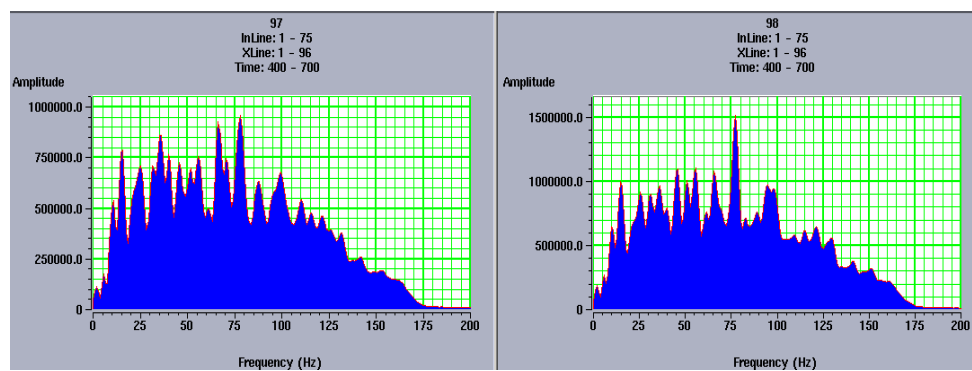


Figure 5. 3 Amplitude spectra of baseline (left, 1997) and monitor (right, 1998) surveys

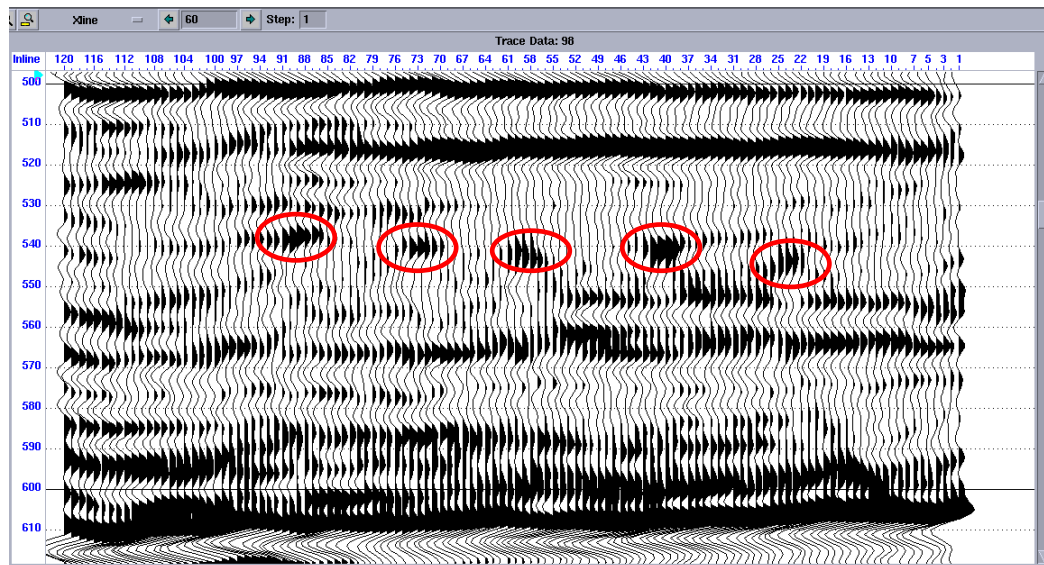


Figure 5. 4 Amplitude anomalies (as indicated by red circles) of 1998 data at 540 ms at five locations. (Note: polarity flipped for striking effect)

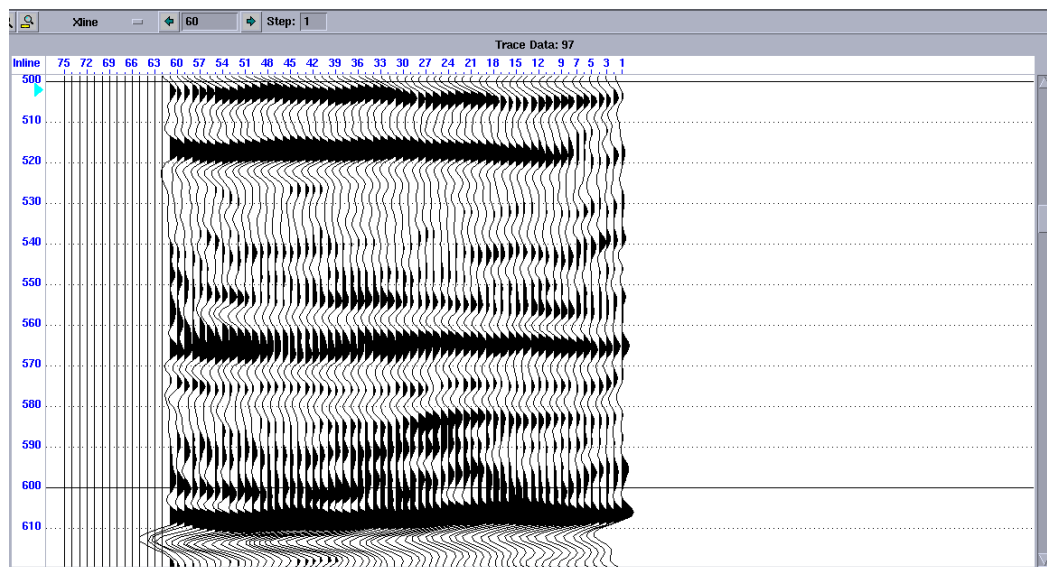


Figure 5. 5 No amplitude anomalies of 1997 data at 540 ms at five locations. (Note: polarity flipped for striking effect)

anomalies to the trajectories of five horizontal wells (Figure 5.6). The slight well path deviation from them probably arises from inaccurate measurements, either in well coordinates or in seismic geometry. When cross correlating trace by trace

It was also observed from other seismic sections that time sag and amplitude attenuation on the top of Devonian and trace disturbance below the reservoir zone exist in 1998 data (Figure 5.8), while they do not appear in 1997 data (Figure 5.9). Furthermore, a horizon along the strong reflection event at the top of Devonian (around 610 ms) was picked for both data sets. Contours of the time (Figure 5.10) and amplitude (Figure 5.11) for this horizon and cross correlating trace by trace the window (560-605ms) between the reservoir bottom and the top Devonian (Figure 5.12) demonstrate a surprise discovery in 1998 data of two potential fracture zones across wells below the reservoir. By calculation, the amplitude on the time sags was attenuated by 500% when compared with that on the background, a substantial decrease that may be caused by gas. As shown in Figures 5.6 and 5.12, the zone of poor cross correlation is corresponding in terms of position and direction, which may display the extension of the two potential fracture zones from top Devonian to McMurry to Clearwater (reservoir). In Figures 5.13 and 5.14, the characteristic time sags and amplitude drawdown across wells do not happen in 1997 data. The fracture zones may have cut into interior Devonian (below 610ms) since there are trace disturbances (Figures 5.15) for 1998 data and none for 1997 data (Figure 5.16), and spatial distribution of poor cross correlation (Figure 5.17). Whether fluids moved upward through the caprock or not is plausible. The traces pattern above the reservoir looks different between 1998 data and 1997 data (Figures 5.18 and 5.19), and the low cross correlation has some spatial regularity as well (Figure 5.20). They may infer fluid upward leakage.

Based on the above graphics and analysis, we can make the tentative hypothesis that being injected along the five horizontal wells, the steam moved mainly downward along the two fractures, which may be initiated by steam injection, through the underlying McMurry formation and probably into Devoni-

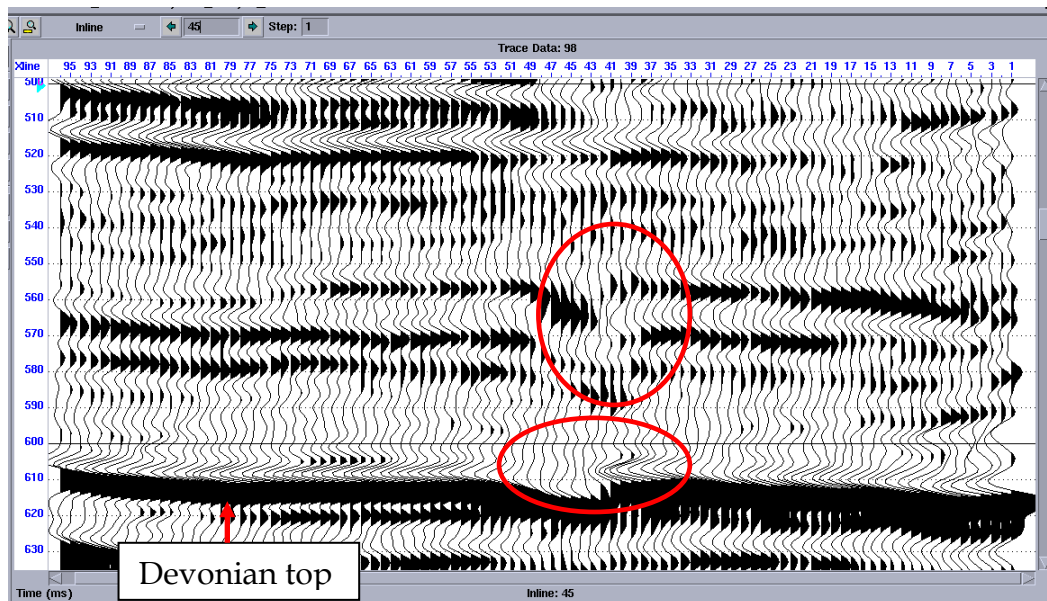


Figure 5. 8 Time sag and trace disturbance below the reservoir for 1998 data

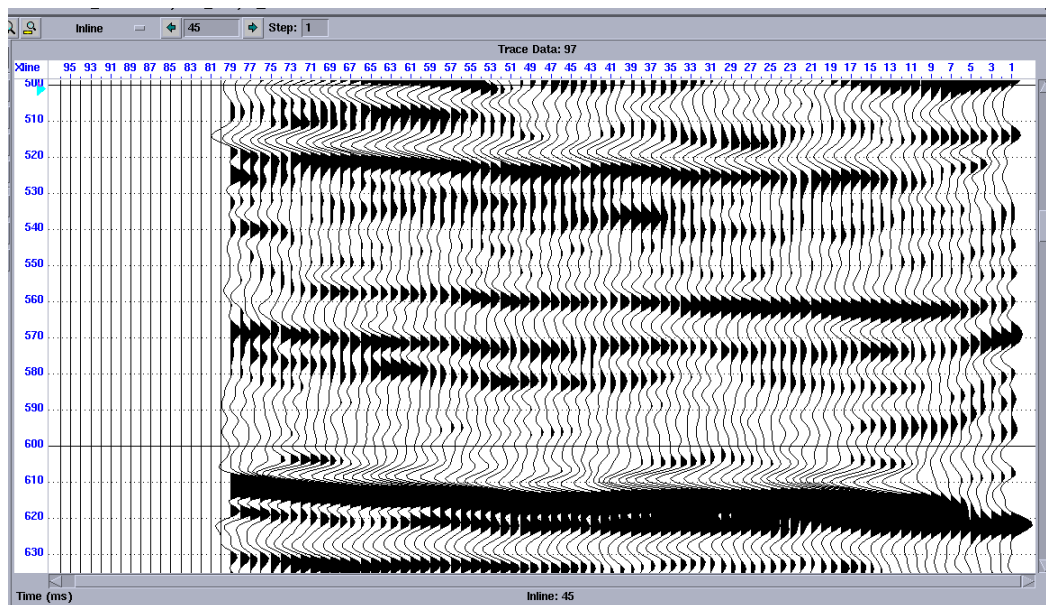


Figure 5. 9 No time sag and trace disturbance below the reservoir zone for 1997 data

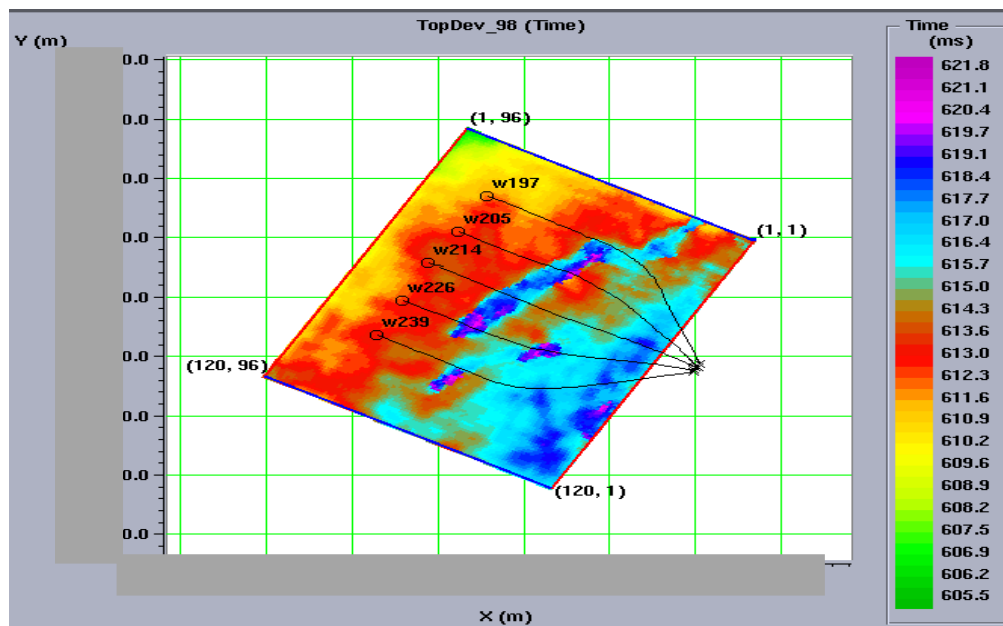


Figure 5. 10 Map of the horizon of Top Devonian for 1998 data, indicating time sags across the wells

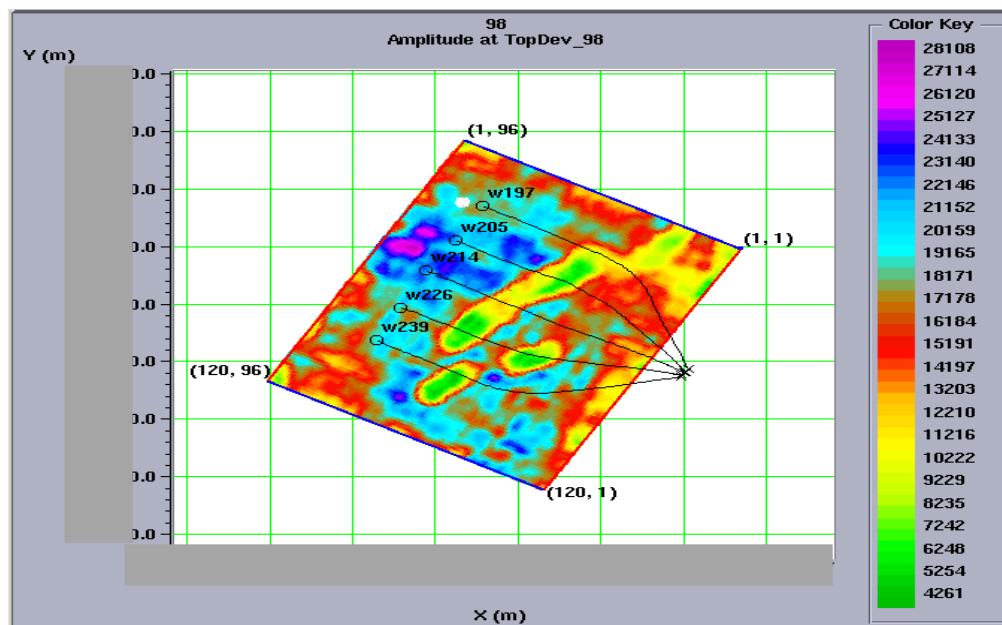


Figure 5. 11 Amplitude map across the wells along the horizon of Top Devonian for 1998 data

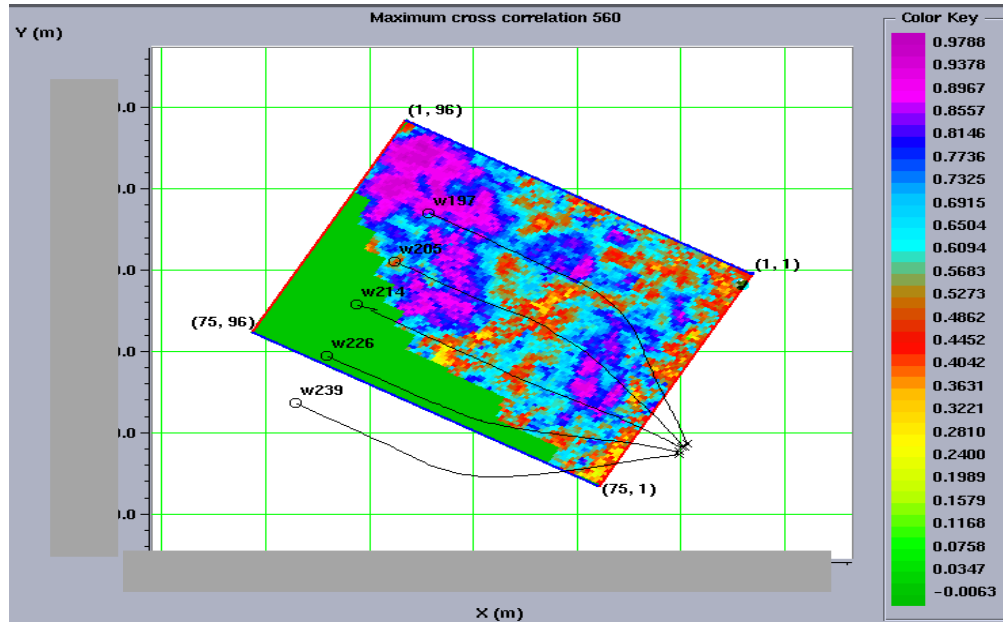


Figure 5.12 Cross correlation of the window of 560-605 ms between 1997 data and 1998 data

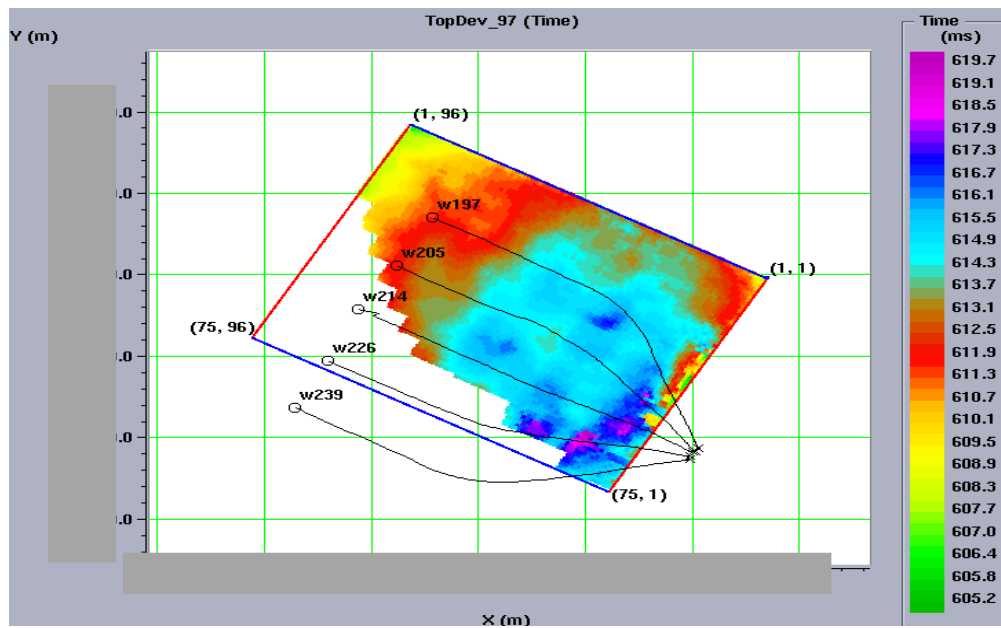


Figure 5.13 No time sag observed across the wells along the horizon of Top Devonian for 1997 data

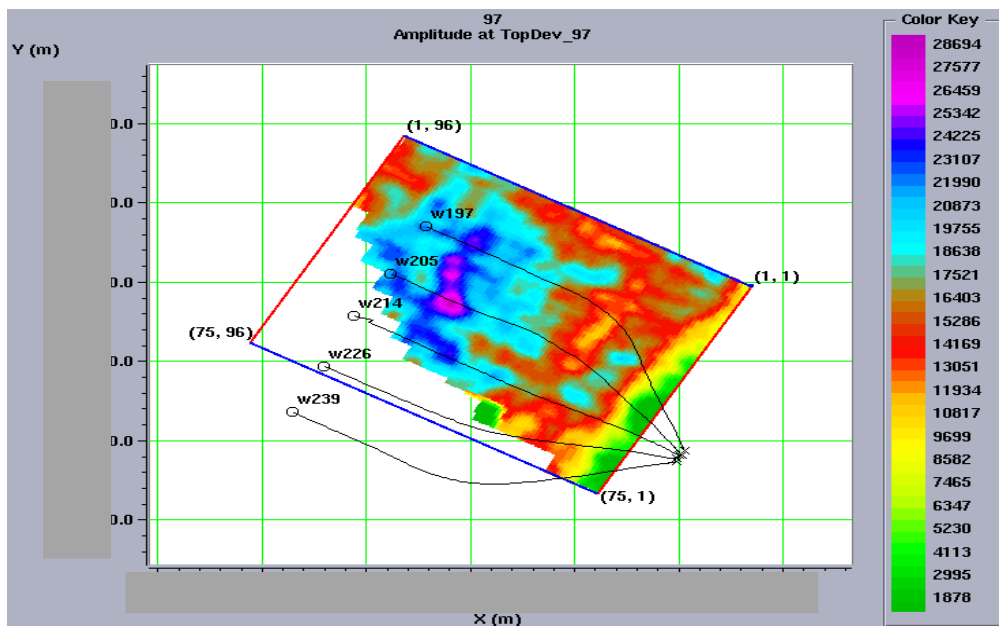


Figure 5.14 No Amplitude attenuation zone observed across the wells along the horizon of Top Devonian for 1997 data

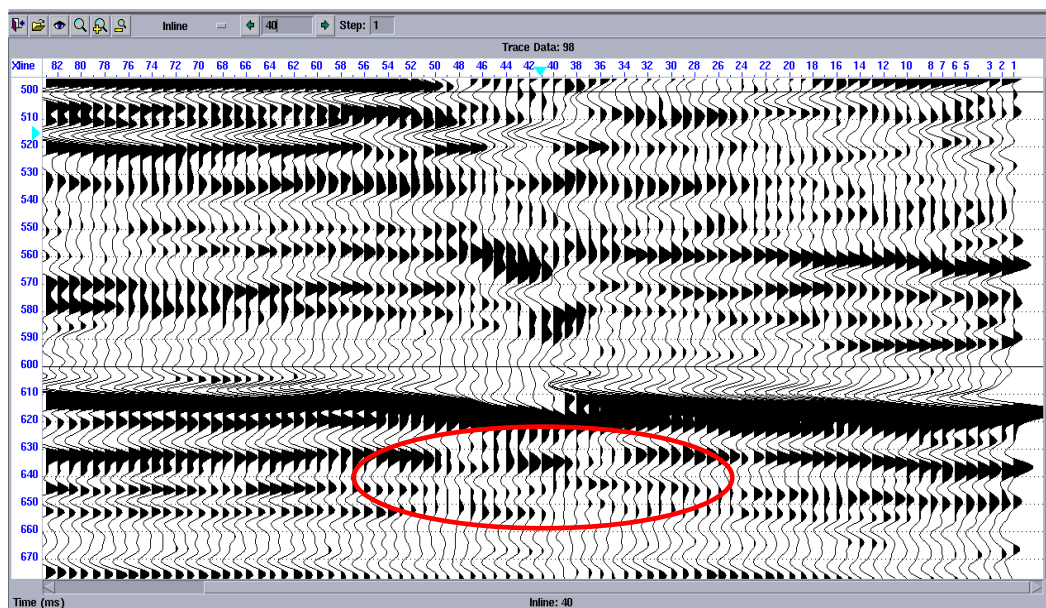


Figure 5.15 Seeming trace disturbance below top Devonian for 1998 data

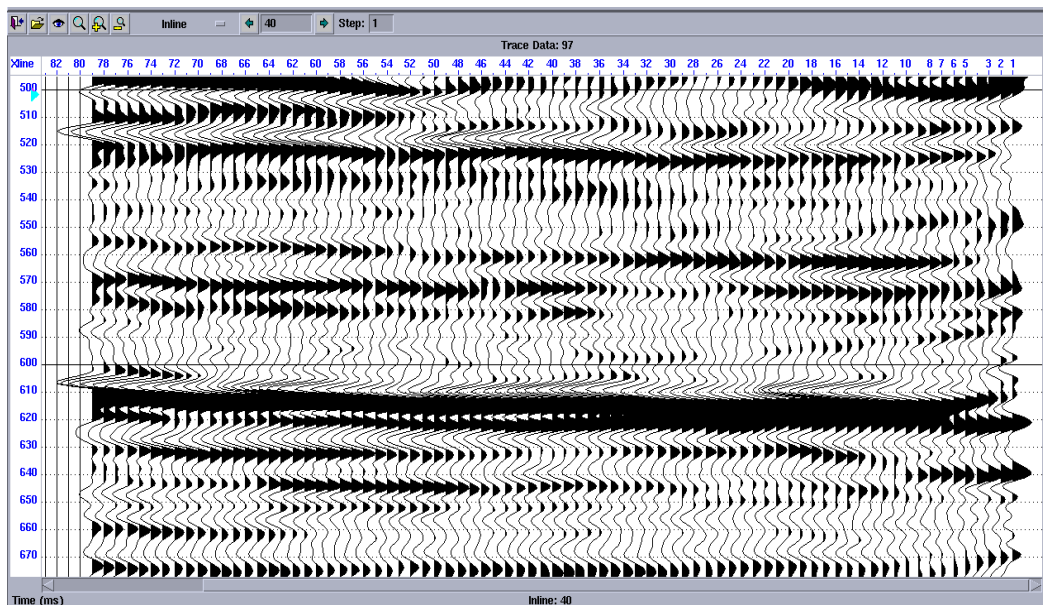


Figure 5.16 No trace disturbance for 1997 data

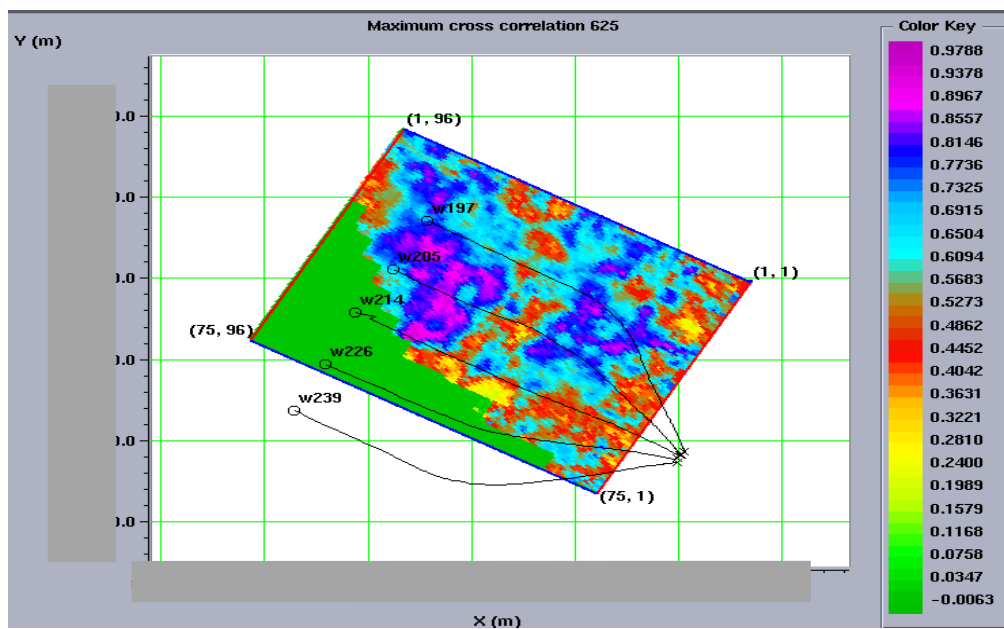


Figure 5.17 Cross correlation of the window of 625-675 ms between 1997 data and 1998 data

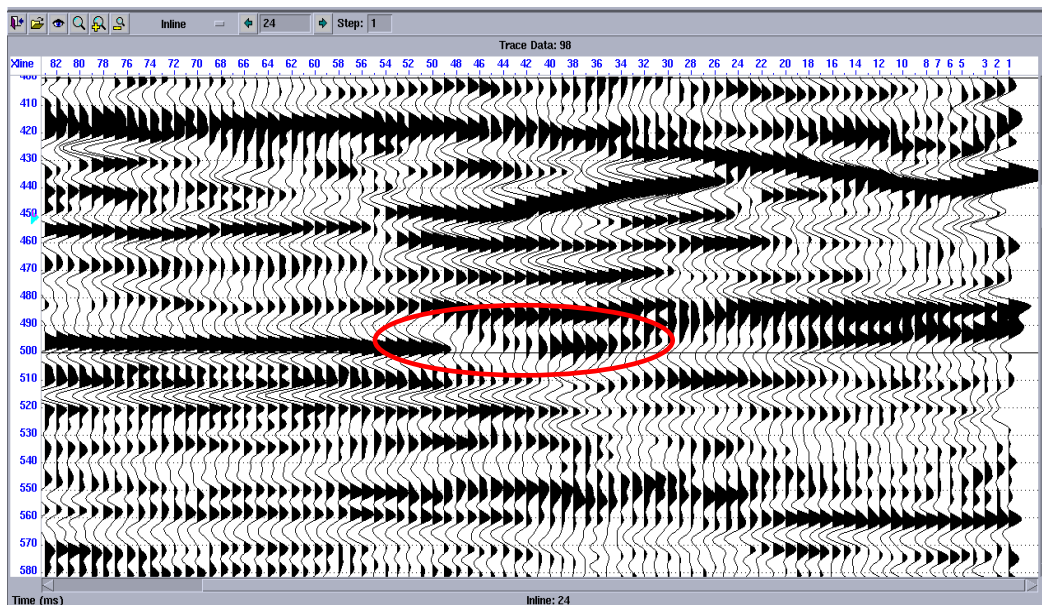


Figure 5. 18 Apparent trace disturbance above the reservoir for 1998 data

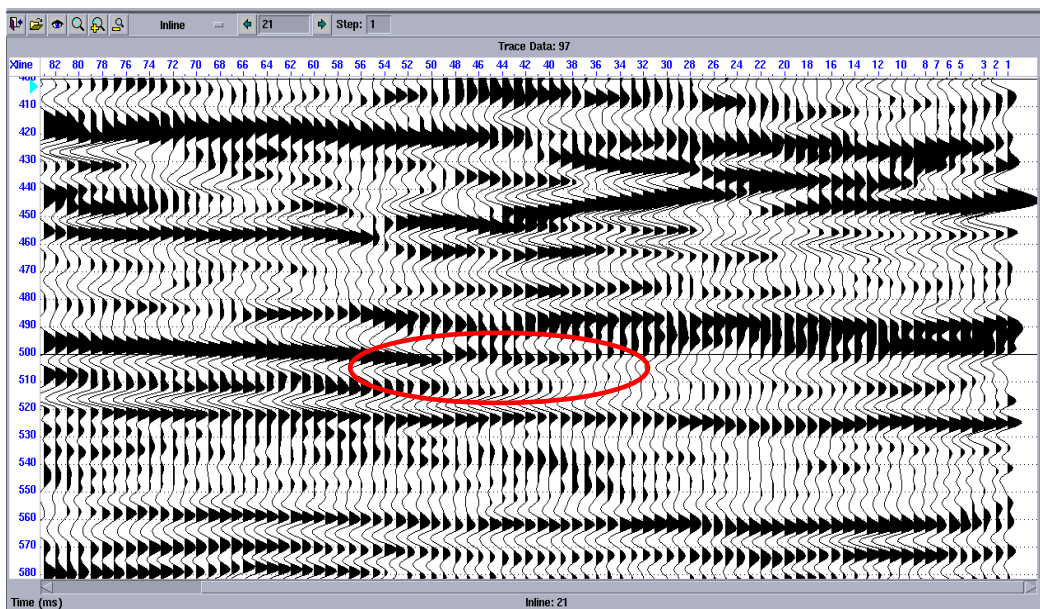


Figure 5. 19 Original undisturbed section of 1997 data

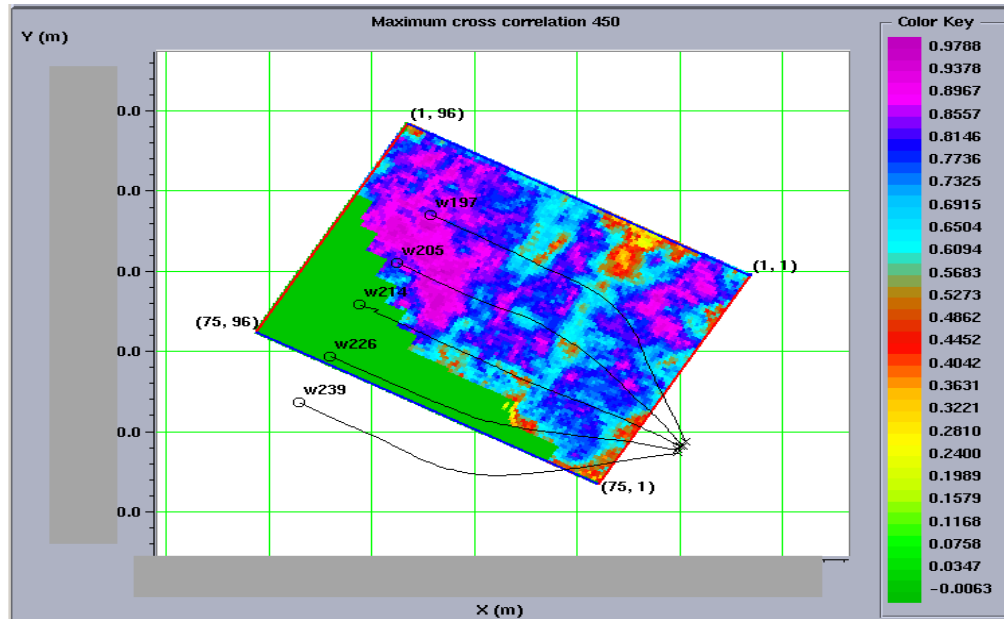


Figure 5. 20 Cross correlation of the window of 450-510 ms between 1997 data and 1998 data

an, also with a portion going upward along the fracture zones and likely leaked into the overlying formations in some locations.

5.3 Time-lapse seismic processing fundamentals

Even though the data acquisition and processing were 4D intended, a direct amplitude subtraction displays a substantial difference (Figure 5.21), and even in areas, where it was not supposed to occur (Figure 5.22). The difference results from the differences in wavelets and in positioning reflection events, which need a technique called Cross Equalization (Ricket and Lumley, 1998) to minimize them. Generally, cross equalization includes temporal and horizontal resampling to account for different sample rates and different CDP locations, amplitude balancing for equal energy level, phase rotation for phase match, shaping filtering to compensate for different wavelets and 3-D cross correlation

to align reflection events. Resampling is not necessary in this project, as mentioned before. Thus, the topics as related to anti-aliasing filtering in f , k_x and k_y domains and interpolation won't covered. The focus will be on the last few steps.

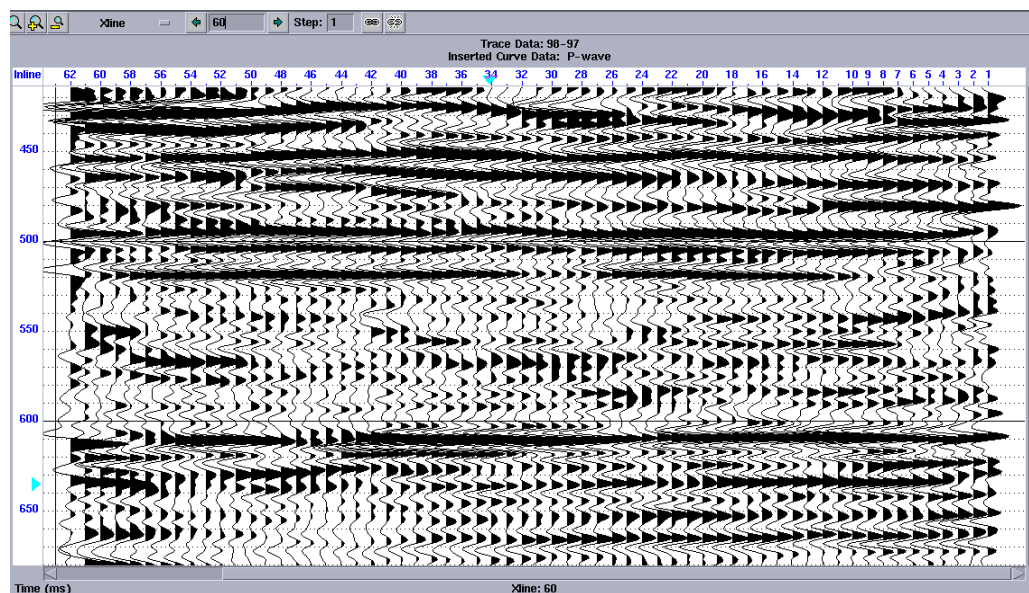


Figure 5.21 Difference seismic section without time-lapse processing

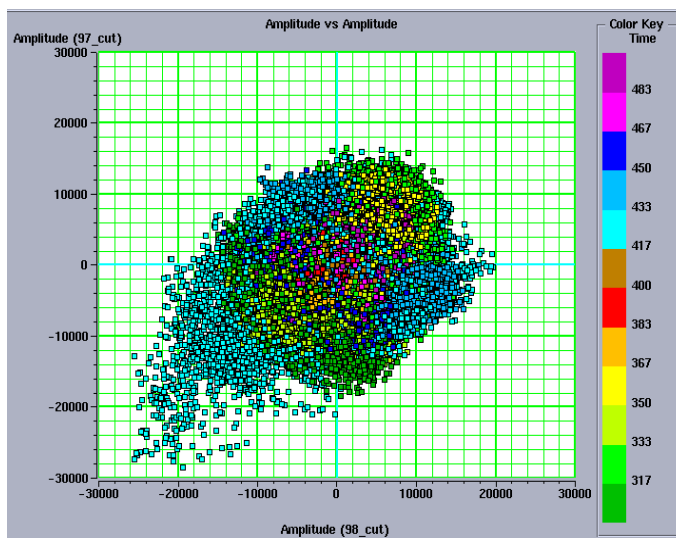


Figure 5.22 Crossplot (on the window of 300-500ms) of 98 and 97 data without time-lapse processing

Trace energy often varies with source strength, anelastic absorption, gain corrections and more. These factors most likely change among seismic surveys shot at different calendar times. It is therefore necessary to balance the energy level in order to remove artifacts occurring in the difference data cubes. A simple way to do this is to calculate the rms amplitudes or envelopes of seismic traces for the baseline and monitor surveys so that a scale factor can be found and applied to the latter. In this operation a longer time window is recommended for the purpose of retaining amplitude changes caused by real reservoir changes.

The time shift (or linear phase shift) is the time, where cross correlation peaks on the cross correlation trace. Subsequent constant phase rotation can be evaluated by the following equation:

$$\frac{\sum_i A(i) \cos[\alpha(i)]}{\sum_i A(i)}_{(baseline)} = C \frac{\sum_i A(i) \cos[\alpha(i)]}{\sum_i A(i)}_{(monitorline)} \quad (5.1)$$

where $A(i)$ is instantaneous amplitude, $\alpha(i)$ is instantaneous phase. It is assumed that trace energy is already balanced before this operation. When C is found, the phase rotation can be computed for the monitor survey.

Shaping filtering is the process by which an input signal is shaped to look like a desired signal in least-square sense (Ricket and Lumley, 1998; Robinson and Treitel, 1980). Mathematically the shaping filter is constructed by minimizing the difference, R , between the shaped output and the designed signal, as shown in the following equation:

$$\mathbf{R} = \mathbf{F} * \mathbf{S}_1 - \mathbf{S}_2 \quad (5.2)$$

where F is the shaping filter, S_1 is the input signal and S_2 is the designed signal. In terms of time-lapse seismic, S_1 and S_2 represent the seismic traces at a certain time window at separate calendar times and F is the filter that tries to increase their similarity. The time window is generally selected to lie above the reservoir or other unaltered zones so that the application of the filter obtained from equation (5.2) to the whole seismic trace including the reservoir can minimize differences in wavelets while keeping differences caused by reservoir changes. Experiments on synthetic seismic traces indicates that the longer that window, the better. The length of the shaping filter is another factor to influence the magnitude of R in equation (5.1). A long filter has a tendency to lower R , but this improvement may not compensate enough for the drawbacks of a long computation time. In some cases, it renders a worse result when the length reaches a certain limit. The suitable length is found by synthetic seismograms to be a few times that of the effective wavelet. Any length greater than that will prolong computation without significant outcome enhancement; any length smaller than that will deteriorate the results.

Ideally speaking, amplitude balancing and phase match are already included in the shaping filter acquired over the design window from the above operation. In other words, after application of the shaping filter, the energy level and phase angles should match well. However, it should be noted that the solution to equation (5.2) has limitations. The convolution in equation (5.2) can be written in matrix form:

$$F * S_1 = A_{S_1} F \quad (5.3)$$

The solution to equation (5.2) can be formulated as:

$$(\mathbf{A}_{S1}^T \mathbf{A}_{S1})\mathbf{F} = (\mathbf{A}_{S1}^T \mathbf{S}_2) \quad (5.4)$$

In some cases, the matrix before \mathbf{F} in equation (5.4) is ill conditioned and the least squares estimate \mathbf{F} amplifies the noise arising from the right hand. Moreover, minimized \mathbf{R} does not necessarily mean that \mathbf{R} is small enough to have a satisfactory match of both amplitude and phase.

By cross correlating a pair of seismic traces, one tries to find the time shift at maximum cross correlation coefficient, and then applies it to the other trace (monitor survey) for better reflection event alignment for this pair. The window of cross correlation can vary in length, depending on specific problems. The operation can be carried out in one dimension (e.g., time) or in three dimensions (time plus x and y). When in the time dimension over the entire seismic trace, it can be used to remove static differences. When in three dimensions over a small window, it can be used to solve the problem of differences in positioning reflection events, which may be due to differences in NMO corrections and migration velocity models. Considering that 3D cross correlation is little discussed in literature, the next section will elaborate regarding its principle and application.

5.4 3D cross correlation algorithms

Conventionally, cross correlation refers to computing the cross correlation coefficients between a pair of traces in the dimension of time. The procedure is based on equation 5.5. Two normalized variables (amplitudes of the baseline and monitor survey) are multiplied with t as the lag (negative shift) of trace A with respect to trace B. This operation creates a cross correlation trace with time shifts

as x axis and cross correlation coefficients as y axis. The maximum value on this trace represents the maximum similarity the two compared traces can reach. As a result, the pair of traces can be made close to each other by shifting the time at this peak. By convention, we shift time on the traces of the monitor survey.

$$\rho_{(t)} = \sum_{i=1}^n (A_{(i+t)} B_{(i)}) \quad (5.5)$$

where $\rho_{(t)}$ is the cross correlation coefficient at time lag t ; A and B are normalized amplitudes for reference trace A and compared trace B, respectively; n is sample length. Normalization means zero mean and unit standard deviation and can be achieved by:

$$X_i^{norm} = \frac{X_i - E(X)}{\sqrt{(\sum_{i=1}^n (X_i - E(X))^2) / n}} \quad (5.6)$$

In practice, the trace is divided into a number of windows and time shift is calculated for each window and can be put in the centre of the window. Time shift for each sample is interpolated from these time shifts. The time shifted samples are used to find by interpolation and extrapolation amplitude values at regular positions of these samples. Interpolation and extrapolation can be many such as linear, cubic, spline, polynomial etc., and the good ones are data dependent and need many tests. In our case, linear algorithms perform well.

As we know, the reflection events are generally three dimensional, and so are the misfits of these events between two 3D surveys. The conventional time dimension match realizes a mere portion of 3D match. For better results, it is

essential to do the same for the other two directions (x and y). 3D cross correlation can be defined as:

$$\rho_{(t,x,y)} = \sum_{i=1}^{n_t} \sum_{j=1}^{n_x} \sum_{k=1}^{n_y} (A_{(i+t,j+x,k+y)} B_{(i,j,k)}) \quad (5.7)$$

where $\rho_{(t,x,y)}$ is the cross correlation coefficient at time lag t , inline lag x , and crossline lag y ; A and B are normalized amplitudes for reference trace A and compared trace B, respectively; n_t , n_x , n_y are sample lengths in three directions t , inline and crossline, respectively.

Similar to 1D case, we can design the algorithms and procedure for 3D computation. First, 3D data volume is divided into many small cubes and equation 5.7 is applied to each one. The computed lags for each cube are put in its centre. Second, the lags (t , x , y) for each sample (total length of time \times total length of inline \times total length of crossline) are interpolated from these lags. Finally, the amplitudes on regular positions are interpolated and extrapolated from the amplitudes on shifted positions. However, there are two difficulties involved in the operation. First, we need to convert time to depth before interpolation, which incurs a tremendous amount of work. Second, the results are sensitive to interpolation methodologies and experiments are often daunting.

A simplified or quasi 3D cross correlation was proposed in the project. It treats each direction as a trace. Normally, the trace exists in time. As a matter of fact, the other directions (inline and crossline) can be viewed as traces as well. It would be reasonable to do 1D cross correlation individually for three directions in a more straightforward and easier way instead of 3D cross correlation. The concrete steps are as follows:

1D cross correlation applied to the time direction, and subsequent time shifts and amplitudes interpolated for the whole volume. It is expected that the difference will be down and the match will improve.

The same procedure applied to the directions of inline and crossline, respectively. The match will further improve.

Iteration of the above to more satisfactory results.

There are varieties of flow charts based on the principle of the quasi 3D cross correlation. For example, three 1D cross correlation for three directions can be performed at the same time before interpolation. The first 1D cross correlation can be conducted in inline or cross line direction, and so on. Experiments are needed to determine which flow is the best.

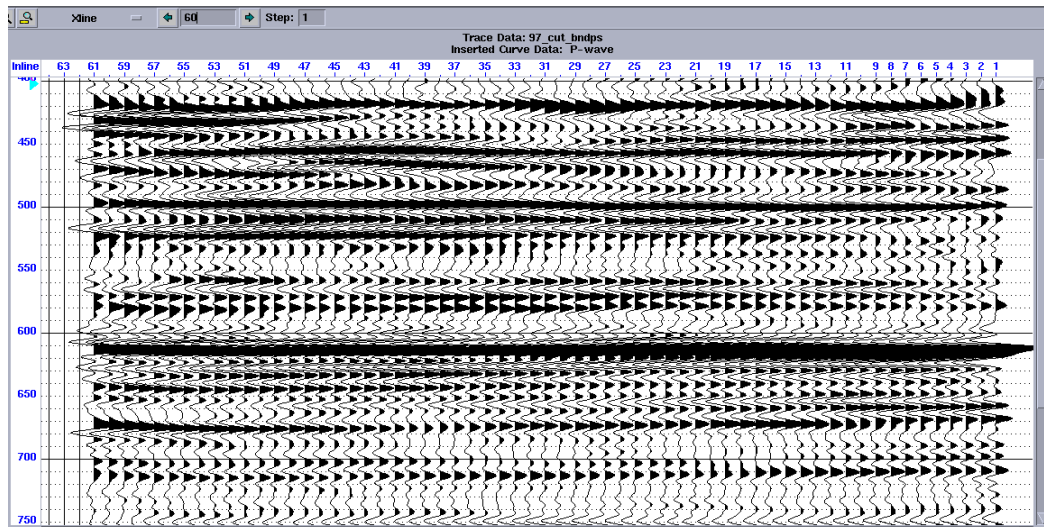
The quasi-3D cross correlation was applied to the 1998 data with the 1997 data as the reference volume. Compared with the amplitude (absolute) mean and standard deviation of 1997 data, those of the difference volume decrease with 1D time cross correlation, and further decrease with 1D cross correlation in two other directions of inline and crossline, as shown in the follow:

Before cross correlation:	84.7% (amplitude)	84.0% (standard deviation)
After 1D time cross correlation:	64.0% (amplitude)	59.2% (standard deviation)
After two other cross correlations:	56.1% (amplitude)	57.1% (standard deviation)

5.5 Time-lapse seismic processing and interpretation

The baseline survey (1997 data) missing a considerable portion, the monitor survey was first cut to match the geometry of the former. In order to attenuate noise and match the frequency band closely as well, both data sets were band pass filtered on the frequency range of 10/20-110/150, as shown in Figure 5.23. Despite match improvement when compared with Figure 5.22, their cross plot in Figure 5.24 indicates the presence of considerable mismatch (see Appendix 1 for the definitions of the mismatch indices). It arises from wavelet differences, which include different energy level, time shift and phase rotation, and amplitude spectra misfit (Figure 5.25). These differences can be minimized step by step by 4D processing scheme, proposed in the previous section.

First, global amplitude match was applied to 98 data so that the energy level would be balanced. In this operation, RMS amplitude on the widow of 300-900ms for these two volumes was made equal globally by scaling 98 data. Compared with the match in Figure 5.24, that in Figure 5.25 is improved slightly.



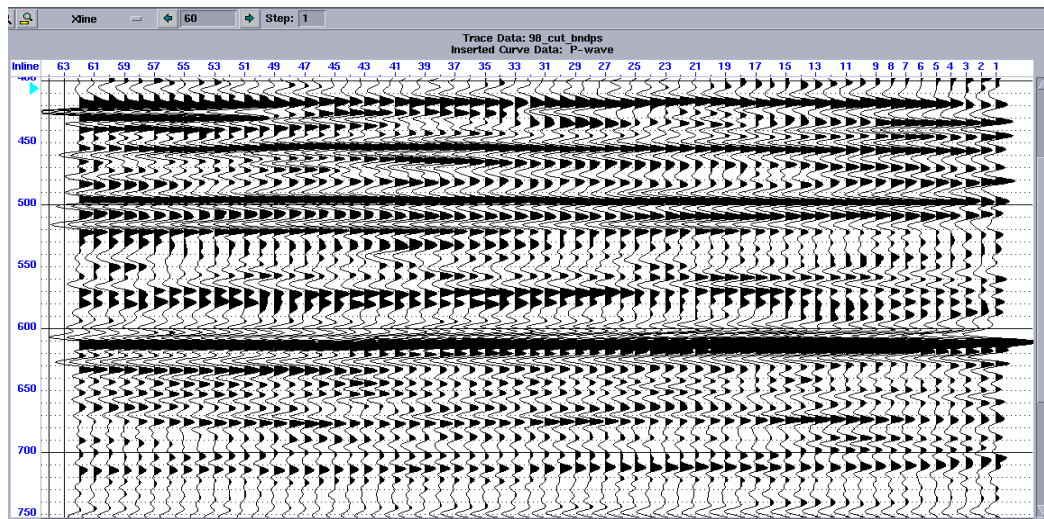


Figure 5. 23 Band pass filtered seismic sections of baseline (upper, 1997) and monitor (lower, 1998) survey

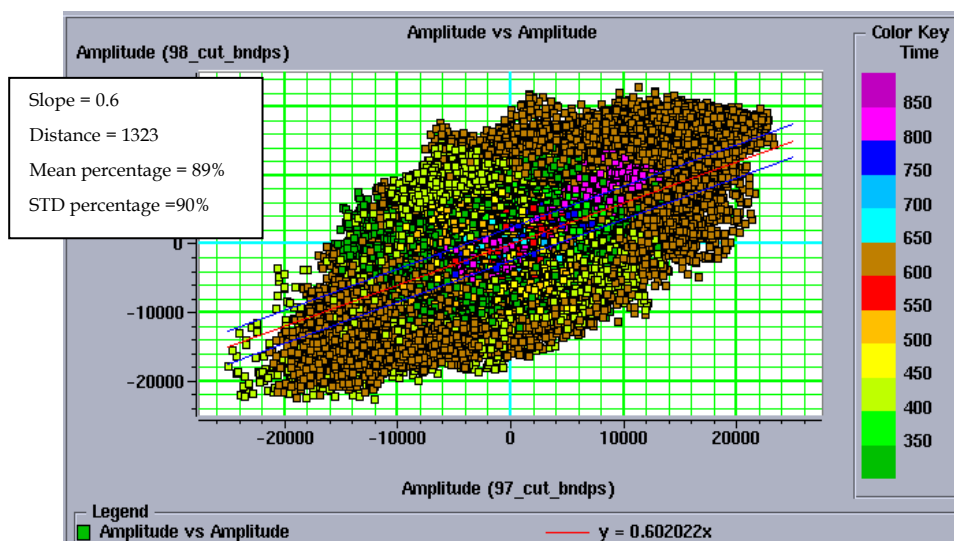


Figure 5. 24 Crossplot (on the window of 300-500ms) of 98 and 97 data with band pass filter applied to both volumes

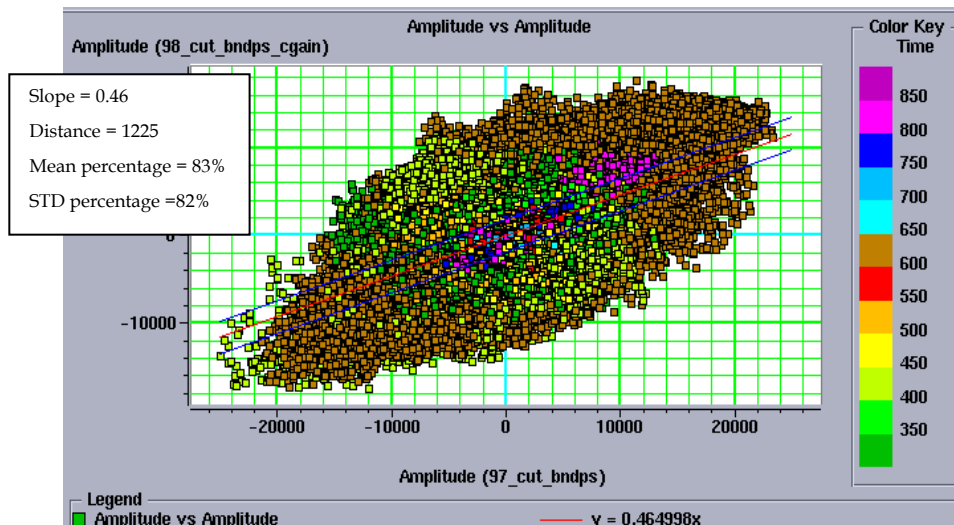


Figure 5. 25 Crossplot (on the window of 300-500ms) of 98 and 97 data with global amplitude scaling further applied to 98 data

Second, global phase and time shifts were calculated based on cross correlation on the window of 300-900 ms with a threshold of cross correlation coefficients 0.6. They were applied to 98 data. The match in Figure 5.26 further increases.

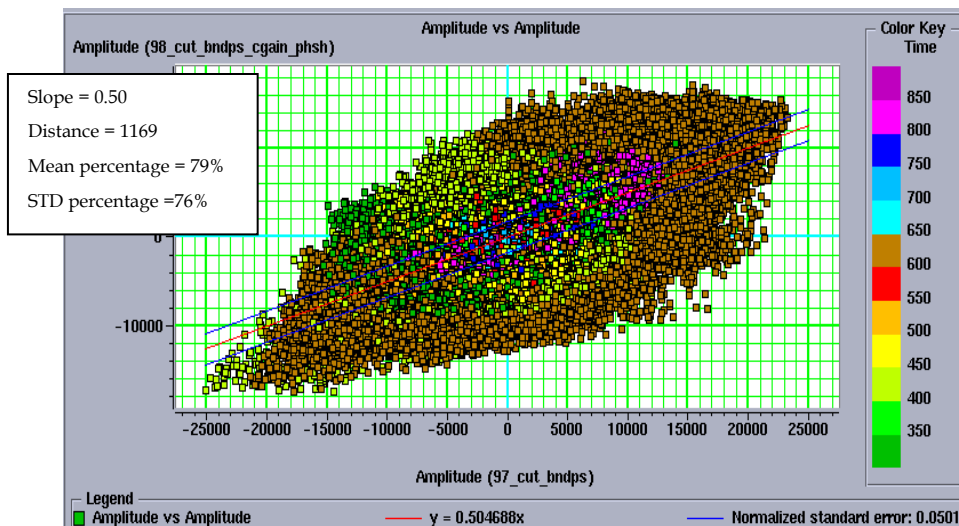


Figure 5. 26 Crossplot (on the window of 300-500ms) of 98 and 97 data with global time and phase shifts further applied to 98 data

Third, global shaping filter was designed on the window of 300-900 ms with a threshold of cross correlation coefficients 0.6, which we believe avoided the reservoir zone. It was then applied to the whole traces of 98 data. The match improves, as shown in Figure 5.27.

Fourth, seismic events alignment by way of 3D cross correlation was applied to 98 data. The match in Figure 2.28 improves significantly. The abnormal points come from noisy traces in the geometry edges due to incorrect 3D time shift. Removing these edge traces, the deviations are gone, as indicated in Figure 5.29. The final processed dataset is shown in Figures 5.30-31, in which the event of the Top Devonian and others are pushed up and aligned with that in

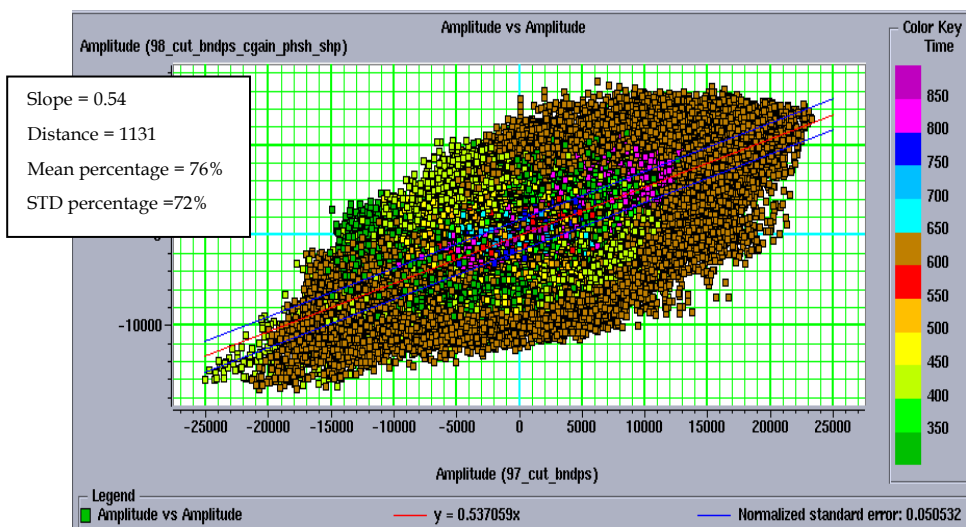


Figure 5. 27 Crossplot (on the window of 300-500ms) of 98 and 97 data with shaping filter further applied to 98 data

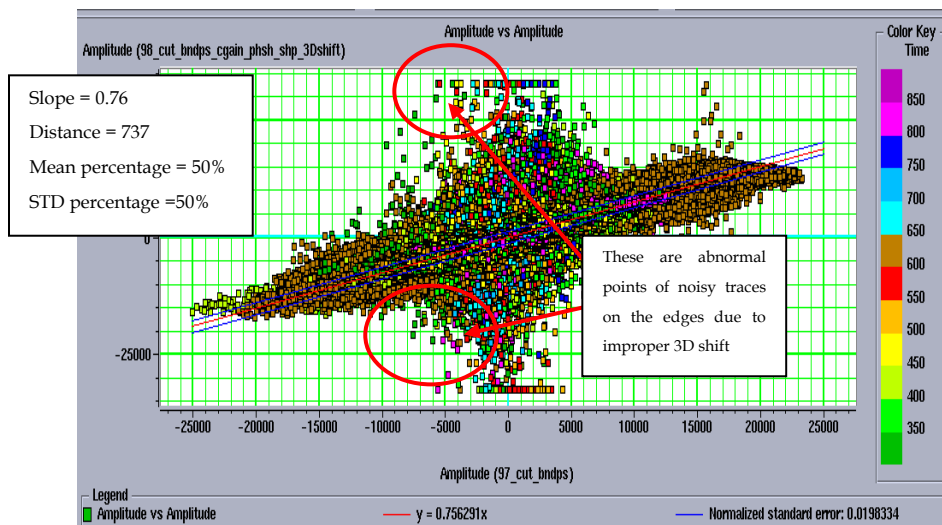


Figure 5. 28 Crossplot (on the window of 300-500ms) of 98 and 97 data with seismic events alignment by way of 3D cross correlation further applied to 98 data

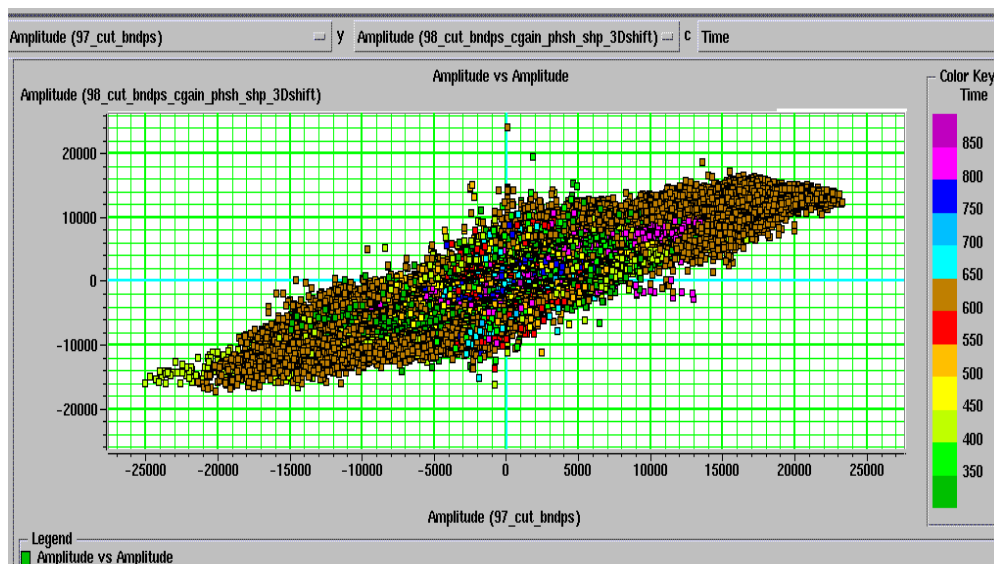


Figure 5. 29 Redrawing of Figure 5.28 with removal of edge traces

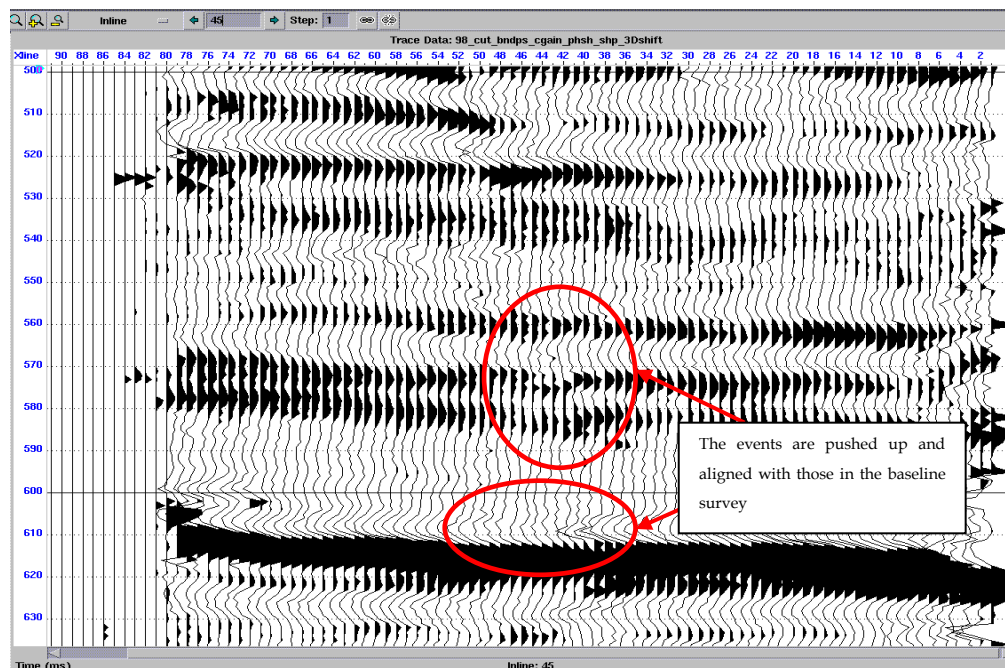


Figure 5.30 Final processed section (Inline45) of the monitor survey

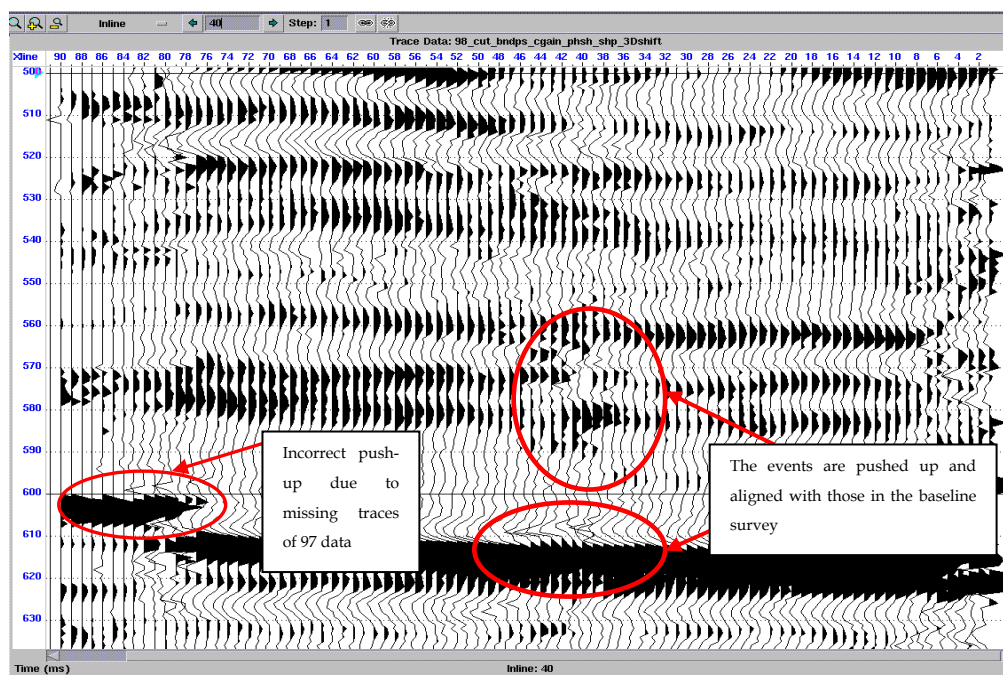


Figure 5.31 Final processed section (Inline 40) of the monitor survey

the baseline survey in Figures 5.9 & 16. The delayed events in Figures 5.8 & 15 are in sharp contrast with the aligned ones in Figures 5.30 & 31. The excessive time uplift on left in Figure 5.31 is due to missing traces in that portion of the baseline survey, which has led to incorrect cross correlation and time shift.

The example of the difference dataset, which was obtained by subtraction of the baseline from the processed monitor survey, is displayed in Figure 5.32. When compared between Figures 5.31 and 5.32, substantial events unrelated to 4D appear to be fairly removed. 4D anomalies could be delineated by high amplitude in Figure 5.32. The instantaneous amplitude map (Figure 5.33) sliced from this difference dataset below the reservoir (560-590ms) sketches the oblique fracture zone in the same position and direction as previously done in Figures 5.10-12. The general direction of the fractures appears not to conform to the regional orientation of the major principle stress, as indicated in Figure 5.33. In

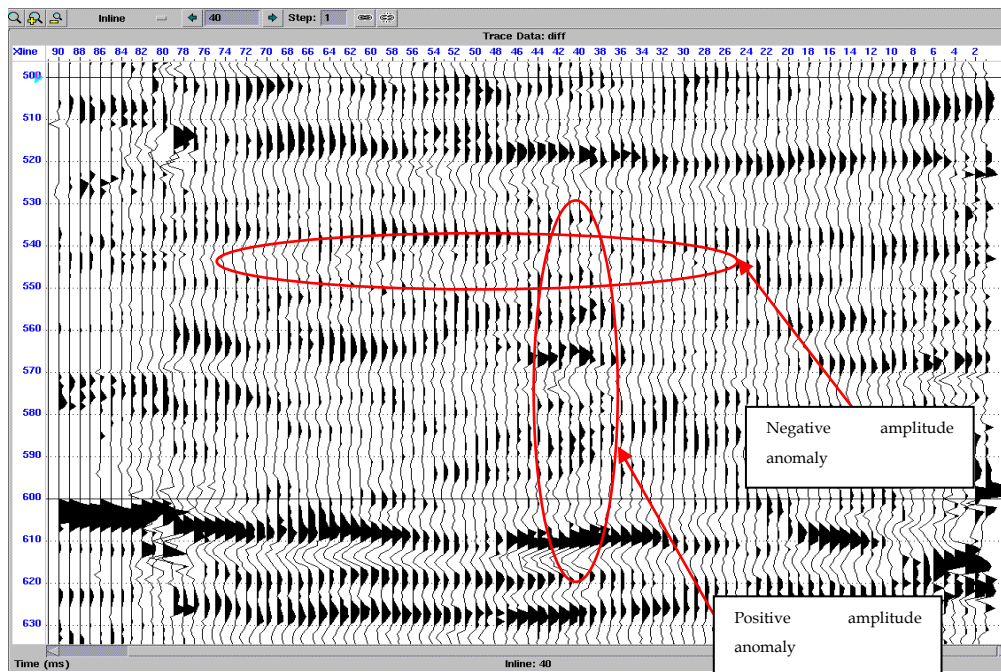


Figure 5.32 Difference section (Inline 40)

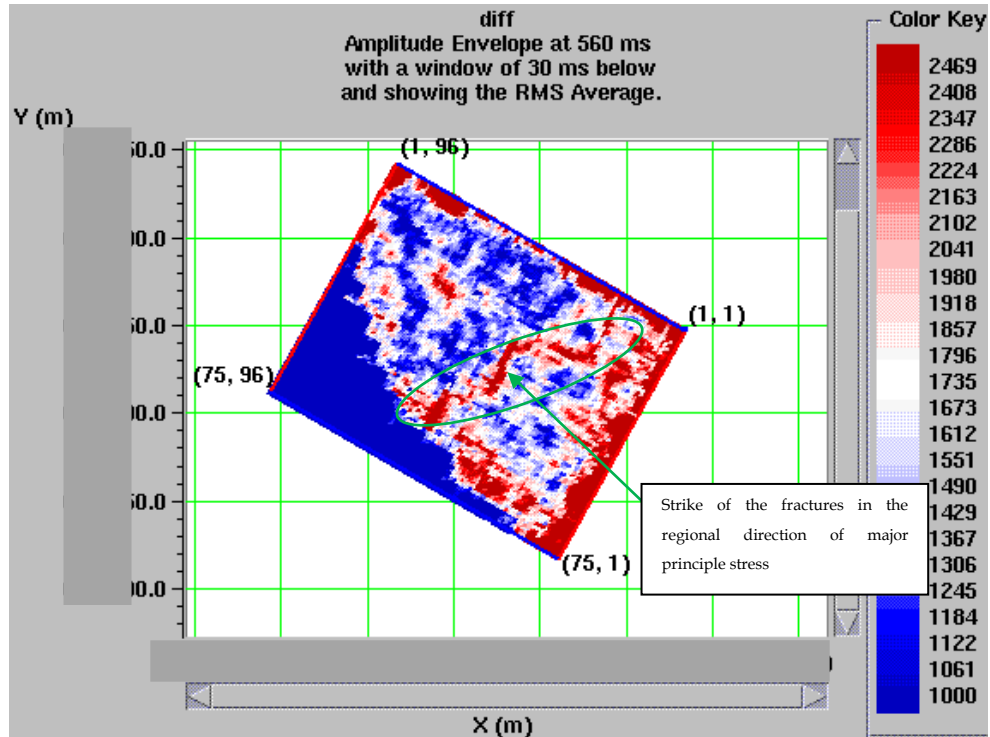


Figure 5.33 Contour map of Inst. amplitude on the window of 560-590ms

the zone of the reservoir, the slice on the window of 525-560ms in Figure 5.34 uncovers a picture similar to that in Figure 5.7, i.e., the parallel well paths cut by the oblique fracture zone. The injected steam may have leaked upwards. In Figure 5.35, the map on the window of 510-535ms implies potential leaking points to overlying formations along the fracture zone, as also evidenced by Figure 5.18. The fluid breakthrough downward has happened unequivocally, as shown in Figure 5.33, and Figures 5.10-12. The steam has likely invaded deep into the internal Devonian carbonate, as shown in Figure 5.36 and Figure 5.15.

In summary, when steam was injected into the wellbores, the immediately adjacent areas surrounding them absorbed part of the steam and heated, and simultaneously, the oblique fracture zone was potentially initiated downwards and likely upwards as well. Leaking led to considerable amounts of steam lost in the first stage of CSS process.

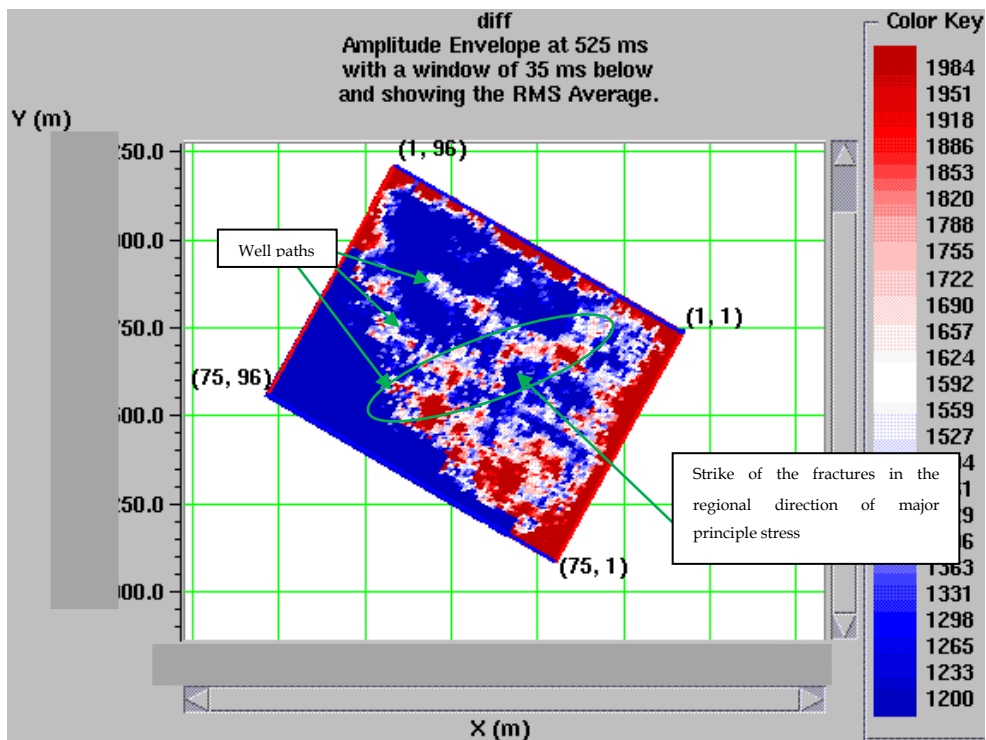


Figure 5. 34 Contour map of Inst. amplitude on the window of 525-560ms

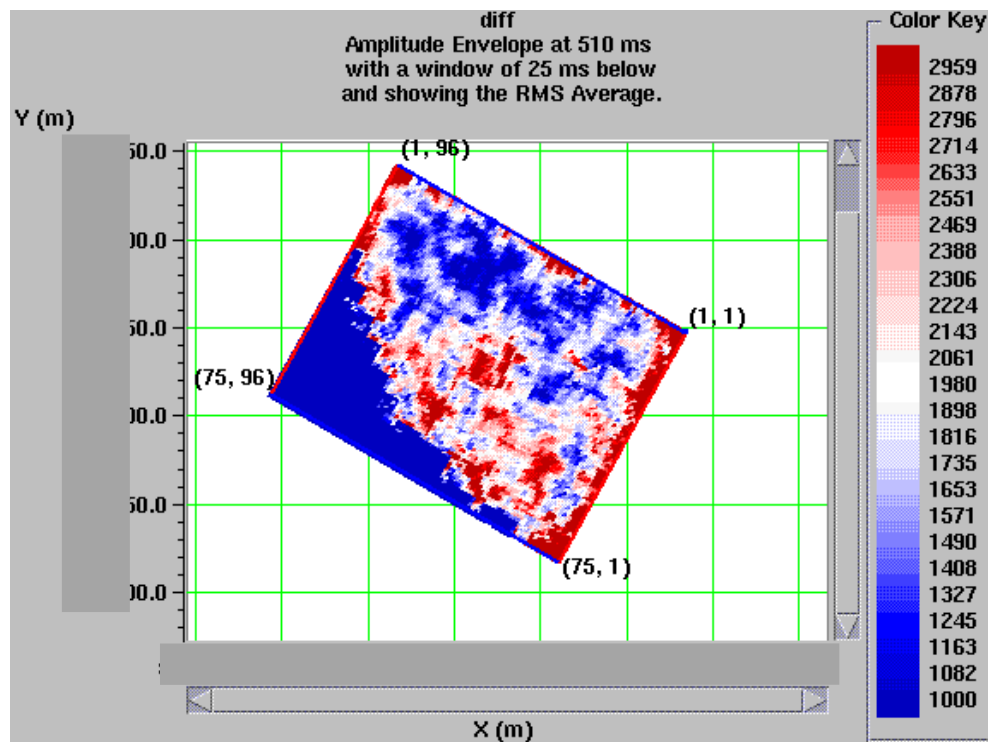


Figure 5. 35 Contour map of Inst. amplitude on the window of 510-535ms

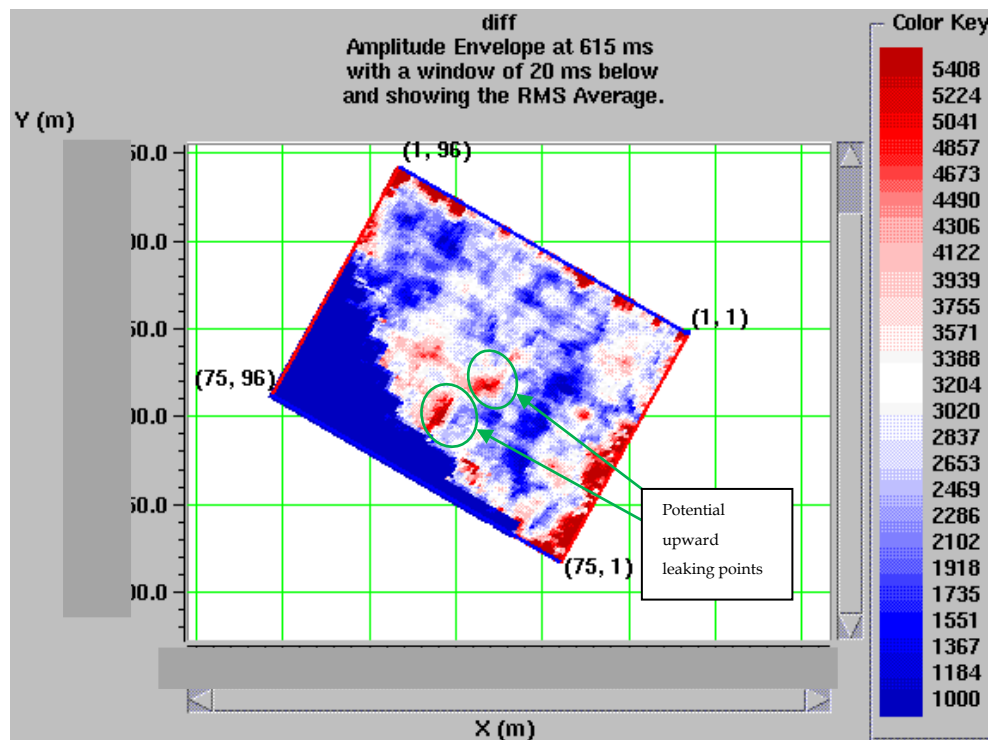


Figure 5. 36 Contour map of Inst. amplitude on the window of 615-635ms

CHAPTER 6 WAVELET TRANSFORM AND ITS APPLICATION TO TIME-LAPSE SEISMIC PROCESSING AND INTERPRETATION

6.1 Introduction

Unlike in mathematics, any object in the real world has its size. The molecule and atom range in nanometers. The tree is mostly from a few centimetres to a few meters. And the star and planet are far larger. These observables form a huge dimension gap, and obviously can't be displayed only on one picture. It makes no sense to gauge the flow rate in a river and measure H_2O Brownian movement at the same time. Any survey system or apparatus or equipment targets a specific range of scale. On the microscope, tiny bacteria and even cells are visible. But it is difficult to examine both much smaller particles such as atoms and much larger mass such as organs. The daily-used ruler can measure the length of around a fraction of millimetres to a few ten centimetres or so. It is absurd to use it for Calgary Tower measurement.

An observation system has its lower limit called the sample rate. It is the minimum size it can see. Any smaller objects or structures will be invisible. For instance, the pixel in a photo is the smallest identifiable and the colour and brightness and other properties within the size are combined or averaged into single values. The system also has its upper limit that is the maximum spatial magnitude of observables. For instance, the photo by 30cm x 30cm can't bring a mountain of 100km across into view. The giant structures displayed in the aerial picture or satellite image such as Mediterranean Sea or Sahara Desert or Rocky

Mountains are significantly scaled down and each pixel may represent a few hundred meters instead of millimetres or smaller.

Certain objects or structures appear at certain scales. The anatomy of bacteria can be operated on microscope, but not in butcher shops. In order to find the right objects or structures, the range of scales must be specified before viewing. If the scales are unknown, scanning all scales is necessary to fulfil the task. This work is called Multi-Scale Space representation in computer vision and image processing. Given an image, which has a sample rate and on the scale of most resolvable, an operation called smoothing or convolution in technical terms can be performed to locate objects or structures on coarser scales. Objects or structures in one dimension can be simply defined as local minima or maxima and the number of them can be counted as the number of these local minima or maxima. It must be noted that these local extrema will change with scales in location and number. In other words, different objects or structures occur at different scales.

The requirement for the operation is that the number of local extrema can not increase with increasing scales, or the number of local extrema at coarser scales cannot exceed that of the counterparts at finer scales. Furthermore, these local extrema can't be enhanced from fine to coarse scales. Gaussian function as the kernel can satisfy these conditions and are commonly used to convolve with a function for smoothing at different scales, as shown in equation 6.1:

$$\begin{aligned}
 L(x;t) &= f(x) * g_t(x) \\
 &= f(x) * \frac{1}{\sqrt{2\pi t}} e^{-\frac{x^2}{2t}}
 \end{aligned}
 \tag{6.1}$$

where $f(x)$ is the original image, $g(x)$ is the Gaussian kernel (normal distribution PDF function, t is the square of standard deviation) with t representing the scale (the larger t , the more smoothed L), $L(x;t)$ is the smoothed version of $f(x)$ at scale t . Interestingly, equation 6.1 is the solution of the diffusion partial differential equation (6.2) with the initial condition as $f(x)$ at $t=0$. Intuitively from daily life experience, the diffusion process (e.g., temperature conduction) starting at the initial condition $f(x)$ will neither create new local extrema nor enhance old ones. It will either remove local extrema or subdue them.

$$\frac{\partial L}{\partial t} = \frac{1}{2} \nabla^2 L \quad (6.2)$$

There is no exception in seismic exploration. The minimal size of geological bodies (like pixel size in photo) the system can see depends on the dominant wavelength of the wavelet (Mukerji et al., 1995; Sheriff et al., 1995) generated by a source on surface. The shorter wavelength, the smaller size it can observe. A comparison can be made between camera and wavelet. A camera with 10 million pixels can resolve small features and take clear photos. Similarly a wavelet with the dominant wavelength of a few meters can see thin layers of very small scales. The difference is that the camera directly measures optical properties. If an inversion is performed from received seismic traces to rock properties, the aforementioned multi-scale space representation can be applied for interpretation at different scales.

The seismic trace is a convolution of wavelet with a reflectivity series created from acoustic impedance boundaries. The minimal size bound by these boundaries is approximately one-eighth of the dominant wavelength, below which the reflections of any embedded layers from top and bottom will be much like a single wavelet, implying indistinguishable (Widess, 1973). From the point

of transmitted waves, any objects lower than one-tenth of the dominant wavelength will contribute to the velocity field in a way as effective media; bigger ones will show their own distinct elastic properties and velocities (after Mukerji et al., 1995). The question arising here is “Can we decrease the minimal size of measurement?” We say ‘no’ to camera since the pixel is the minimum size it can see. We say ‘possible’ to seismic reflections since the embedded wavelet can potentially be filtered to create new ones with higher dominant frequency and lower dominant wavelength. As shown in Figure 6.1 for the amplitude spectrum of the Ricker wavelet, the dominant frequency is 50 hz, but the frequency range spans to over 100 hz. It is therefore possible to decimate the frequency band by designing an appropriate operator and to obtain another wavelet with desired dominant frequency and dominant wavelength. In other words, we can obtain the desired size of resolution, whether it is bigger or smaller. The technique to extract different ranges of frequency is called Subband Coding or Wavelet Transform in signal processing.

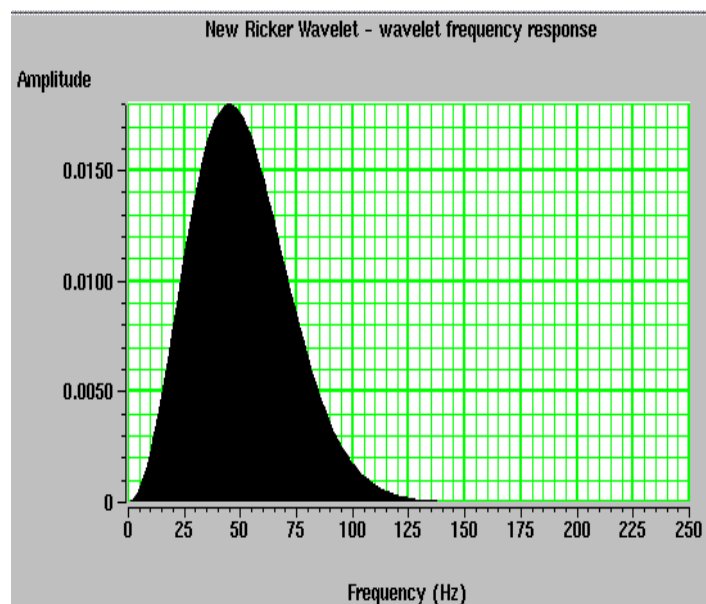


Figure 6. 1 Amplitude spectrum of Ricker wavelet

6.2 Principles

There are different requirements regarding how to subdivide the band toward different purposes. In terms of spectral decomposition in seismic exploration, two conditions should be satisfied for the selected filter or convolution kernel, i.e., high time resolution in time domain and high frequency resolution in frequency domain, or high time-frequency localization. A short-time window or compact support can ensure frequency information extracted locally. A big window will include reflections from other boundaries, which are not desired in terms of resolution. As shown in Figure 6.2, the wavelet of short window as convolution kernel will operate independently on reflection events; while one of long window will add information from second event when convolving with first one, and vice versa.

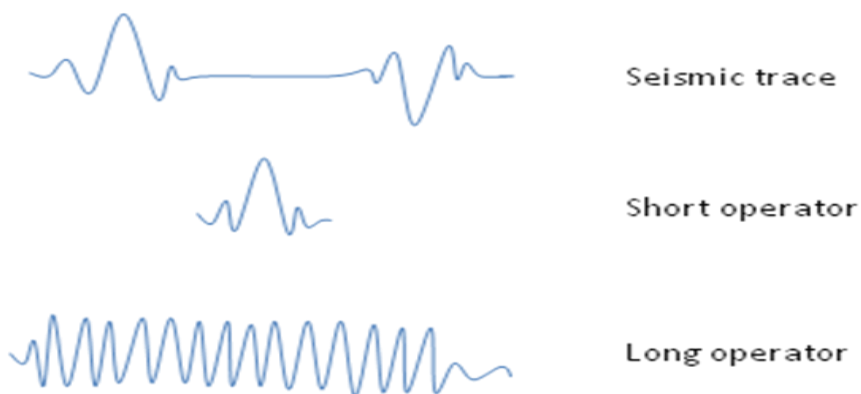


Figure 6. 2 Wavelet time localization

Our goal is to cut into different frequency bands, which is achieved by frequency localization. Without this compact support, the work defined previously would be compromised, or even not attainable. The extreme case is the spike function, which has perfect time resolution, but no frequency

resolution. The convolution of a signal with this function will be the signal itself and this operation will be meaningless.

However, the Heisenberg uncertainty principle states that certain pairs of physical properties, like time and frequency, can't both be known to arbitrary precision. The narrower (more precise) it is for one, the wider (less precise) it is for the other. Gabor (1946) derived the time-frequency localization as:

$$\Delta t \Delta f \geq \frac{1}{2} \quad (6.3)$$

where Δt is the effective duration defined in equation 6.4 and Δf is the effective frequency band width defined in equation 6.5.

$$\Delta t = \sqrt{2\pi E\{[t - E(t)]^2\}} \quad (6.4)$$

$$\Delta f = \sqrt{2\pi E\{[f - E(f)]^2\}} \quad (6.5)$$

where E refers to the mean. Δt can be viewed as the square root of 2π times r.m.s. deviation of the operator and Δf as the square root of 2π times r.m.s. deviation of the operator's Fourier transform.

Now the time-frequency localization requirement may be able to adjust to minimizing $\Delta t \Delta f$, instead of both of Δt and Δf simultaneously. According to equation 6.3, the minimized value must be $\frac{1}{2}$. Interestingly, Gaussian function satisfies the equality of equation 6.3 as follows:

$$f(t) = \frac{1}{\sqrt{2\pi}\sigma} e^{-\frac{t^2}{2\sigma^2}} \quad (6.6)$$

$$\begin{aligned}
F(f) &= \frac{1}{\sqrt{2\pi\sigma}} \int_{-\infty}^{+\infty} e^{-\frac{t^2}{2\sigma^2}} e^{-i2\pi ft} dt \\
&= \frac{1}{\sqrt{2\pi\sigma}} \int_{-\infty}^{+\infty} e^{-\frac{t^2}{2\sigma^2}} \cos(2\pi ft) dt \quad (6.7) \\
&= e^{-\frac{f^2}{2[1/(2\pi\sigma)]^2}}
\end{aligned}$$

$$\Delta t = \sqrt{\pi\sigma^2} \quad (6.8)$$

$$\Delta f = \sqrt{\pi/(2\pi\sigma)^2} \quad (6.9)$$

$$\Delta t \Delta f = \frac{1}{2} \quad (6.10)$$

Equation 6.6 is the Gaussian function, Equation 6.7 is its Fourier transform, Equations 6.8 and 6.9 are effective duration and band width respectively, equation 6.10 is the multiplication of effective duration and band width. This property of best time-frequency localization enables it to be a popular choice as the convolution kernel for multiple-scale space representation. For example, the box moving average or mean filter can't guarantee the conditions of multiple-scale space representation to be satisfied, but the Gaussian average or filter does.

Gaussian function, a low pass filter, can't directly decimate the frequency band, as required. If multiplied by the harmonic function, then the task of band cutting is tractable. The new function enjoys Gaussian's time-frequency localization property (Gabor, 1946) and band subdivision as well, which is the basis of Morlet wavelet transform (Goupillaud et al., 1985), as follows:

$$\Phi(t) = \frac{1}{\sqrt{2\pi\sigma}} e^{-\frac{t^2}{2\sigma^2}} \cos(2\pi f_0 t) \quad (6.11)$$

where $\Phi(t)$ is the operator, the amplitude of the harmonic function is Gaussian function, f_0 is the reference frequency. f_0 must be greater than 0.8 in order to meet the requirement of inverse wavelet transform (Daubechies, 1992). Its Fourier transform is Gaussian function (only the positive frequency range is displayed):

$$\Psi(f) = e^{-\frac{(f-f_0)^2}{2[1/(2\pi\sigma)]^2}} \quad (6.12)$$

As shown in equation 6.12, the Gaussian function can shift in f axis depending on f_0 while keeping $1/2\pi\sigma$ (effective band width) constant. This is what exactly the windowed Fourier transform does, in which other functions (for example, box function) instead of Gaussian one can be chosen as the window or amplitude of the harmonic function in equation 6.11. This technique has shortcomings of not changing time localization with frequency because the Gaussian function parameters in frequency domain are fixed. Obviously, for high frequency the window may be too wide to reveal frequency details (no time resolution); for low frequency the window may be too short to extract desired low-frequency information (no frequency resolution). The only way to tackle the problem is to have the window size adjusted with frequency. The higher frequency, the shorter window; the lower frequency, the longer window. This idea can be achieved by multiplication of a scale factor $1/a$ before variable t in equation 6.11, as follows:

$$\Phi(t) = \frac{1}{\sqrt{2\pi\sigma}} e^{-\frac{(t/a)^2}{2\sigma^2}} \cos(2\pi f_0 t / a) \quad (6.13)$$

Equation 6.13 can be reformulated as:

$$\Phi(t) = \frac{1}{\sqrt{2\pi}\sigma} e^{-\frac{(t)^2}{2(\sigma a)^2}} \cos[2\pi(f_0/a)t] \quad (6.14)$$

From the above equation, the scale parameter (a) determines both the window size and frequency. When a is small, frequency (f_0/a) is large and window size (σa) is small; when a is big, frequency is small and window size is large. Then the wavelet transform can be formulated as:

$$T(a,b) = \frac{1}{\sqrt{a}} \int_{-\infty}^{+\infty} f(t) \Phi^*\left(\frac{t-b}{a}\right) dt \quad (6.15)$$

T is the transform coefficient, a function (a,b); f(t) is the function to be analyzed; $\Phi(t)$ is Morlet wavelet family; * denotes complex conjugate; a is the scale parameter; b is the time shift.

6.3 General applications

The thought of multiple-scale space representation discussed previously can apply to sedimentary sections, which deposited in stratigraphical cycles of different orders of magnitude in terms of both thickness and duration (Goldhammer, 2003). These stratigraphical cycles or layers can measure in millimetres formed in a few days or in meters accumulated in millions of years. In most cases, there are ample variations in velocity and density to produce seismic reflections between these layers of different orders, even where reflections may be low in amplitude (after Vail et al., 1977). Therefore, the wavelet transform can be used to view seismic images of sediment layers of different orders. This multiple-scale seismic viewing can enhance both resolution

and interpretation, and it is a better tool than we normally do using single-order viewing.

Figure 6.3 is an example of synthetic seismic generated from convolution of well logs with 60 hz Ricker wavelet, where strong positive and negative reflections embody the boundaries of sediments at the corresponding scale. Some reflections separate formations well, and others located within formations (because they are very thick). It is noted that the boundaries at smaller scales are not brought up and resolution is limited. Yet, this situation may be good for stratigraphical interpretation of well-separated formations.

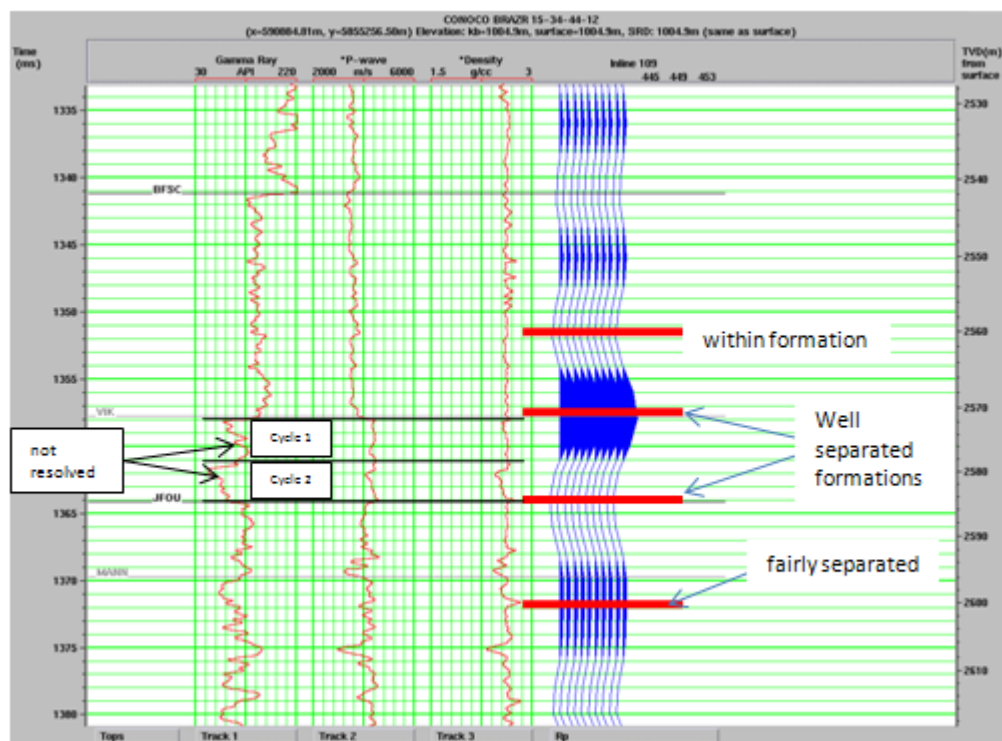


Figure 6. 3 Synthetic seismic section (60 hz wavelet)

Moving the dominant frequency of wavelet to 150 hz, smaller thicknesses are visible from reflections and resolution is improved, as shown in Figure 6.4. This situation is favourable for targets of thin beds. However, some formation

boundaries well separated at the previous larger scale lose their distinctive reflections. For JFOU formation top, the amplitude becomes small and obscure and the polarity is flipped because acoustic impedance contrast depends on local acoustic impedance changes. Multiple-scale seismic images generated by wavelet transform deserve further studies for their applications to sequence stratigraphy and thin-bed exploration.

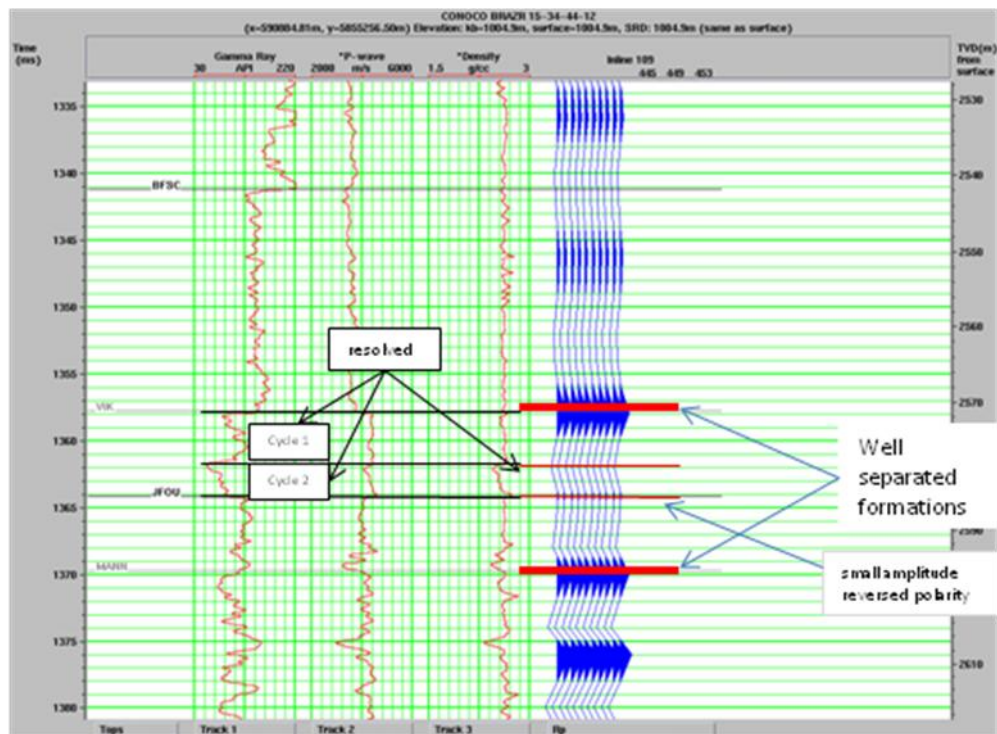


Figure 6. 4 Synthetic seismic section (150 Hz wavelet)

Another important application of wavelet transform is its ability to denoise signals (Donoho, D. L., 1993; Mallet and Hwang, 1992; Selesnick, 2007; Trad and Travassos, 2000). In terms of seismic data, it can be used to remove random and coherent noise (Deighan and Watts, 1997; Miao and Cheatle, 1998; Nguyen and Mars, 1998; Zhang and Trad, 2002). For a signal contaminated with small amplitude random Gaussian noise, a threshold in wavelet domain can be set to zero out small coefficients considered as noise and then inverse transform

can be performed to bring back the noise attenuated signal. As shown in equation 6.15, $T(a,b)$ is the wavelet representation of the noisy signal. It is noted from the assumption that the standard deviation of the noise-free signal is much wider than that of the noise (σ) itself. If a value $T(a,b)$ falls within -3σ to $+3\sigma$, it is regarded as noise because the noise has 99.73% chance to be in this range. In the contrary, the values outside of -3σ to $+3\sigma$ belongs most likely to the signal. In addition, Lee proposed other techniques to this end (Lee, 2000). If there are individual high-amplitude noise outliers, another larger threshold based on the statistical parameters of the signal can be set to weigh down the coefficients in wavelet domain (Zhang and Trad, 2002). After the above two passes, $T(a,b)$ coefficients are noise attenuated, and, when transformed back to the time domain, they are the noise attenuated signal.

Coherent noise such as ground roll can also be reduced in a similar fashion, i.e., zeroing out the coefficients related to the noise. The example (Deighan and Watts, 1997) shows that ground rolls display discernible energy at scale 4 (low frequency) and remaining lower-frequency scales, and beginning with time 275ms. Zeroing out the coefficients in the specified range and then transforming back to the time domain, the seismic data looks cleaner and better than with f-k filtering.

The third application is the extension of the first, i.e., multiple-scale seismic imaging, which is employed to image targets of different thicknesses. As we know, the object such as channel sands we are trying to find varies in thickness. It may be not obviously visible in conventional seismic sections since the dominant wavelength is either too big or too small to stand out its reflections. In the case of the former, its distinct elastic properties are subdued or obscured due to the effective medium theory. In the case of the latter, the acoustic

impedance contrast from the surrounding formations may be small and it could be worse when local acoustic impedance variations generate inconsistent reflections. However, at some tuning wavelength or frequency, the amplitudes from the target are maximized and may be so big that it becomes clearly noticeable. The following section will detail this principle and its application to time-lapse seismic.

6.4 Application to time-lapse seismic

At the tuning wavelength or frequency, the reflections from the top and bottom of a formation will interfere most constructively with each other with highest amplitudes to be observed. Not knowing the thickness of the target, frequency scanning or multiple-scale imaging is necessary to make the features as easily detectable as possible. This is the underlying principle for spectral decomposition to locate sand channels and other reservoirs (Marfurt, 2003).

Time-lapse seismic surveys attempt to capture the fluid flow paths and sweeping areas, maybe temperature and pressure fronts depending on seismic quality and rock physics response feasibility. Likewise, the thickness of these abnormal zones varies with recovery processes, and not known beforehand. It is therefore also required to do multiple-scale imaging for best results.

As shown in Figure 6.5, it is a wedge model of high acoustic impedance embedded within the background of low acoustic impedance. Convolved with a 100 hz Ricker wavelet, the profile of synthetic seismic gives a good presentation of how wavelet interferences change with bed thickness. At high thickness in the right of the picture (Figure 6.5), the reflections from top and bottom do not affect

each other and the amplitude keeps constant (Figure 6.6), in which case the bed may be hardly detectable if noise is added. With decreasing thickness to 80-90ms, two reflections start to interfere with each other constructively. When thinning to around 4.2ms (trace 13), the amplitude culminates. Compared with the peak amplitude without constructive interference, the maximized peak amplitude has been boosted by 45% (from 0.248 to 0.358 in this specific case). Obviously, the seismic images facilitate interpretation for delineation of the bed. Further decreasing in thickness will generate destructive interference with amplitudes shrinking until zero, at which the thickness is negligibly small when compared with the dominant wavelength.

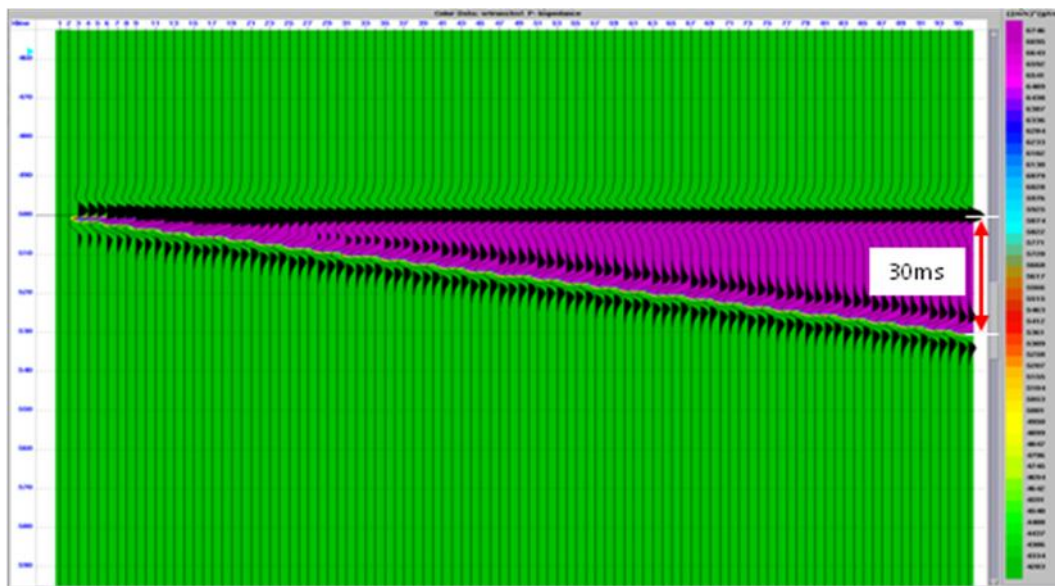


Figure 6. 5 Wedge model and its synthetic (using 100hz Ricker wavelet)



Figure 6. 6 Amplitude cross section along the reflection peaks on the top boundary

The technique of wavelet transform for multiple-scale imaging is to decompose the picture of Figure 6.5 into a series of pictures, each with a definite dominant wavelength or frequency and a maximum tuning thickness. As shown

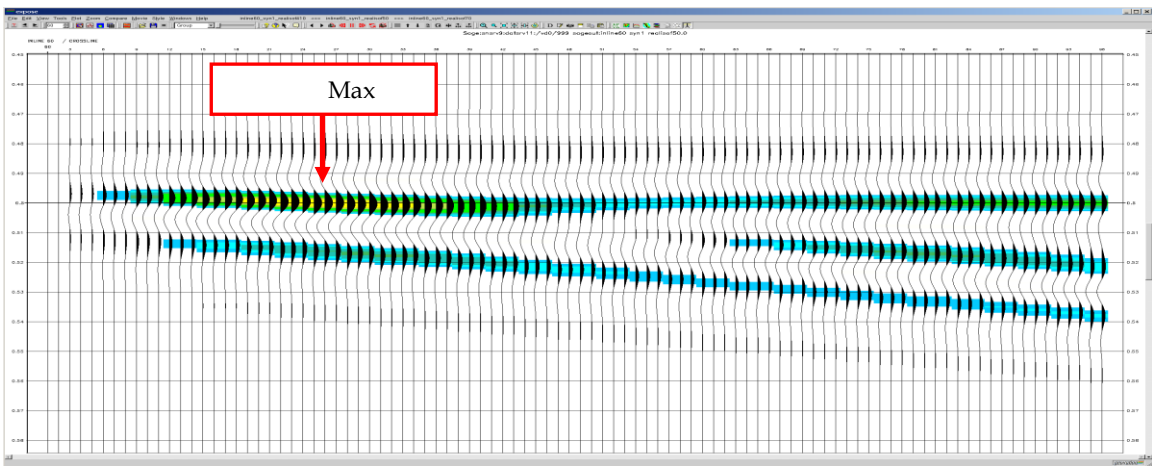


Figure 6.7 Wavelet transform of Figure 6.5 at 50 hz dominant frequency

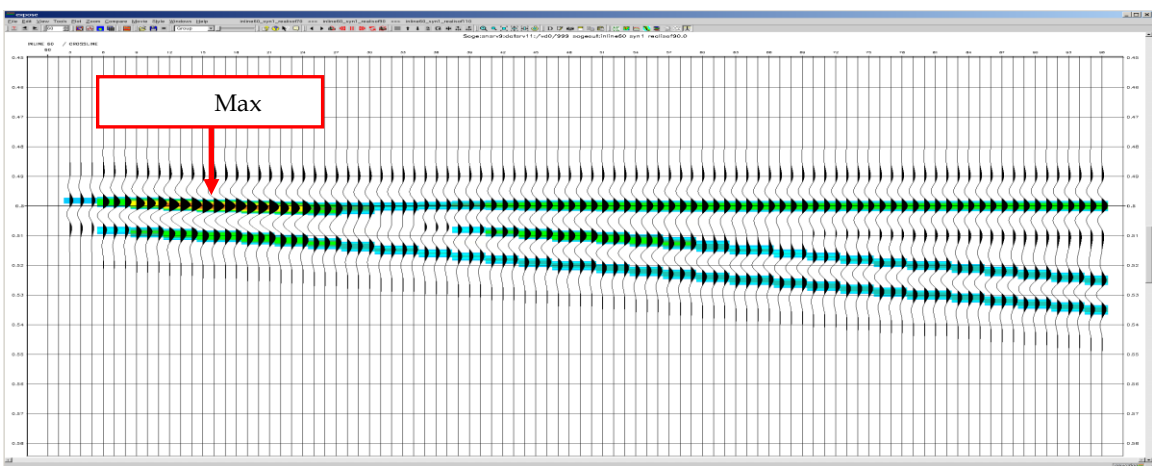


Figure 6.8 Wavelet transform of Figure 6.5 at 90 hz dominant frequency

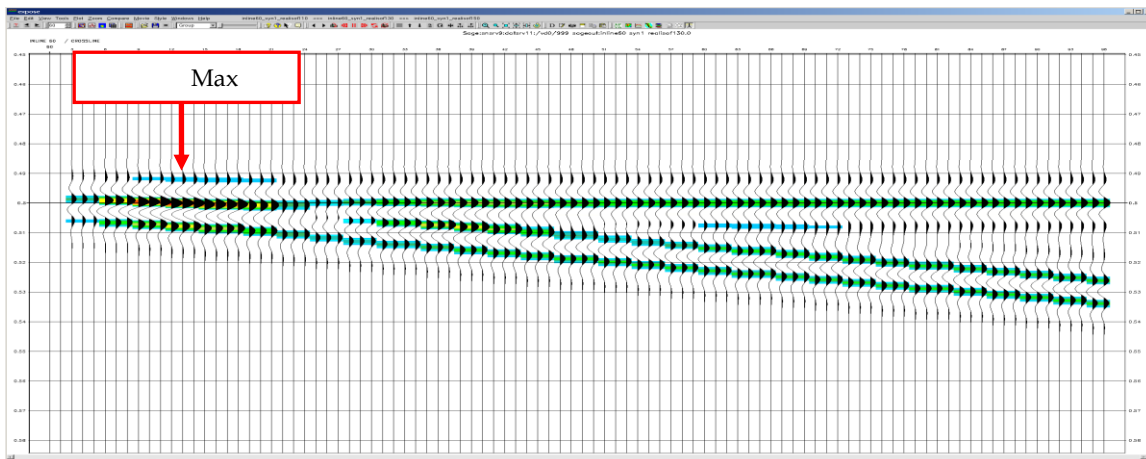


Figure 6. 9 Wavelet transform of Figure 6.5 at 130 hz dominant frequency

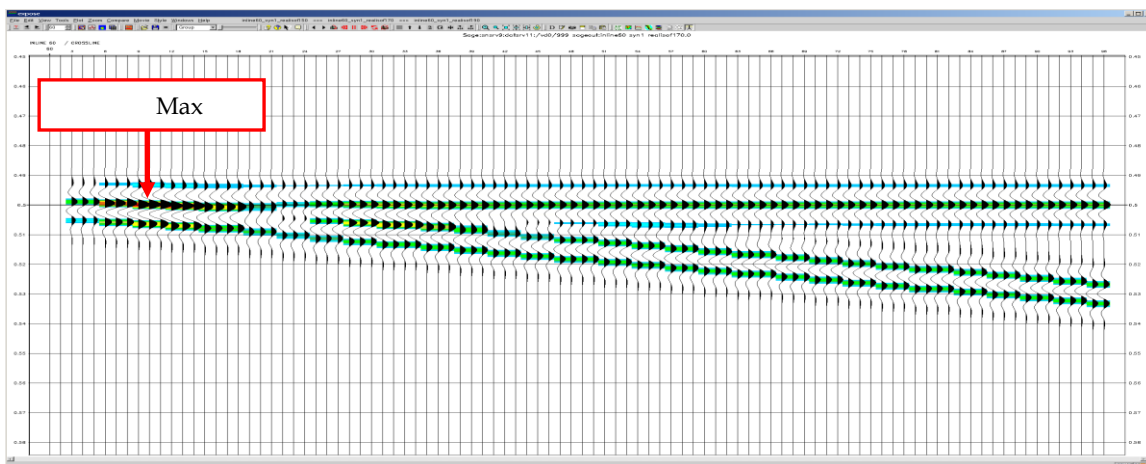


Figure 6. 10 Wavelet transform of Figure 6.5 at 170 hz dominant frequency

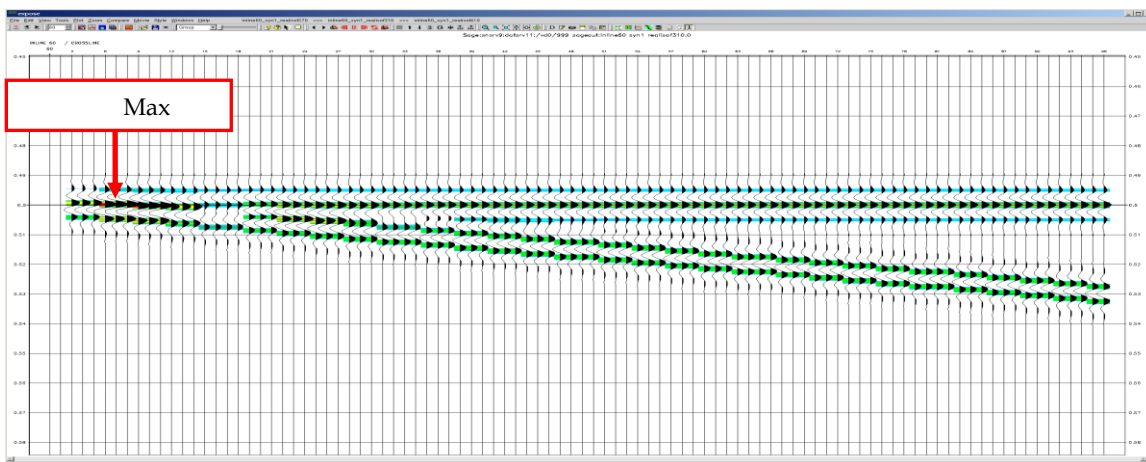


Figure 6. 11 Wavelet transform of Figure 6.5 at 310 hz dominant frequency

Table 6.1 Relation of dominant frequency and max-tuning thickness

frequency (hz)	tuning thickness (ms)	trace number
50.00	8.21	26
90.00	5.05	16
130.00	4.10	13
170.00	3.16	10
310.00	2.20	7

in Figures 6.7-11, the maximum tuning thickness shortens toward the high dominant frequency (also see Table 6.1). In other words, the higher the dominant frequency, the thinner the maximum tuning thickness. Scanning a series of wavelet transform generated pictures can locate the optimal images of targets. This is the power of wavelet transform in this application.

6.5 Case studies

As discussed in the last chapter, the baseline survey missed quite a chunk of seismic data, which limited our efforts to track the fluid flow paths for the whole area by extracting seismic attributes through comparison of these two datasets. A solution to this problem is to work on the monitor survey only in hopes of unravelling the abnormal zones. The discriminant analysis adopted by Eastwood provided an avenue to delineate the hot zone from potential heated areas (Eastwood, 1996; Smith and Perepelecta, 2004), but it confined to mapping, not 3-D imaging. In this section, case application of wavelet transform will be introduced and shown to a better tool.

The monitor survey (1998 data) alone does indicate fair hydrocarbon recovery footprints as shown in Figures 5.4, 6, 8, 10, 11, 15 & 18. Even a 3D view of simple amplitude data can capture the outline of data anomalies illustrated in Figures 6.12-15. However, these pictures look fuzzy and incomplete so that it is difficult to define the flow paths and the relationship of oblique fractures and steam injection well trajectories. Therefore, Morlet wavelet transform was applied with the range of frequency from 5 to 100 hz, aiming at scanning frequency for the maximum tuning effect. Figures 6.16-51 display a few data volumes, which were decomposed by wavelet transform, and corresponding data slices at times of 540ms, 550ms, 566ms and 573ms.

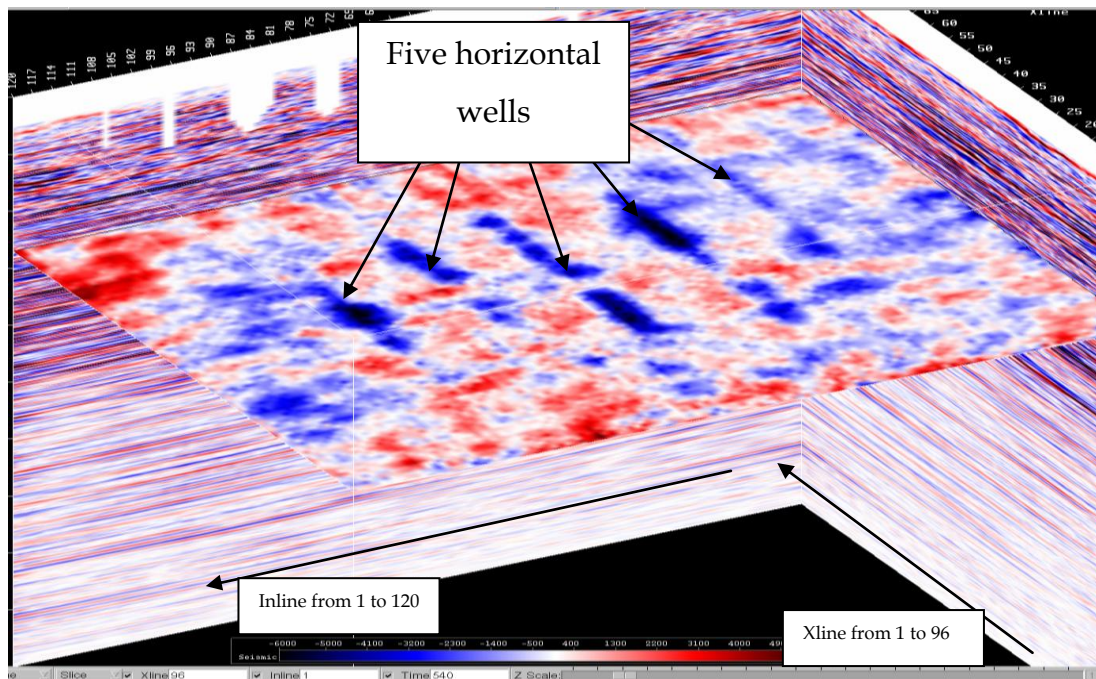


Figure 6.12 Amplitude map at 540 ms from original data

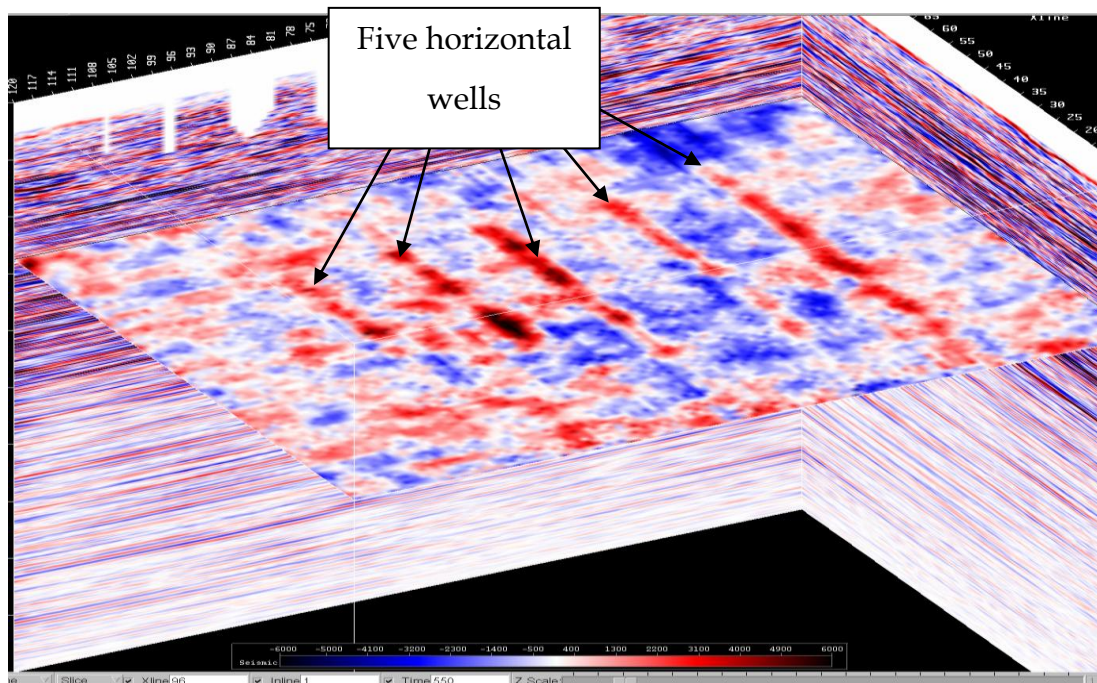


Figure 6. 13 Amplitude map at 550 ms from original data

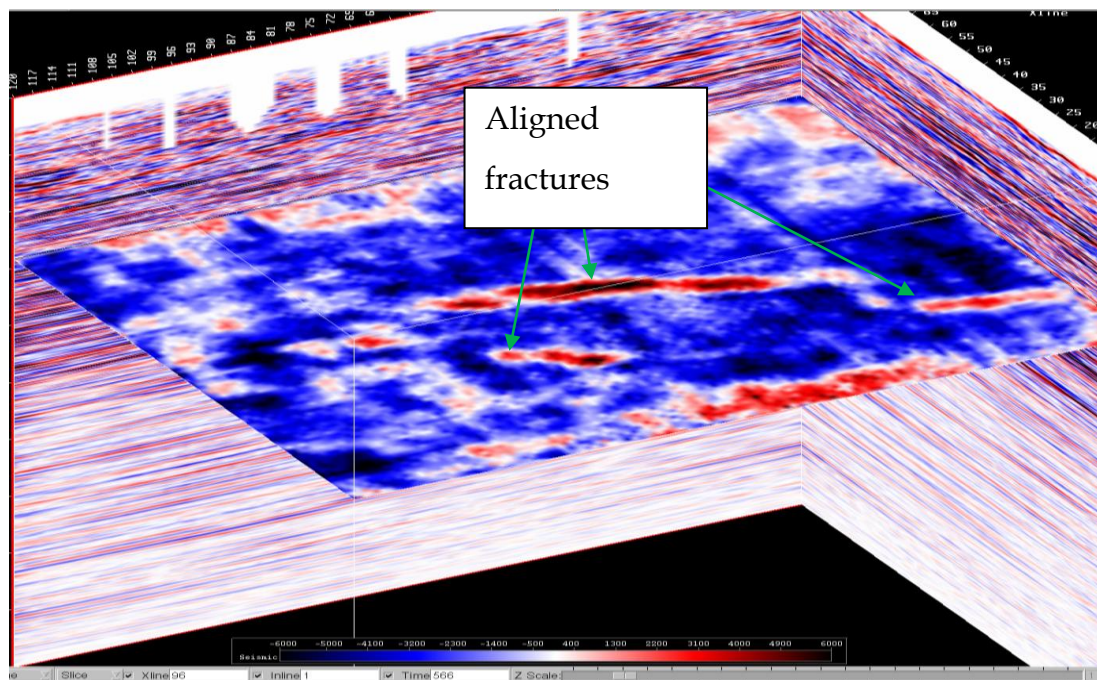


Figure 6. 14 Amplitude map at 566 ms from original data

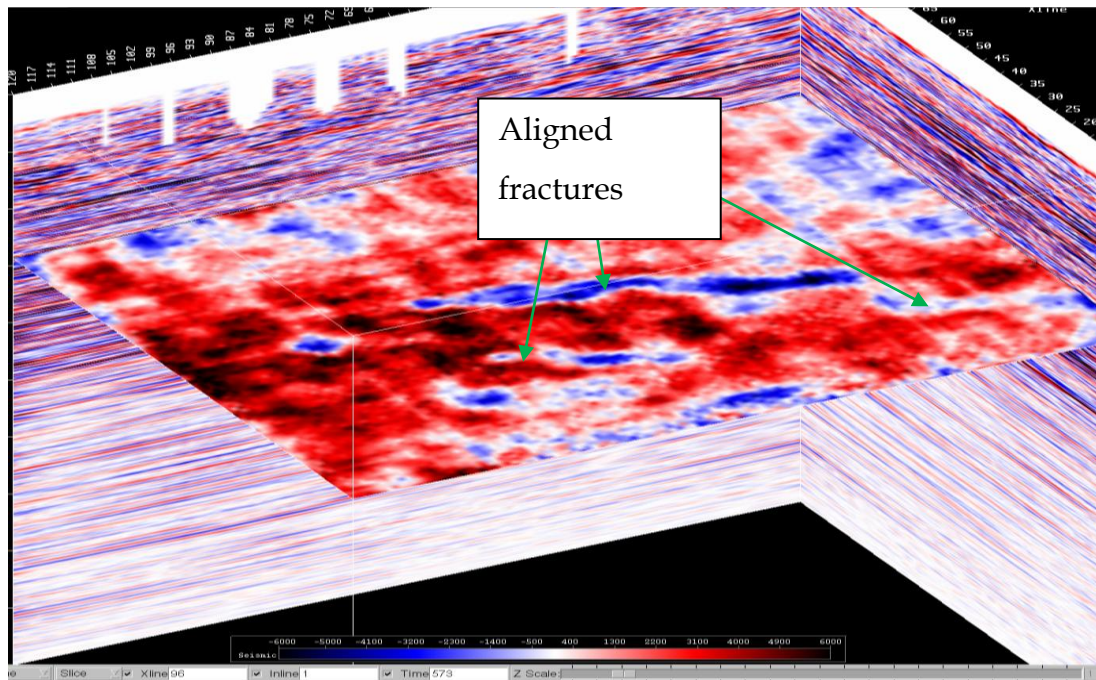


Figure 6. 15 Amplitude map at 573 ms from original data

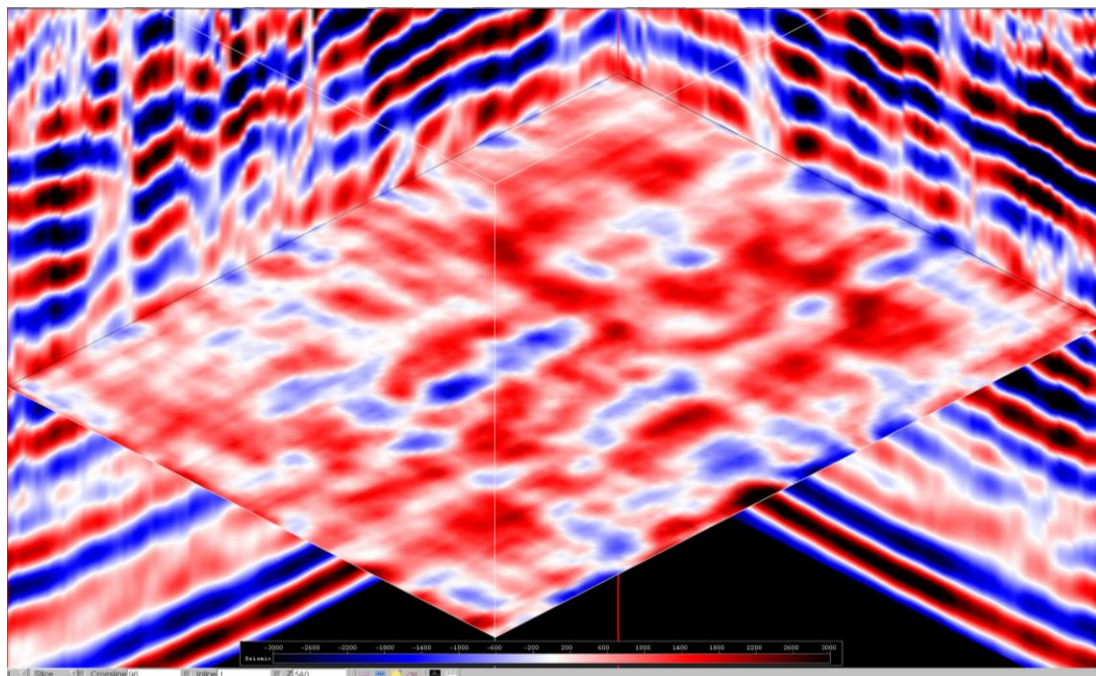


Figure 6. 16 Amplitude map at 540 ms from 10hz data

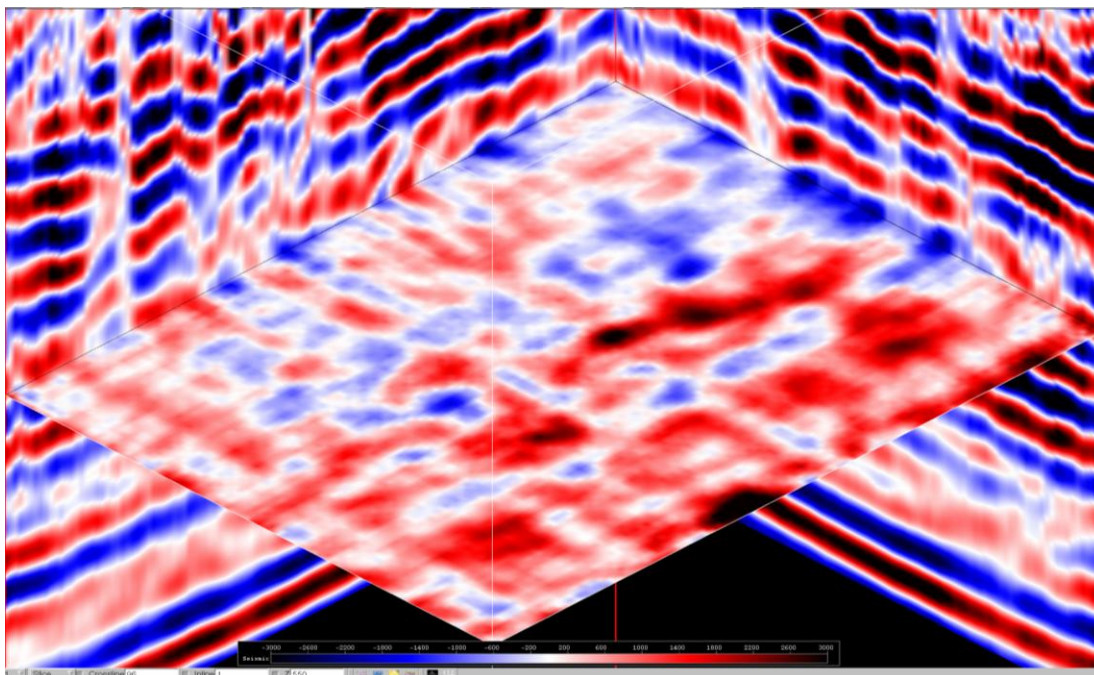


Figure 6.17 Amplitude map at 550 ms from 10hz data

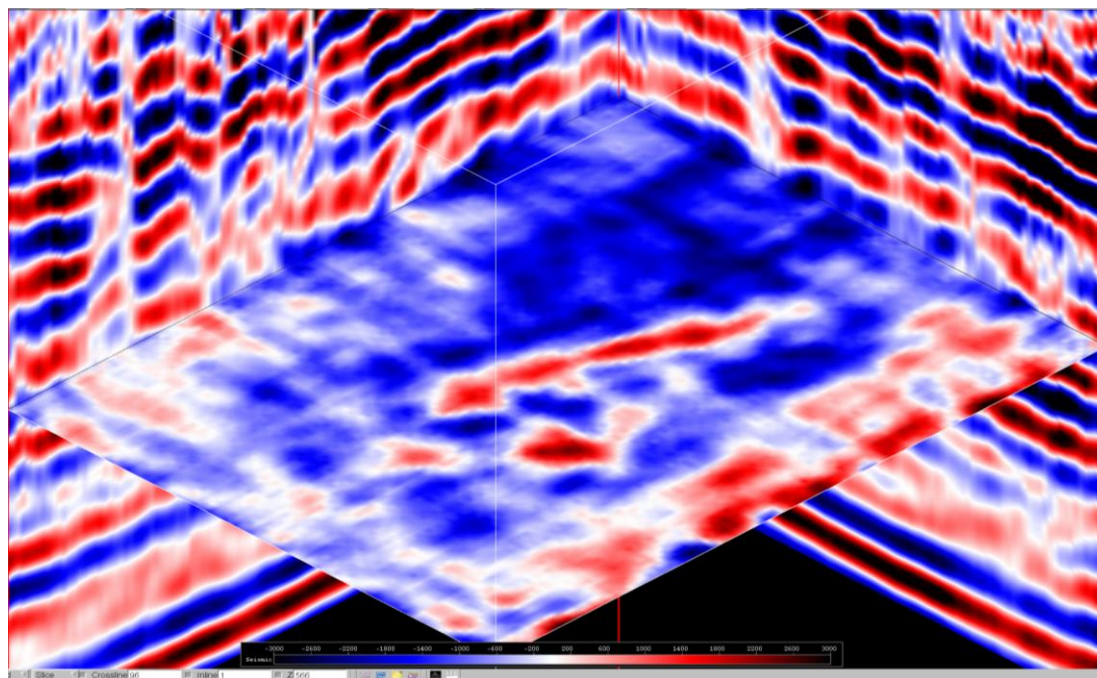


Figure 6.18 Amplitude map at 566 ms from 10hz data

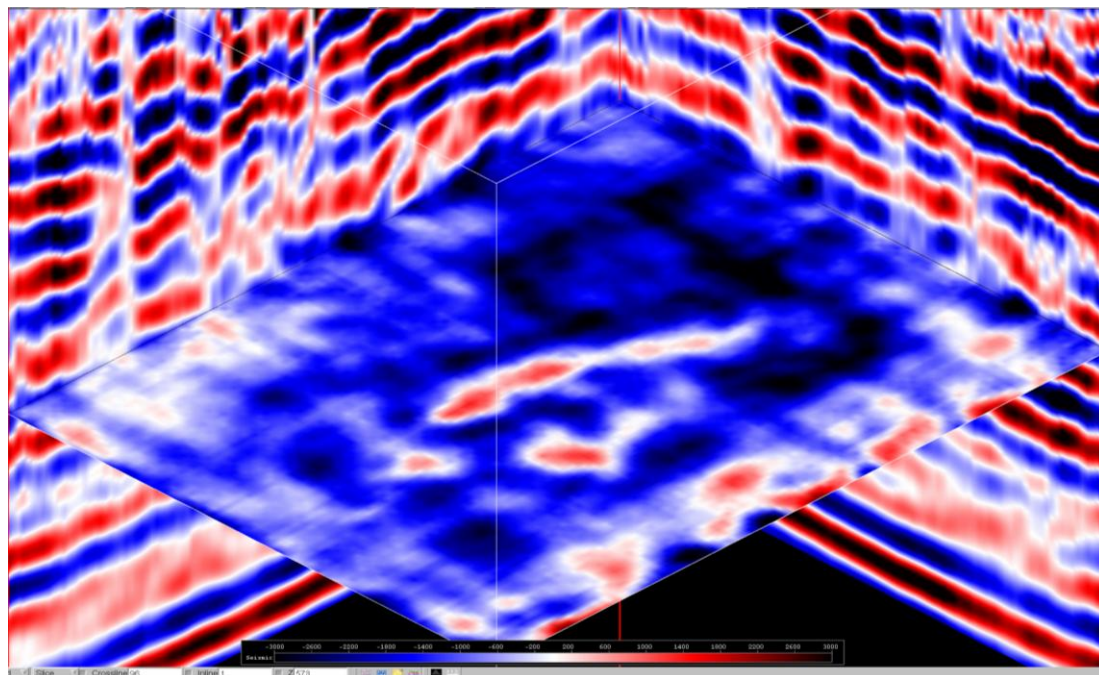


Figure 6. 19 Amplitude map at 573 ms from 10hz data

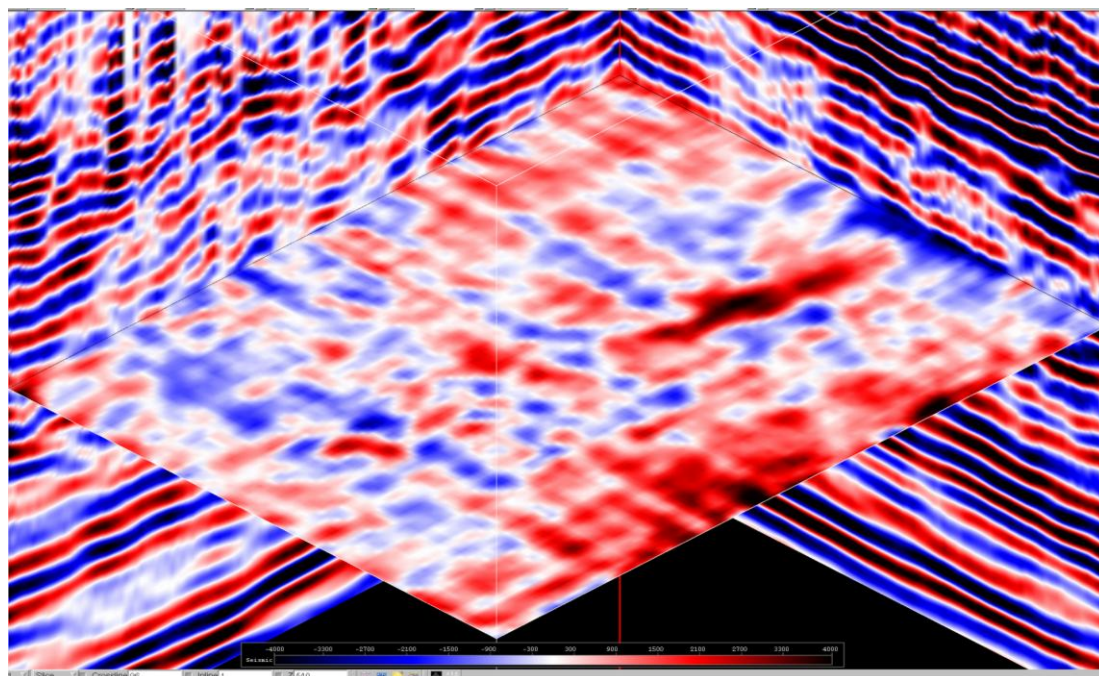


Figure 6. 20 Amplitude map at 540 ms from 20hz data

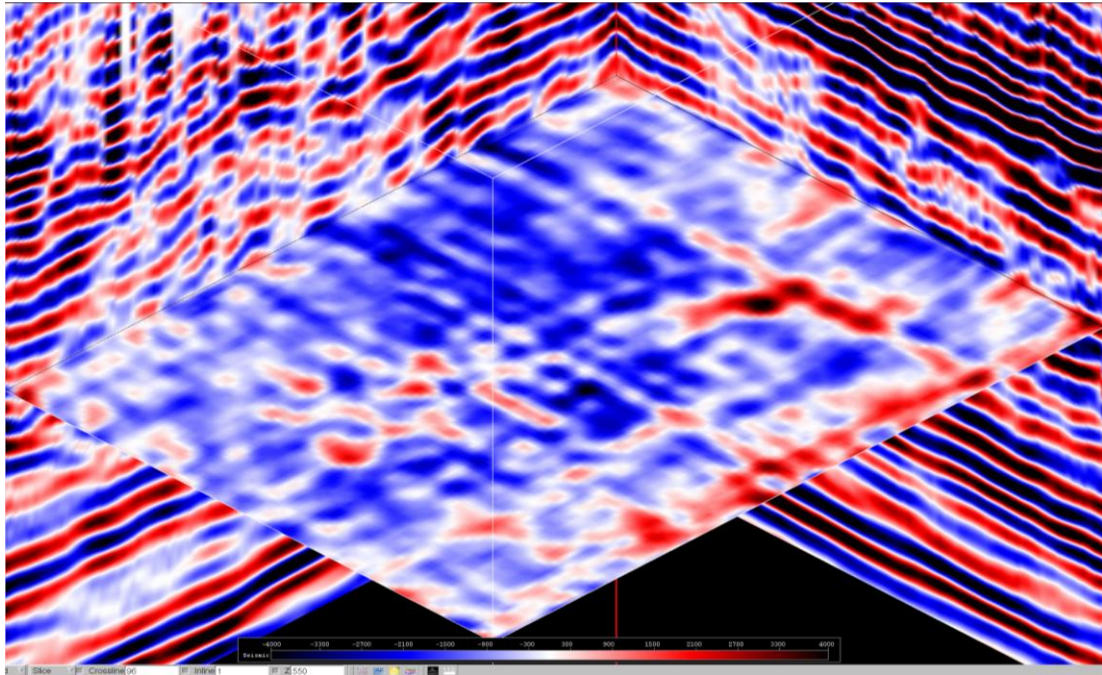


Figure 6. 21 Amplitude map at 550 ms from 20hz data

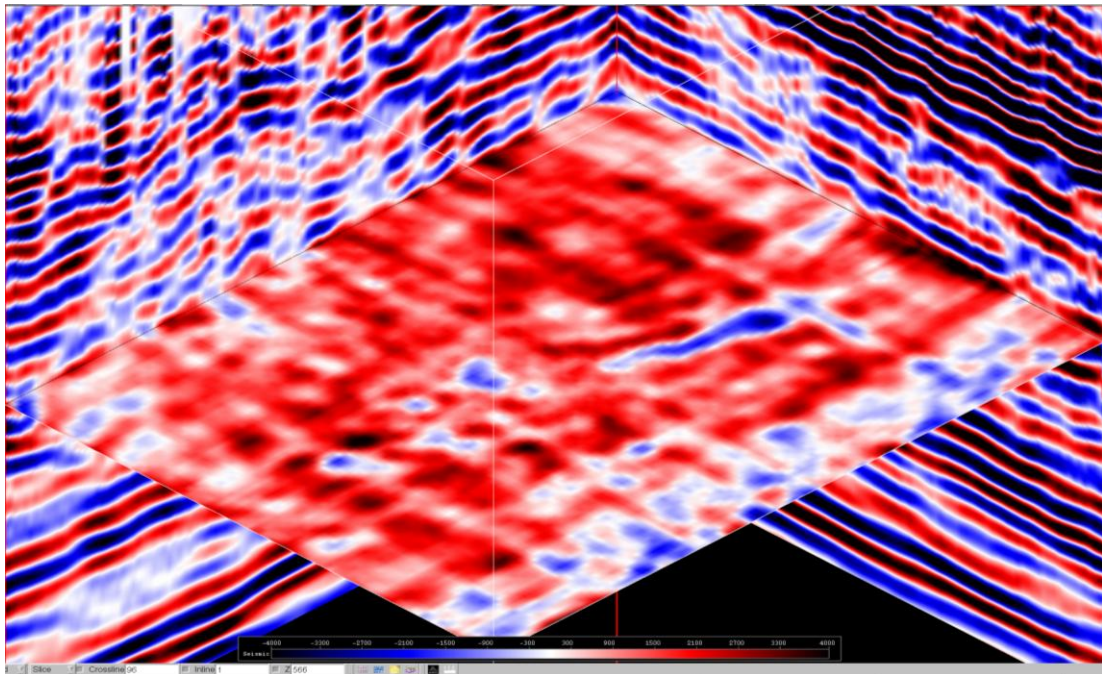


Figure 6. 22 Amplitude map at 566 ms from 20hz data

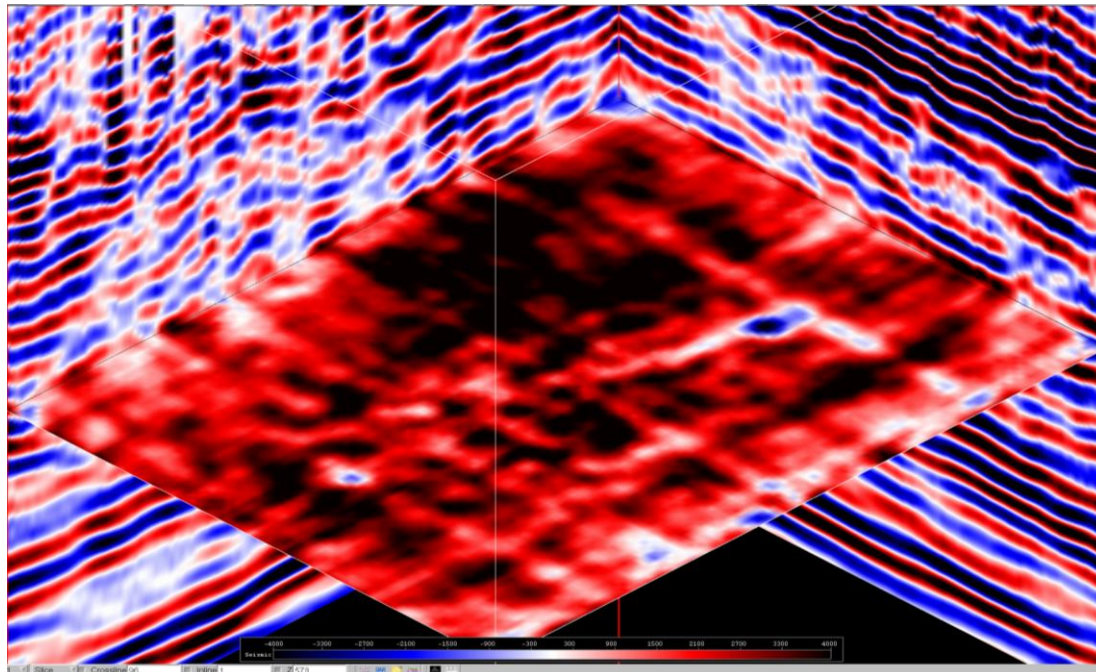


Figure 6. 23 Amplitude map at 573 ms from 20hz data

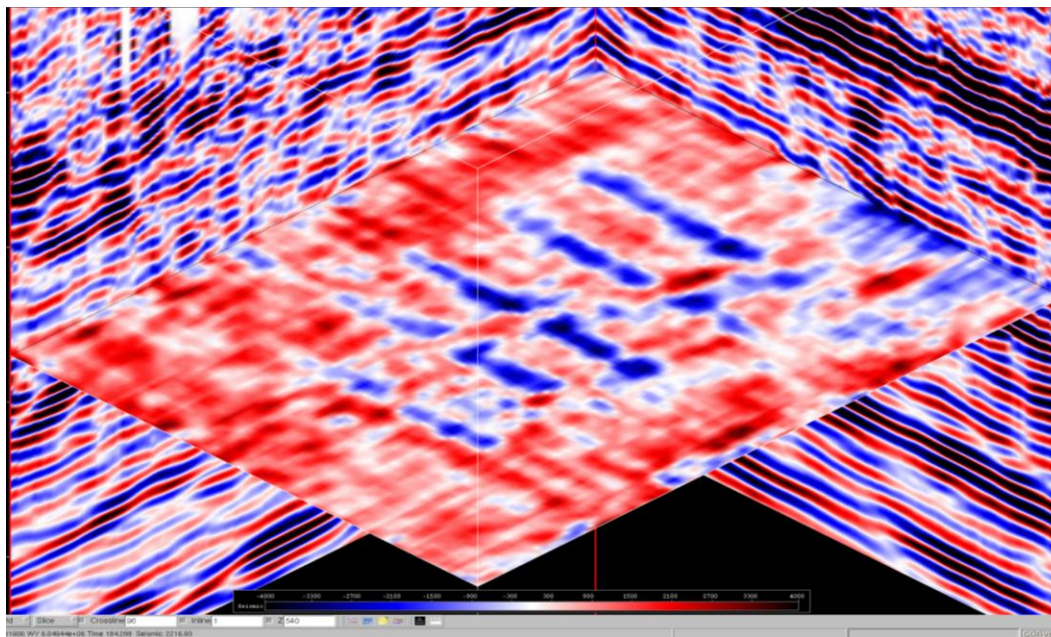


Figure 6. 24 Amplitude map at 540 ms from 30hz data

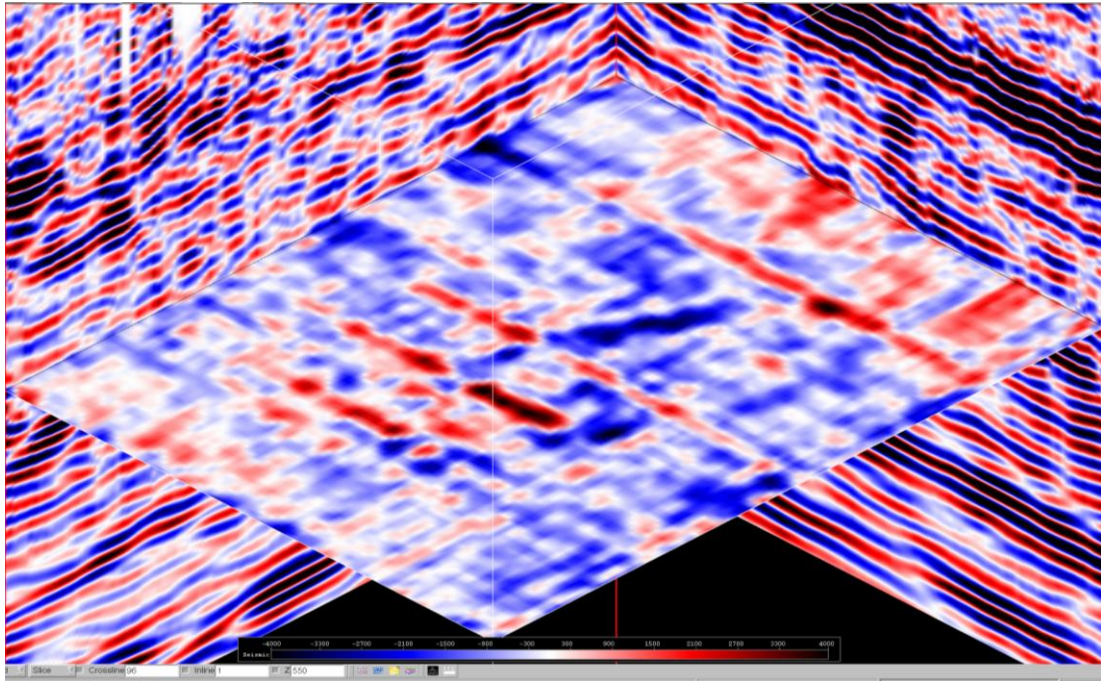


Figure 6. 25 Amplitude map at 550 ms from 30hz data

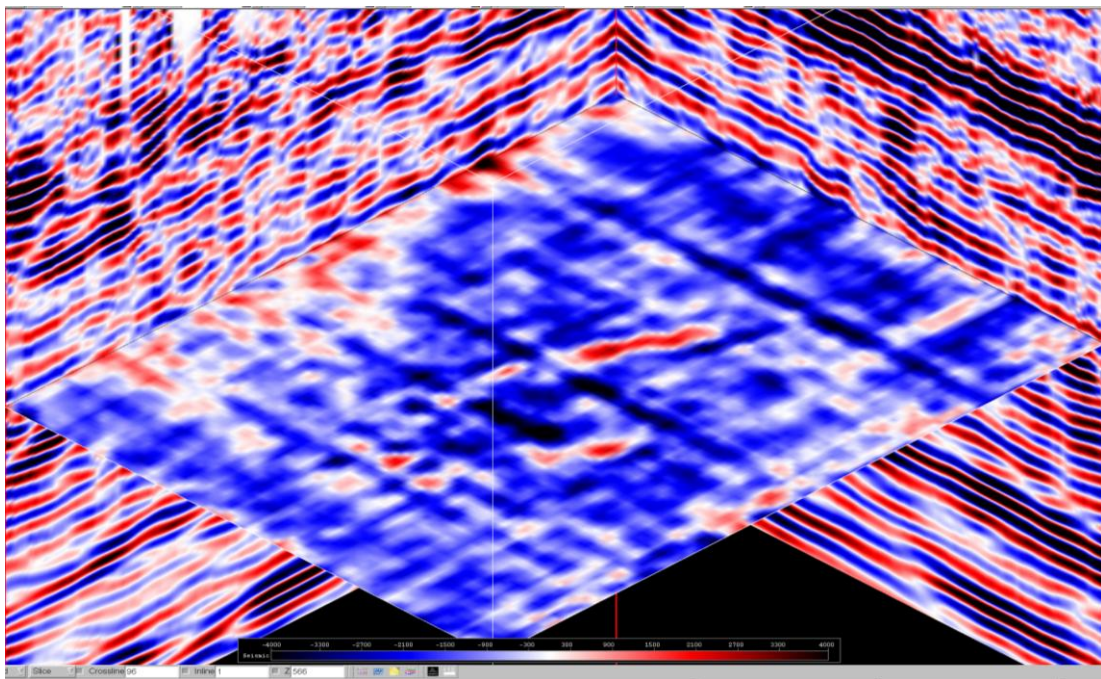


Figure 6. 26 Amplitude map at 566 ms from 30hz data

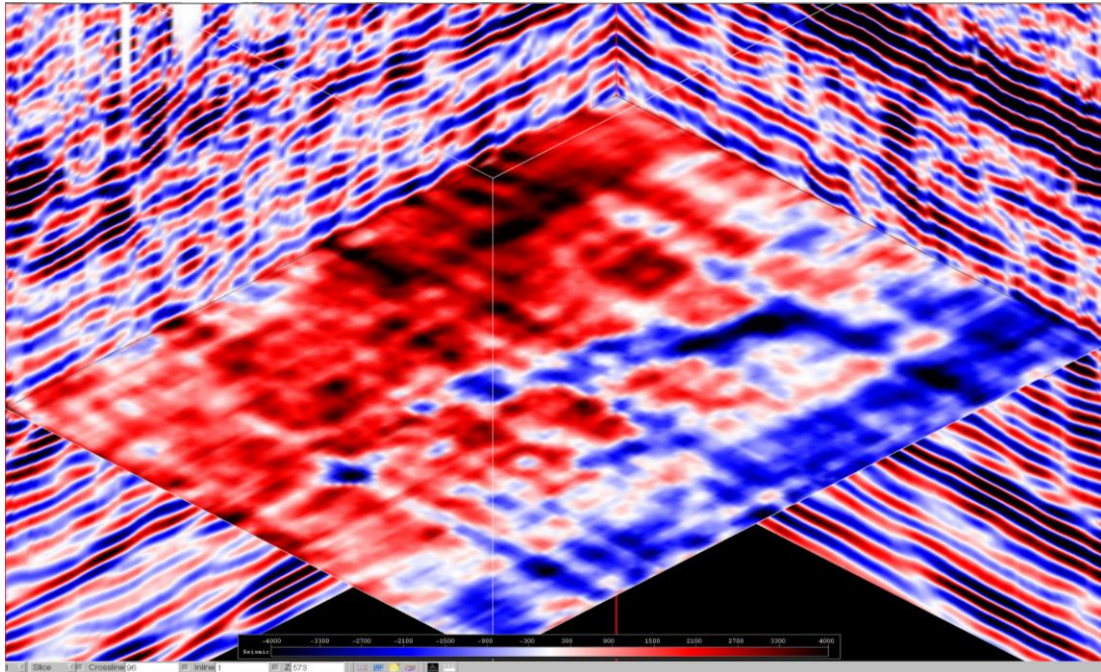


Figure 6. 27 Amplitude map at 573 ms from 30hz data

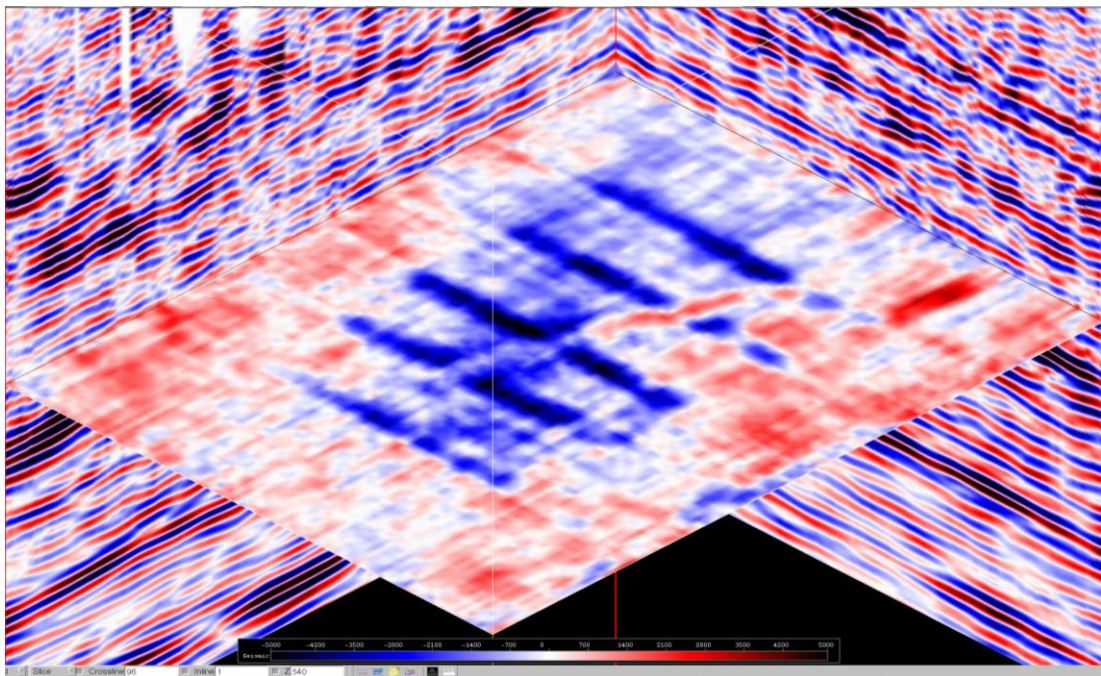


Figure 6. 28 Amplitude map at 540 ms from 40hz data

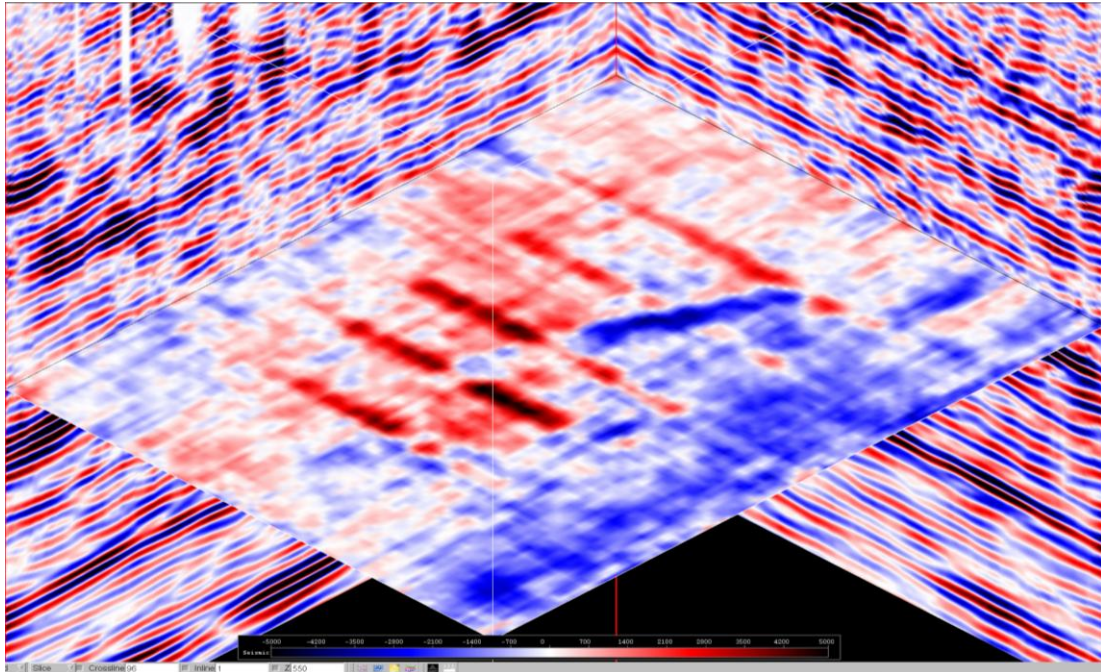


Figure 6. 29 Amplitude map at 550 ms from 40hz data

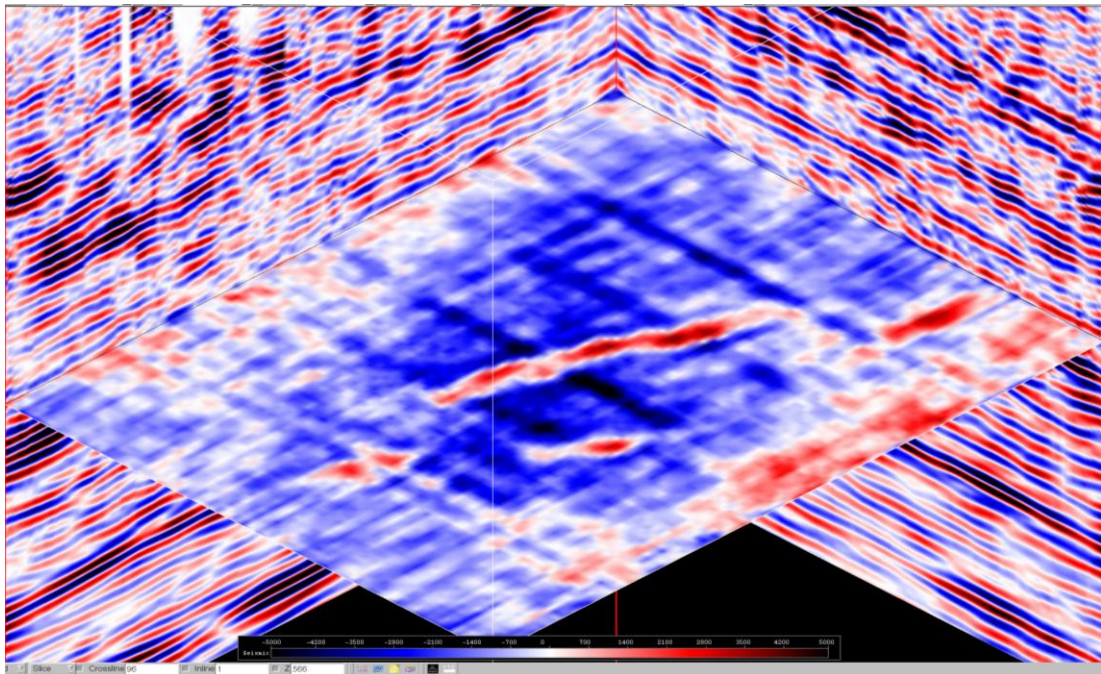


Figure 6. 30 Amplitude map at 566 ms from 40hz data

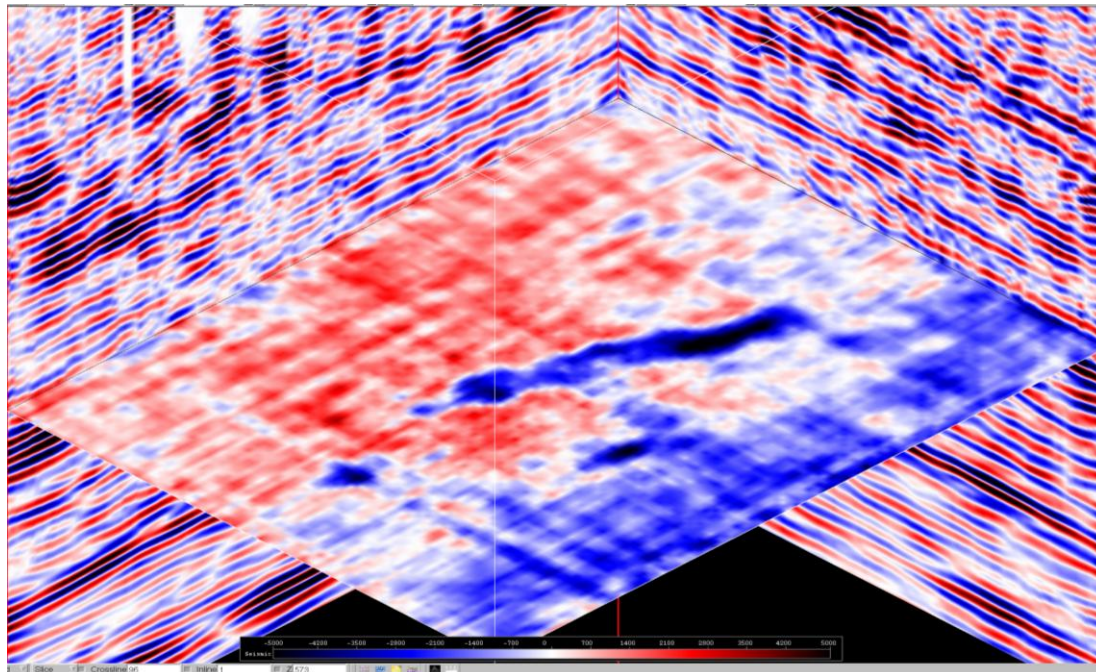


Figure 6. 31 Amplitude map at 573 ms from 40hz data

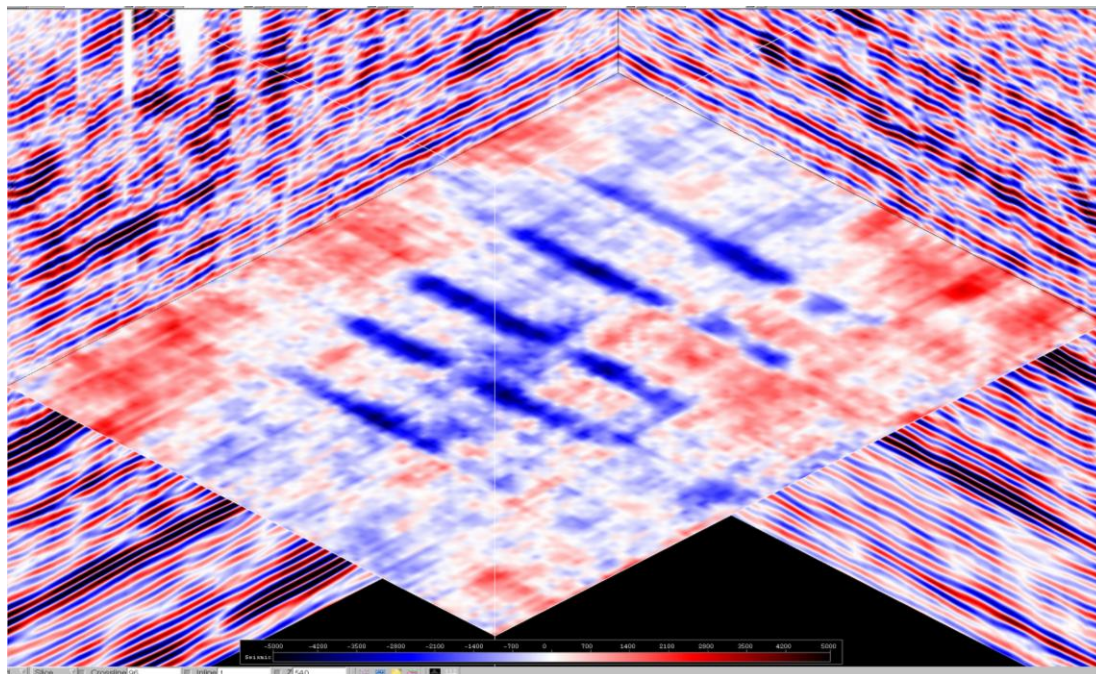


Figure 6. 32 Amplitude map at 540 ms from 50hz data

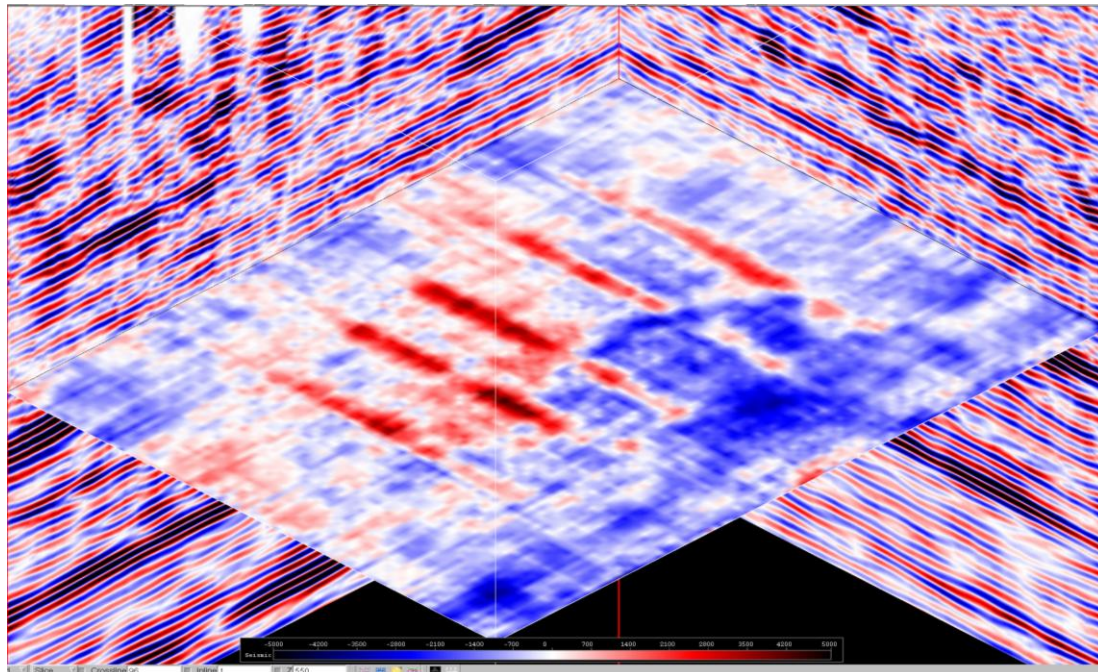


Figure 6. 33 Amplitude map at 550 ms from 50hz data

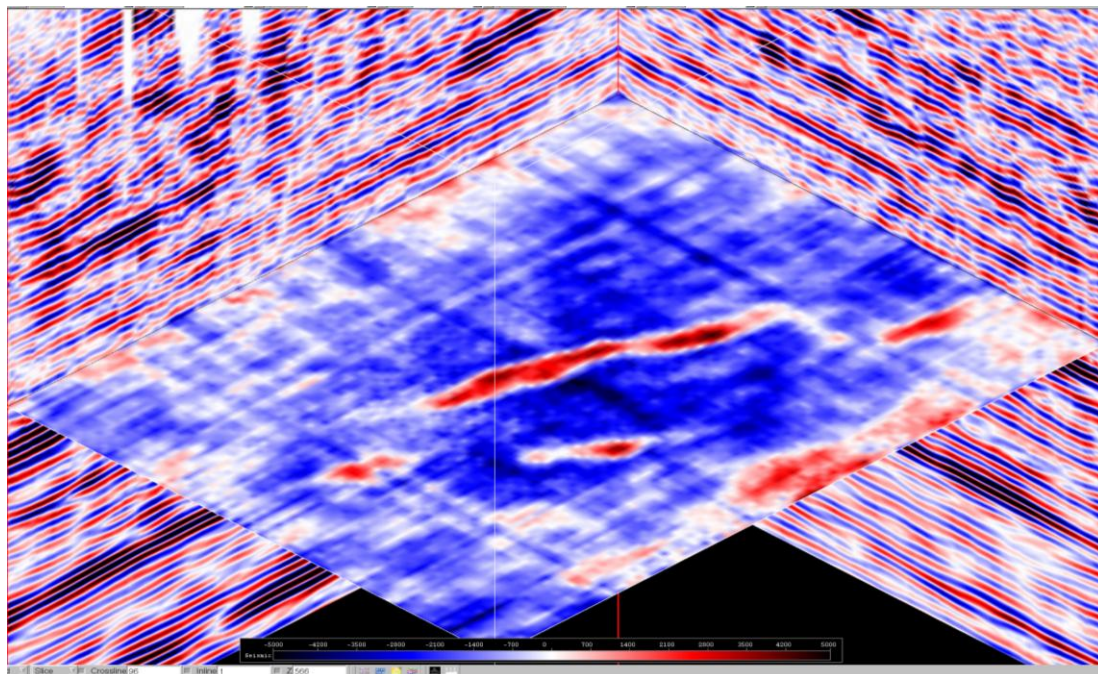


Figure 6. 34 Amplitude map at 566 ms from 50hz data

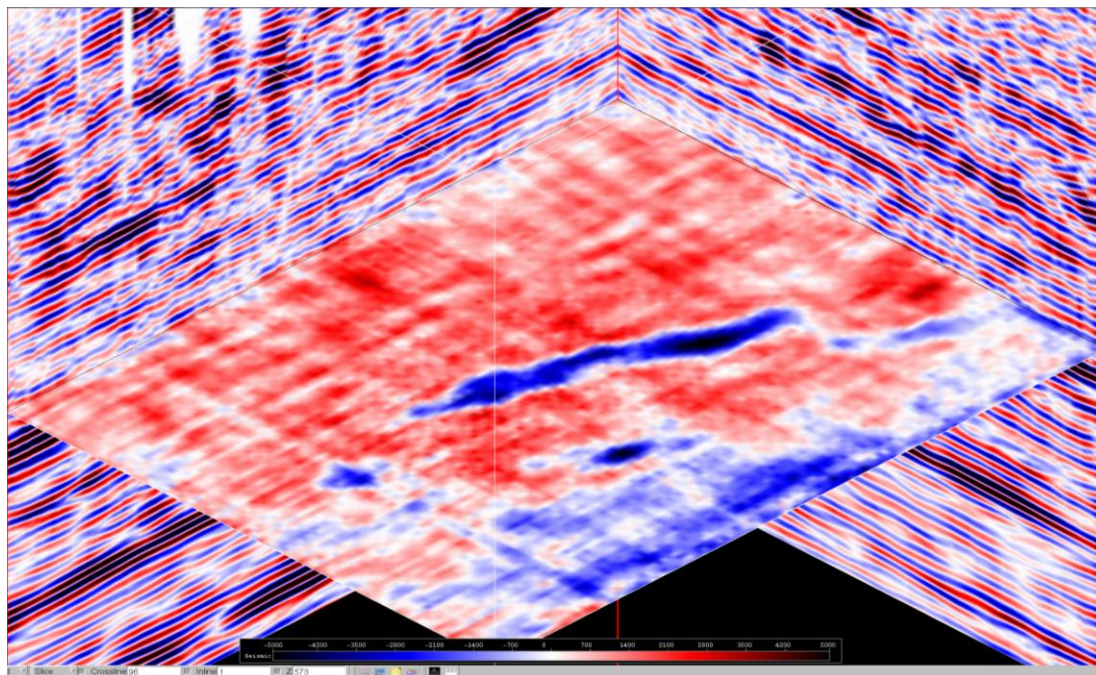


Figure 6. 35 Amplitude map at 573 ms from 50hz data

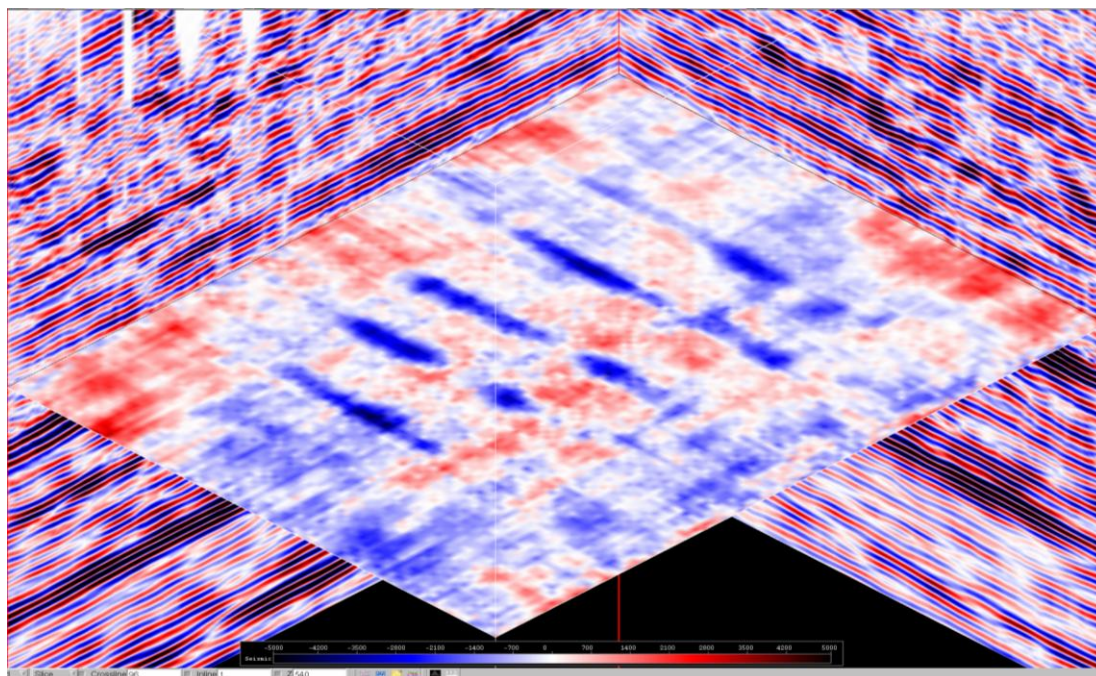


Figure 6. 36 Amplitude map at 540 ms from 60hz data

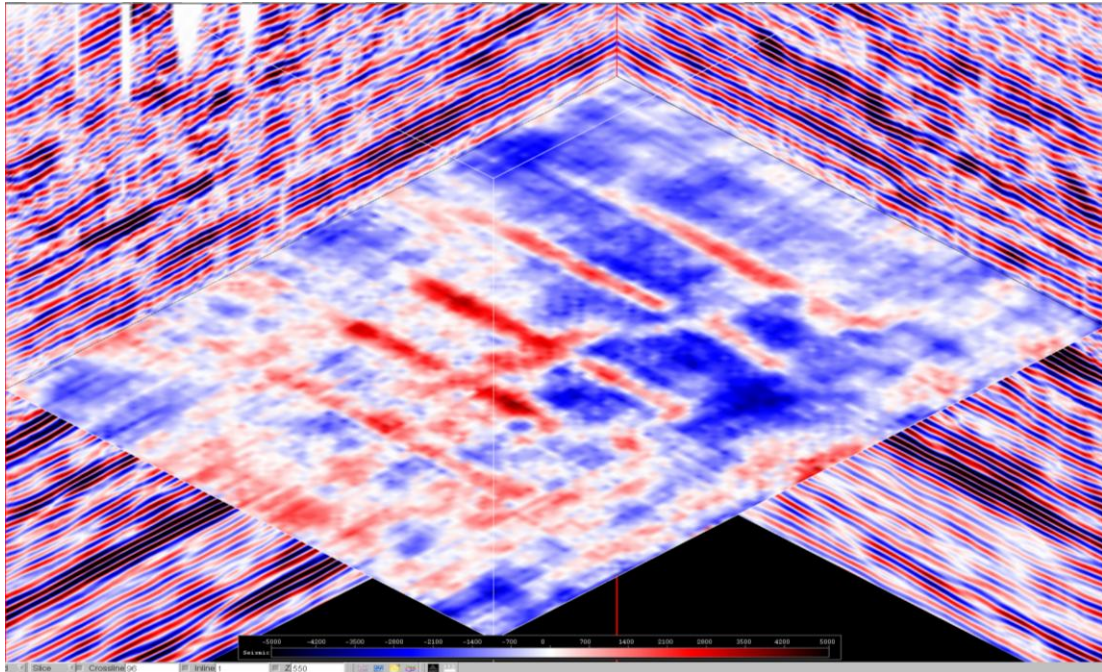


Figure 6. 37 Amplitude map at 550 ms from 60hz data

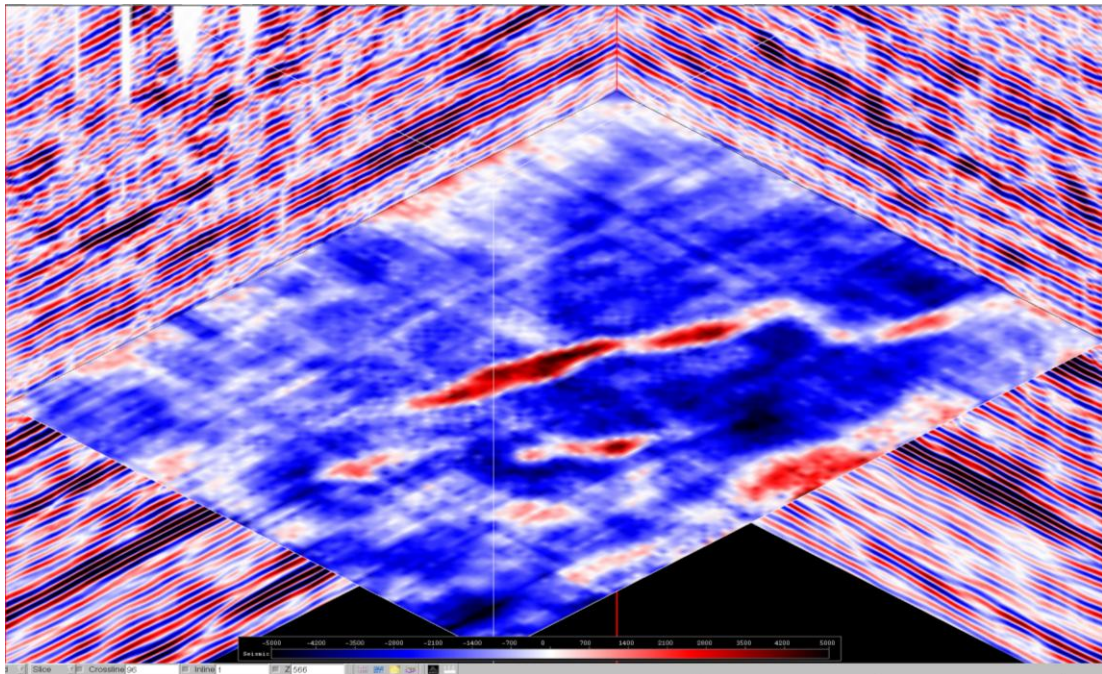


Figure 6. 38 A Amplitude map at 566 ms from 60hz data

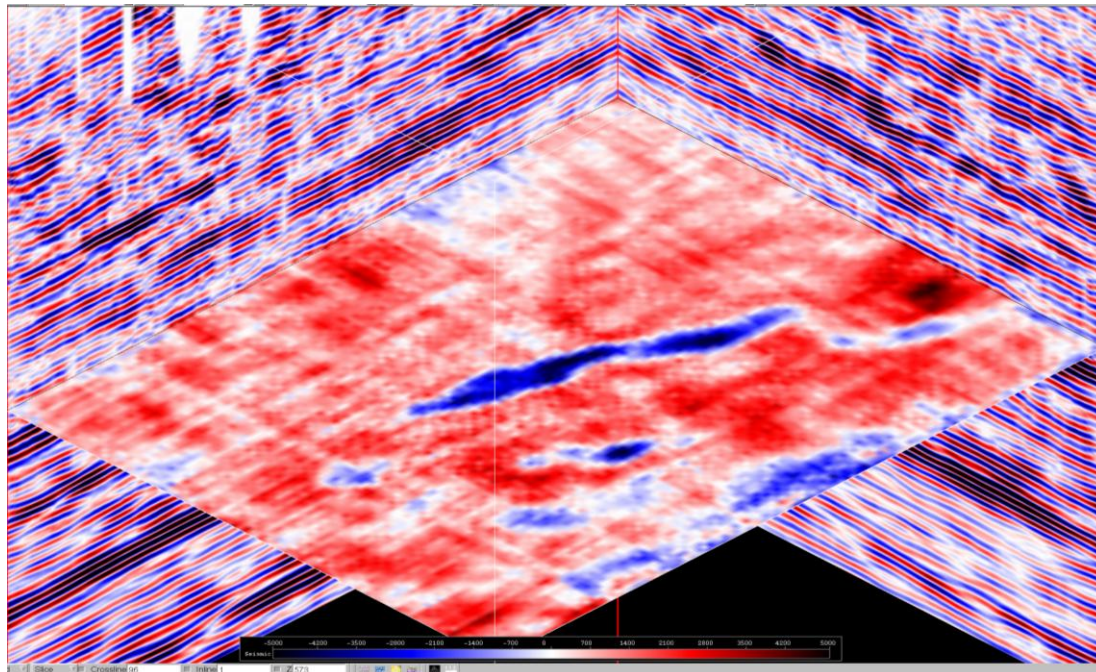


Figure 6. 39 Amplitude map at 573 ms from 60hz data

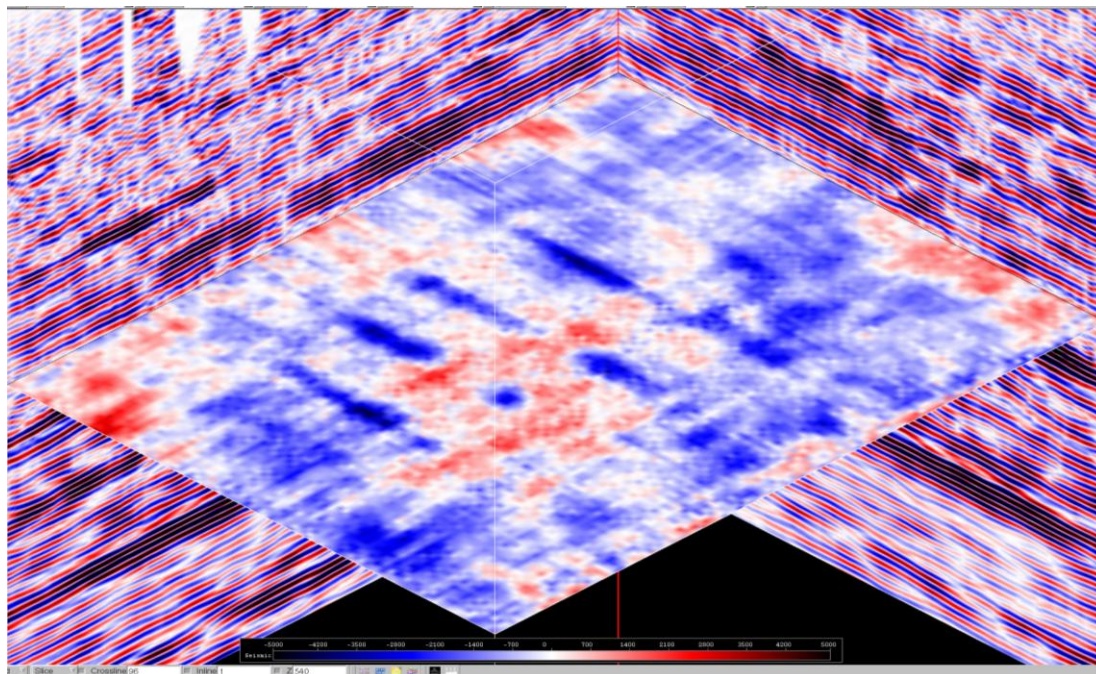


Figure 6. 40 Amplitude map at 540 ms from 70hz data

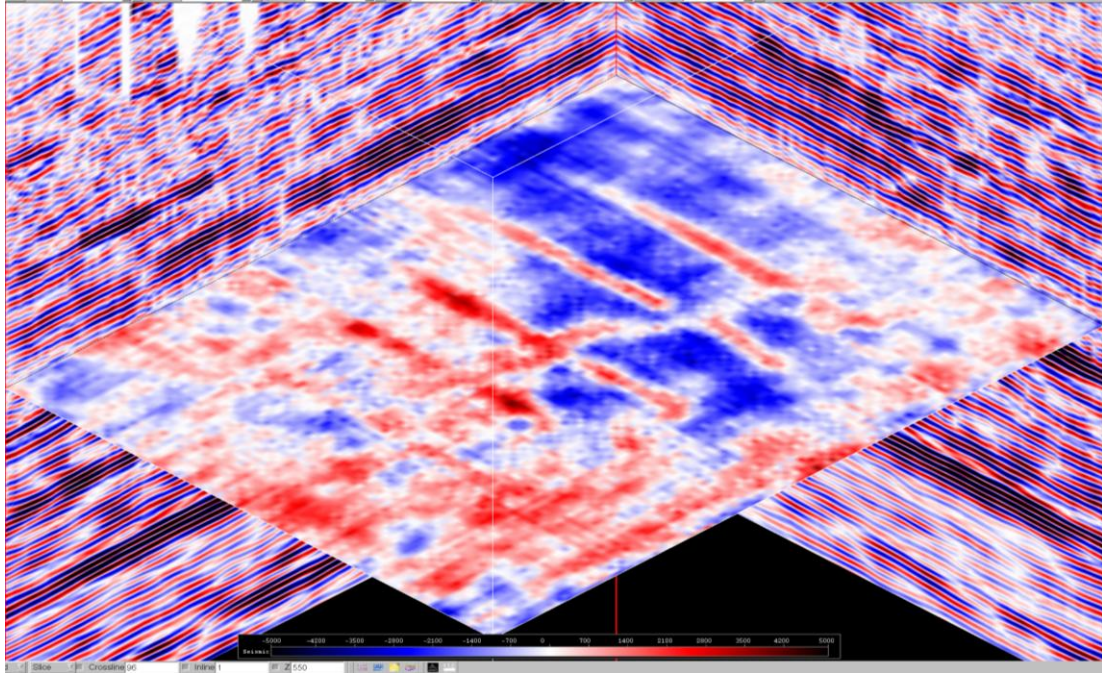


Figure 6. 41 Amplitude map at 550 ms from 70hz data

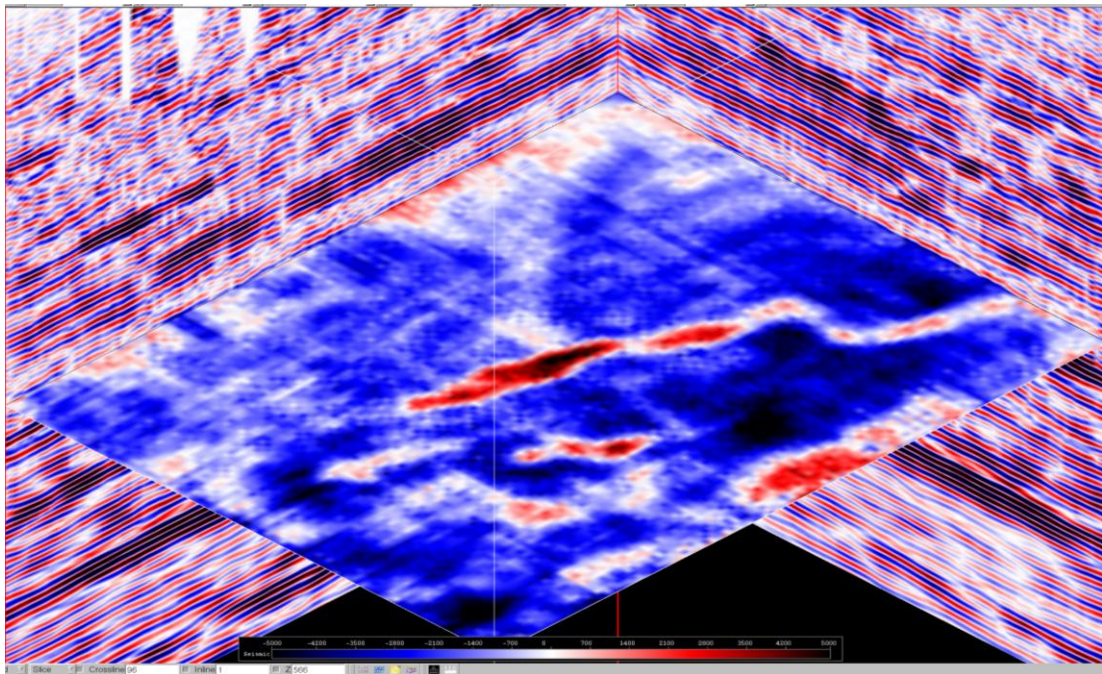


Figure 6. 42 Amplitude map at 566 ms from 70hz data

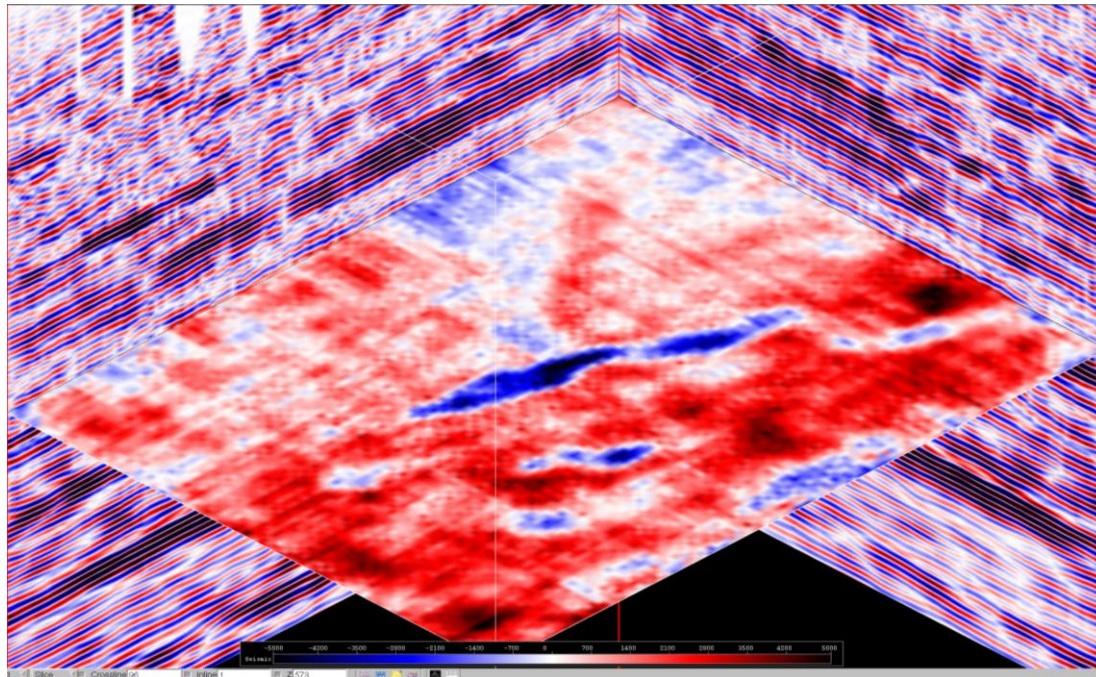


Figure 6. 43 Amplitude map at 573 ms from 70hz data

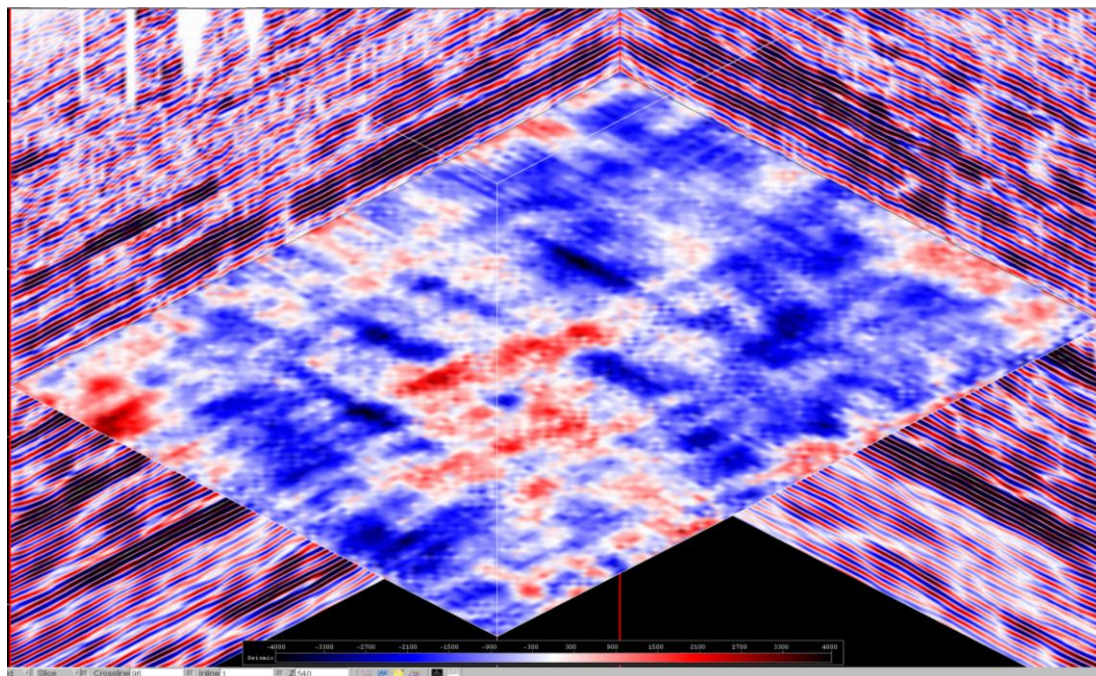


Figure 6. 44 Amplitude map at 540 ms from 80hz data

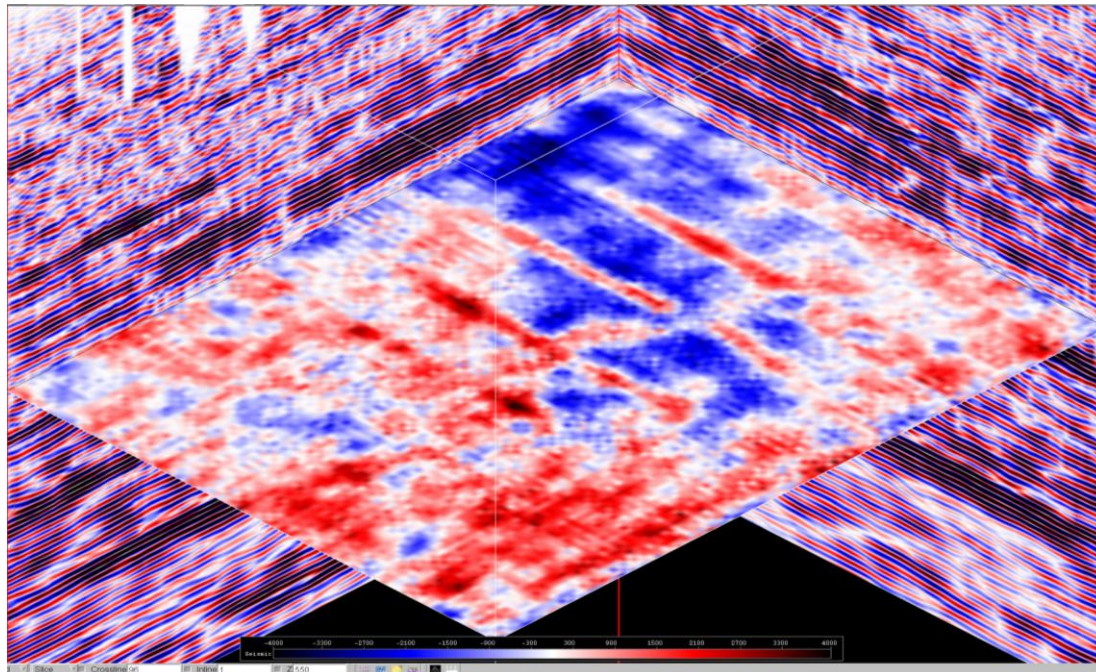


Figure 6. 45 Amplitude map at 550 ms from 80hz data

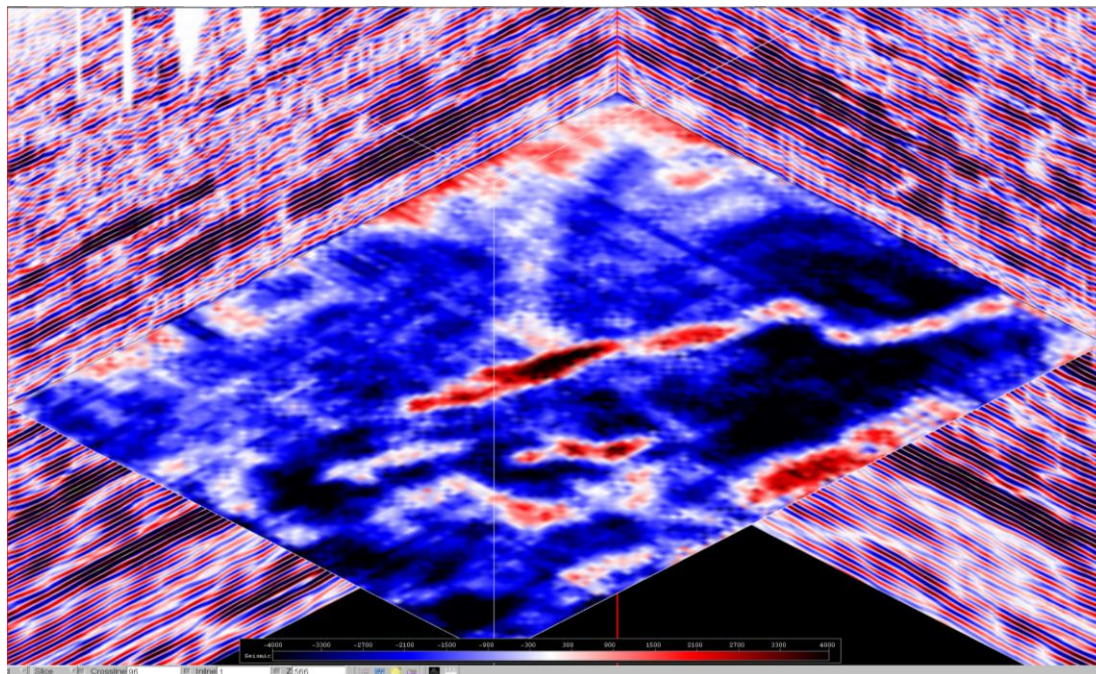


Figure 6. 46 Amplitude map at 566 ms from 80hz data

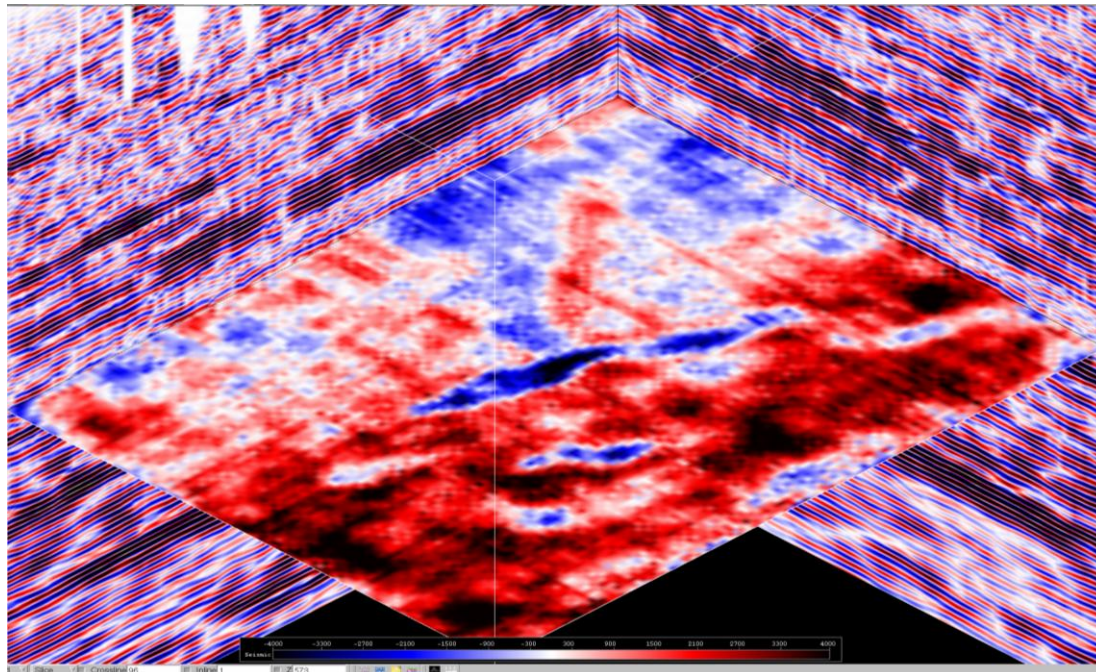


Figure 6. 47 Amplitude map at 573 ms from 80hz data

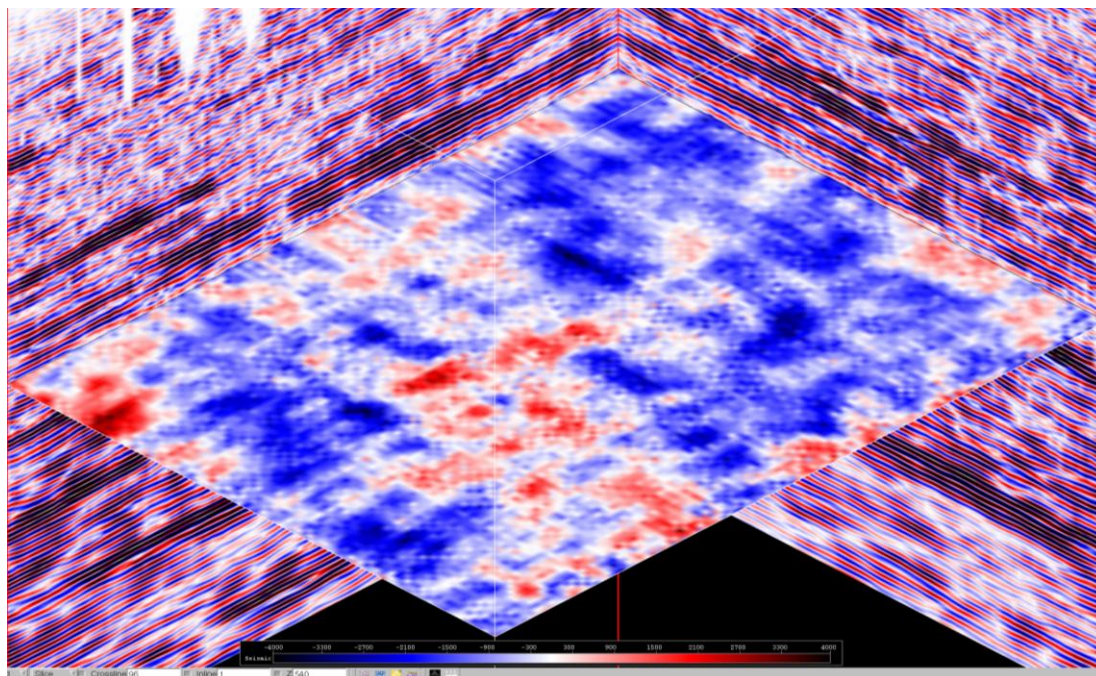


Figure 6. 48 Amplitude map at 540 ms from 90hz data

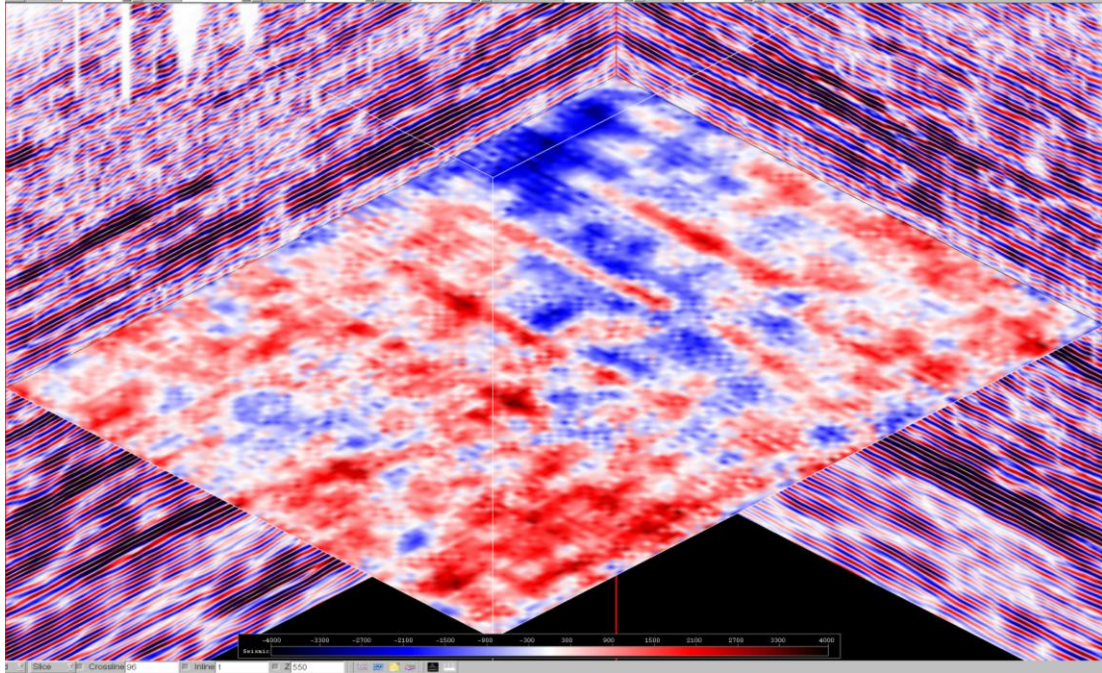


Figure 6. 49 Amplitude map at 550 ms from 90hz data

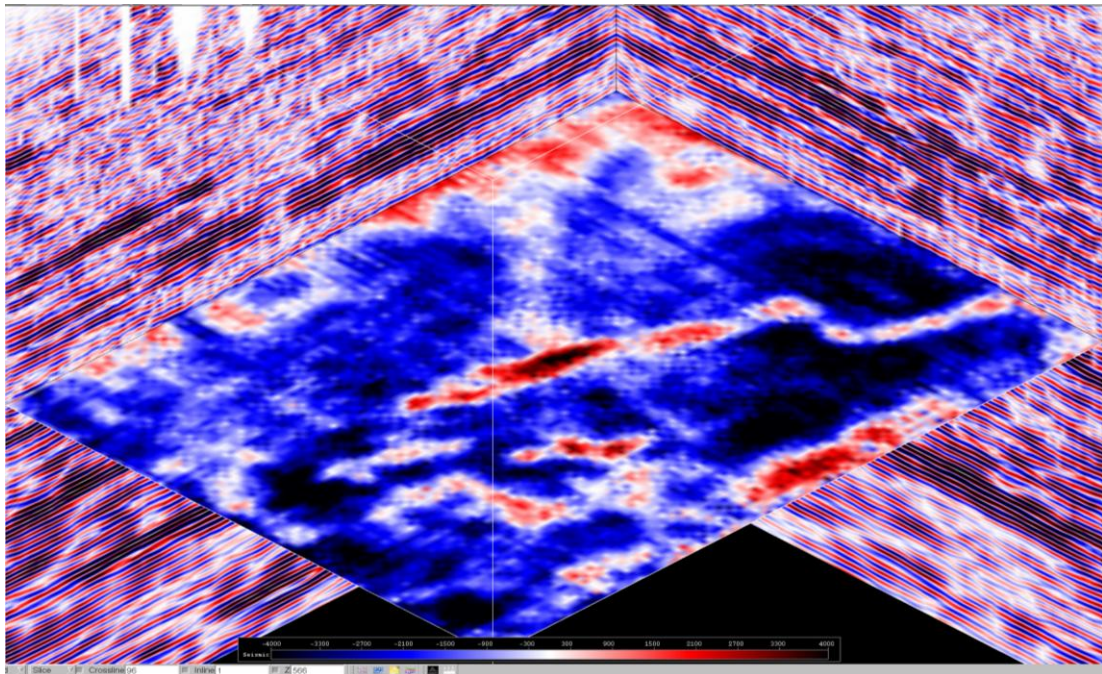


Figure 6. 50 Amplitude map at 566 ms from 90hz data

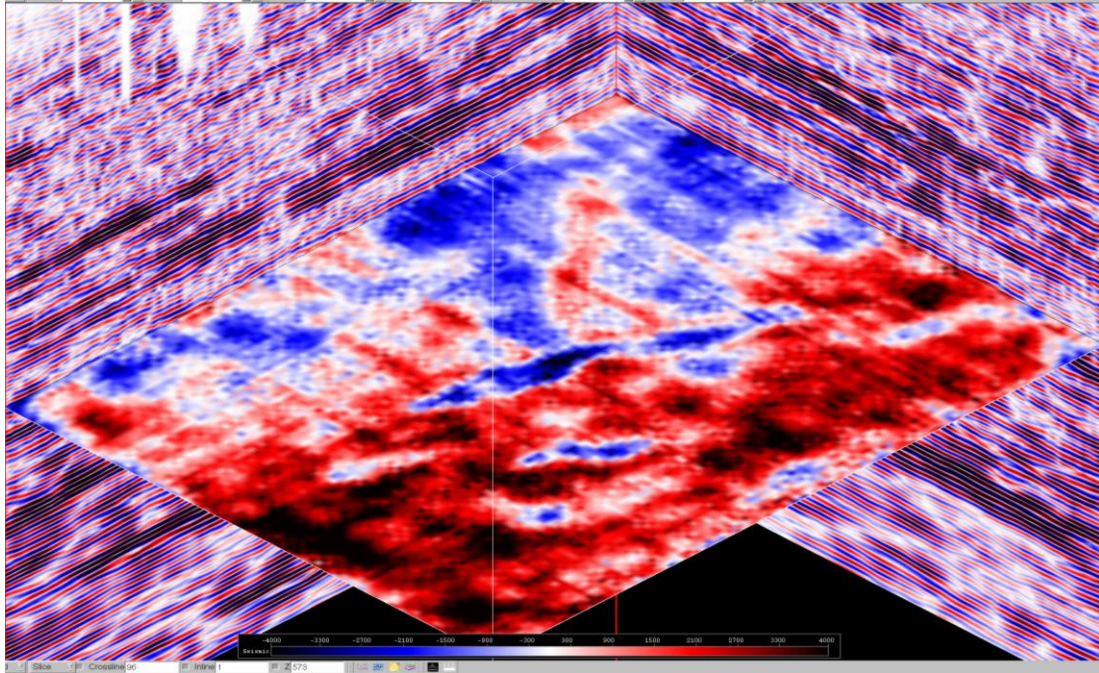


Figure 6. 51 Amplitude map at 573 ms from 90hz data

The slices at 540ms and 550ms cut from the datasets with the range of frequencies attempt to find the optimal pictures of well trajectories and fractures in the reservoir zone (510-560ms). It appears from comparison that the data volume at 40hz is among the best. It has maximized the amplitude anomalies on both the well paths and the fractures. Those at 30hz, 50hz and 60hz are reasonably well too. The images at 10hz (Figures 6.16-17) and at 90hz (Figures 6.48-49) are not favourable indicators.

The maximum tuning at 40hz is also reflected on the cross section as shown in Figures 6.52-56 (Xline 60 cut on the area not complicated by the oblique fractures), in which the image at 40hz (Figure 6.54) stands out the features. For another cross section (Inline 45 cut on the area with the fractures, but not complicated by well paths), the amplitude at 40hz (Figure 6.59) is visible to be maximized on the fractures (Figures 6.57-61). For the cross section complicated

by both well paths and fractures (Xline 56), one well path was masked by the trace disturbance of the oblique fractures, but the others and the fracture zone remain well imaged at 40hz, as illustrated in Figures 6.62-66.

The slices at 566ms and 573ms try to differentiate the oblique fractures from the background below the reservoir zone. Figures 6.14, 15, 18, 19, 22, 23, 26, 27, 30, 31, 34, 35, 38, 39, 42, 43, 46, 47, 50, 51 demonstrate consistently these anomalies on all frequencies except 20hz. The phenomena may render the wavelet transform meaningless because they are visible on all frequencies including on the original data. Careful examination of Figures 6.57-66 found that the events vertically along the oblique fracture zone were attenuated and shifted, in which case the amplitude difference would occur for all frequencies. The amplitude boost at 40hz on the oblique fracture zones within the reservoir (Figures 6.28, 29, 59, 64) may be due to complicated internal reflection interferences, which are accidentally constructive.

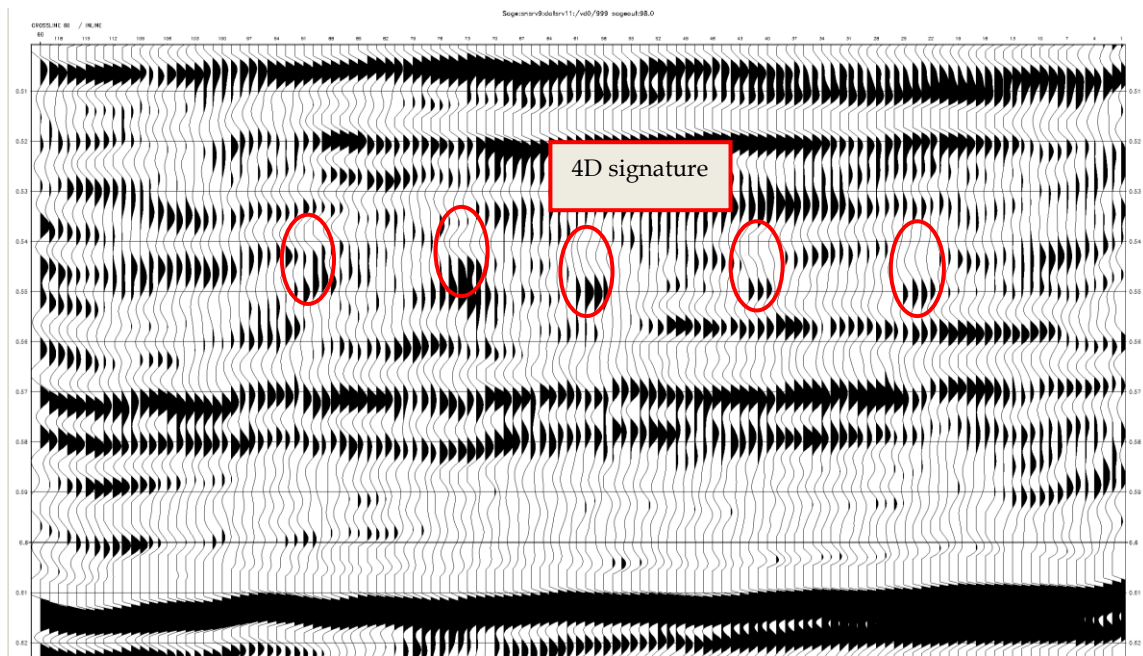


Figure 6. 52 Seismic section of Xline 60 from original data

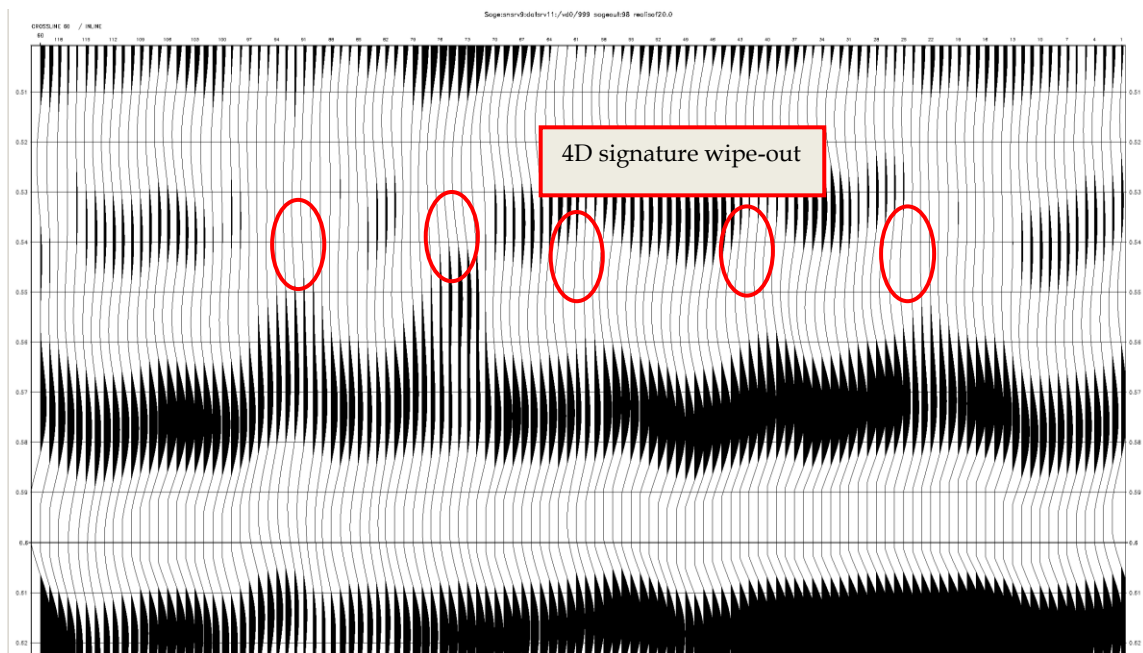


Figure 6. 53 Seismic section of Xline 60 from 20hz data

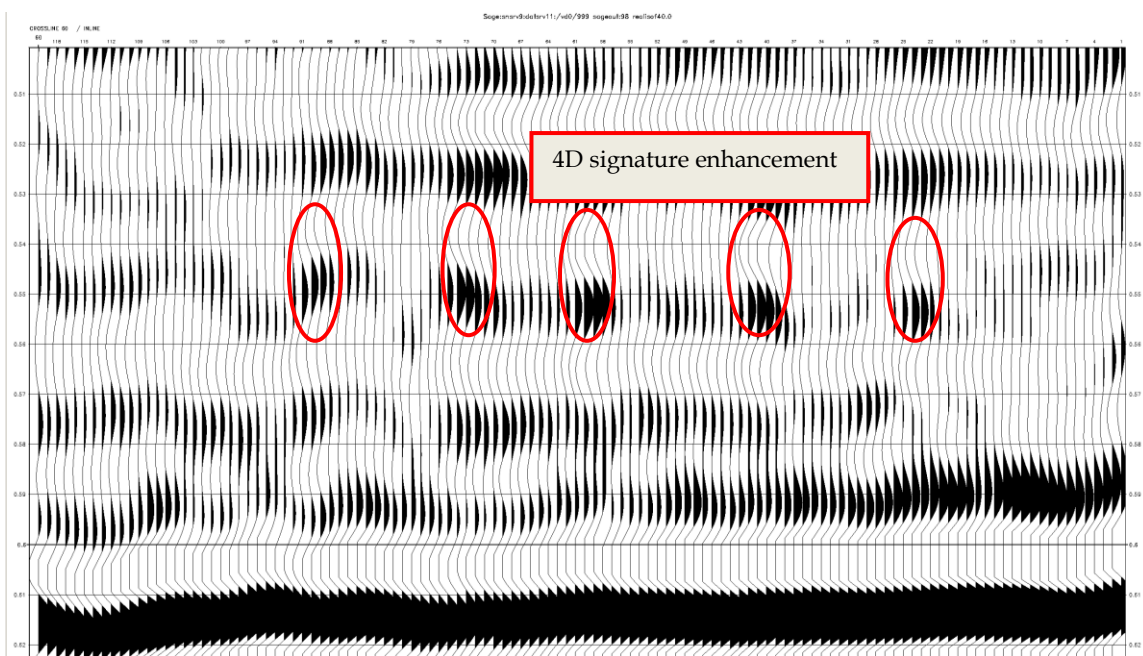


Figure 6. 54 Seismic section of Xline 60 from 40hz data

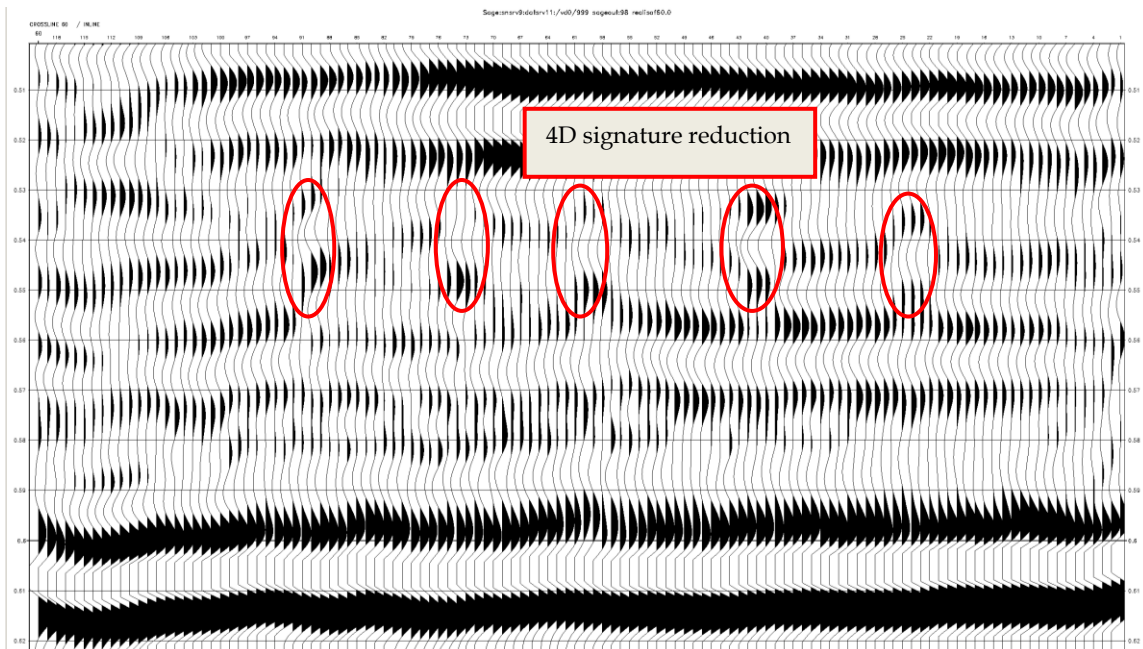


Figure 6. 55 Seismic section of Xline 60 from 60hz data

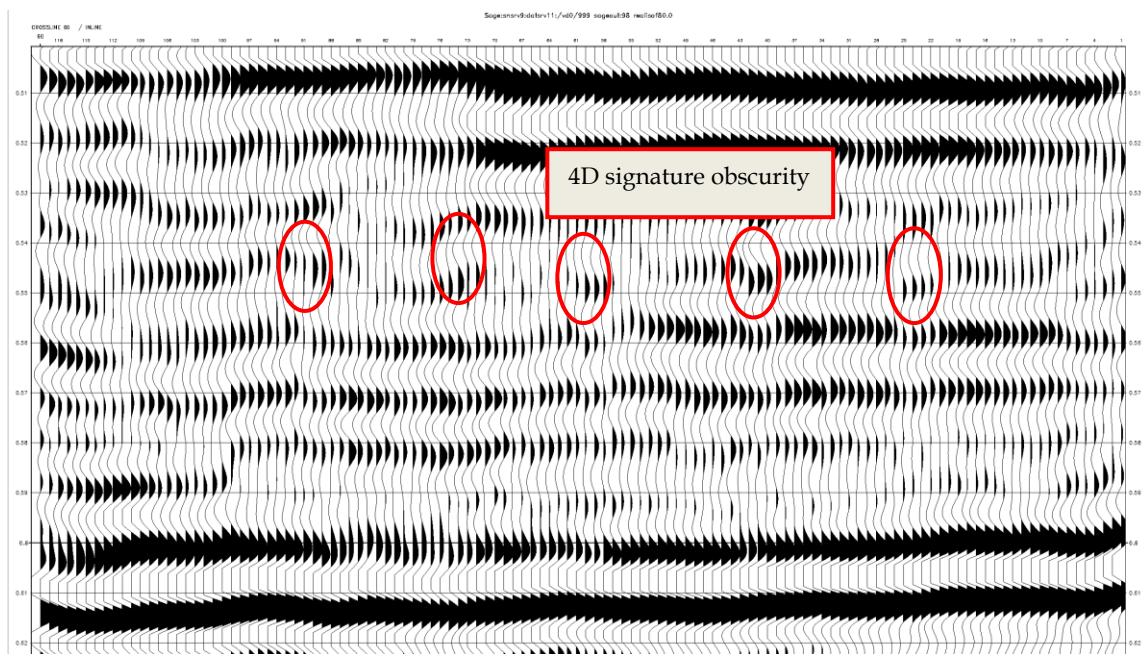


Figure 6. 56 Seismic section of Xline 60 from 80hz data

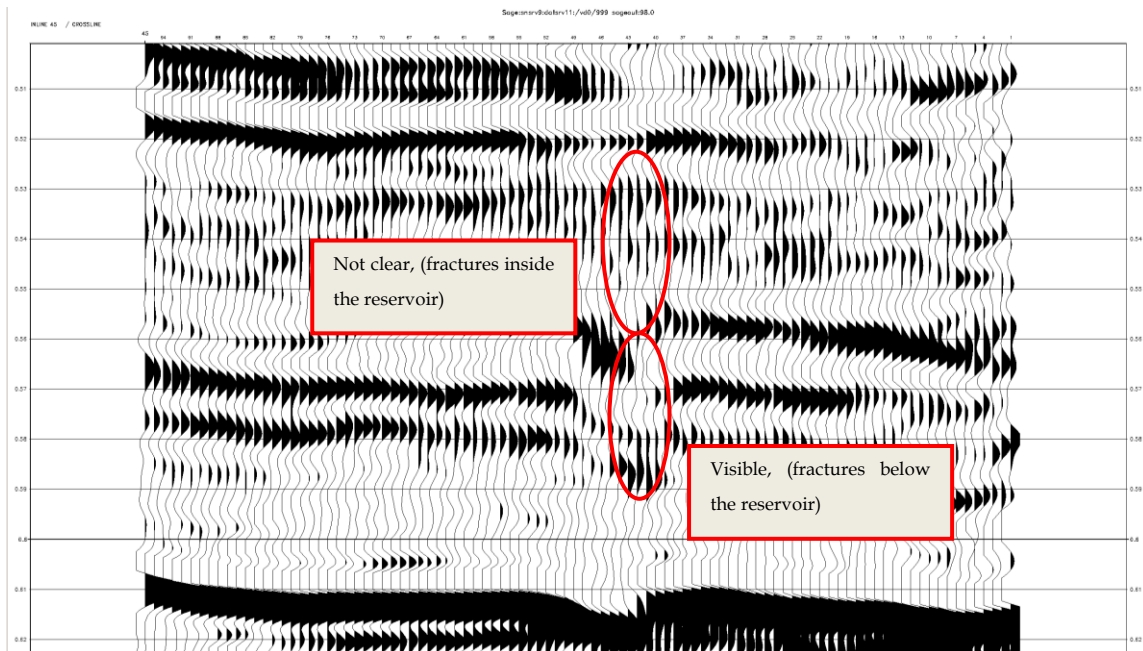


Figure 6. 57 Seismic section of Inline 45 from original data

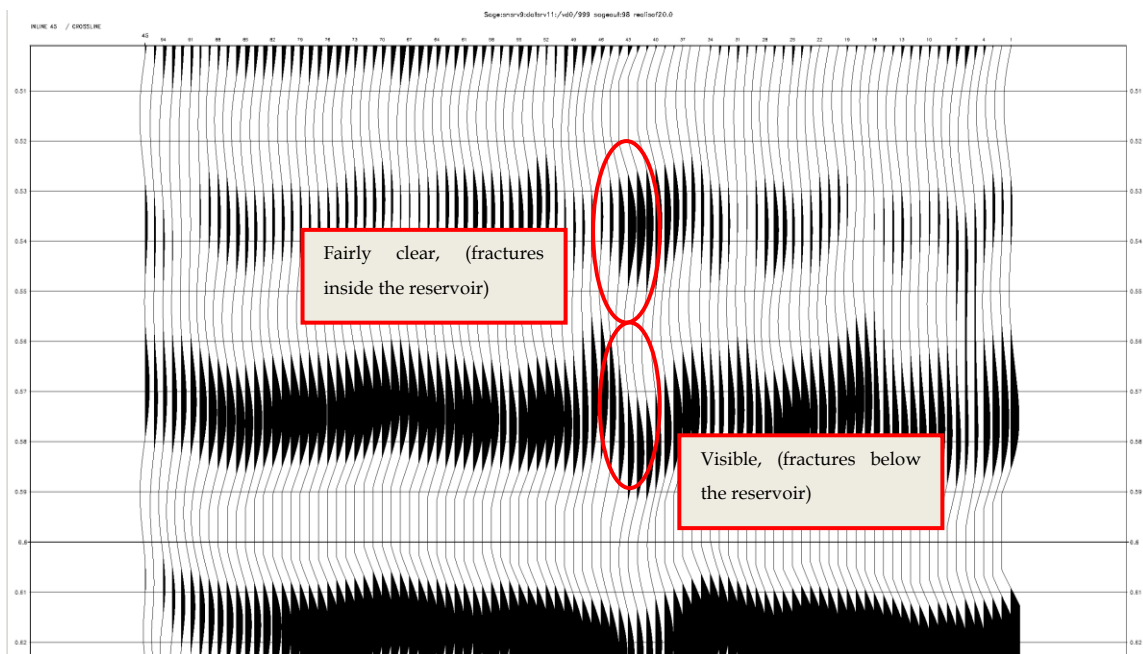


Figure 6. 58 Seismic section of Inline 45 from 20hz data

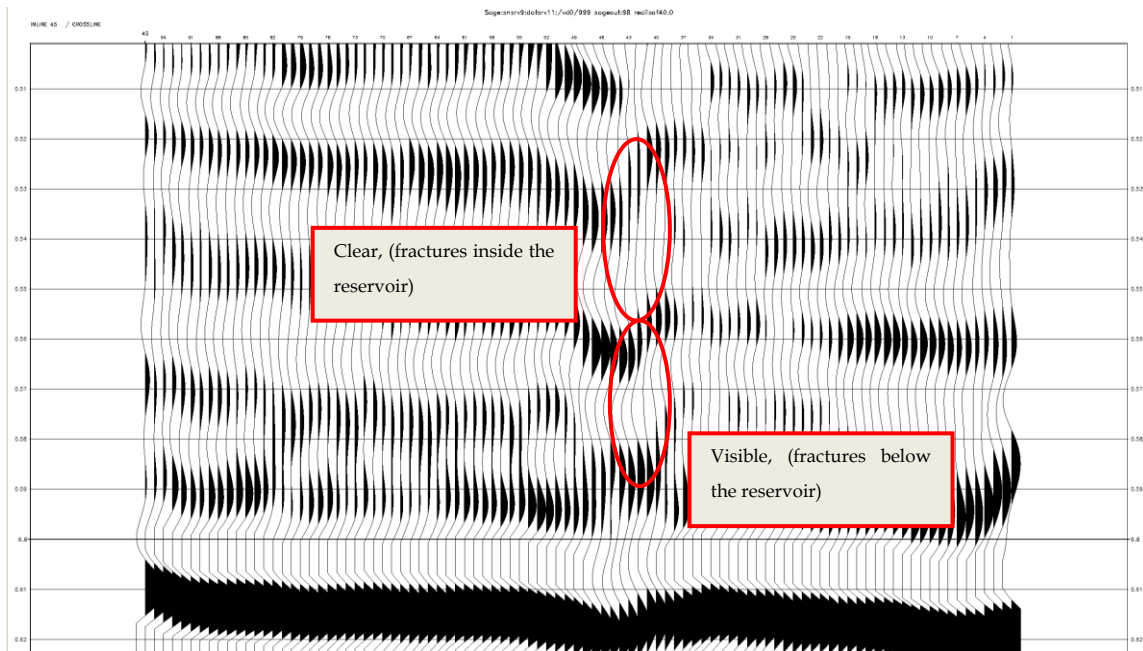


Figure 6.59 Seismic section of Inline 45 from 40hz data

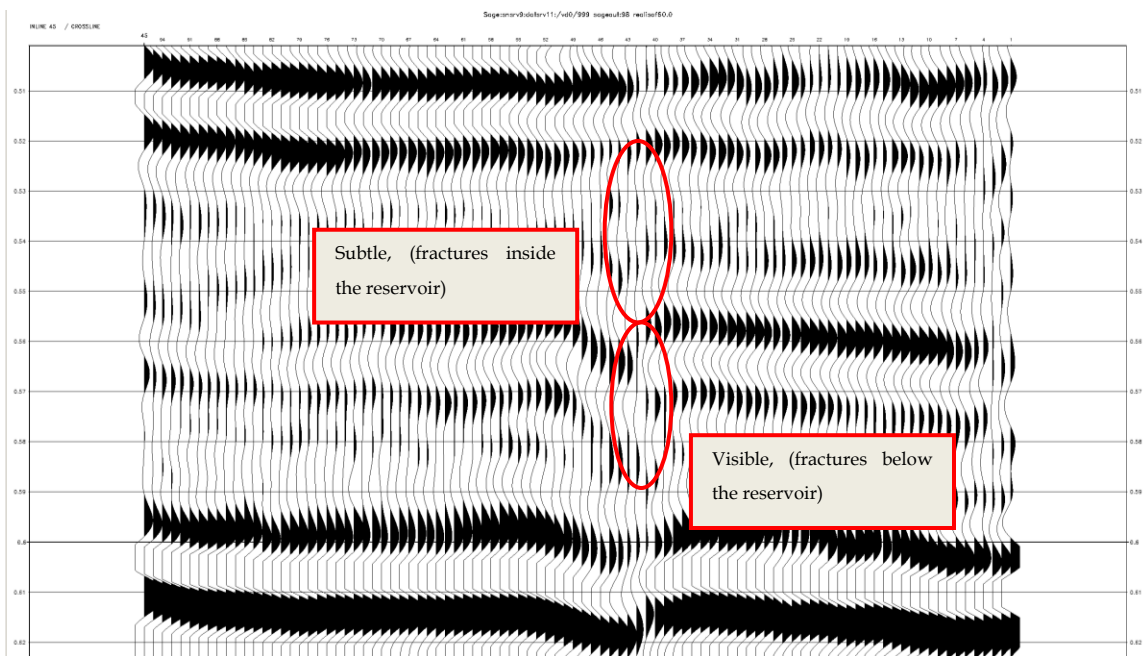


Figure 6.60 Seismic section of Inline 45 from 60hz data

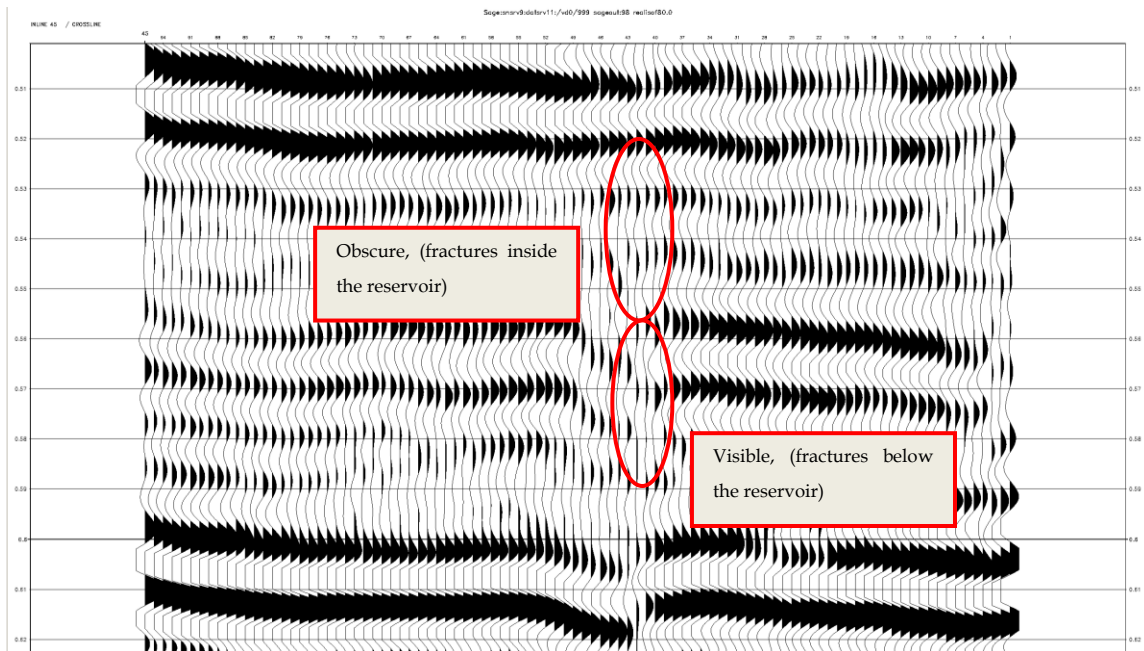


Figure 6. 61 Seismic section of Inline 45 from 80hz data

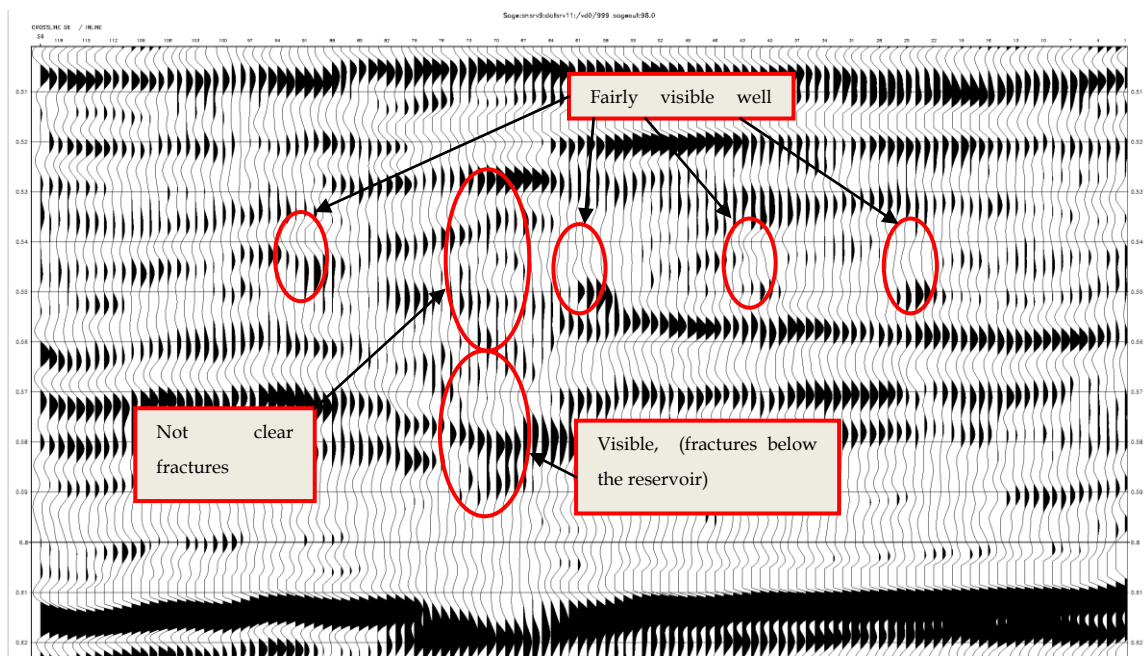


Figure 6. 62 Seismic section of Inline 56 from original data

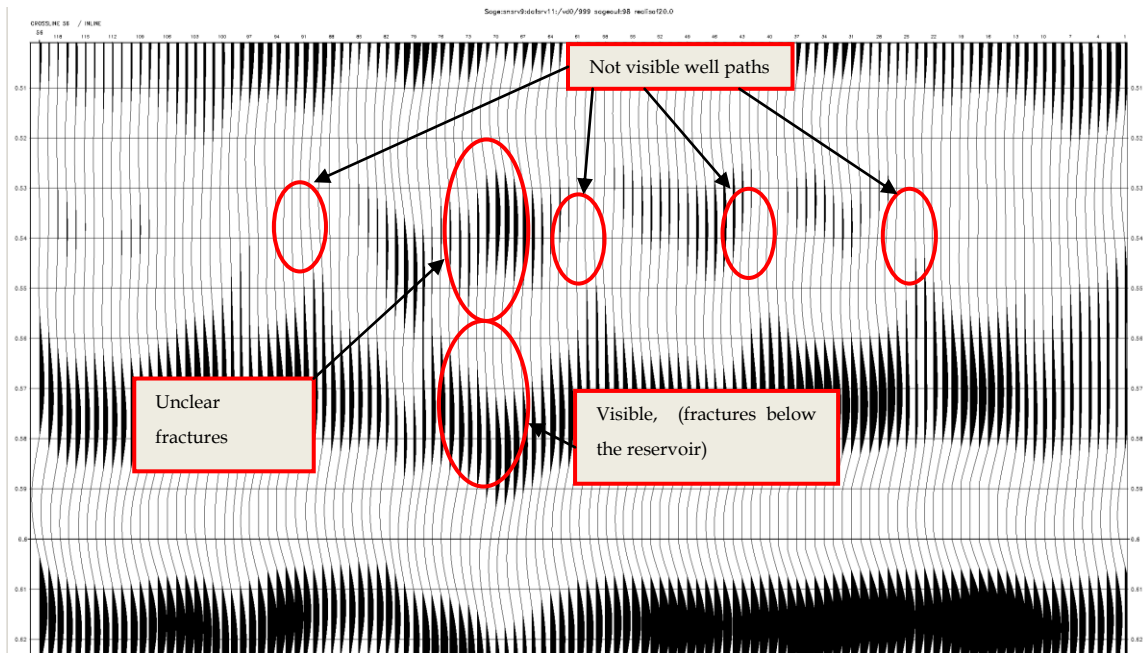


Figure 6. 63 Seismic section of Inline 56 from 20hz data

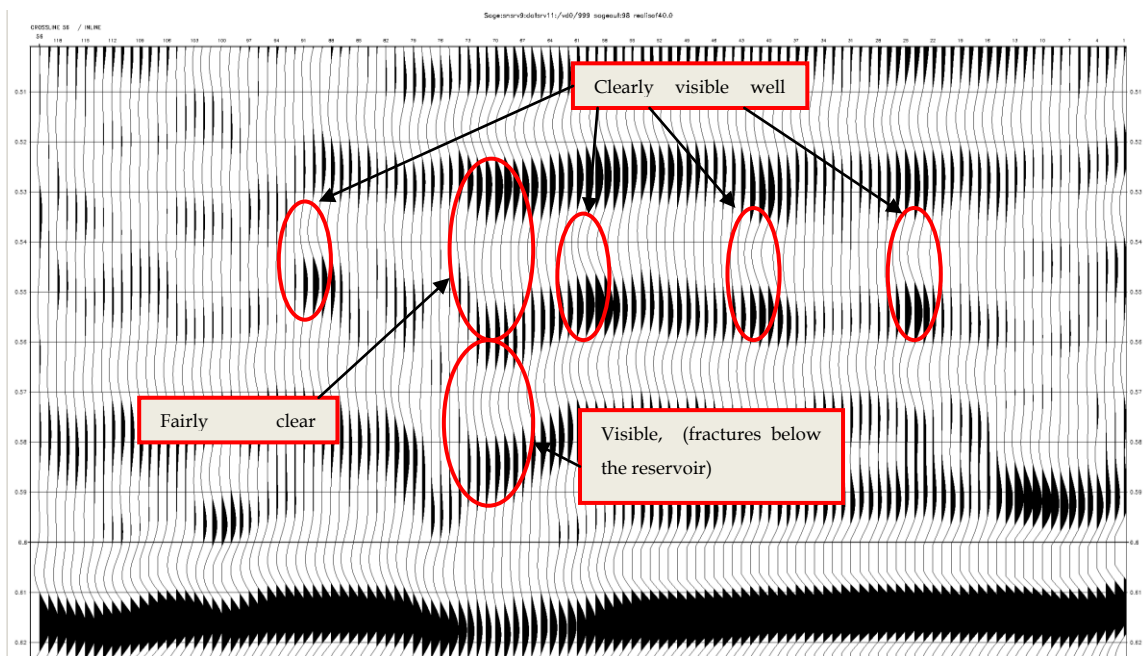


Figure 6. 64 Seismic section of Inline 56 from 40hz data

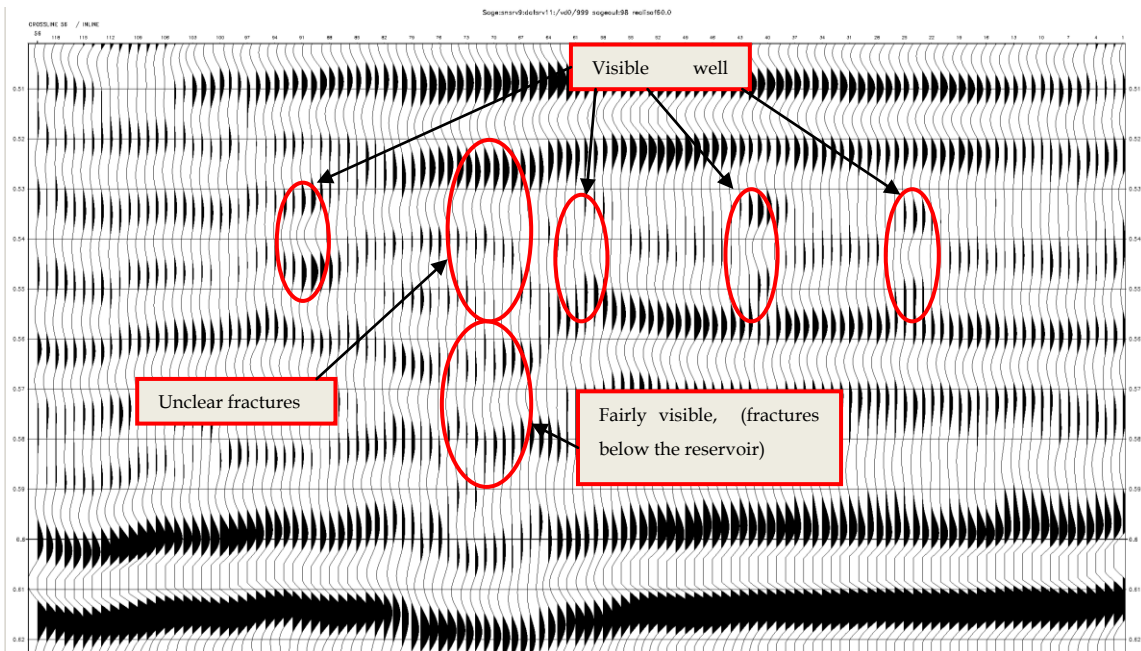


Figure 6. 65 Seismic section of Inline 56 from 60hz data

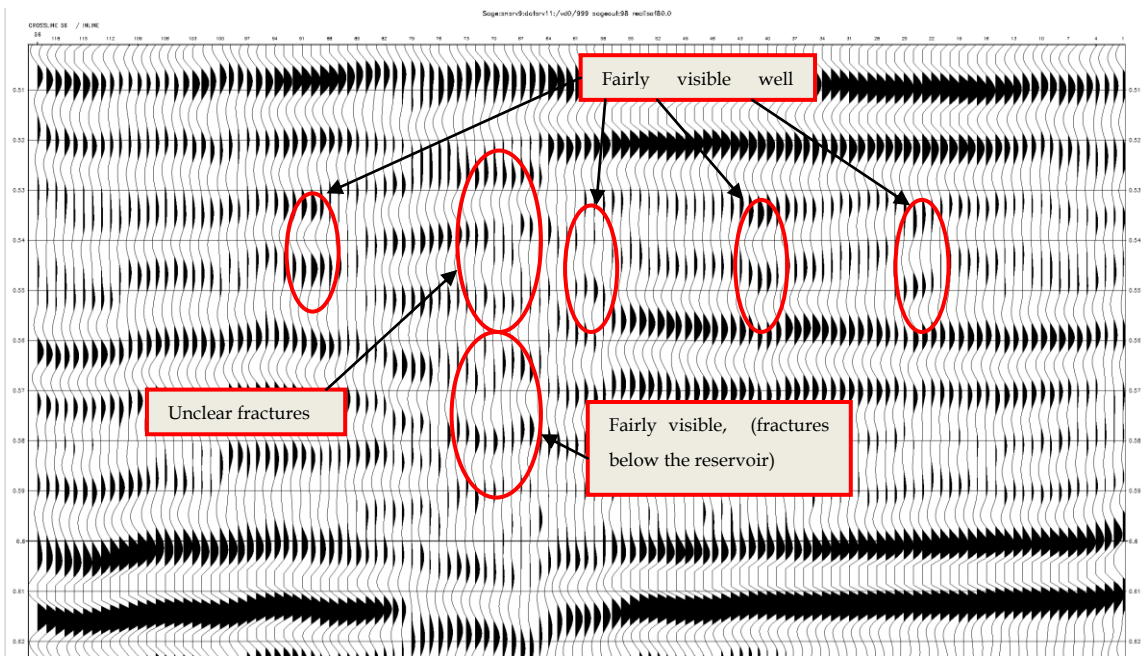


Figure 6. 66 Seismic section of Inline 56 from 80hz data

6.6 Interpretation

Chapter 5 and the above section of this Chapter have already suggested the framework of the fluid flow paths, which visualizes the process as: the steam was injected along the five horizontal wells and created the oblique fracture zones, in which considerable amounts of fluids may have flowed downward to underlying formations (Devonian carbonates) and broken the caprock into overlying formations. The map in Figure 6.67 implies this interpretation. The section will detail the flow paths within the reservoir and beyond using the instantaneous amplitude dataset at 40hz.

Figure 6.68 shows the cross section (Xline 60) cut from the data volume. It is noted that the fluid paths at well locations are located in the central parts of the high-amplitude zones because the two linear events above and below the well paths already existed in the baseline survey, as evidenced in Figures 6.69. The two linear events are also visible outside of the well path area in Figure 6.70. As explained in the Chapter of Reservoir Characterization, they are tight carbonate strings. When steam was injected, the portions of the reservoir that were heated and fluid substituted along the well bores, became lower in velocity and then generated negative reflection events. Choosing the frequency (40hz) for maximum tuning, the instantaneous amplitude was boosted for the newly-created troughs. At the same time, the positive reflections above and below them were augmented, which was likely caused by constructive interference among these three sets of events.

A series of cross sections in the direction of Inline were made in order to view the potential vertical movement along the oblique fractured zones. The first cross section (Inline 12) is outside of the well path area. It displays no well path image, but a vertically-extended high-amplitude swath (Figure 6.71), which is interpreted as a vertical fracture zone to be opened by steam injection since it did

not exist in the baseline survey (Figure 6.72). South-westwards, the second cross section (Inline 24) cut the first well path. As shown in Figure 6.73, the spatial distribution of high instantaneous amplitude manifests the wellbore position and the fracture zone seems weak and may have just started. Further, the third cross section (Inline 32) is situated between two well paths. The fracture zone evolved substantially, as indicated by the vertical length of high amplitude in Figure 6.74. As before, there are no signs of well trajectories. The fourth cross section (Inline 40) cut the second well path, which is delineated by an anomaly of high amplitude in Figure 6.75. The fracture zone propagated deeper into the top of Devonian or even beyond. It may have formed a passage of steam escaping downwards. The fifth cross section (Inline 50) falls between wells again. There is no effect of the well path, and fracturing may have activated both upwards and downwards (Figure 6.76). The sixth cross section (Inline 59) is across the middle well and demonstrates strong amplitude in the well path and weak amplitude in the fracture zone in Figures 6.77. The latter can be verified by the abnormally weak amplitude in Figure 6.78. The seventh cross section (Inline 67) moves to the well gap in Figure 6.79 and has definitely no showings of the well path. The fracture zone is implied by the significantly attenuated amplitude on the top of Devonian. In addition, a new fracture zone emerges as the high-amplitude anomaly did not exist in the baseline survey in Figure 6.80. The eighth cross section (Inline 74) followed the fourth well path, which was dissected into three legs by two weak-amplitude strips in Figure 6.81. Similarly, the strips are regarded as the fractures zones, which demonstrate strong amplitude anomaly and also strong attenuation on the top of Devonian in Figure 6.82. The ninth cross section (Inline 83) shows no well path regularity of high amplitude in Figure 6.83. The fracture zone is weakened to some degree. The tenth cross section (Inline 90) cut the last well path, whose image is indicated by high amplitude in Figure 6.84. As before, the anomaly of low amplitude inside the

reservoir and of strong amplitude attenuation on the top of Devonian mirrors the fracture zone. The final cross section (Inline 99) is out of the well path area in the southwest in Figure 6.85. The fracture zone remains and its amplitude was amplified unlike in the last section.

In summary, the five well bores for steam injection generated consistent discernible images of high amplitude along their respective trajectories. There are two potential oblique parallel fracture zones developed across the wells, which were most likely induced by steam injection. Their amplitude can be weakened or strengthened due to complicated fluid passages. The downward fluid movement with potential breakthroughs into Devonian carbonate appears to be well supported by these pictures and additional ones in Figures 6.86-87, while steam leakage to the overlying formations are obscured even though some anomalies come up in favour of this mechanism, such as in Figure 6.88.

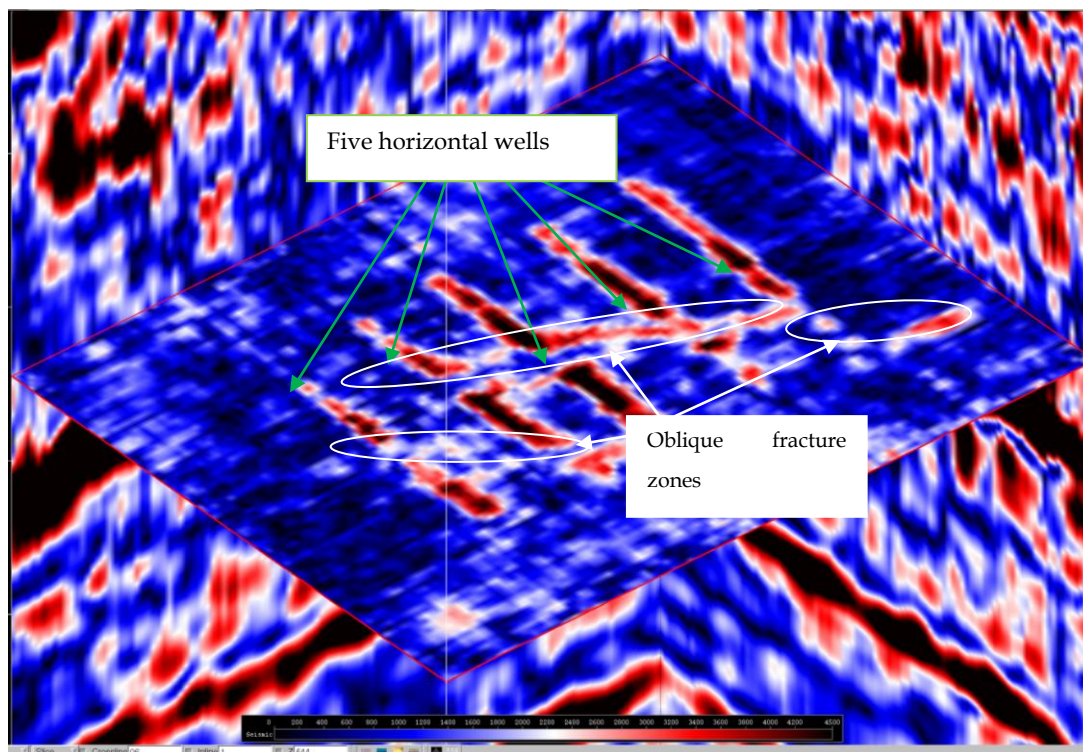


Figure 6. 67 Instantaneous amplitude slice at 544ms cut from the data at 40hz

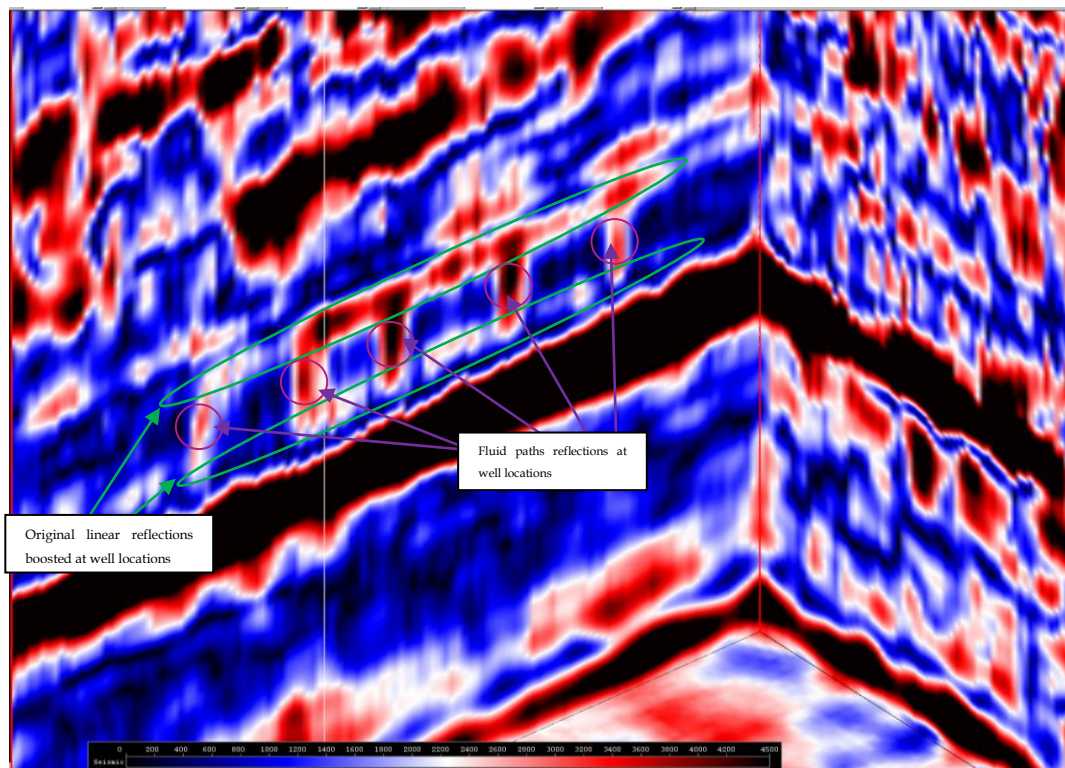


Figure 6. 68 Instantaneous amplitude seismic cross section of Xline 60 at 40hz

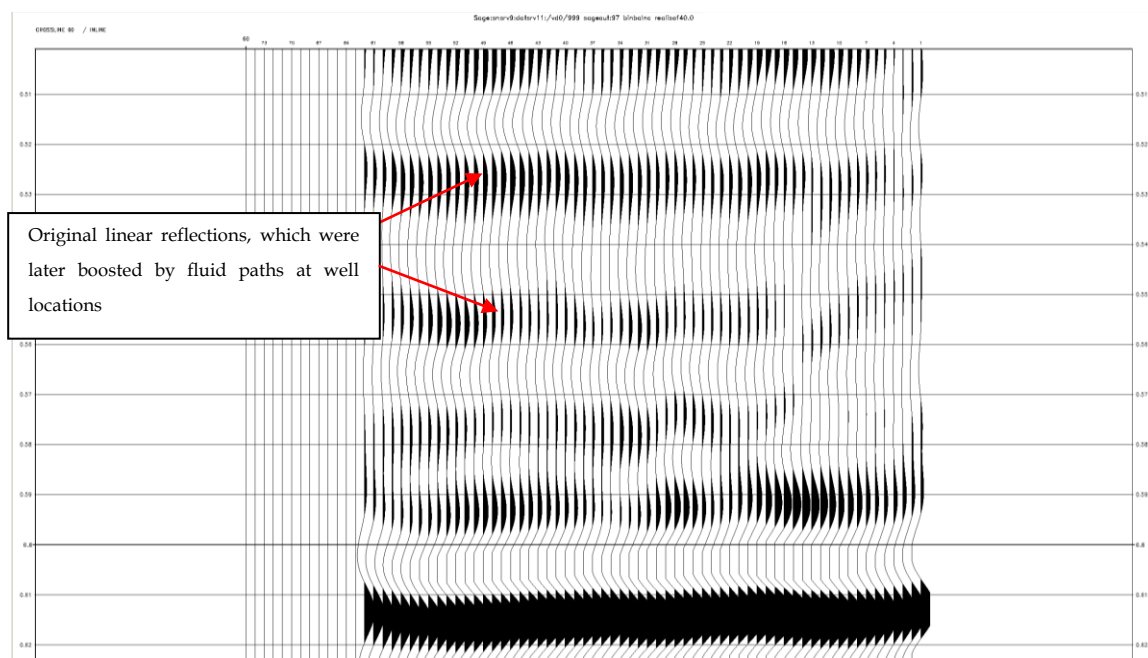


Figure 6. 69 Cross section of Xline 60 at 40hz for the baseline survey (1997)

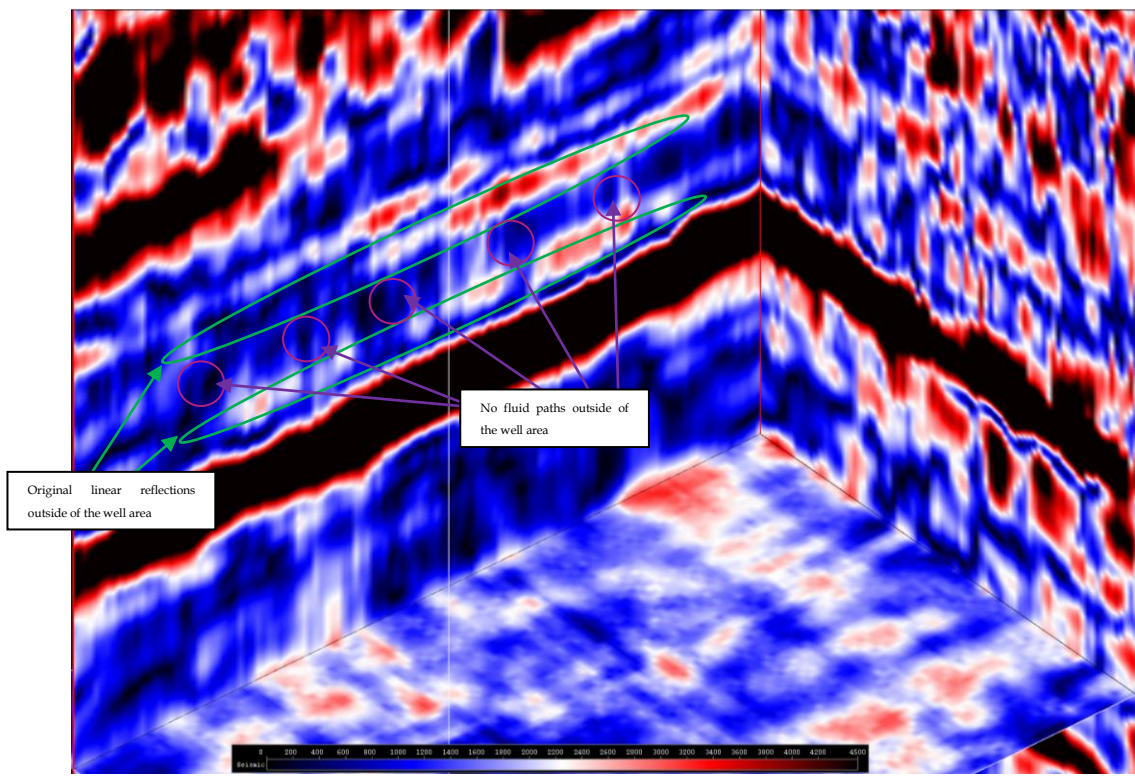


Figure 6. 70 Instantaneous amplitude seismic cross section of Xline 79 at 40hz

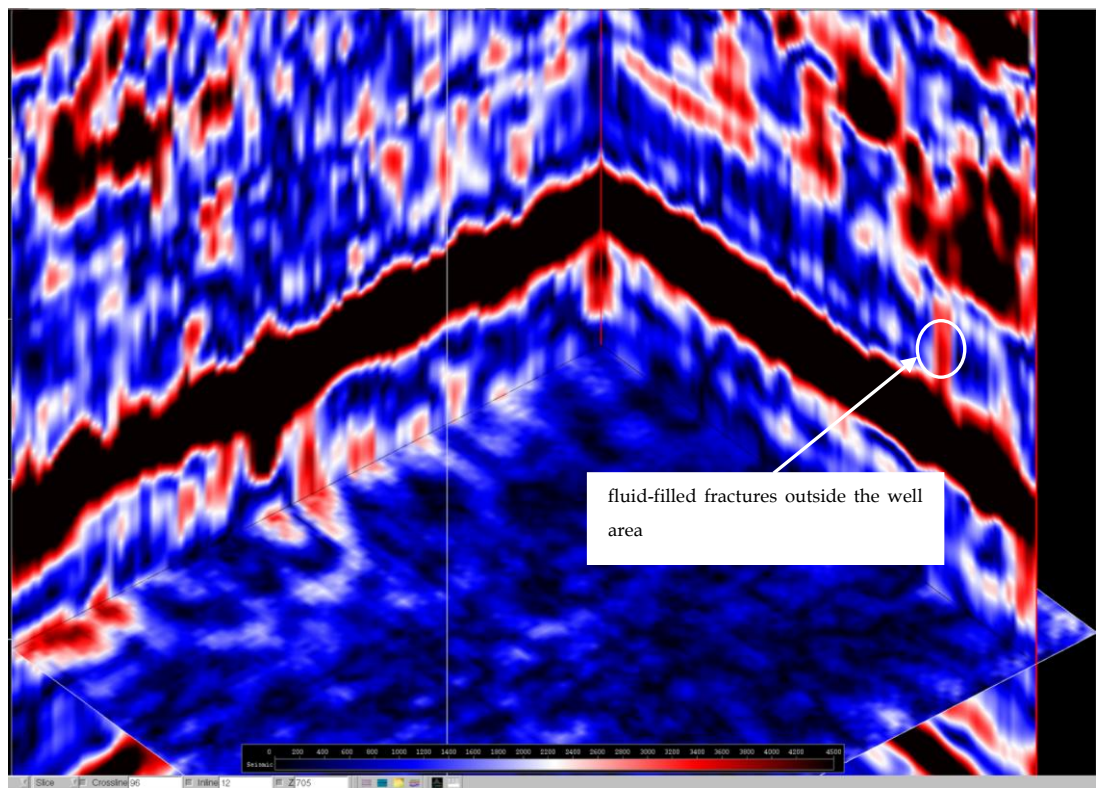


Figure 6. 71 Instantaneous amplitude seismic cross section of Inline 12 at 40hz

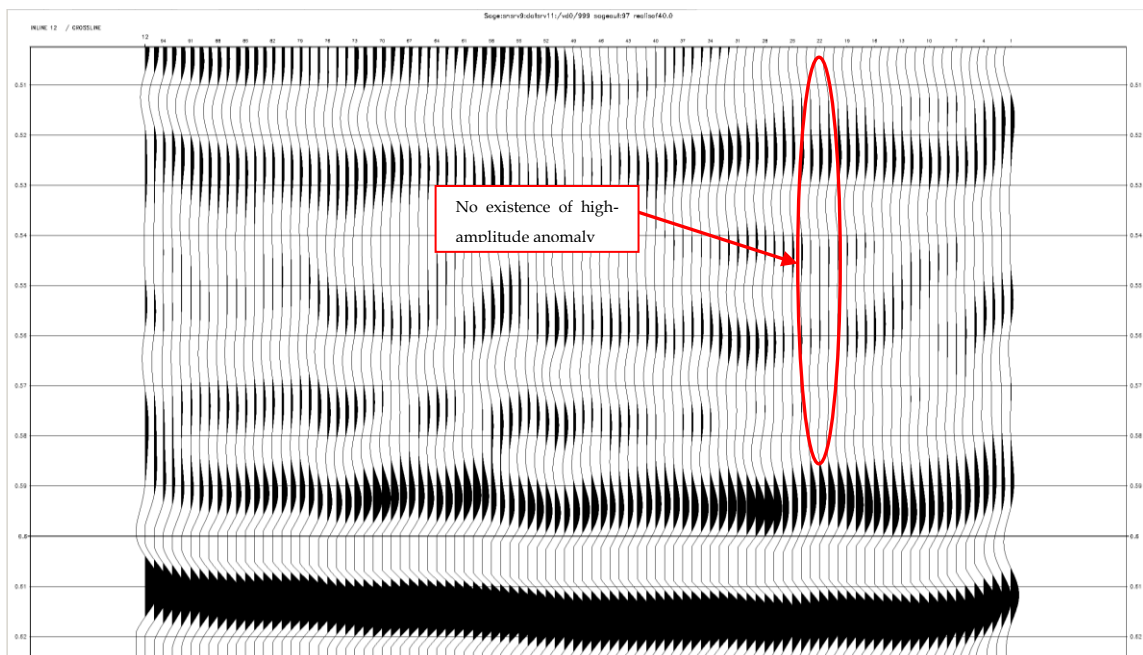


Figure 6.72 Cross section of Inline 12 at 40hz for the baseline survey (1997)

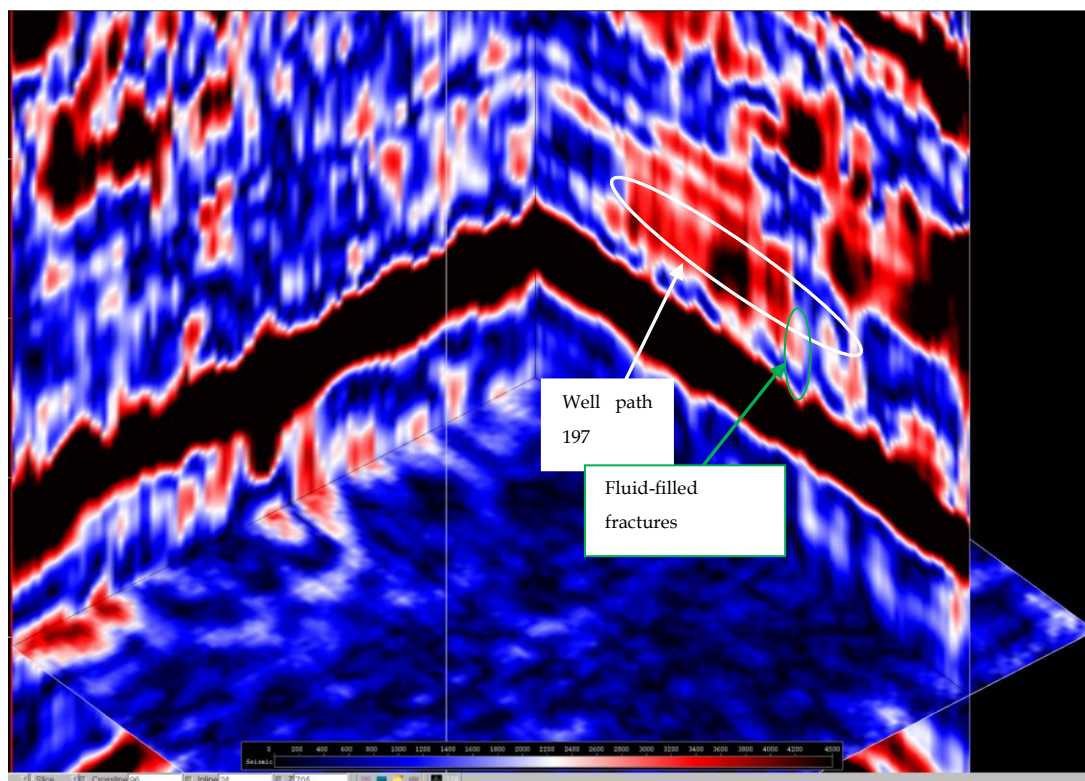


Figure 6.73 Instantaneous amplitude seismic cross section of Inline 24 at 40hz

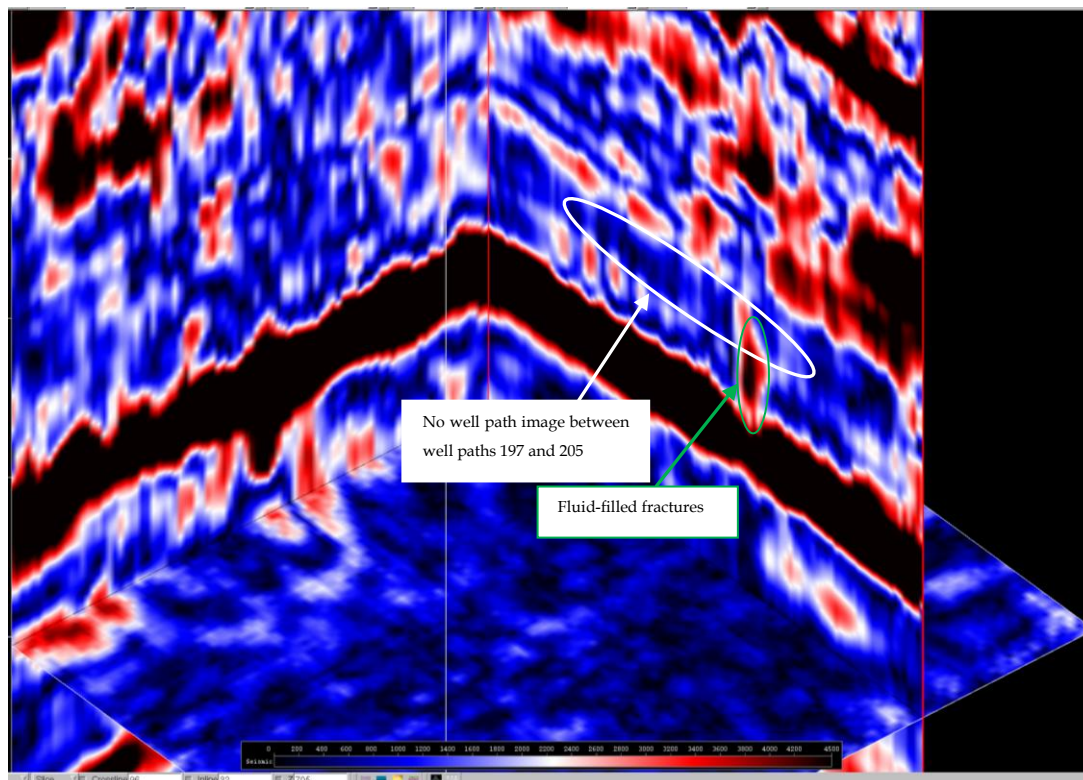


Figure 6. 74 Instantaneous amplitude seismic cross section of Inline 32 at 40hz

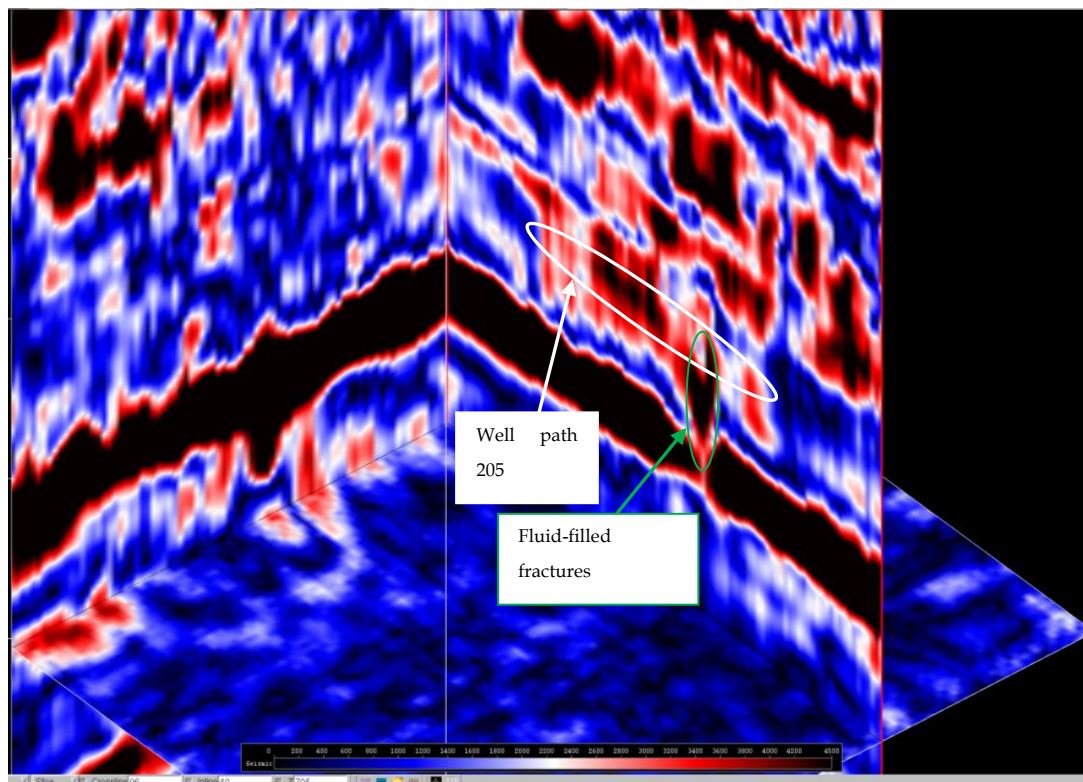


Figure 6. 75 Instantaneous amplitude seismic cross section of Inline 40 at 40hz

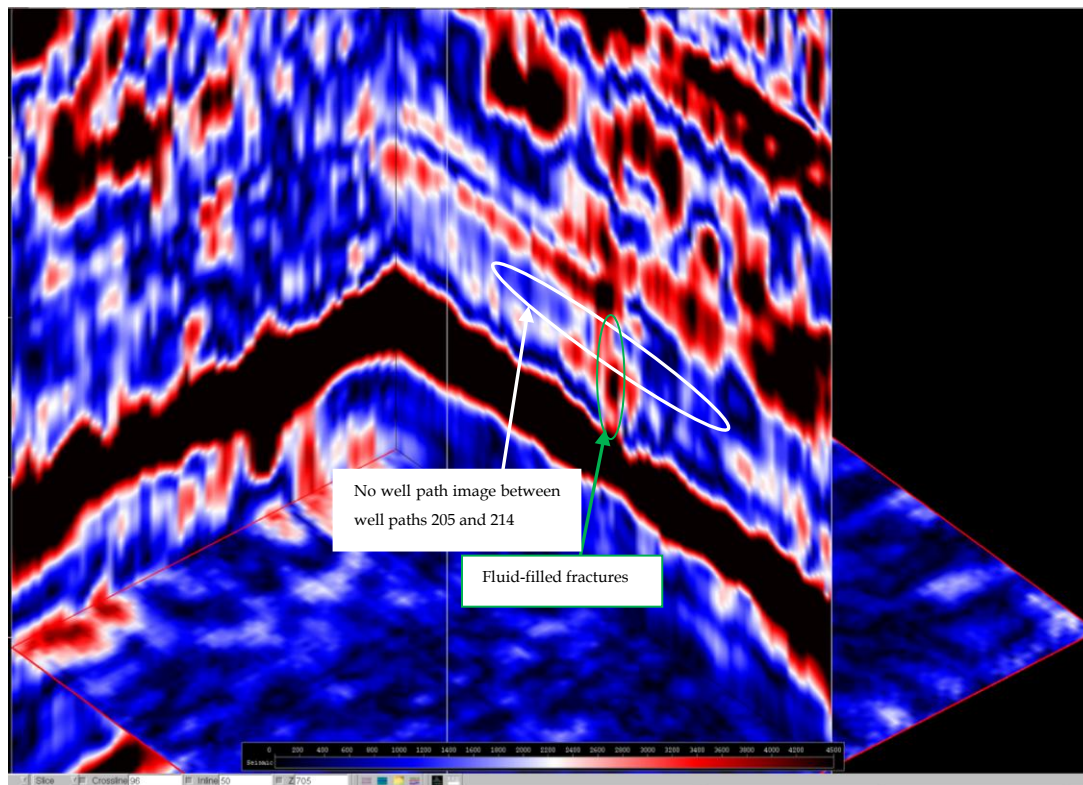


Figure 6.76 Instantaneous amplitude seismic cross section of Inline 50 at 40hz

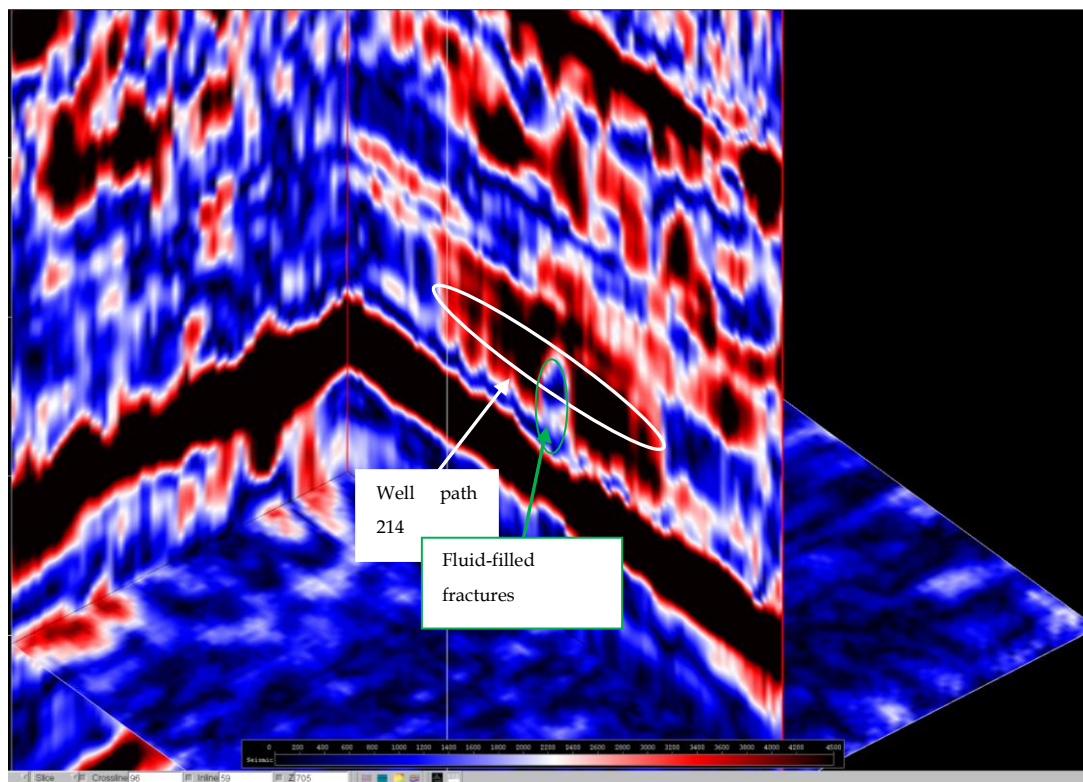


Figure 6.77 Instantaneous amplitude seismic cross section of Inline 59 at 40hz

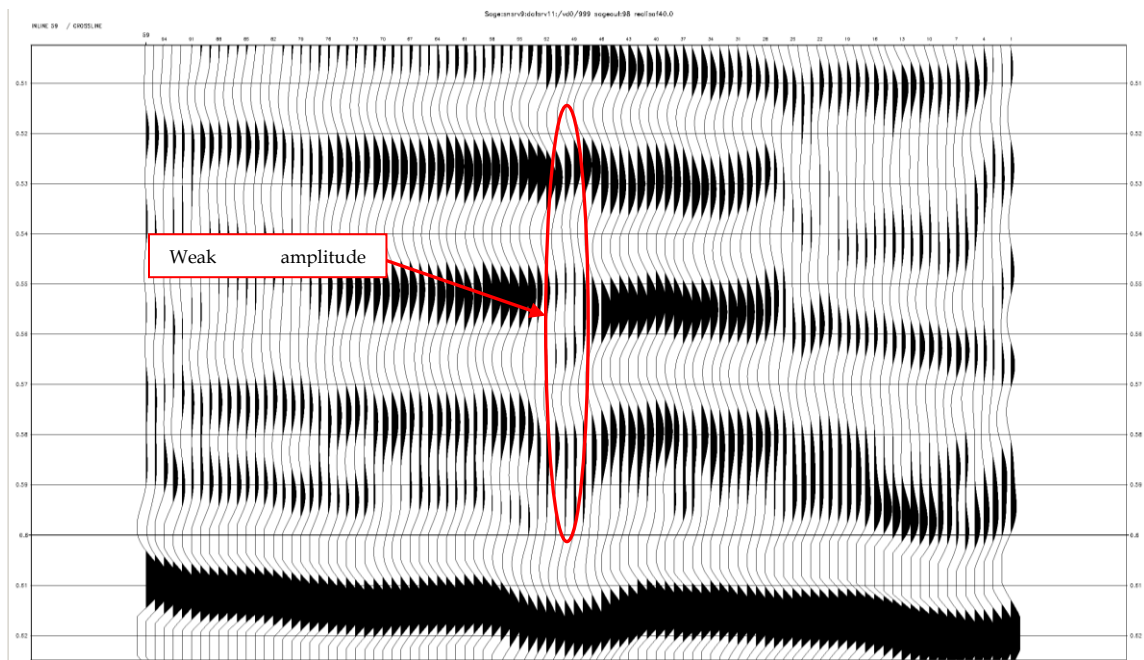


Figure 6. 78 Cross section of Inline 59 at 40hz

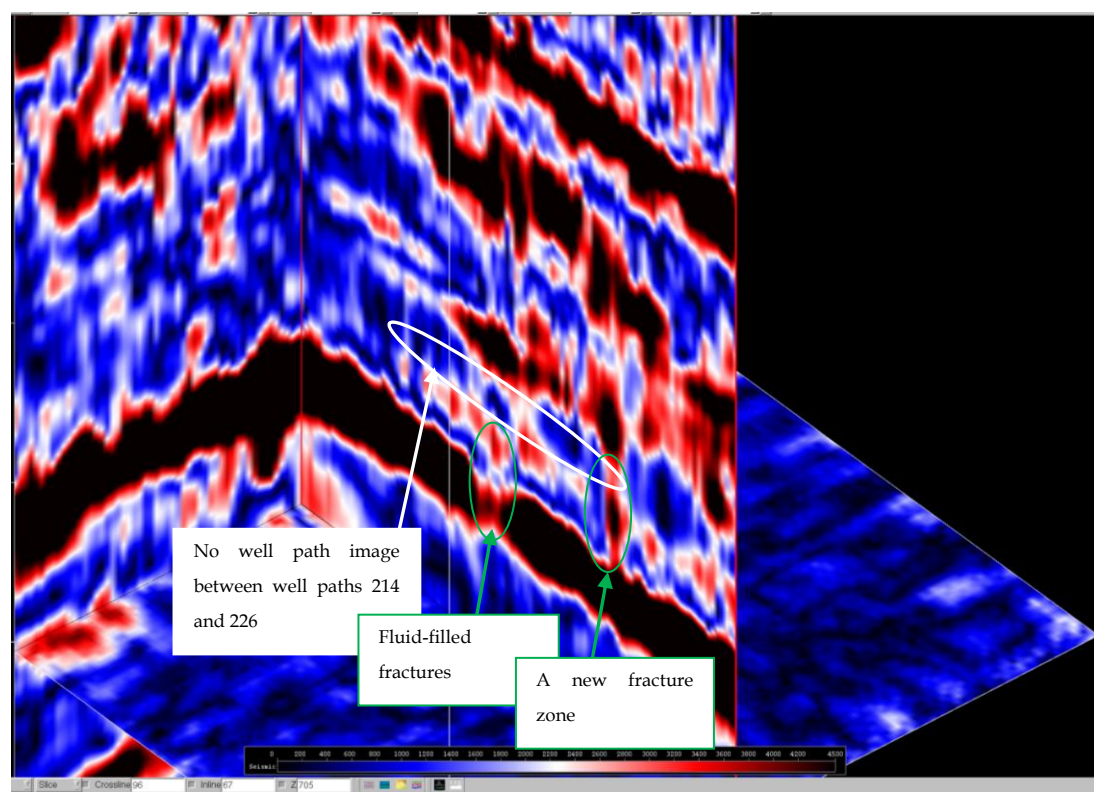


Figure 6. 79 Instantaneous amplitude seismic cross section of Inline 67 at 40hz

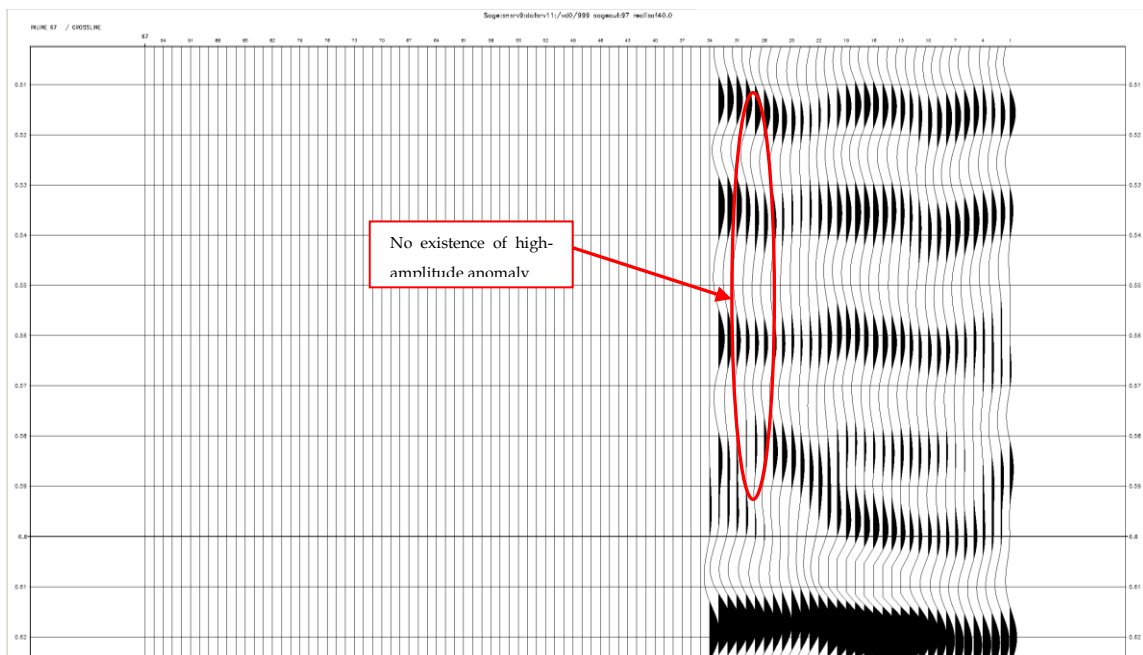


Figure 6. 80 Cross section of Inline 67 at 40hz for the baseline survey (1997)

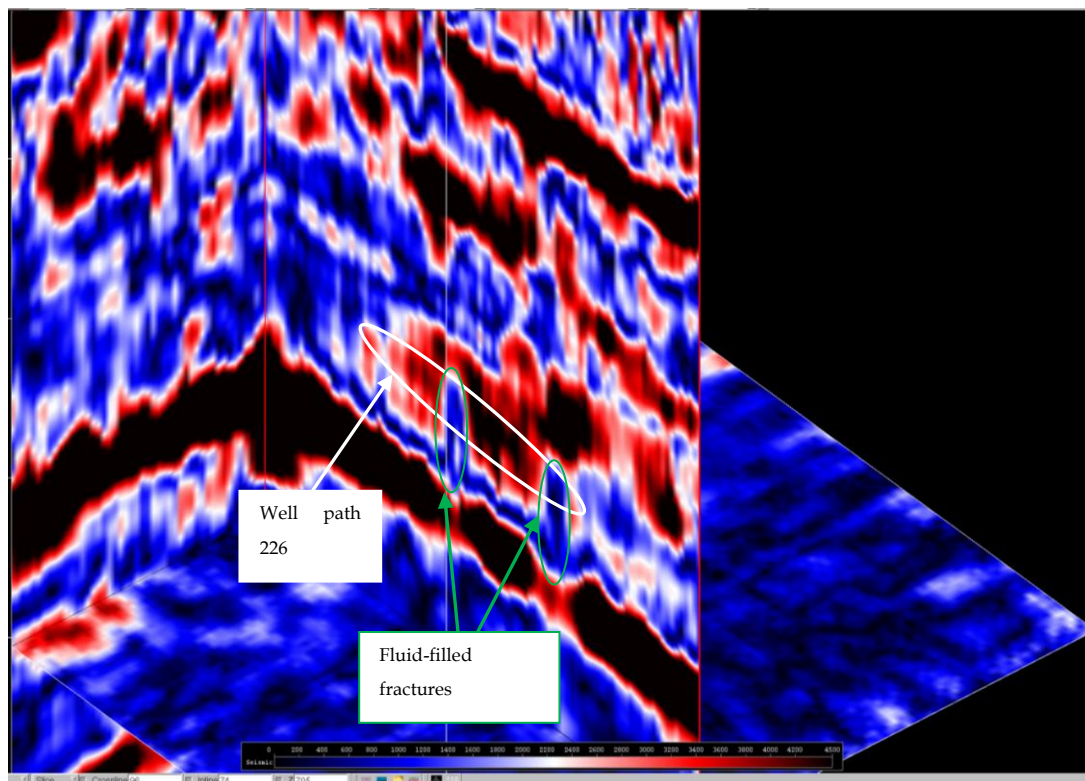


Figure 6. 81 Instantaneous amplitude seismic cross section of Inline 74 at 40hz

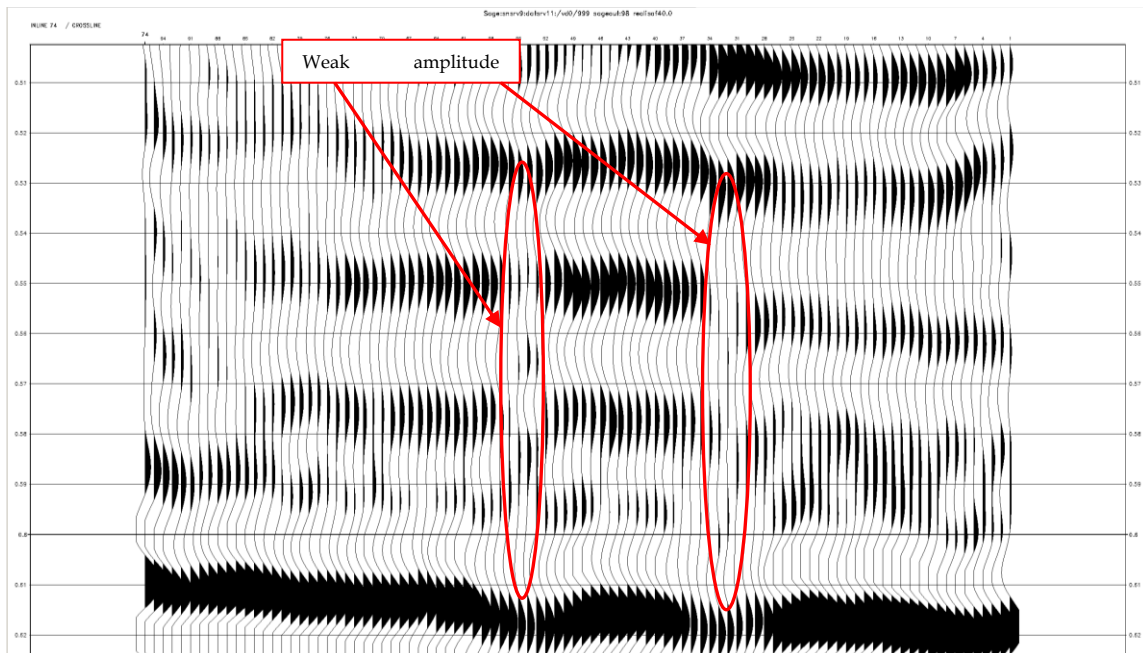


Figure 6. 82 Cross section of Inline 67 at 40hz

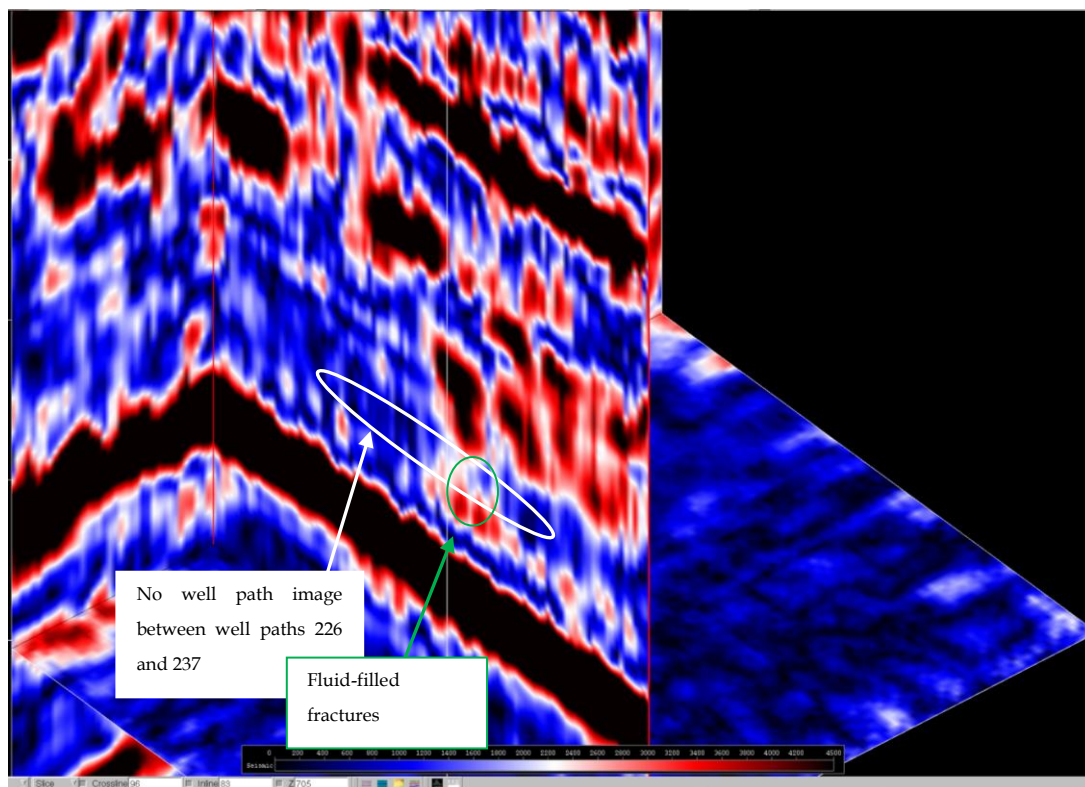


Figure 6. 83 Instantaneous amplitude seismic cross section of Inline 83 at 40hz

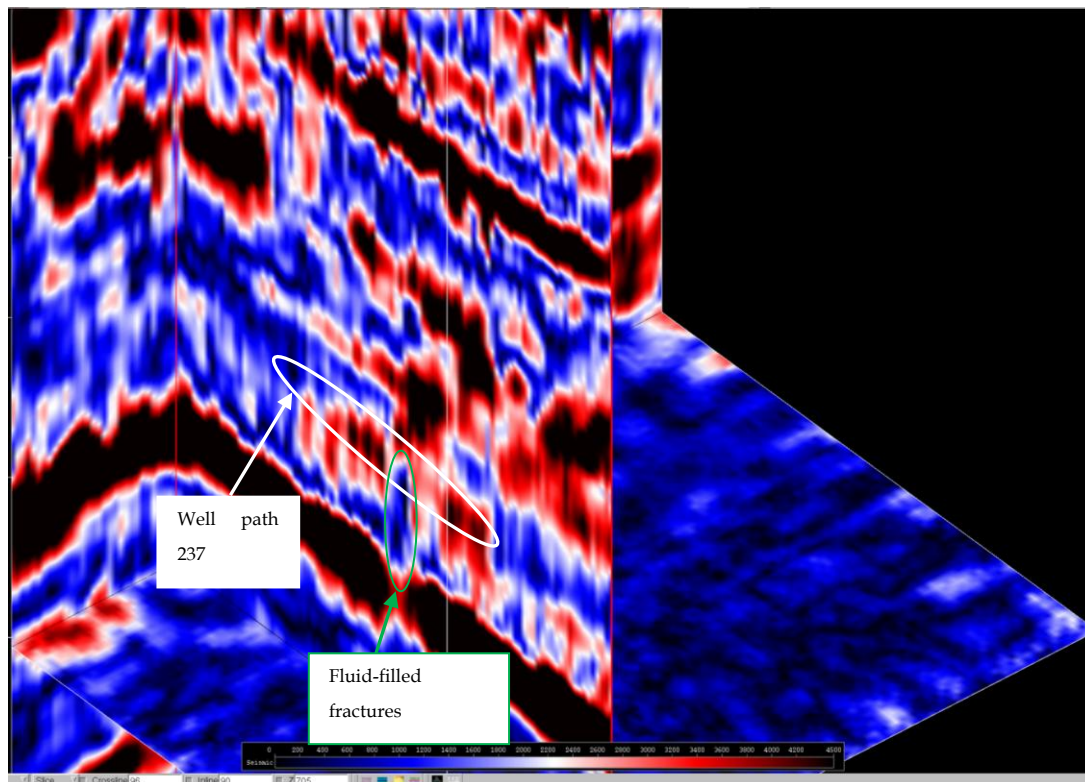


Figure 6. 84 Instantaneous amplitude seismic cross section of Inline 90 at 40hz

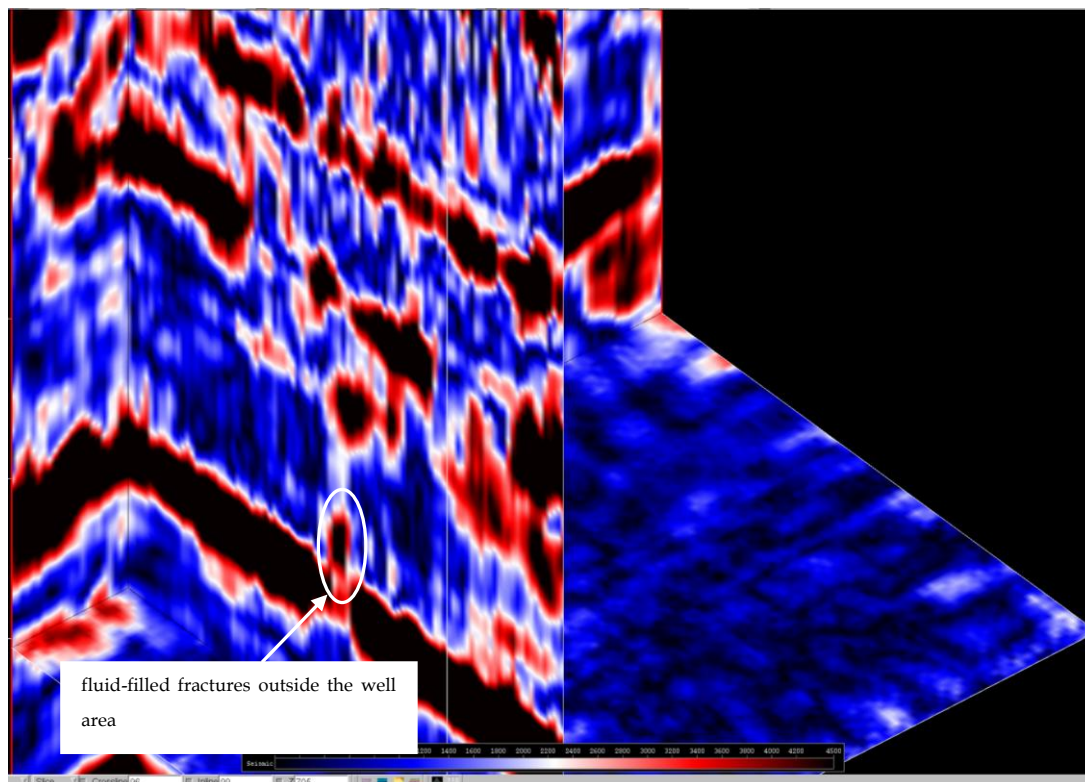


Figure 6. 85 Instantaneous amplitude seismic cross section of Inline 99 at 40hz

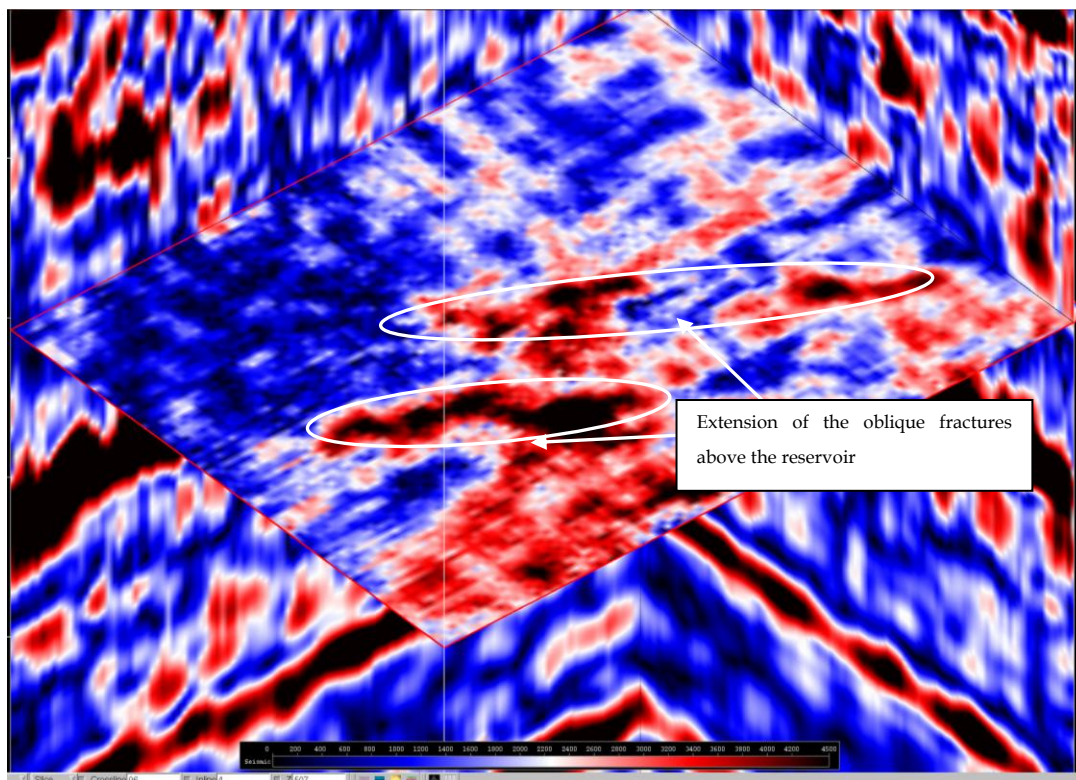


Figure 6. 86 Instantaneous amplitude slice at 507ms cut from the data at 40hz

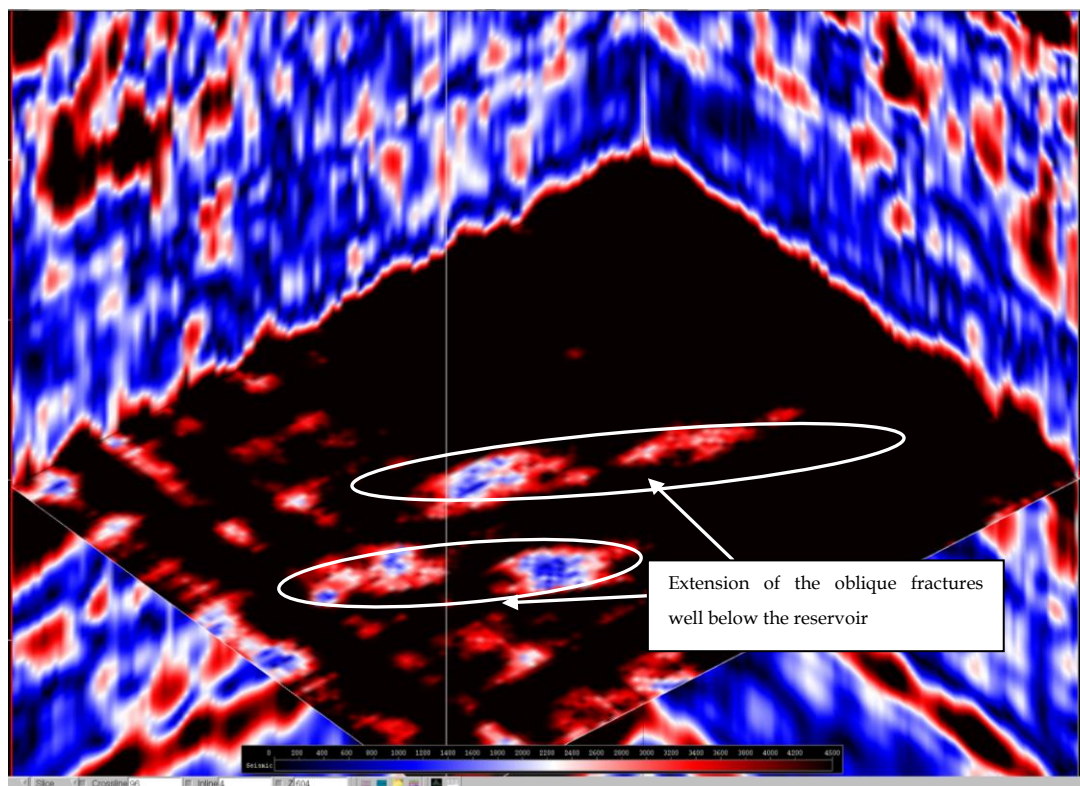


Figure 6. 87 Instantaneous amplitude slice at 604ms cut from the data at 40hz

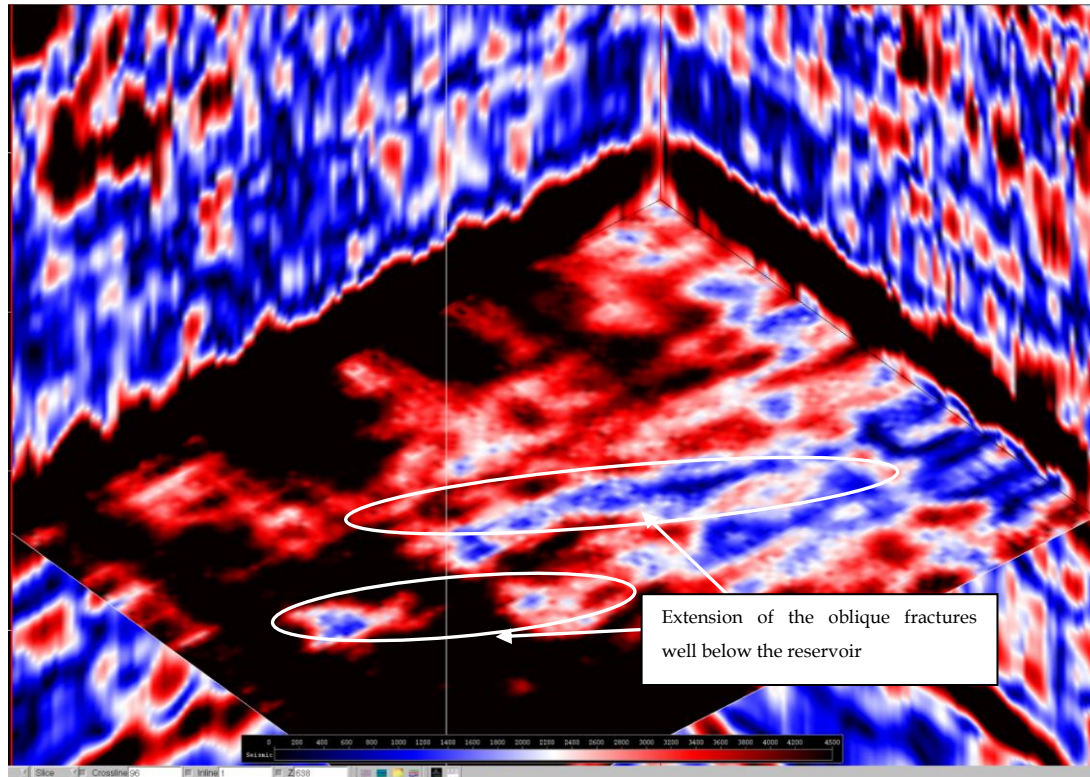


Figure 6. 88 Instantaneous amplitude slice at 638ms cut from the data at 40hz

CHAPTER 7 IMPROVING RESERVOIR SIMULATION WITH TIME-LAPSE SEISMIC DATA

7.1 Introduction

Reservoir simulation has become routine in reservoir development planning and management since it can realize with considerable accuracy quantitative forecasting of reservoir properties both in space and time. Classic reservoir engineering deals with the reservoir on a gross average basis (tank model) and cannot adequately fulfill the task of prediction (Aziz and Settari, 1979). The acquired parameters and numbers from reservoir simulation can also improve our understanding of the recovery process, which can't be easily visualized through thinking and reasoning. Despite the power and elegance, simulation is a risky business and can be a dangerous tool, as evidenced in many cases by faulty or even misleading results calculated with incredible precision (after Carlson, 2003). The severe deviation of reservoir simulation from reality comes mostly from incomplete knowledge of the reservoir, its dynamics under recovery and subsequent fluid flow patterns. Reservoirs are much more heterogeneous and anisotropic than anybody likes to believe and the interaction between injecting fluids and reservoir rocks are so complicated that nobody is able to predict where fluids are really moving despite a good match to production data. We still do not know what is exactly going on between the wells and how fluids migrate within the reservoir. This is the great weakness of reservoir (or any other) simulation and therefore we look for other independent tools to constrain the simulation problem and reduce the uncertainty and non-uniqueness. Among most direct and feasible ones is the time-lapse seismic that has been treated in the last two chapters.

7.2 Mismatch of reservoir simulation and seismic observables

The recovery plan of CSS (cyclic steam stimulation), also known as Huff and Puff, is to pump steam into the reservoir at high rates sufficient to create dynamic formation fracturing in order to heat the formations (injection cycle). After a certain period of shut-in time (soak) or immediately after the injection cycle, the well is put on production (production cycle). Heated viscous heavy oil is more mobile around the well, resulting in increased rates. The process is repeated several times until the production rate is low, beyond which other thermal methods can take over. Although the majority of CSS wells in the past have been vertical, horizontal or inclined wells are now being employed for maximum contact with the reservoir.

For this project, it was hoped that the analysis would show that horizontal hydraulic fractures could be opened at high formation pressure caused by steam injection, and extended far away from the horizontal wells. By this process, better sweep efficiency would be achieved. However, geomechanical modeling in chapter 4 indicates the dominance of vertical fracturing since the minimum principle stress is horizontal, not vertical. The direct seismic observation also suggests that considerable amounts of fluids were driven downward to McMurry formation and even deep into Devonian carbonates along two groups of fractures oblique to the well trajectory. Fluids may also have burst upward into the caprock and beyond. The details can be found in Figures 6.67, 73-77, 79, 81, 84-88 in the last chapter.

It appears that some assumptions for our reservoir simulation are significantly incorrect. The no-flow boundary was violated as the fluids moved upwards and downwards away from the reservoir. The fractures initiated by

hydraulic tension (negative effective stress) did not seem to play as much of a role in network connection as thought previously. The direction of oblique fractures as the main passages for fluid migration implies that shear failure had happened before any tensile fractures developed and the shear fractures may have prevailed in the entire process of recovery. This is an outstanding example of how we would have insufficient data for reservoir simulation without time-lapse seismic investigation.

7.3 Design of new reservoir parameters

Two groups of oblique fractures of high permeability had most likely been generated by shearing due to the decrease of effective stress in the first stage of steam injection. Shin et al. (2008) found that shear failure in uncemented sediments is often formed under burial due to reduced lateral stress, which is caused by volume contraction. The conceptual diagram of shear failure in oil sands due to steam injection is illustrated in Figure 7.1.

The current code of reservoir simulation (GeoSim) is not capable of incorporating shear failure and resultant permeability enhancements in the modelling dynamically in space and time. If the location of shear planes is known beforehand, it is possible to use "joint" elements, which can be linked to improving permeability, but this requires complex grid construction that would have grid planes along the failure planes. The only practical way we can represent shear fractures is to assume the zones of high permeability along the fractures as the initial condition, which we believe would not distort or mislead the simulation results because fracturing took place at the very early stage of injection. As indicated in Figure 7.2, the two groups of high permeability

fractures are superimposed on the original distribution. They are also assumed to cut the five horizontal wellbore vertically from the top to the bottom of the reservoir, forming a network of fluid flow.

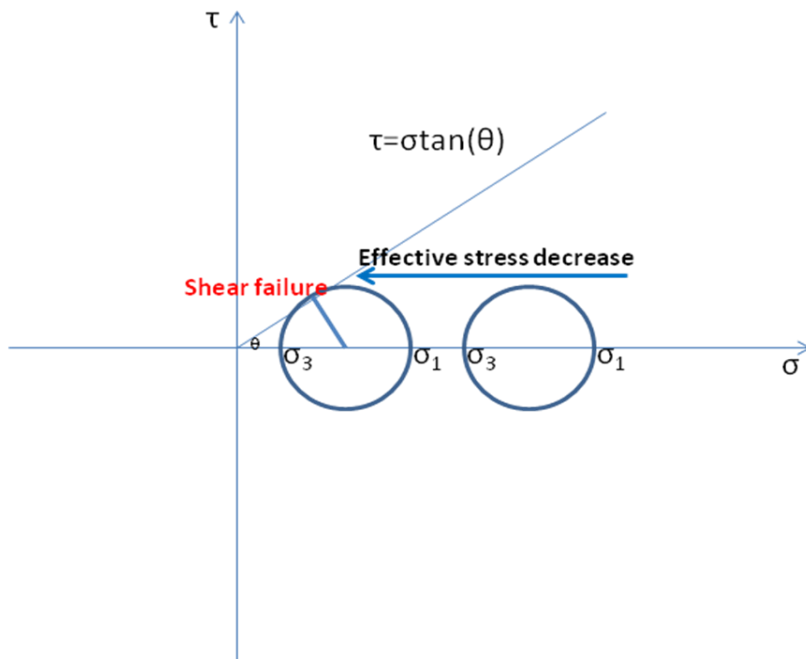


Figure 7. 1 Conceptual diagram of shear failure in oil sands

The leakage of fluids into overlying/underlying formations is a most challenging problem in this study. It can be assumed that the major leak points downwards are located in a few places below the reservoir, as in Figure 7.3. They are evidenced by the breakings of the strong and continuous reflection events between the underlying McMurray clastic sediments and Devonian carbonates. The upward break-through to the caprock is not completely ascertained and is omitted in the modelling. The amount of leaked fluids is a parameter we need to adjust in order for simulation results to match approximately the history data.

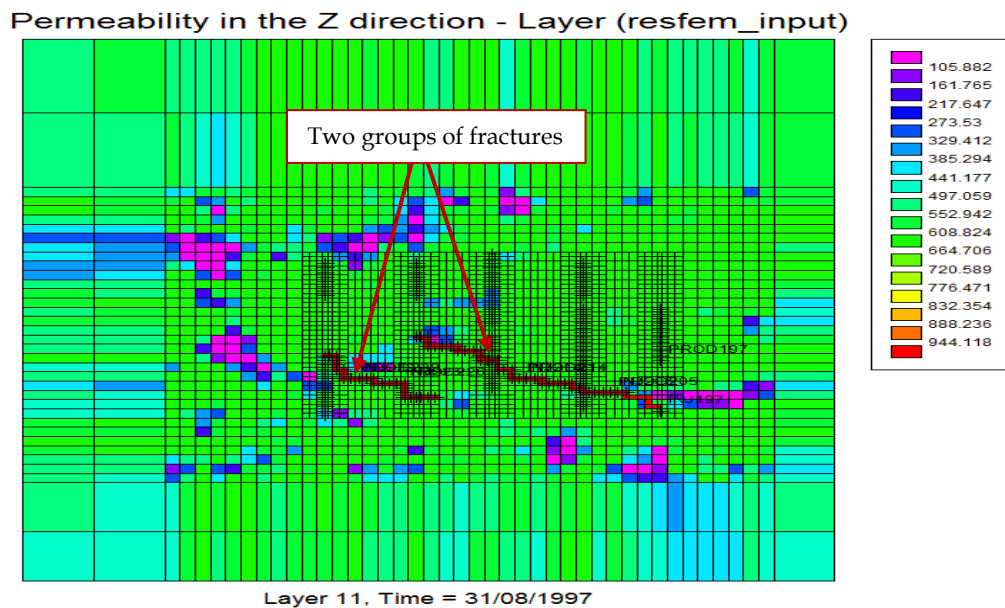


Figure 7.2 Two groups of fractures of high permeability

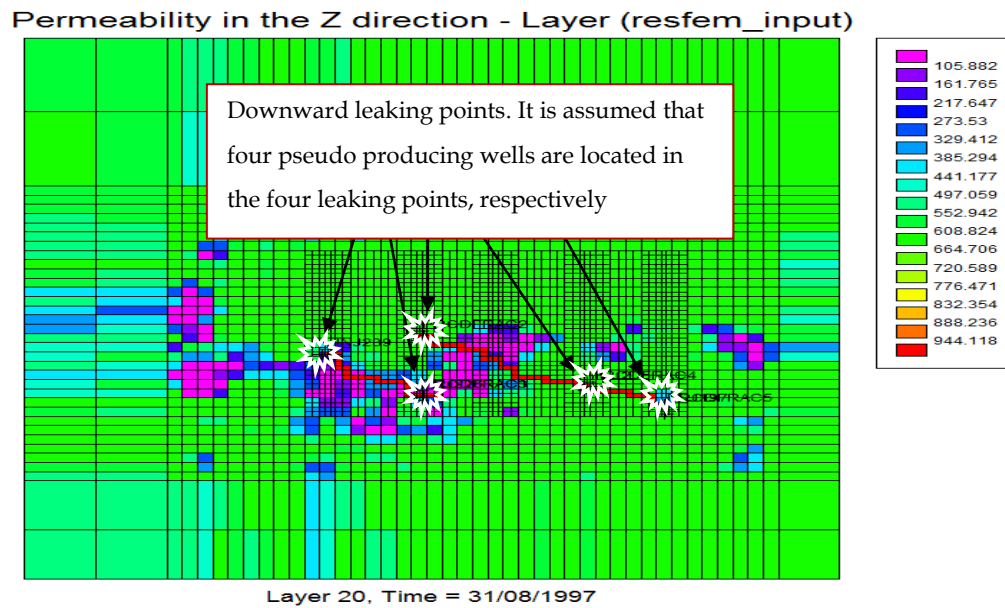


Figure 7.3 Bottom of the reservoir showing downward leaking points

In this case, we created the pseudo-wells at these points in the bottom of the reservoir, which would produce fluids the same way as under normal conditions.

7.4 Match of fluid pressure and production data

Improving reservoir simulation in our case is to adjust the reservoir parameters, which were generation of two groups of oblique fractures, and other uncertainties, which were the fluid production at leaking points, for a better match of the results to available production data, which were the pressure and water production. In the following, we will discuss how well the improved simulation results fit the pressure and water production.

The accurate pressure measurements haven't been released to this study due to confidentiality issues, but they can be inferred from the timing of the first monitoring survey, at which the reservoir pressure should be around the bubble point to have gas ex-solved from heavy oil for better time-lapse seismic imaging. As shown in Figure 7.14, the pressures have decreased to a reasonable range of 2-3 MPa along the wellbores, and have further lowered along two groups of fractures. The pressures are higher in the surrounding areas, which enables the reservoir to maintain the continuing production. Gas has been out of heavy oil and resided chiefly in these fractures in Figure 7.15. The outline of Figures 7.14 and 7.15 presents a network pattern of fluid flow in the reservoir. This is similar to that interpreted from time-lapse seismic dealt with in Chapters 5 and 6.

The water production data for the five horizontal wells can be compared with the corresponding simulation results. The comparison can infer the degree of enhancement.

It seems from Figures 7.4, 6, 8, 10 and 12 that oil cumulative production matches very well between the field data and the simulation output (the misfit of the end point in Figures 7.4 and 7.6 is due to data input errors). This is because the latter is input to simulation, not necessarily meaning that the match has no problem. The match of water cumulative production, an indication of real match performs well for wells 205 and 239 (Figures 7.7 and 7.13), but there exist considerable differences for the rest (Figures 7.5, 9 and 11). The misfits are likely caused by the injected steam that escaped upwards and/or downwards in larger quantities than specified by simulation. Another possible explanation is the hysteresis of water relative permeability that is well known to exist in oil sands recovery.

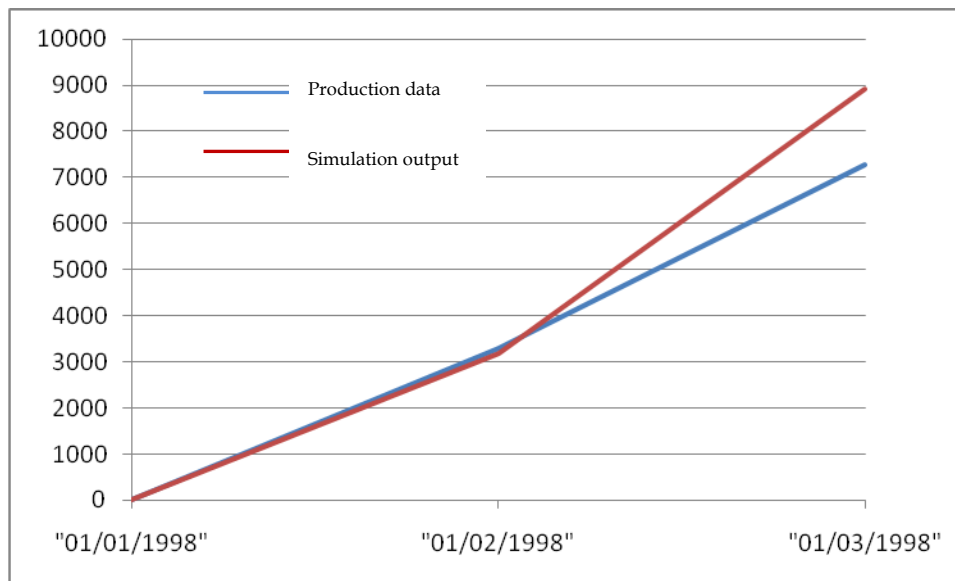


Figure 7. 4 Match of cumulative oil production for well 197 (unit: m³)

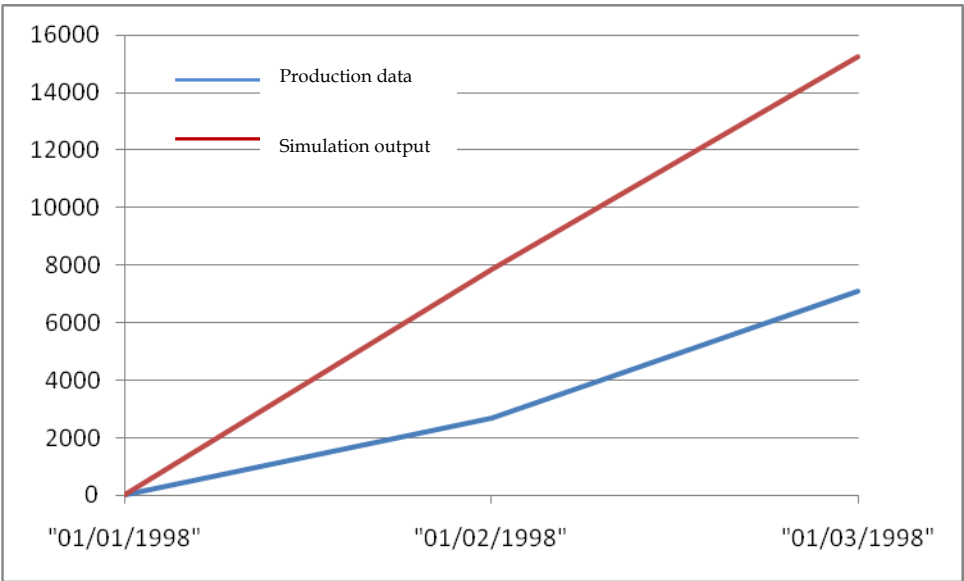


Figure 7. 5 Match of cumulative water production for well 197 (unit: m³)

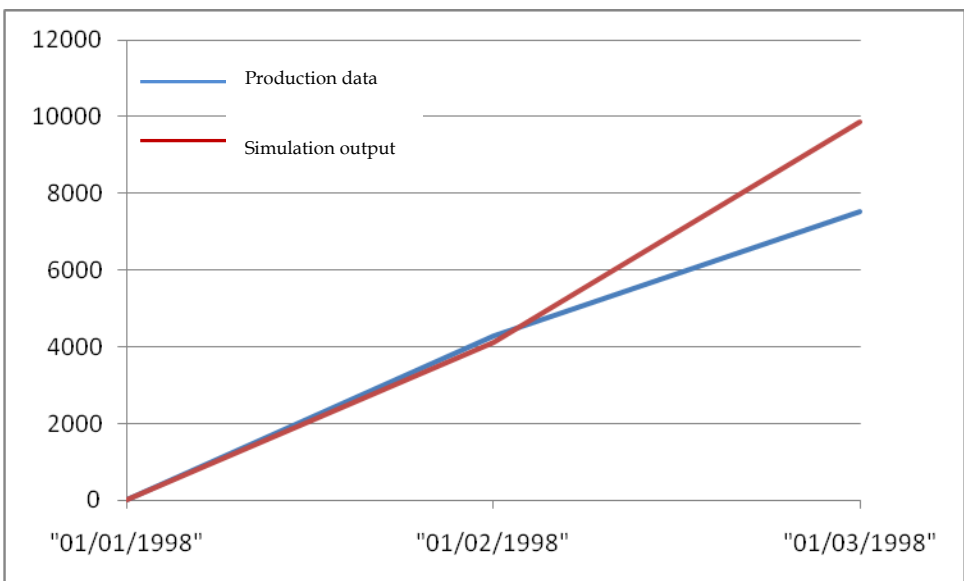


Figure 7. 6 Match of cumulative oil production for well 205 (unit: m³)

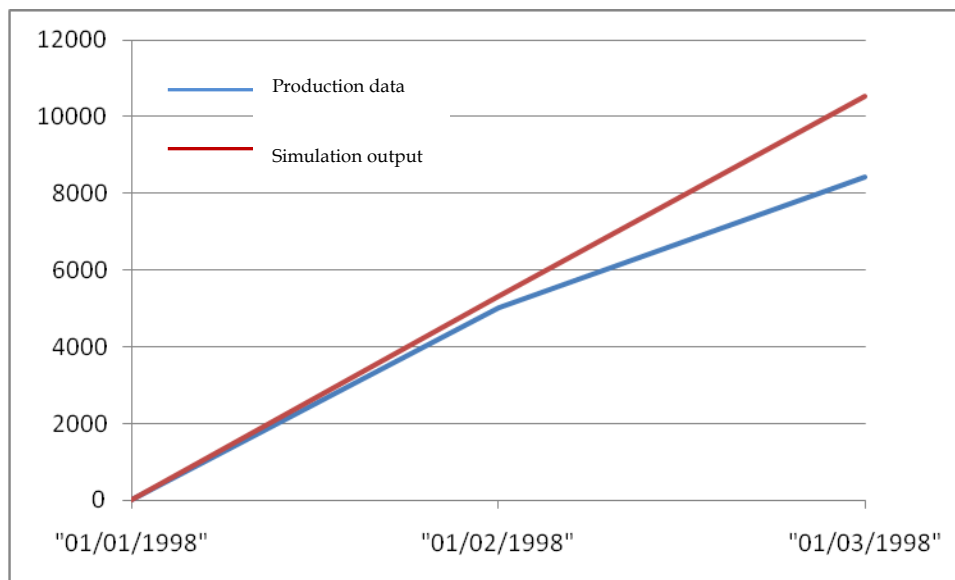


Figure 7.7 Match of cumulative water production for well 205 (unit: m³)

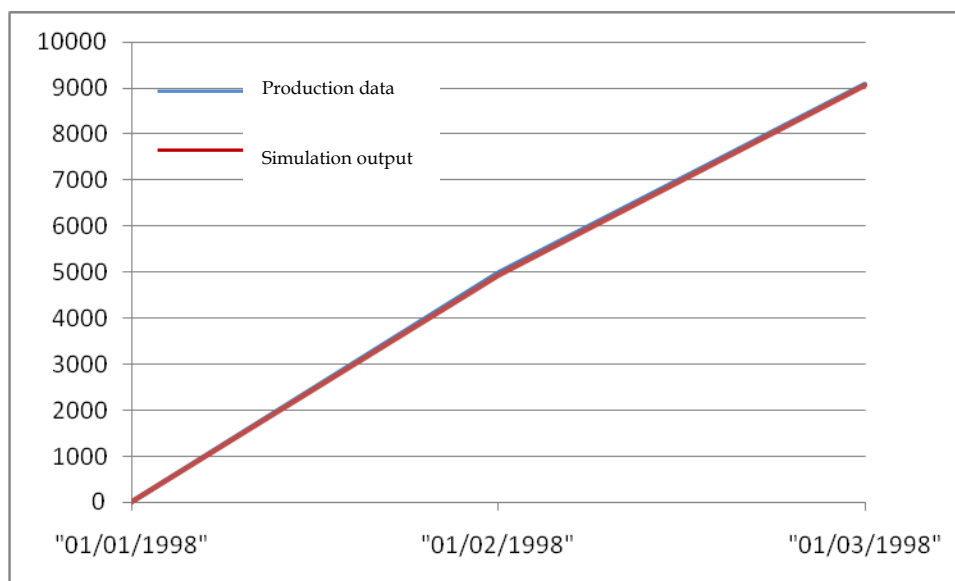


Figure 7.8 Match of cumulative oil production for well 214 (unit: m³)

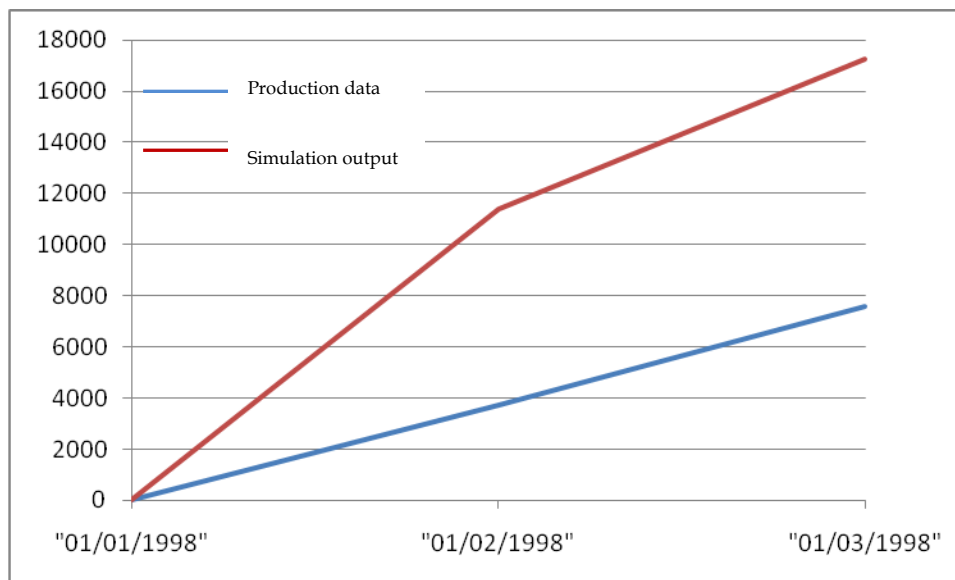


Figure 7. 9 Match of cumulative water production for well 214 (unit: m³)

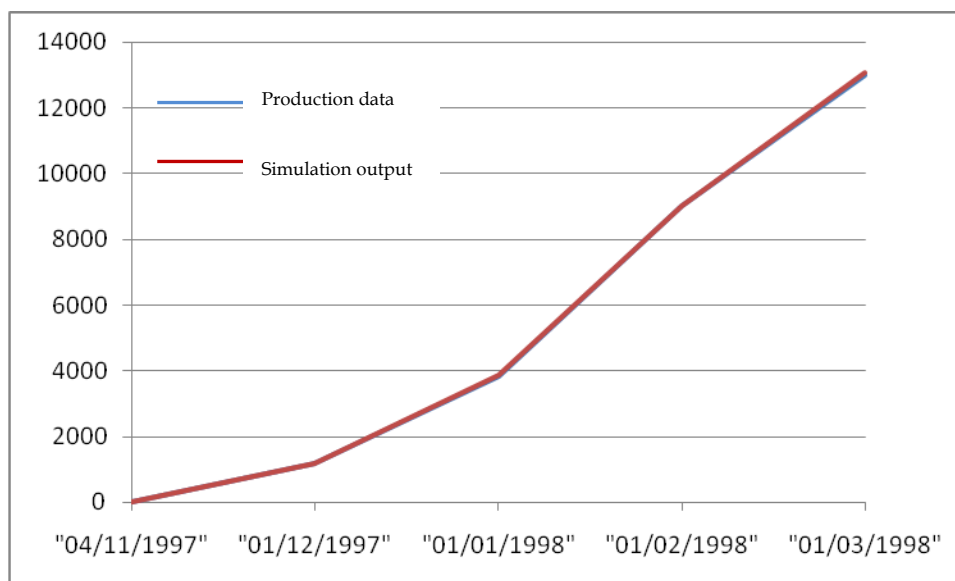


Figure 7. 10 Match of cumulative oil production for well 226 (unit: m³)

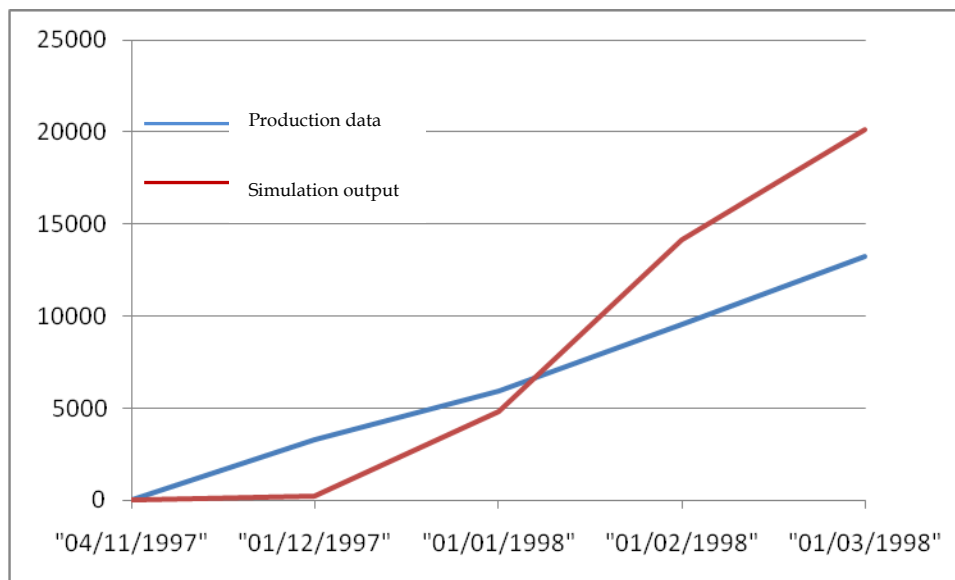


Figure 7.11 Match of cumulative water production for well 226 (unit: m³)

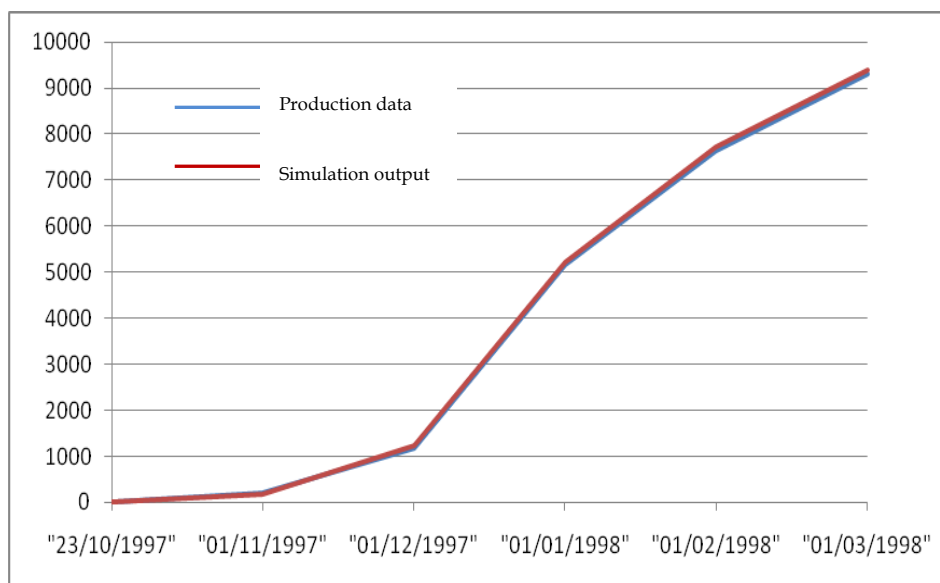


Figure 7.12 Match of cumulative oil production for well 239 (unit: m³)

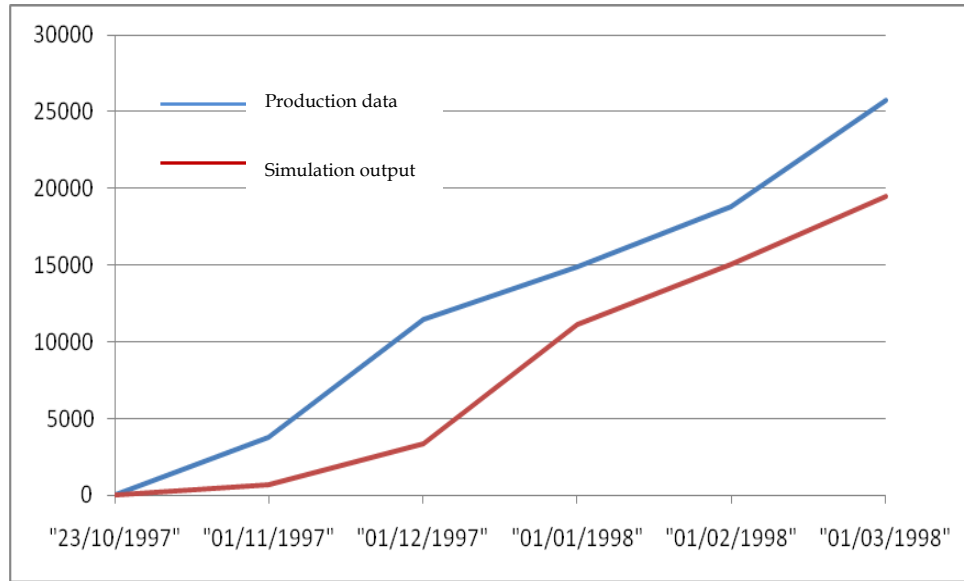


Figure 7.13 Match of cumulative water production for well 239 (unit: m³)

7.5 Results of updated reservoir simulation

As discussed repeatedly, we believe that the injected steam engendered two groups of shear fractures and then was driven downwards to the underlying formations at some locations below the wells. The fluid patterns of the early stage when three wells were injected are simulated and displayed from Figures 7.16-33, which are different than in Figures 4.8-22. It can be observed that there are oil banks around strongly altered zones along the well bores and in fractures on oil saturation sections. This is very important information for selecting infill drilling locations. The front of high fluid pressure always extends far beyond the front of saturations since the disturbance of stress field always propagates much faster and much more widely than material exchanges. The front of temperature anomalies consists with the front of saturations, which indicates that heat transfer is dominated by convection through fluid replacement.

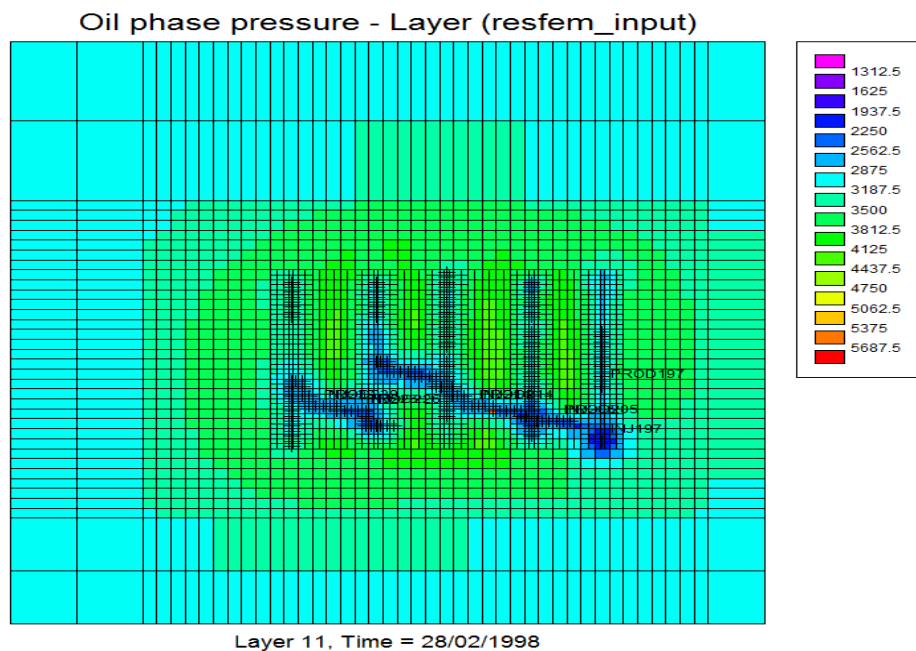


Figure 7. 14 Map of reservoir pressure (KPa) at the end of Feb. 1998

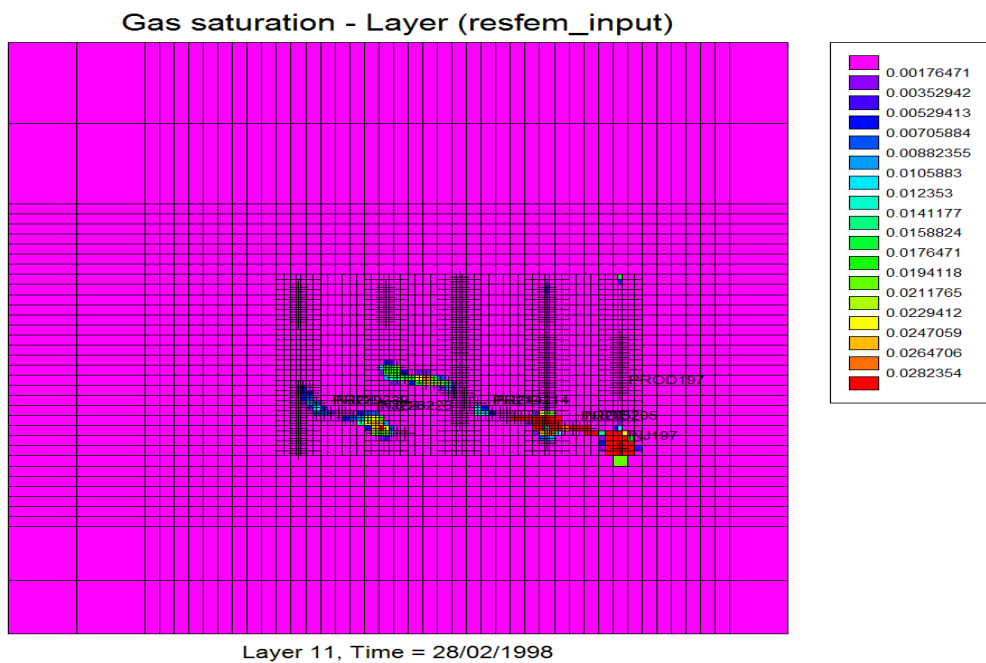


Figure 7. 15 Map of reservoir pressure (KPa) at the end of Feb. 1998

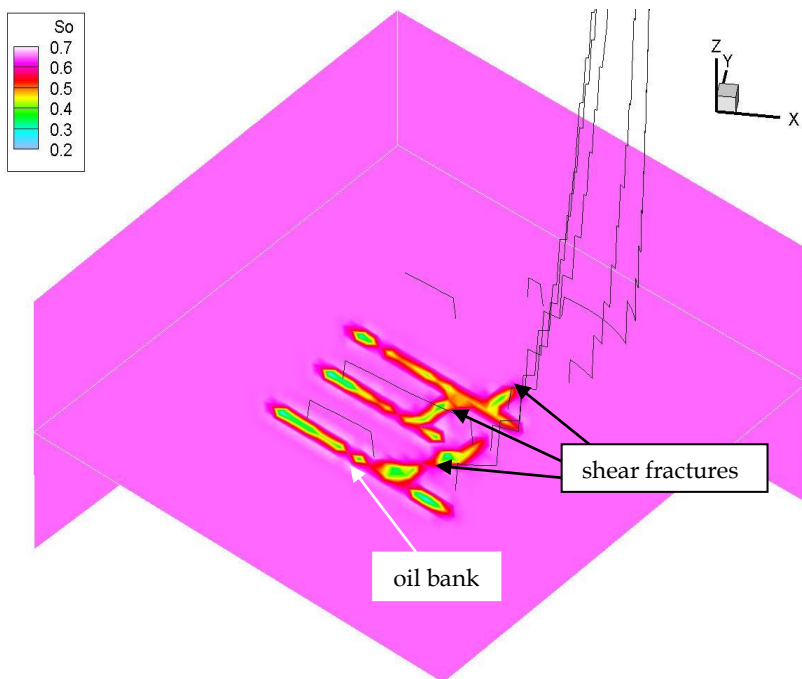


Figure 7. 16 Oil saturation on K-plane on Oct 16, 1997

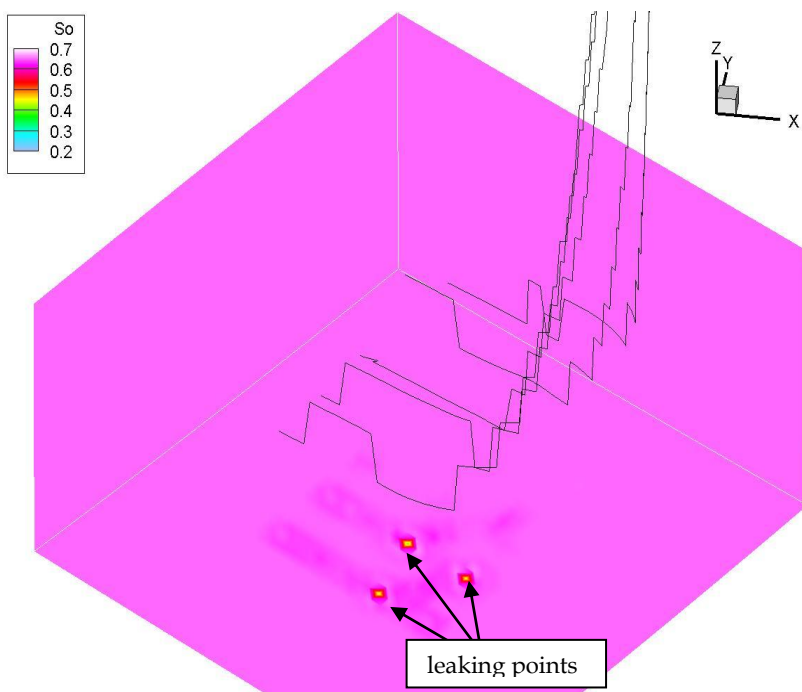


Figure 7. 17 Oil saturation on reservoir bottom on Oct 16, 1997

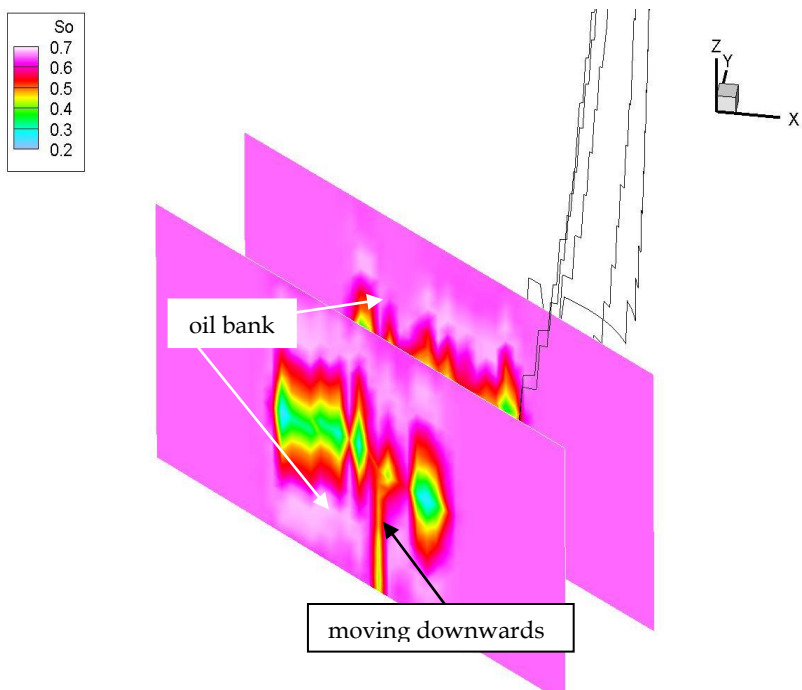


Figure 7.18 Oil saturation on I-plane on Oct 16, 1997

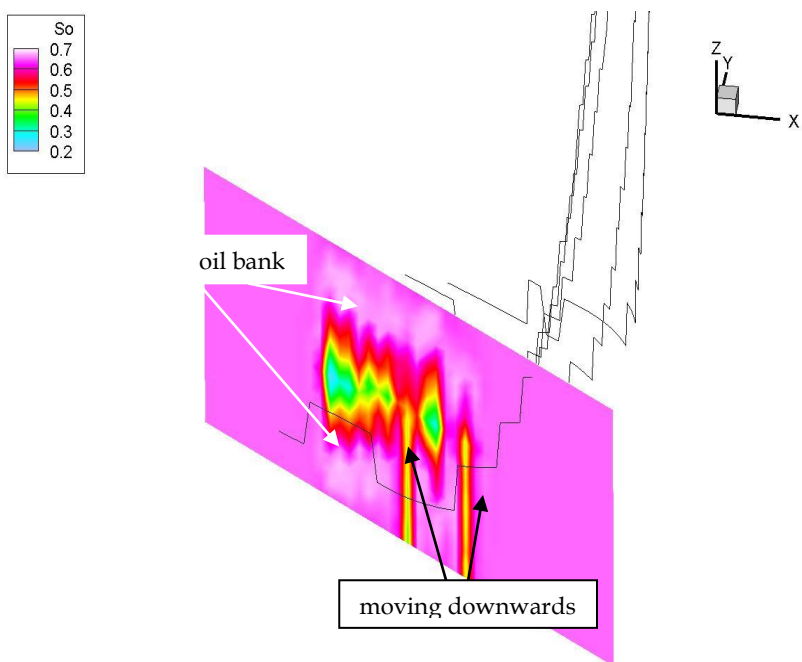


Figure 7.19 Oil saturation on I-plane on Oct 16, 1997

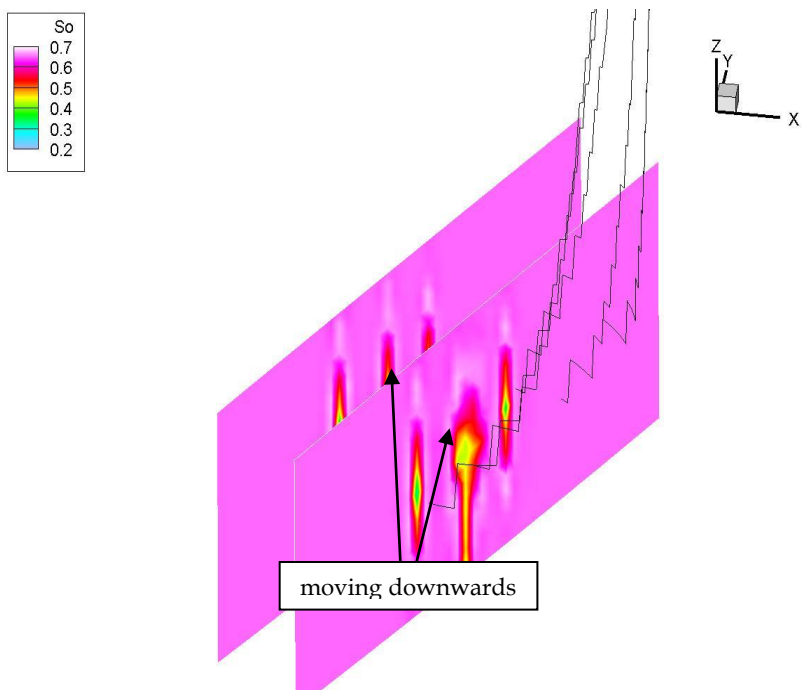


Figure 7. 20 Oil saturation on J-plane on Oct 16, 1997

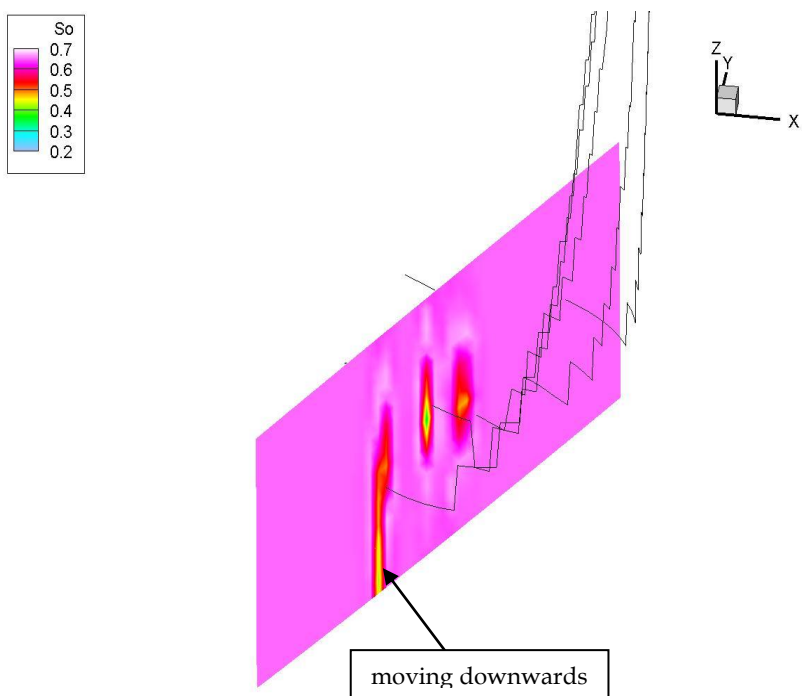


Figure 7. 21 Oil saturation on J-plane on Oct 16, 1997

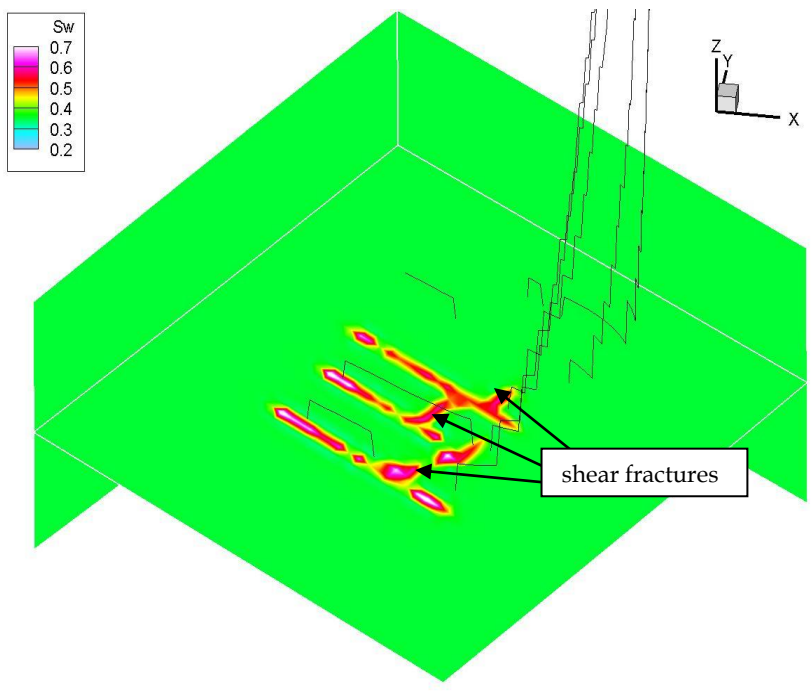


Figure 7. 22 Water saturation on K-plane on Oct 16, 1997

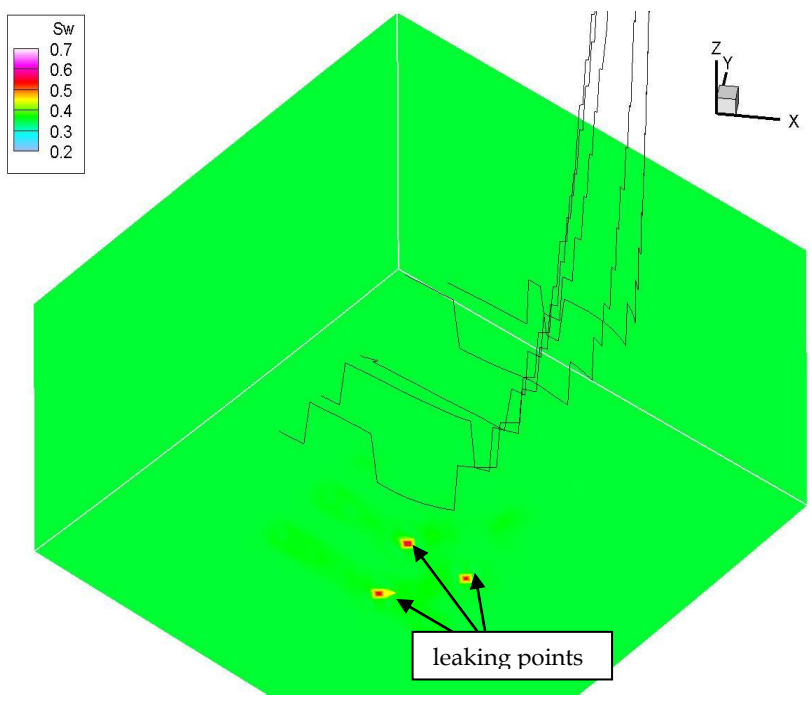


Figure 7. 23 Water saturation on reservoir bottom on Oct 16, 1997

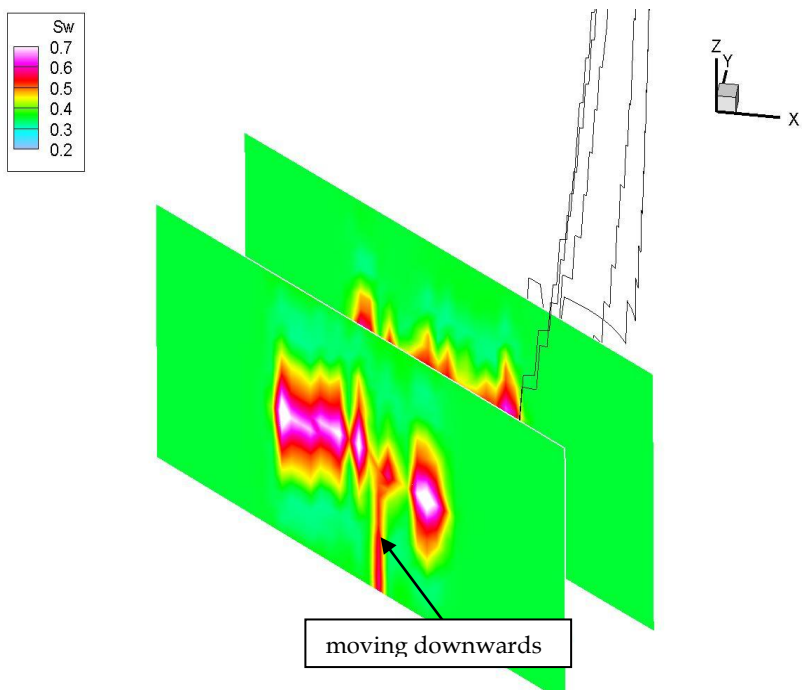


Figure 7. 24 Water saturation on I-plane on Oct 16, 1997

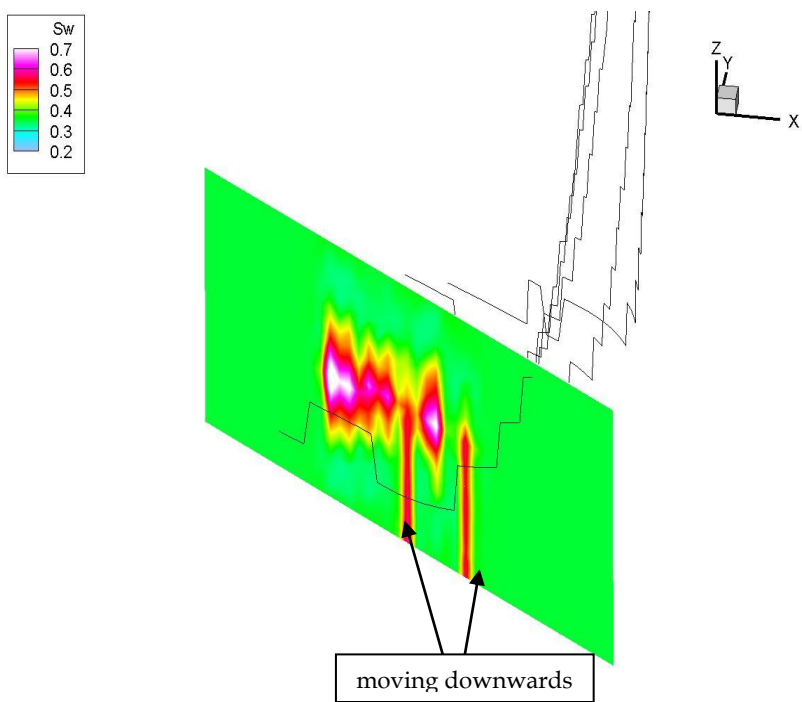


Figure 7. 25 Water saturation on I-plane on Oct 16, 1997

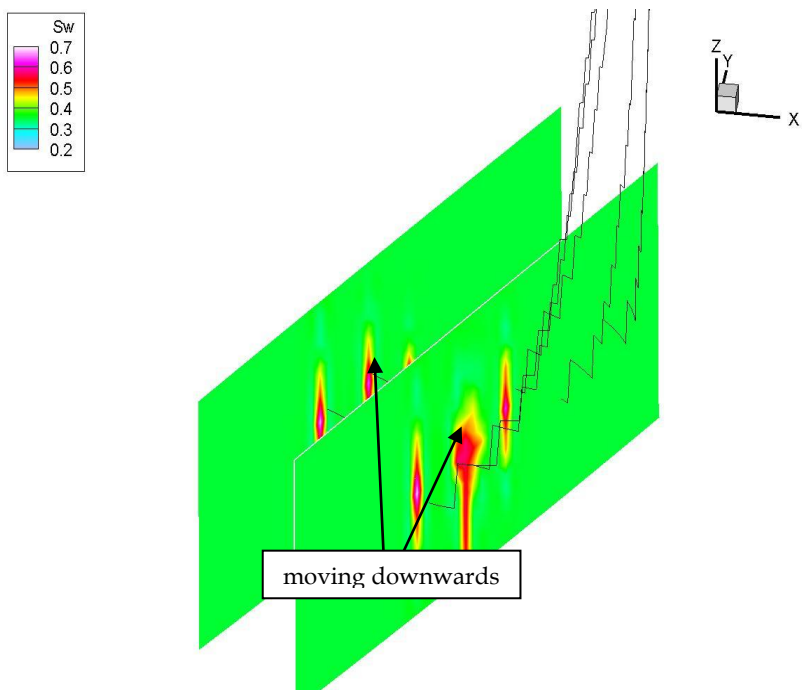


Figure 7. 26 Water saturation on J-plane on Oct 16, 1997

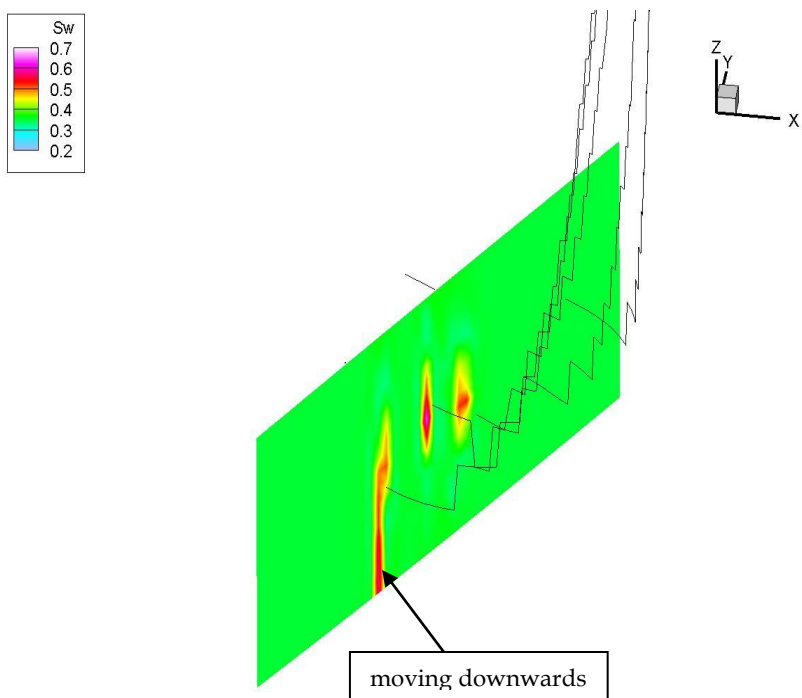


Figure 7. 27 Water saturation on J-plane on Oct 16, 1997

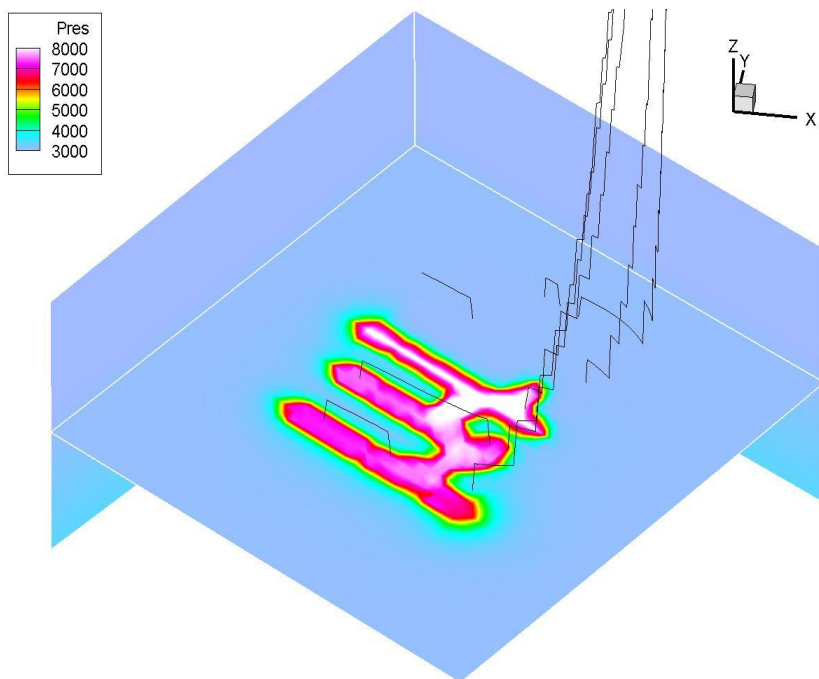


Figure 7. 28 Fluid pressure on K-plane on Oct 16, 1997 (unit: KPa)

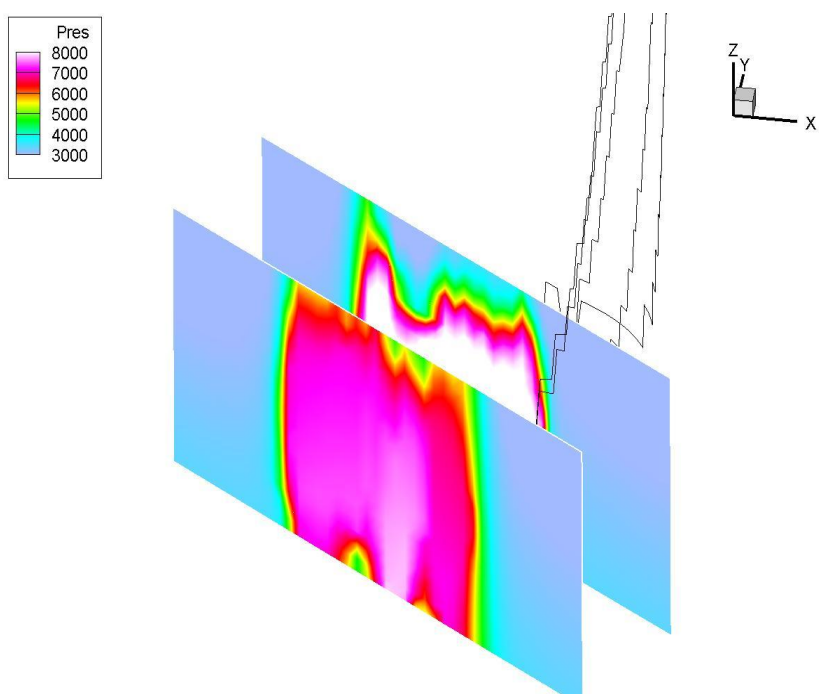


Figure 7. 29 Fluid pressure on I-plane on Oct 16, 1997 (unit: KPa)

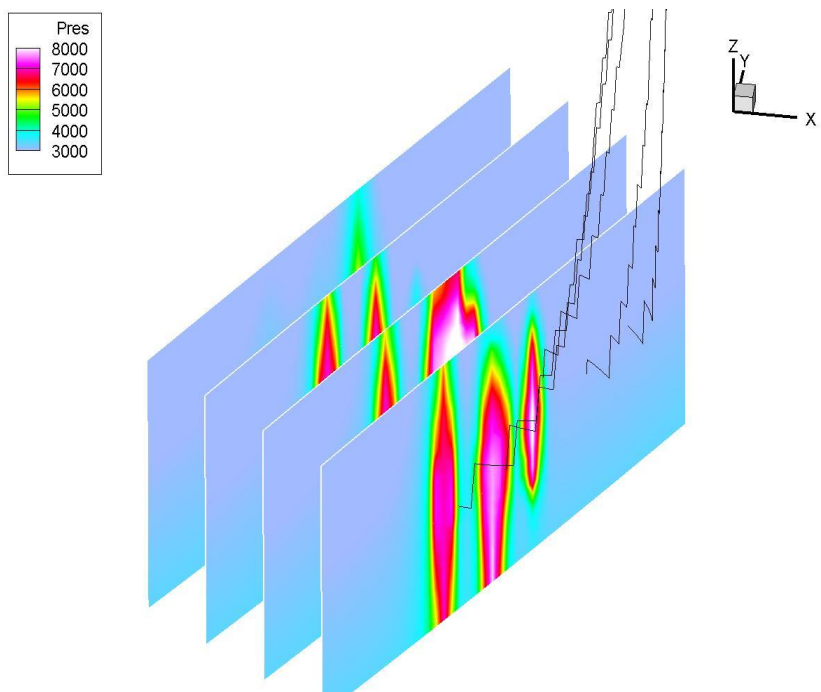


Figure 7. 30 Fluid pressure on J-plane on Oct 16, 1997 (unit: KPa)

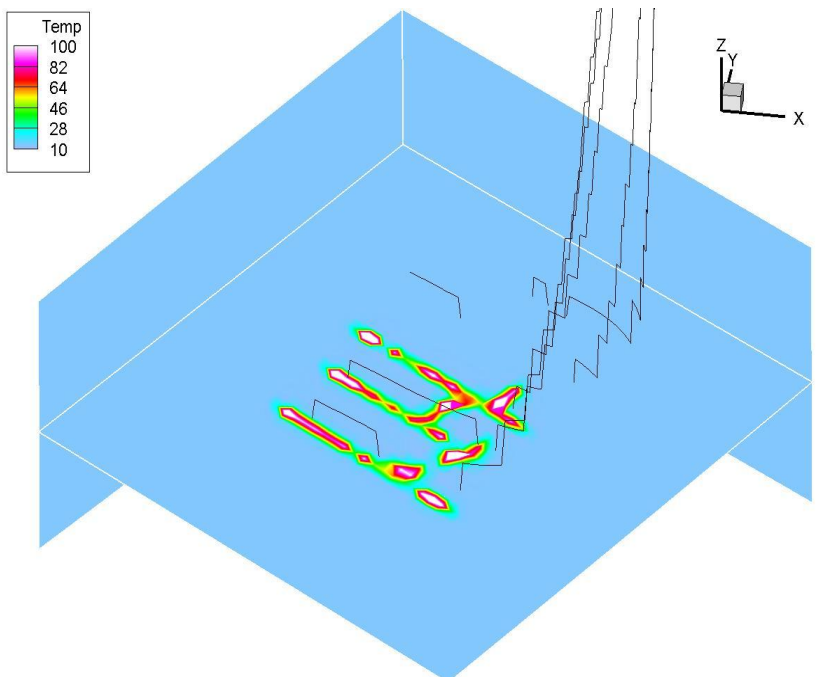


Figure 7. 31 Temperature on K-plane on Oct 16, 1997 (unit: Celsius)

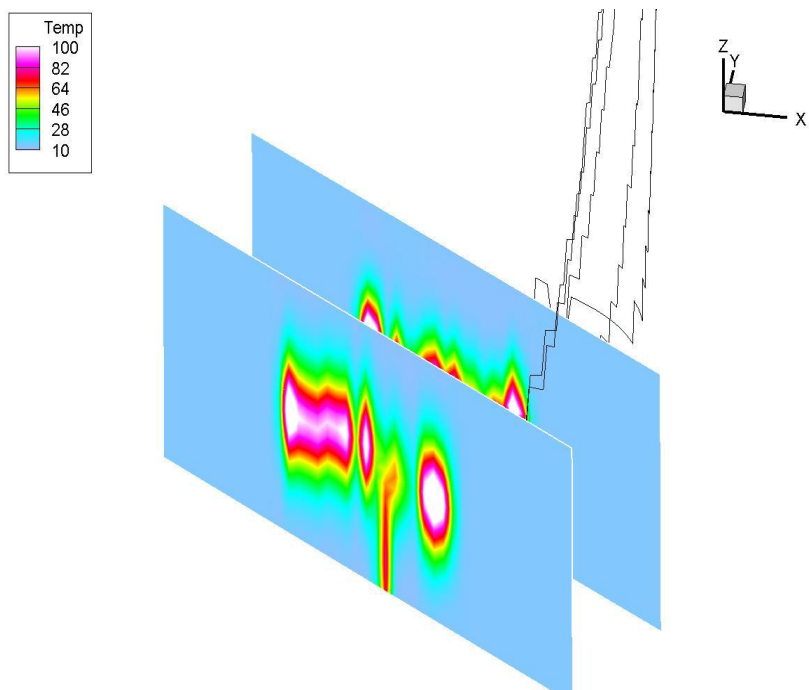


Figure 7. 32 Temperature on I-plane on Oct 16, 1997 (unit: Celsius)

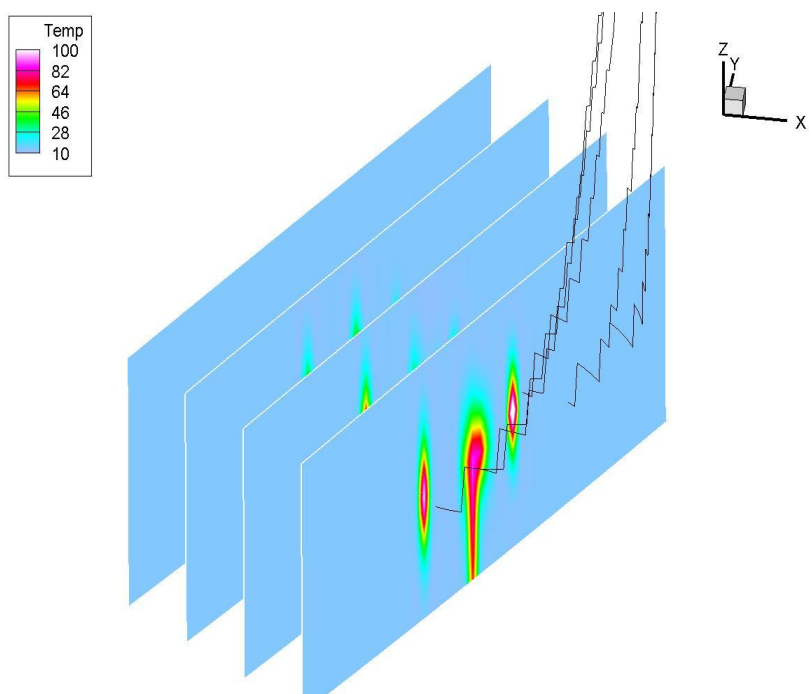


Figure 7. 33 Temperature on J-plane on Oct 16, 1997 (unit: Celsius)

At the same time, the stress field was disturbed by injection. The anomalies can differentiate the zone of fractures, as in Figures 7.34-39.

Compared with the displacements from not updated simulation results in Figures 4.32-40, the magnitude is smaller for the updated case in Figures 7.40-48. There are anomalies of stress and displacement along well bores and zones of fractures in Figures 7.40-48. The vertical displacement U_z reaches the maximum on the top of the reservoir, where the effective stress is not minimal. This appears intuitively to contradict the intuition. As stated previously, however, stress anomalies result from strain anomalies, which are the derivatives of displacement with regard to space, not displacement itself. This is an example of how coupled reservoir simulation improves significantly our understanding of recovery processes.

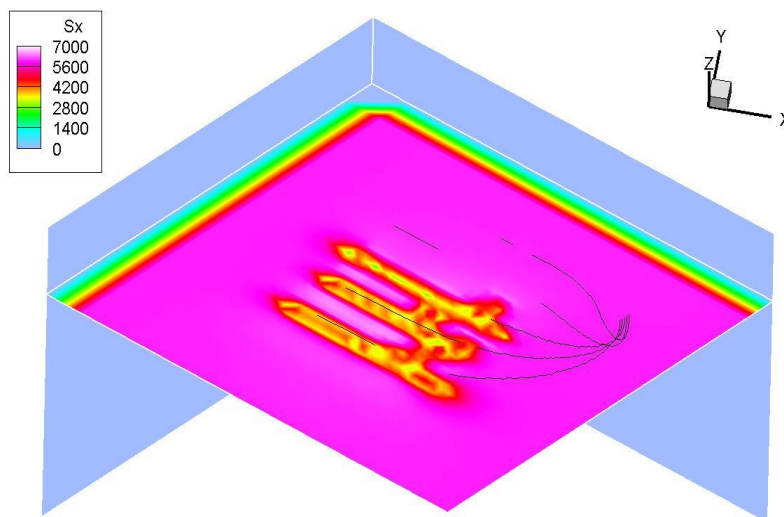


Figure 7. 34 S_x distribution in the middle of the reservoir on Oct 16, 1997 (unit: KPa)

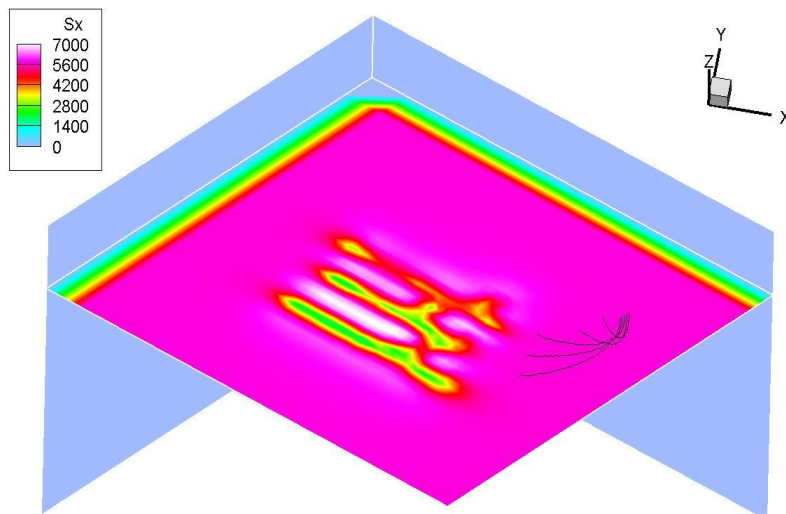


Figure 7. 35 S_x distribution on the top of the reservoir on Oct 16, 1997 (unit: KPa)

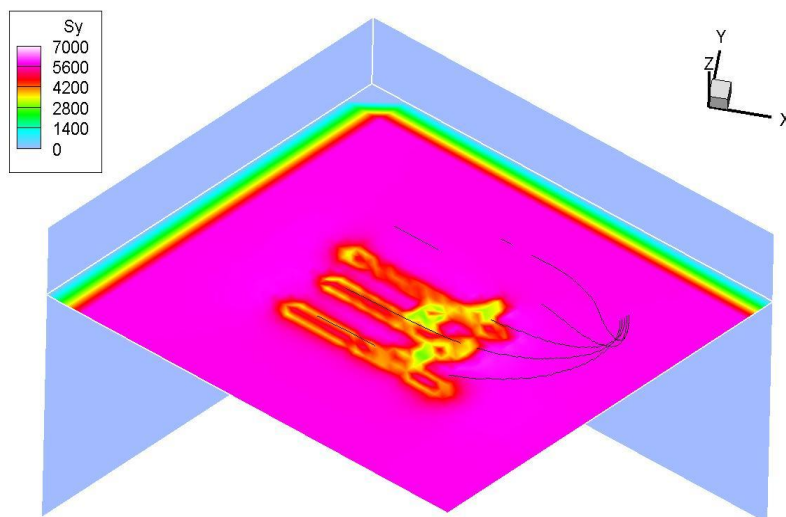


Figure 7. 36 S_y distribution in the middle of the reservoir on Oct 16, 1997 (unit: KPa)

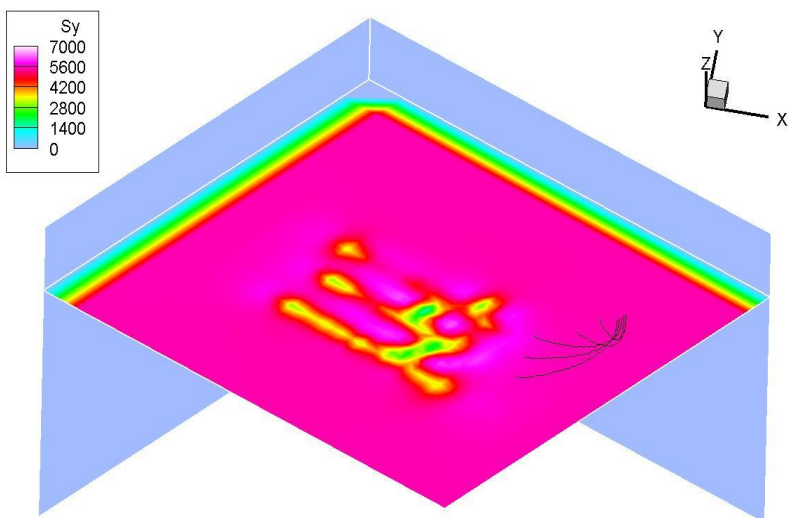


Figure 7. 37 S_y distribution on the top of the reservoir on Oct 16, 1997 (unit: KPa)

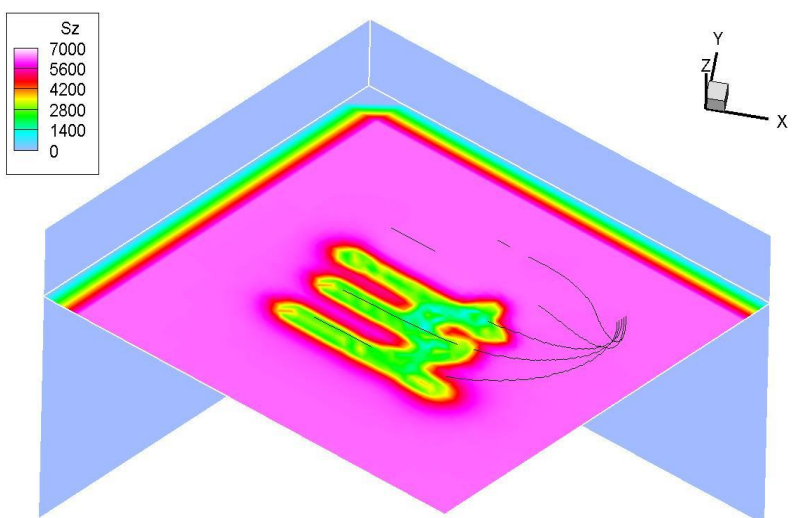


Figure 7. 38 S_z distribution in the middle of the reservoir on Oct 16, 1997 (unit: KPa)

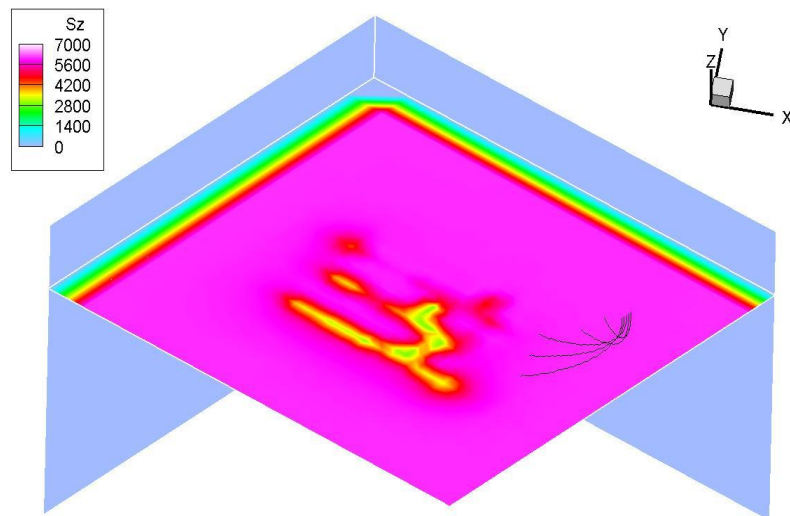


Figure 7. 39 S_z distribution on the top of the reservoir on Oct 16, 1997(unit: KPa)

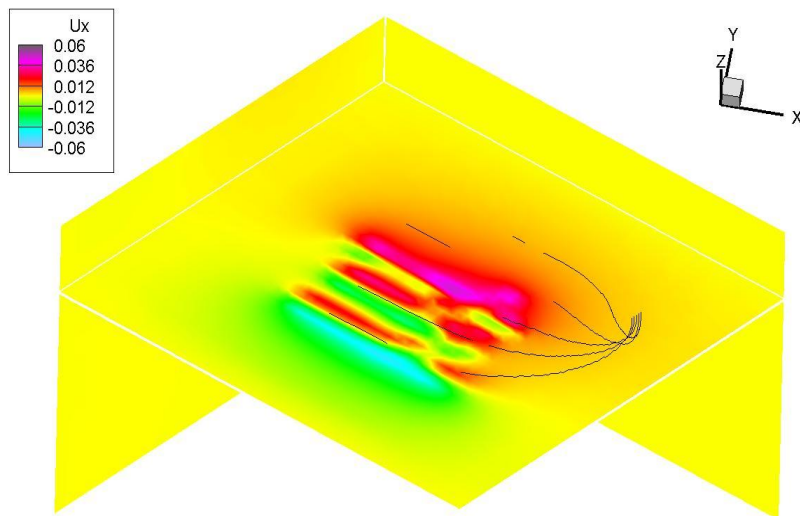


Figure 7. 40 U_x distribution in the middle of the reservoir on Oct 16, 1997 (unit: m)

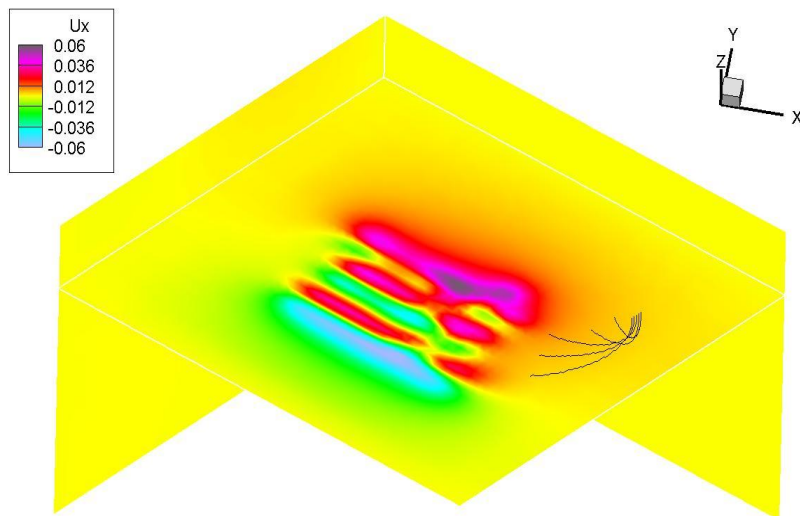


Figure 7. 41 U_x distribution on the top of the reservoir on Oct 16, 1997 (unit: m)

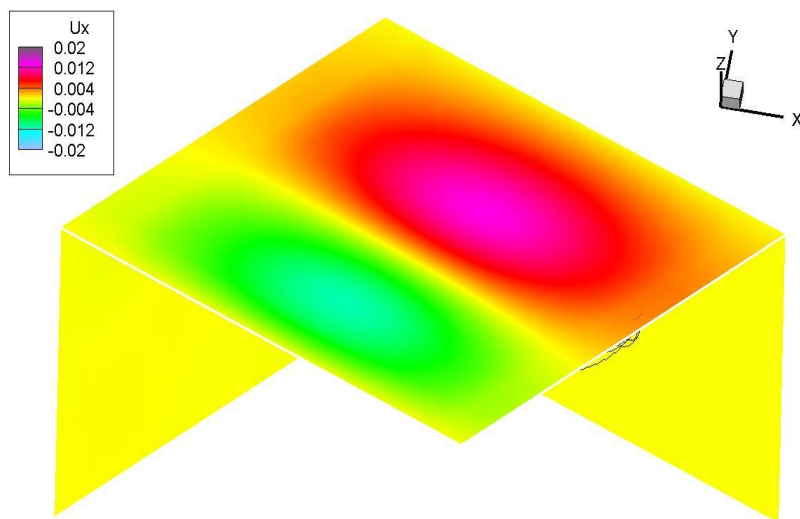


Figure 7. 42 U_x distribution on the ground on Oct 16, 1997 (unit: m)

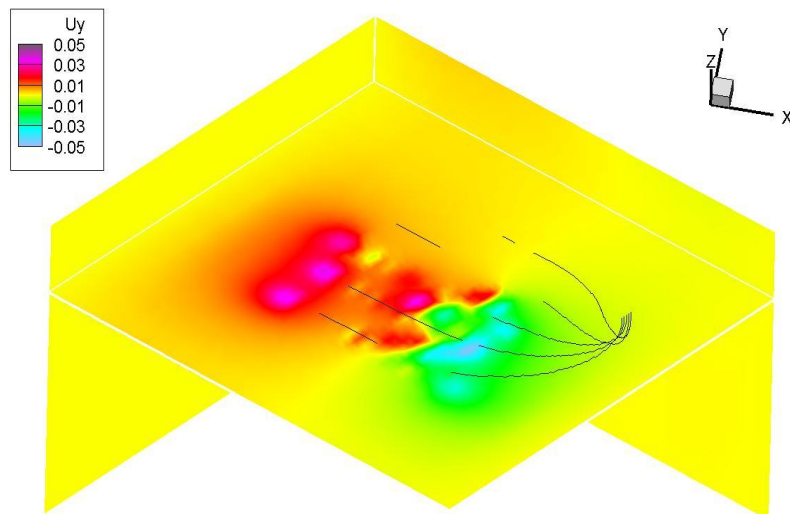


Figure 7. 43 U_y distribution in the middle of the reservoir on Oct 16, 1997 (unit: m)

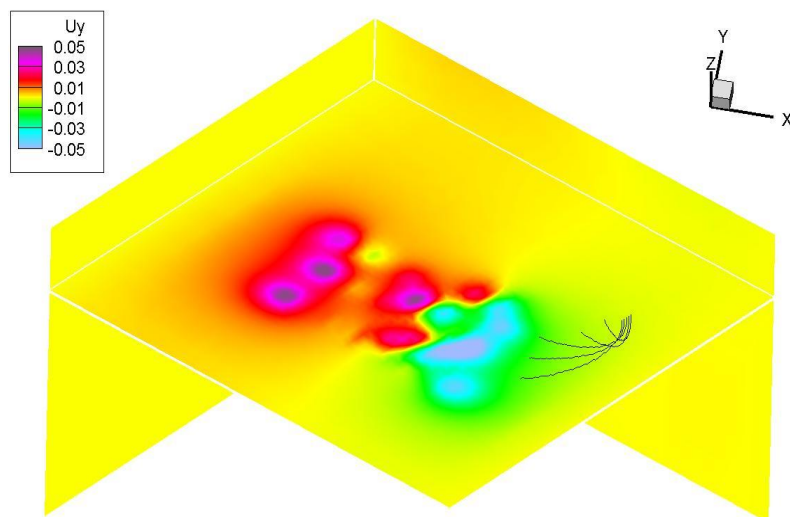


Figure 7. 44 U_y distribution on the top of the reservoir on Oct 16, 1997 (unit: m)

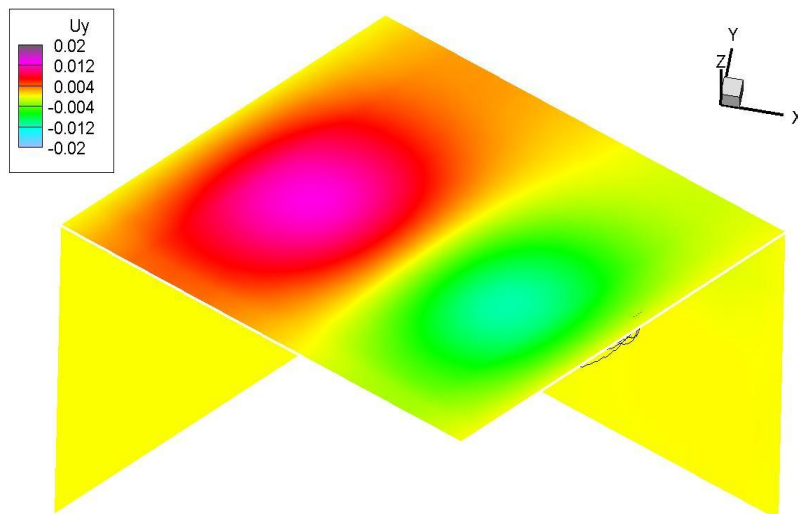


Figure 7. 45 U_y distribution on the ground on Oct 16, 1997 (unit: m)

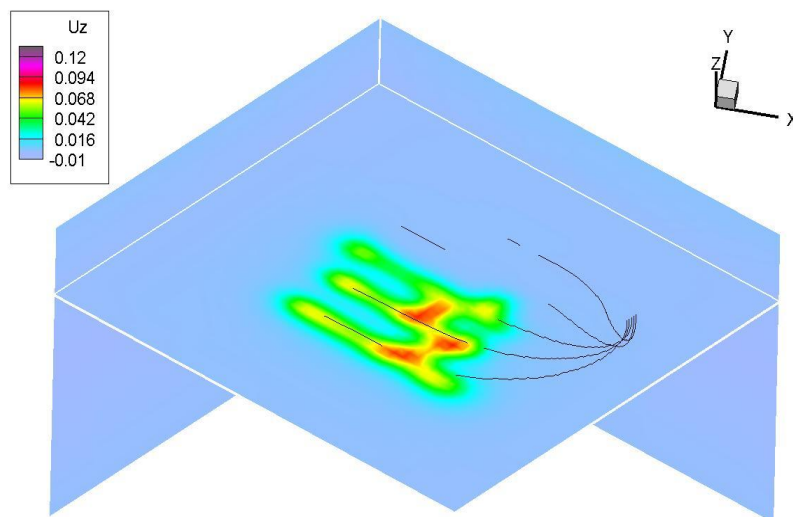


Figure 7. 46 U_z distribution in the middle of the reservoir on Oct 16, 1997 (unit: m)

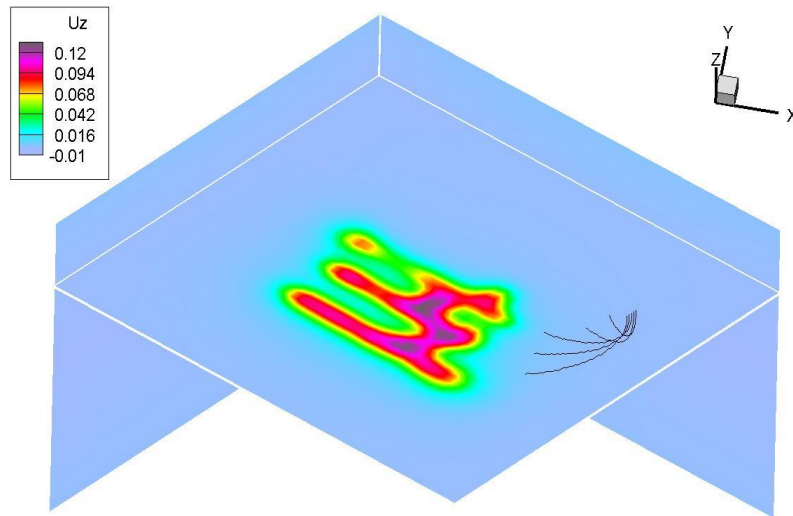


Figure 7. 47 U_z distribution on the top of the reservoir on Oct 16, 1997 (unit: m)

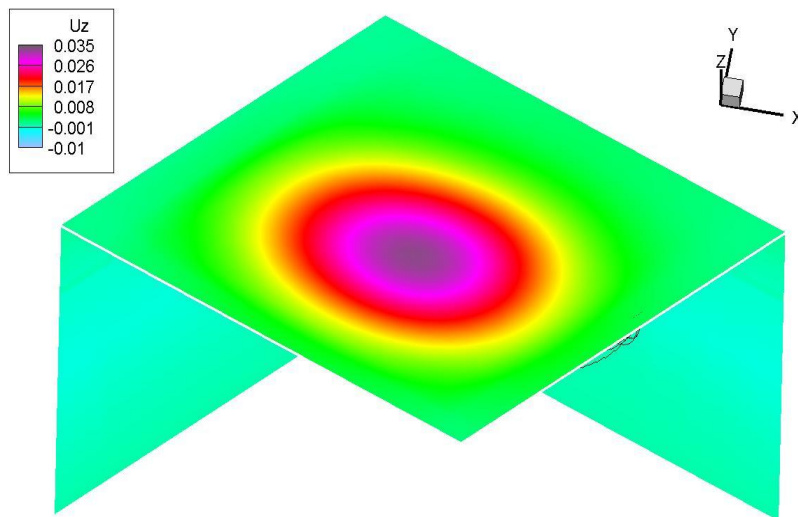


Figure 7. 48 U_z distribution on the ground on Oct 16, 1997 (unit: m)

At the end of Feb. 1998, the first monitor seismic survey was conducted. The results of updated reservoir simulation at this time are shown in Figures 7.49-69. Due to a few months of production, the fluid pressure dropped down and gas started to exsolve in some places from heavy oil. Oil displaced by steam and hot water at high pressures returned to the well bores. The fluid passages are still networked by the well bores and the zones of fractures. The leakage appeared to be reduced due to production. The flow patterns reflect what we observed on seismic sections in Chapters 5 and 6.

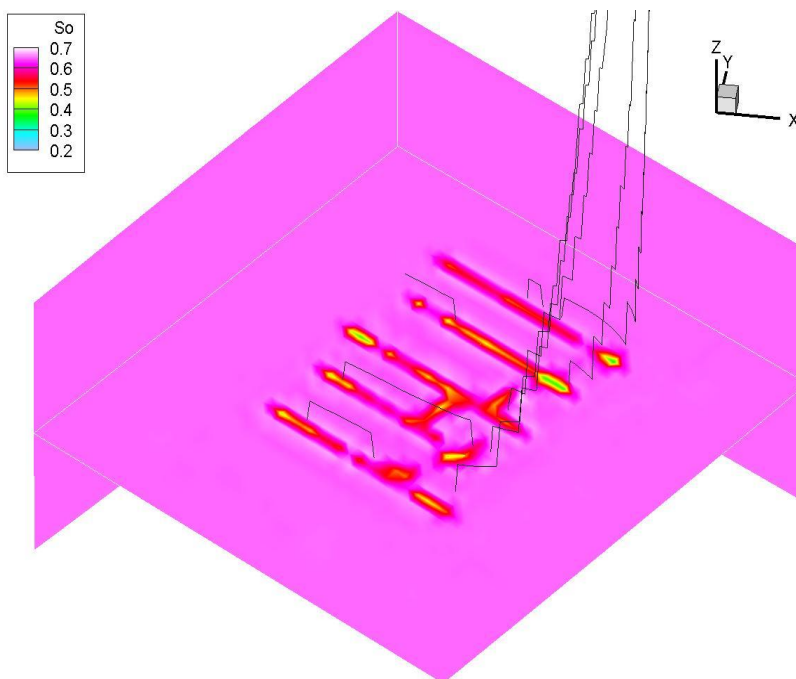


Figure 7. 49 Oil saturation in the middle of the reservoir on Feb 28, 1998

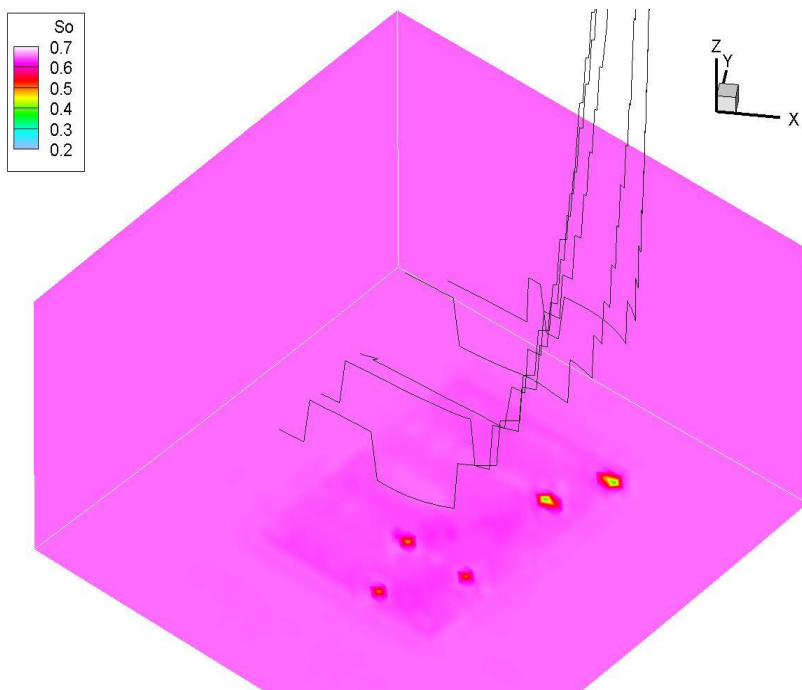


Figure 7. 50 Oil saturation on the bottom of the reservoir on Feb 28, 1998

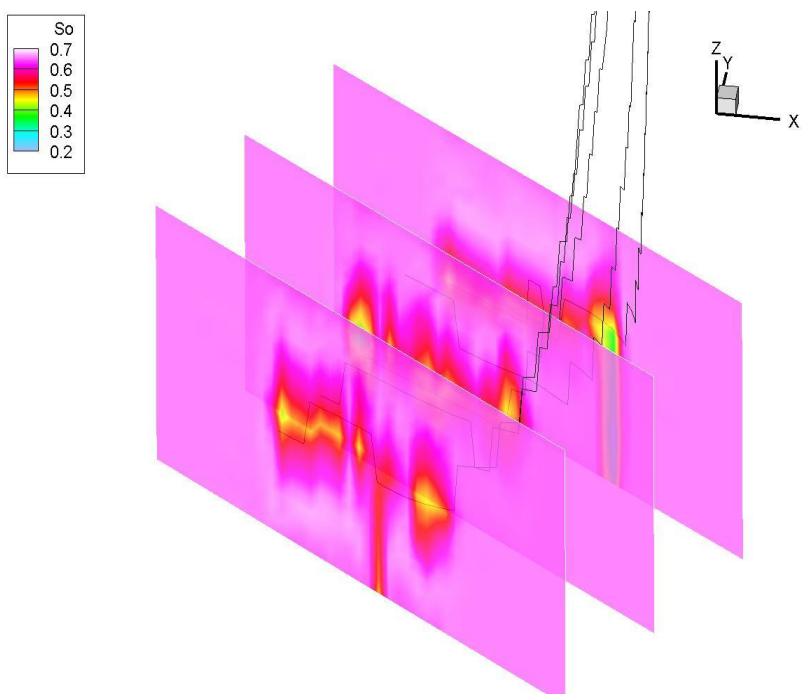


Figure 7. 51 Oil saturation on I-plane on Feb 28, 1998

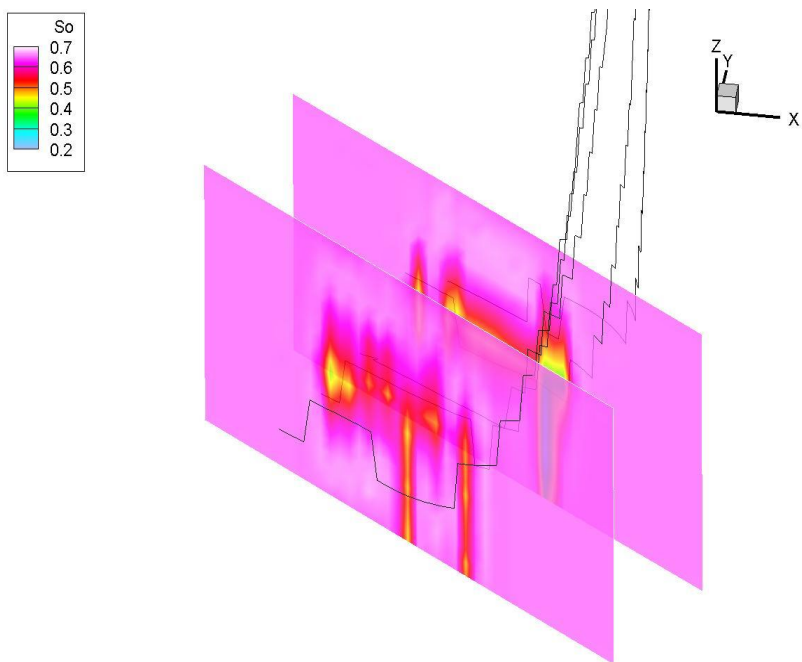


Figure 7. 52 Oil saturation on I-plane on Feb 28, 1998

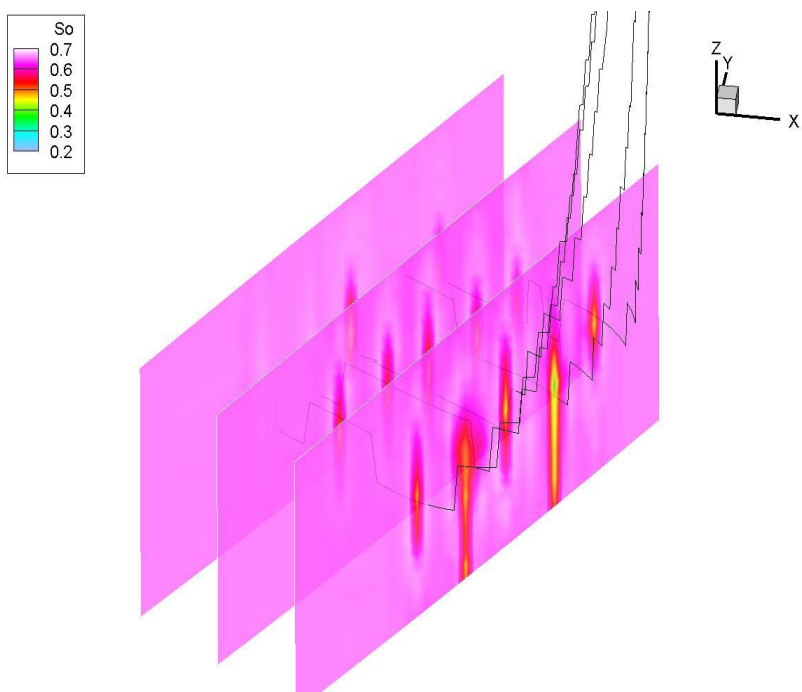


Figure 7. 53 Oil saturation on J-plane on Feb 28, 1998

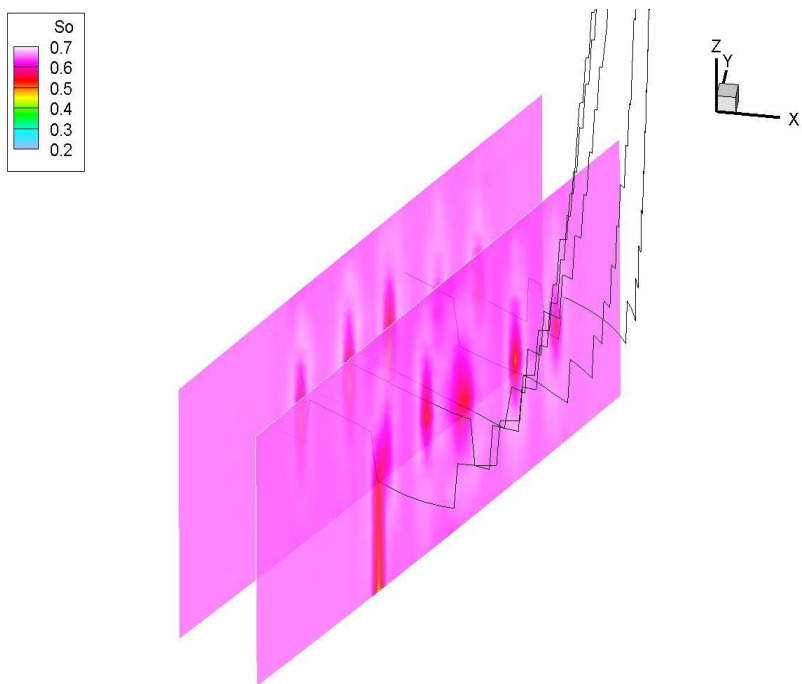


Figure 7. 54 Oil saturation on J-plane on Feb 28, 1998

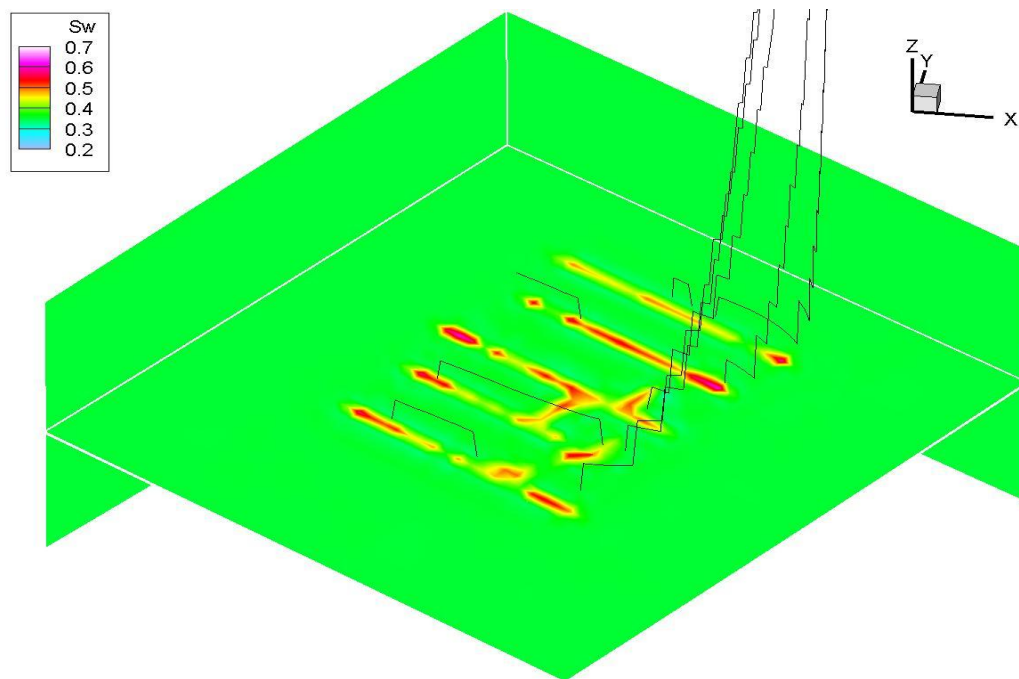


Figure 7. 55 Water saturation in the middle of the reservoir on Feb 28, 1998

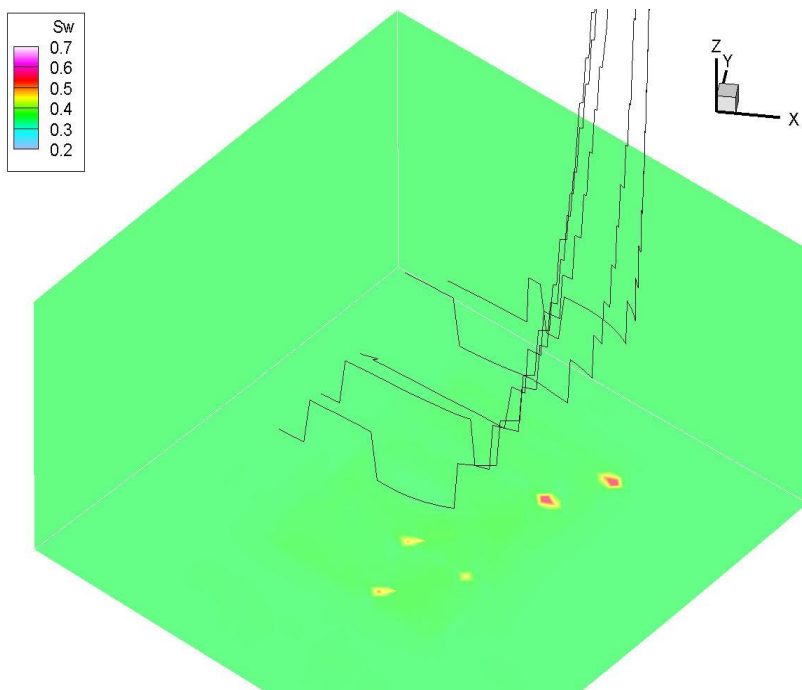


Figure 7. 56 Water saturation on the bottom of the reservoir on Feb 28, 1998

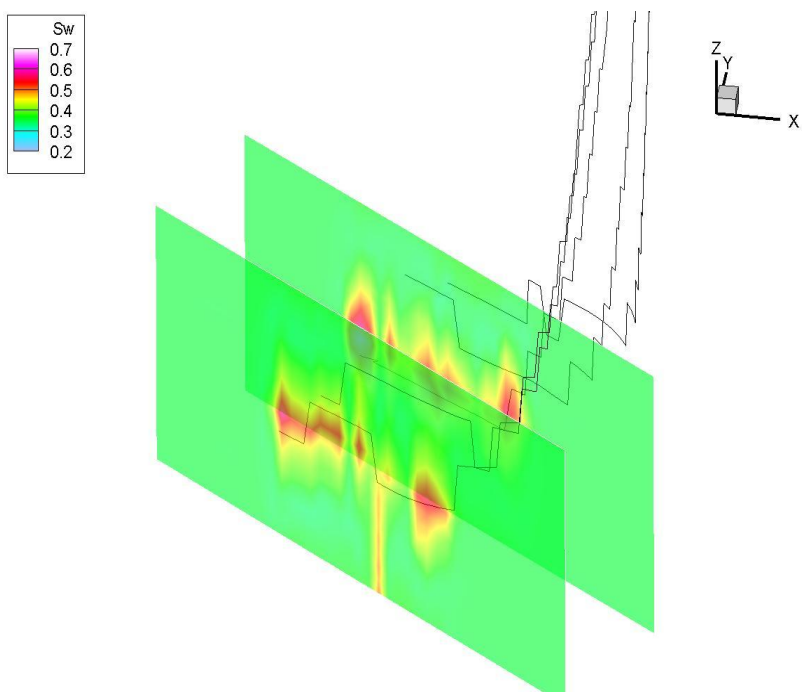


Figure 7. 57 Water saturation on I-plane on Feb 28, 1998

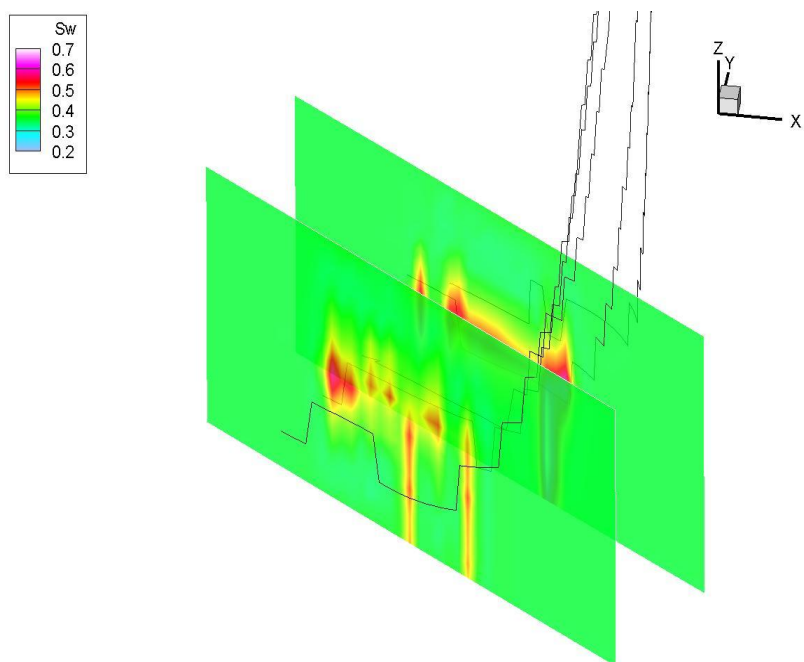


Figure 7. 58 Water saturation on I-plane on Feb 28, 1998

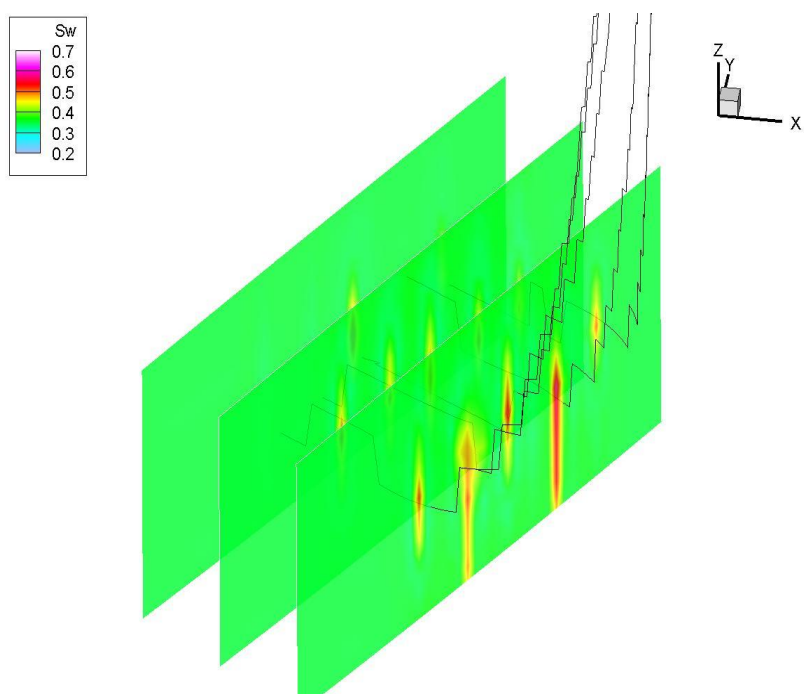


Figure 7. 59 Water saturation on J-plane on Feb 28, 1998

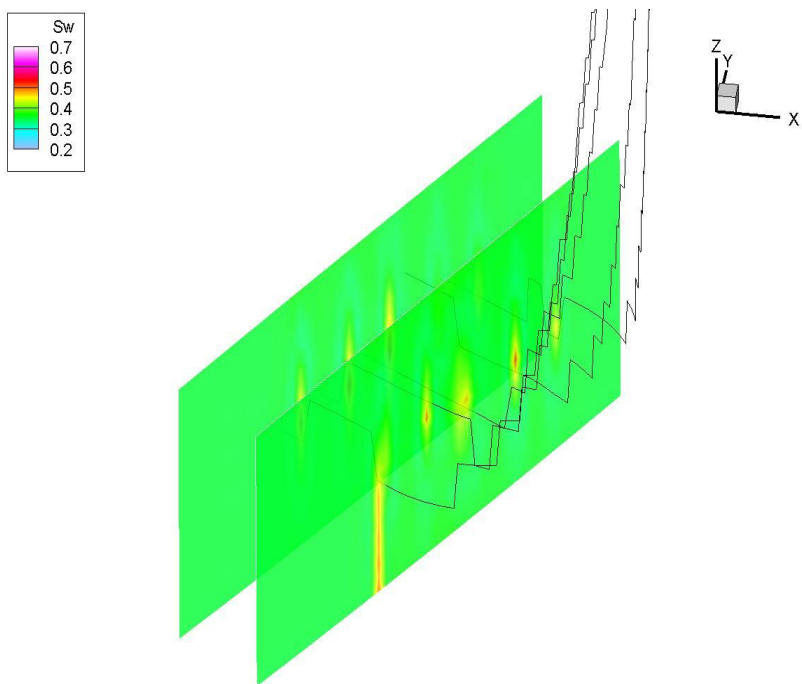


Figure 7. 60 Water saturation on J-plane on Feb 28, 1998

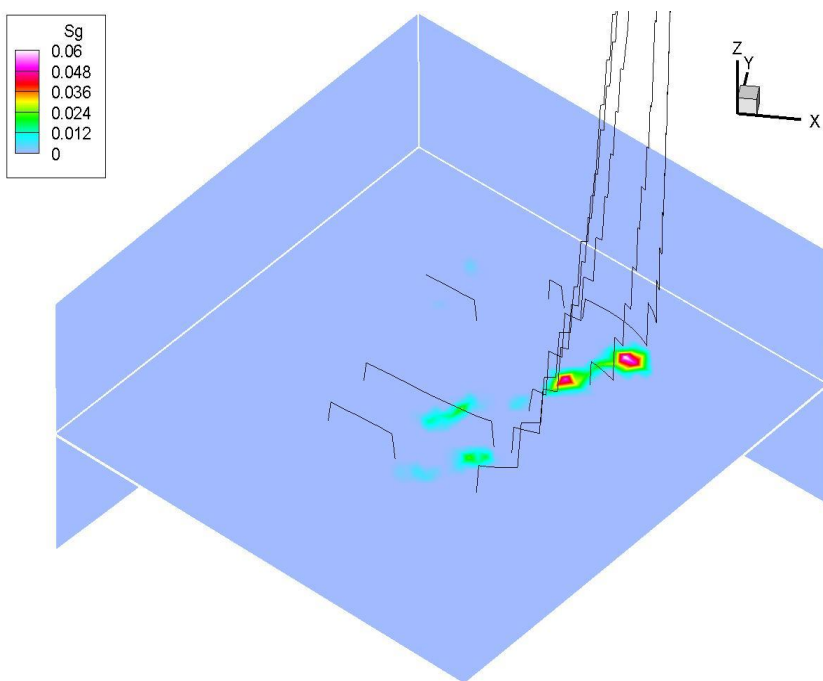


Figure 7. 61 Gas saturation in the middle of the reservoir on Feb 28, 1998

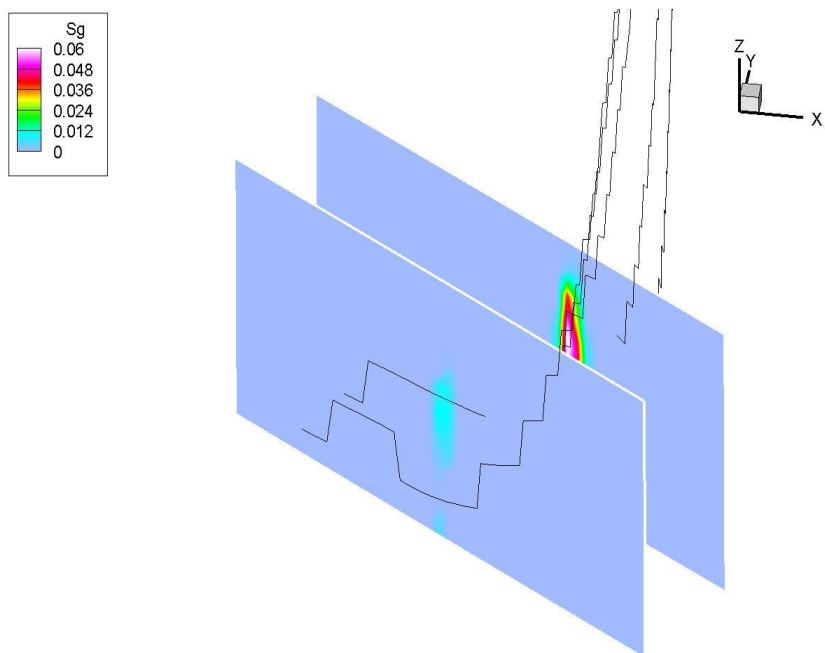


Figure 7. 62 Gas saturation on I-plane on Feb 28, 1998

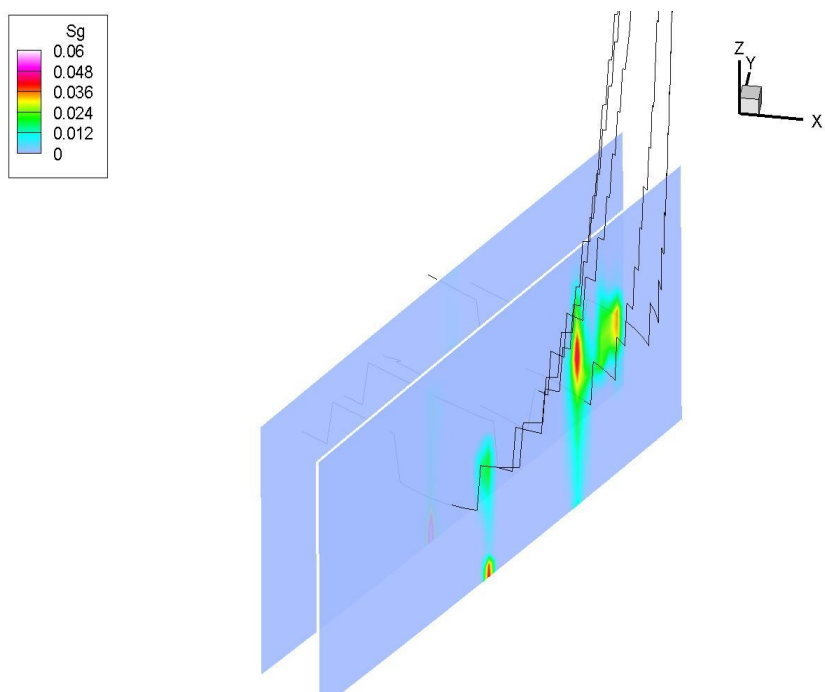


Figure 7. 63 Gas saturation on J-plane on Feb 28, 1998

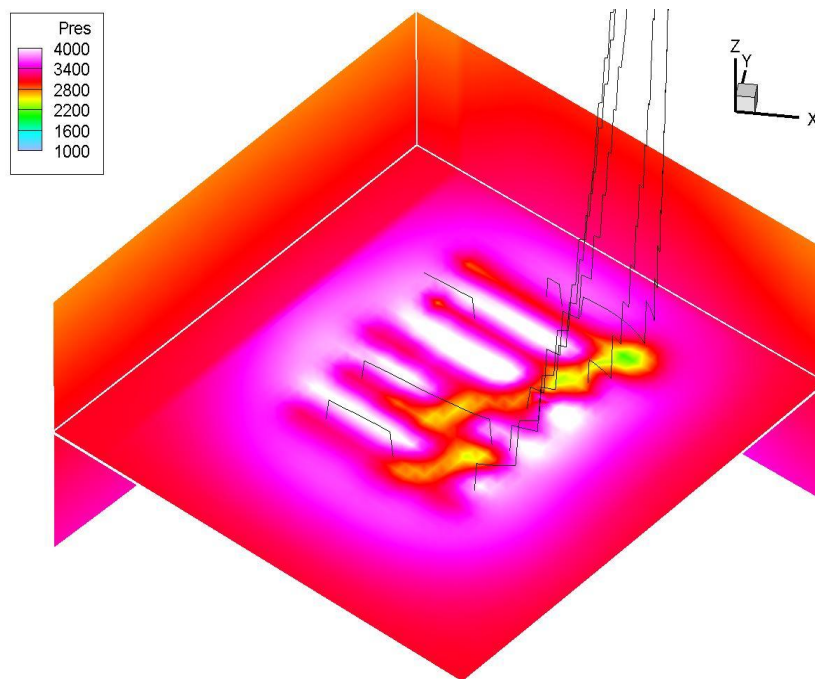


Figure 7. 64 Fluid pressure in the middle of the reservoir on Feb. 28, 1998(unit:KPa)

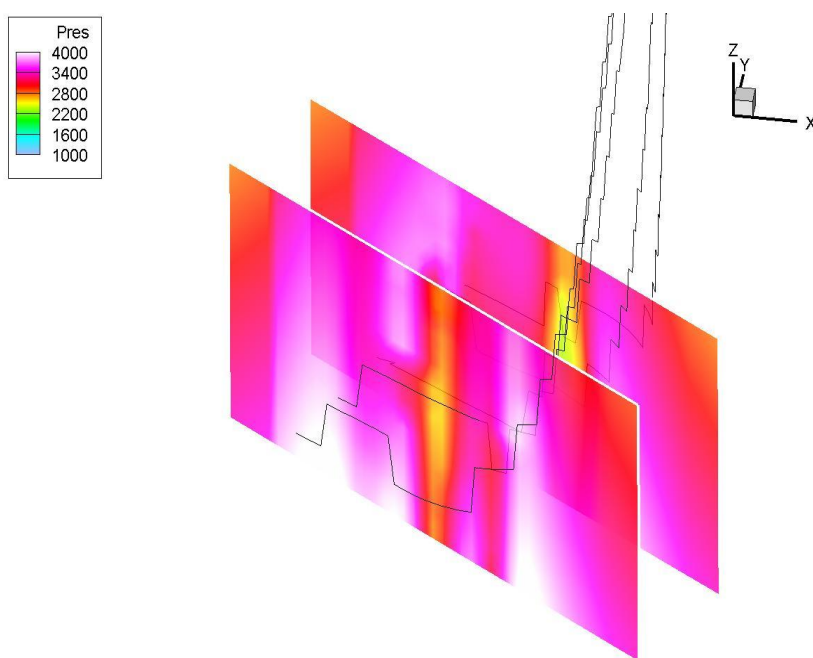


Figure 7. 65 Fluid pressure on I planes on Feb. 28, 2008 (unit: KPa)

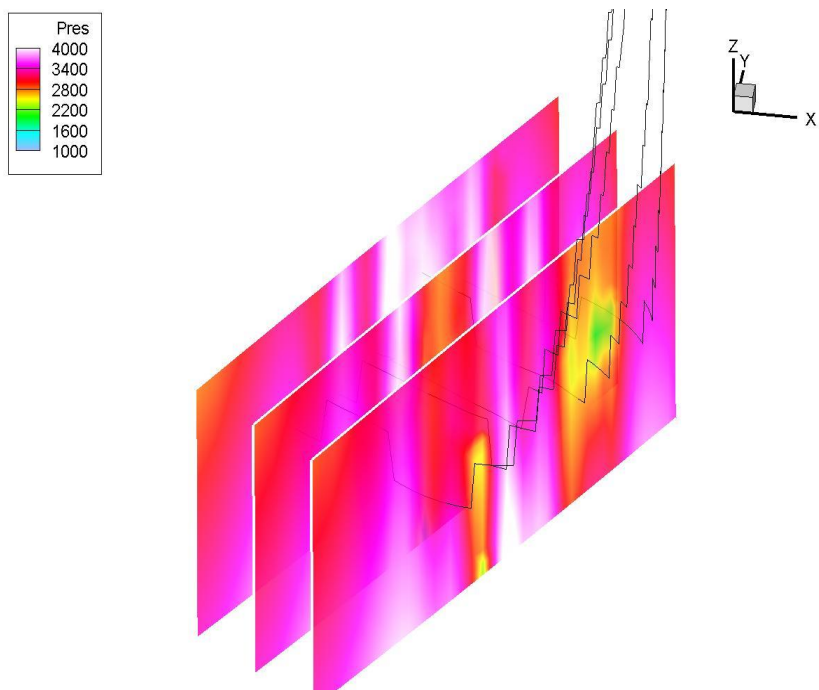


Figure 7. 66 Fluid pressure on J planes on Feb. 28, 2008 (unit: KPa)

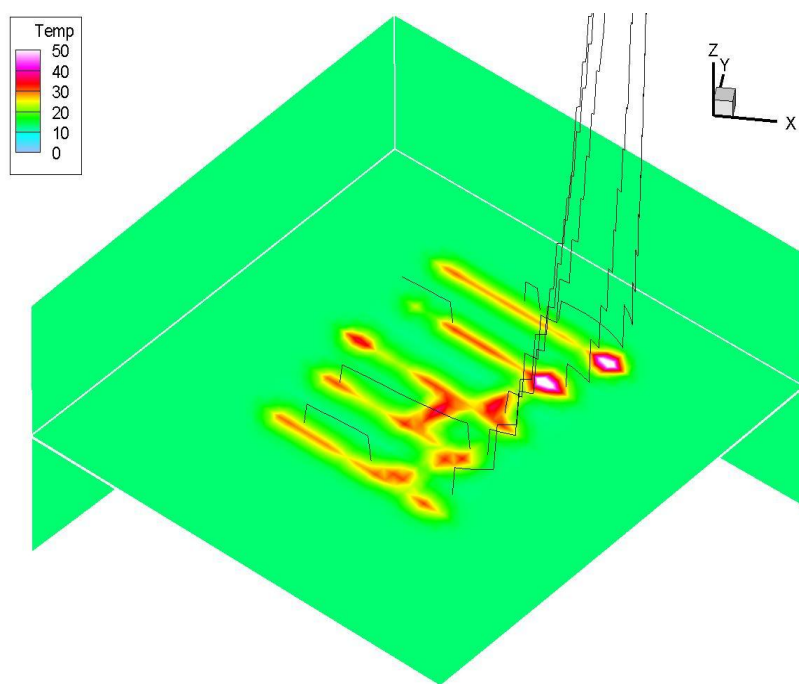


Figure 7. 67 Temperature in the middle of the reservoir on Feb. 28,1998(unit:Celsius)

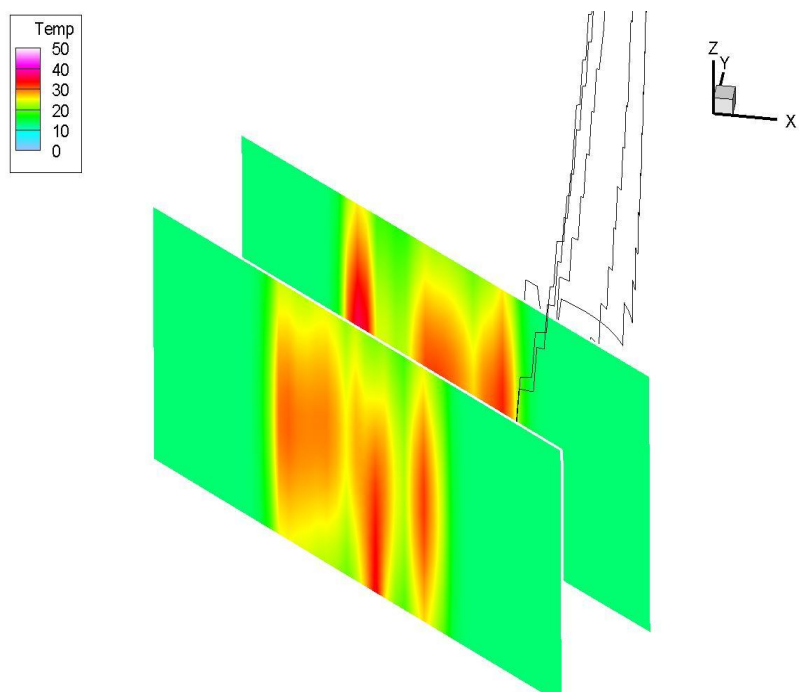


Figure 7. 68 Temperature on I planes on Feb. 28, 1998 (unit: Celsius)

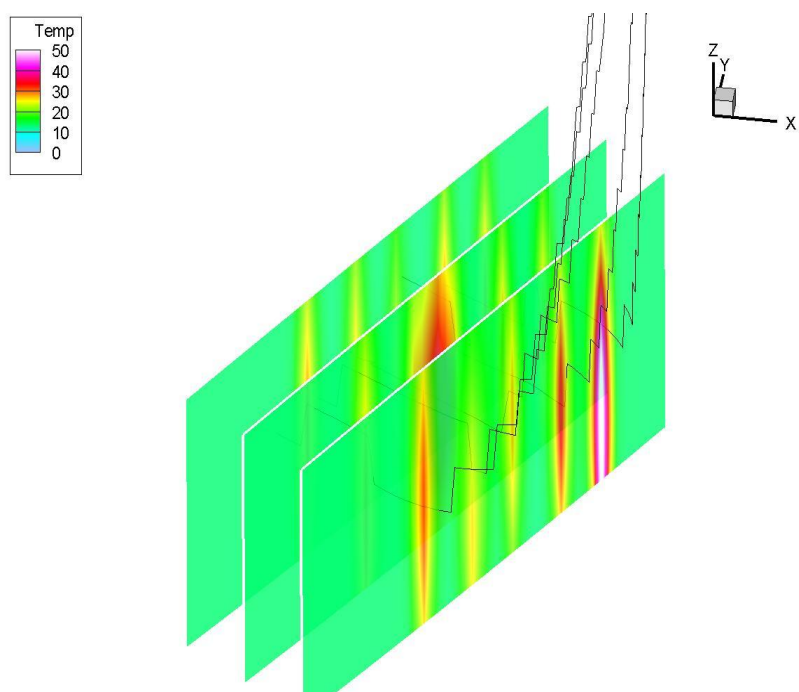


Figure 7. 69 Temperature on J planes on Feb. 28, 1998 (unit: Celsius)

Compared with the effective stress in Figures 7.34-39, those in Figures 7.70-75 increase substantially due to production. Subsequently, the displacements adjust accordingly in Figures 7.76-84. It is noted that the vertical displacements on the ground differ in magnitude and distribution between the initial simulation (Figure 4.48) and the updated simulation (Figure 7.84). There are considerable differences in other regards. These parameters are very important in reservoir management.

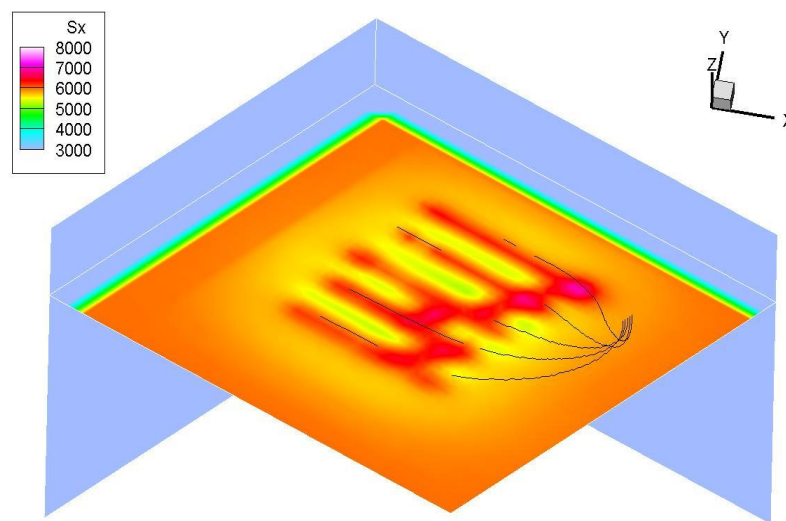


Figure 7. 70 S_x distribution in the middle of the reservoir on Feb 28, 1998 (unit: KPa)

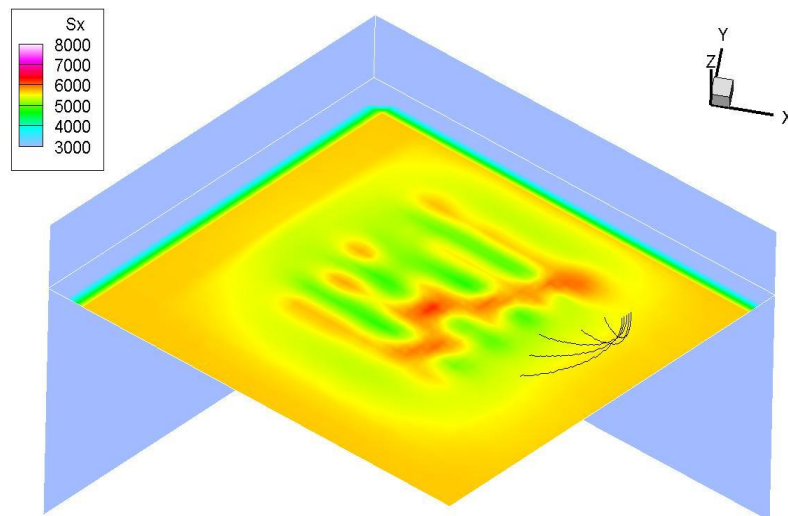


Figure 7. 71 S_x distribution on the top of the reservoir on Feb 28,1998 (unit: KPa)

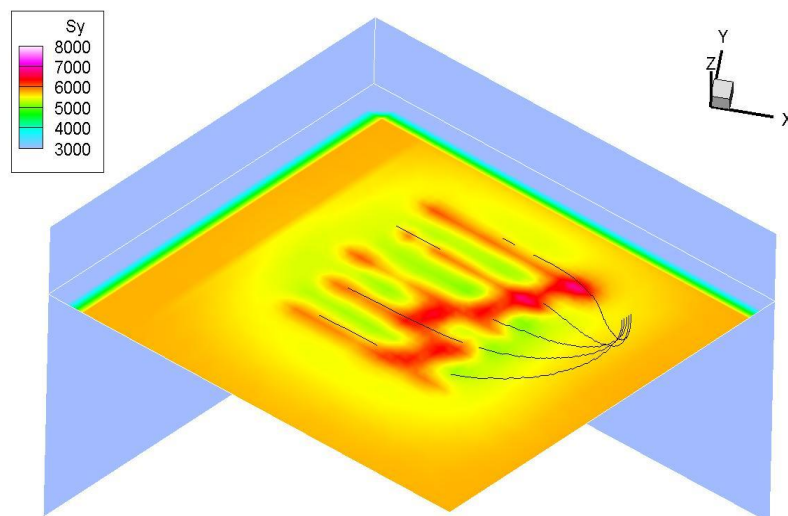


Figure 7. 72 S_y distribution in the middle of the reservoir on Feb 28, 1998 (unit: KPa)

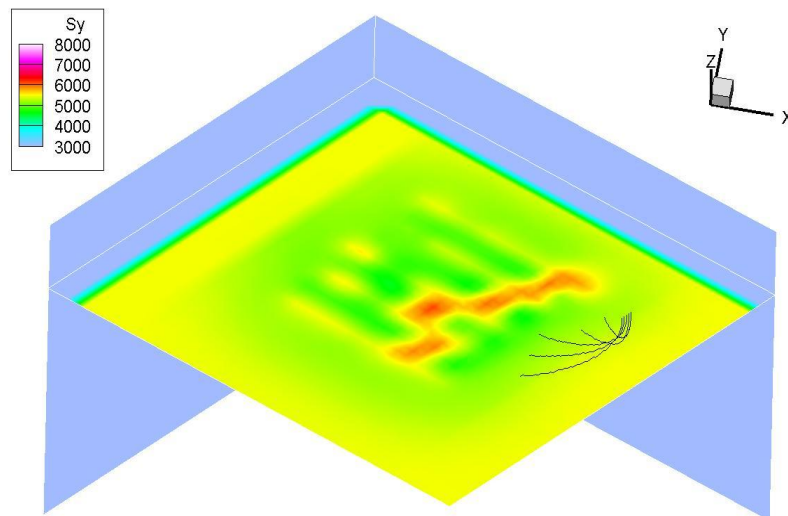


Figure 7.73 S_y distribution on the top of the reservoir on Feb 28, 1998 (unit: KPa)

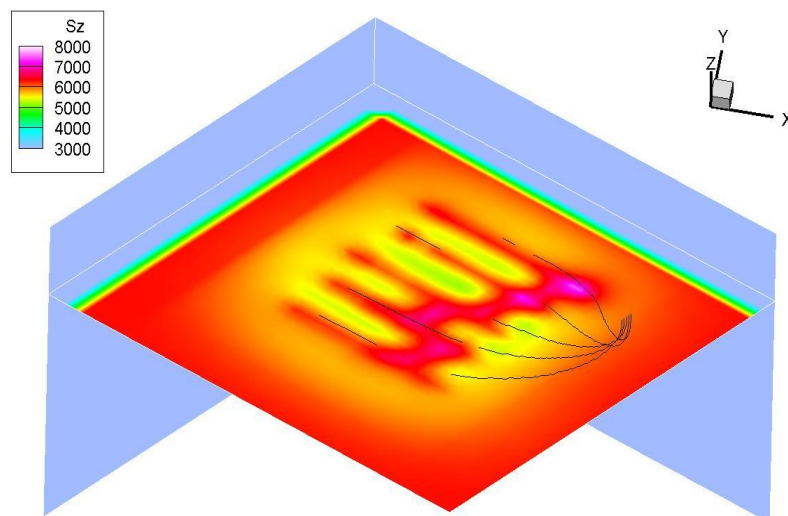


Figure 7.74 S_z distribution in the middle of the reservoir on Feb 28, 1998 (unit: KPa)

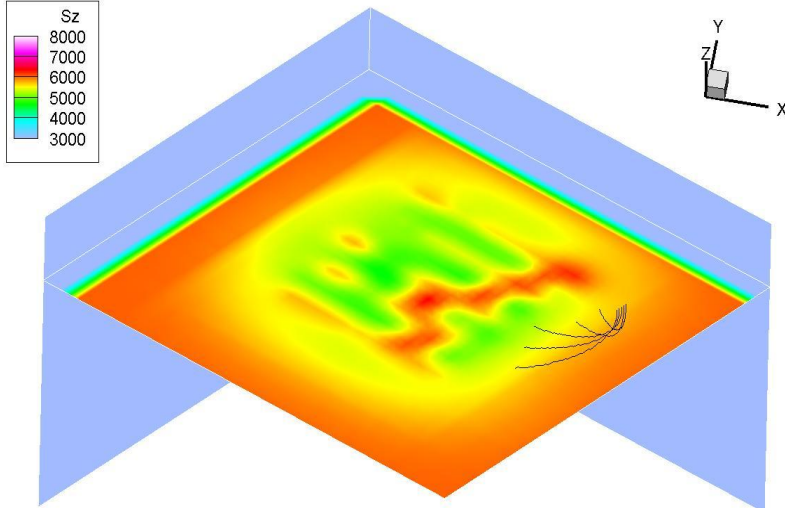


Figure 7. 75 S_z distribution on the top of the reservoir on Feb 28, 1998 (unit: KPa)

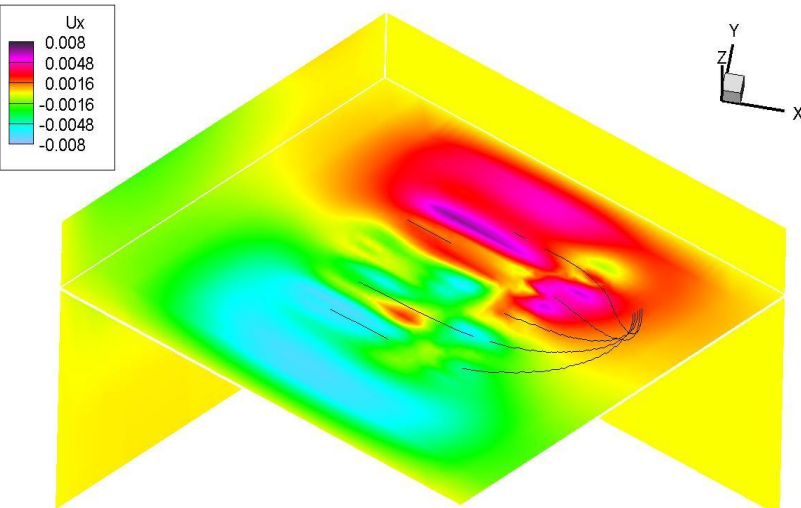


Figure 7. 76 U_x distribution in the middle of the reservoir on Feb 28, 1998 (unit: m)

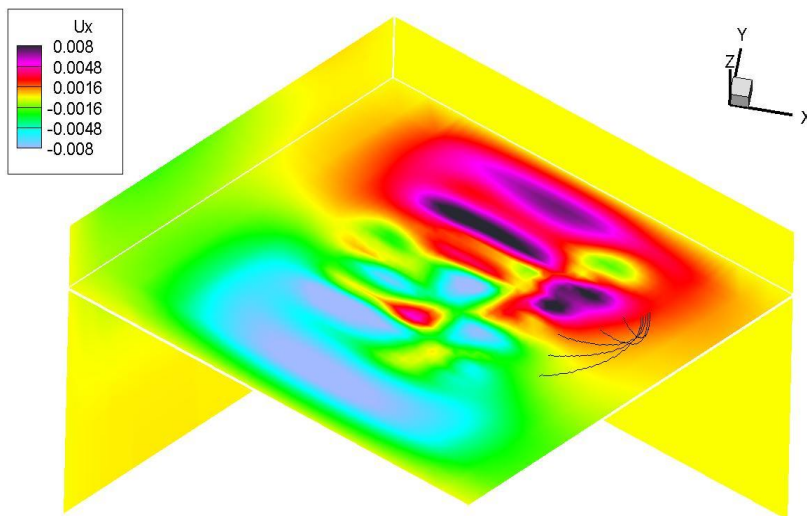


Figure 7.77 U_x distribution on the top of the reservoir on Feb 28, 1998 (unit: m)

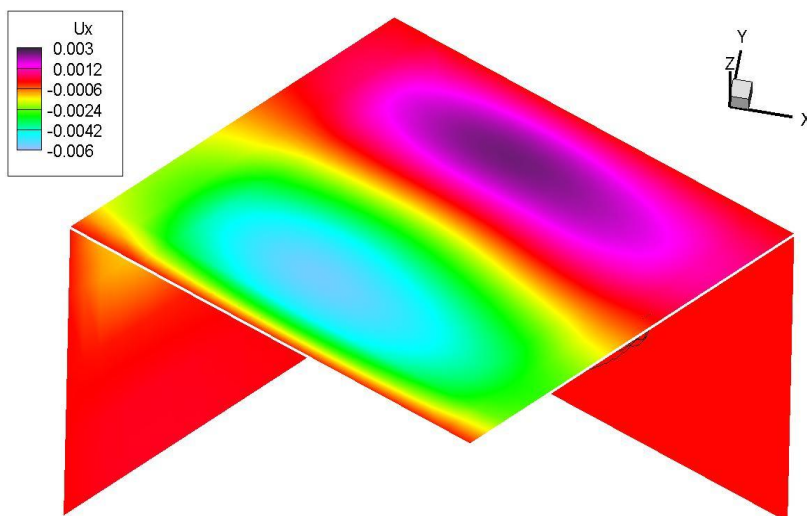


Figure 7.78 U_x distribution on the ground on Feb 28, 1998 (unit: m)

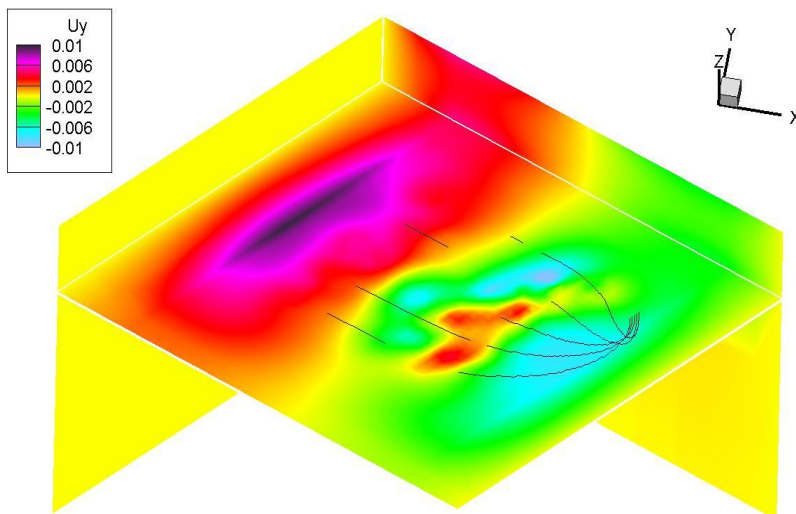


Figure 7. 79 U_y distribution in the middle of the reservoir on Feb 28, 1998 (unit: m)

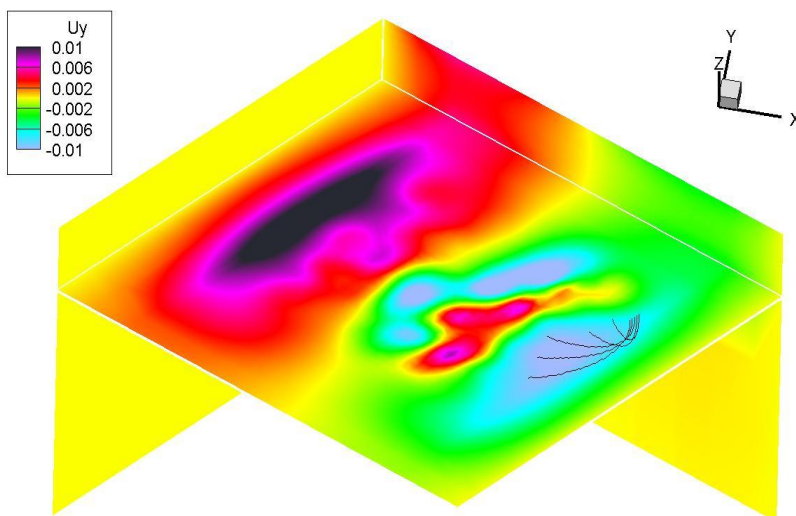


Figure 7. 80 U_y distribution on the top of the reservoir on Feb 28, 1998 (unit: m)

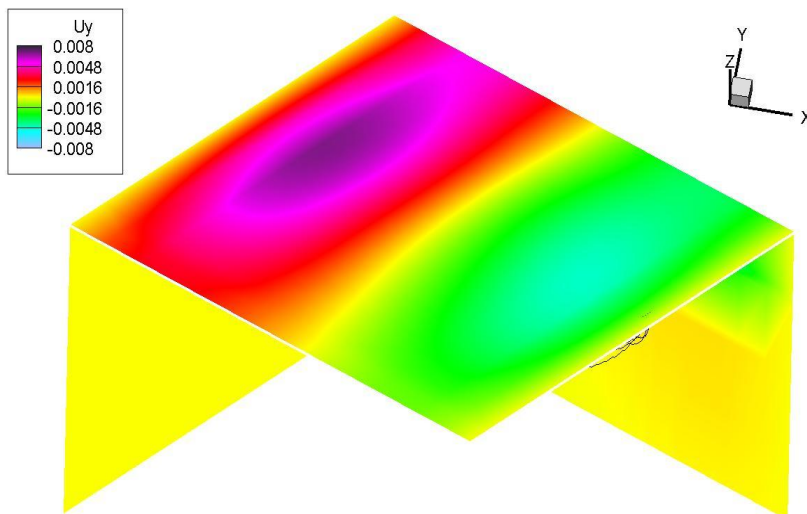


Figure 7. 81 U_y distribution on the ground on Feb 28, 1998 (unit: m)

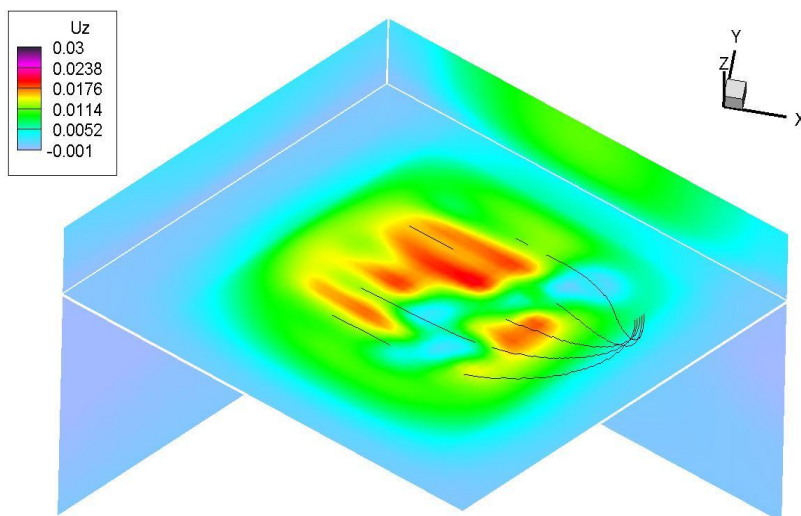


Figure 7. 82 U_z distribution in the middle of the reservoir on Feb 28, 1998 (unit: m)

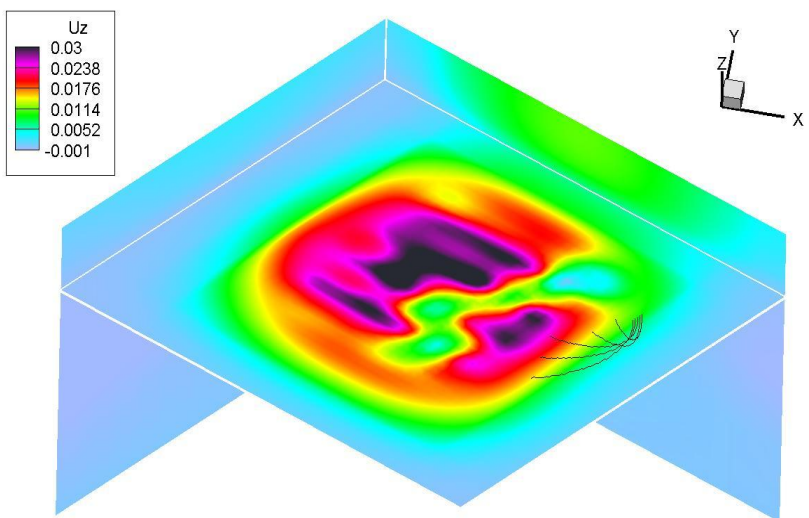


Figure 7. 83 U_z distribution on the top of the reservoir on Feb 28, 1998 (unit: m)

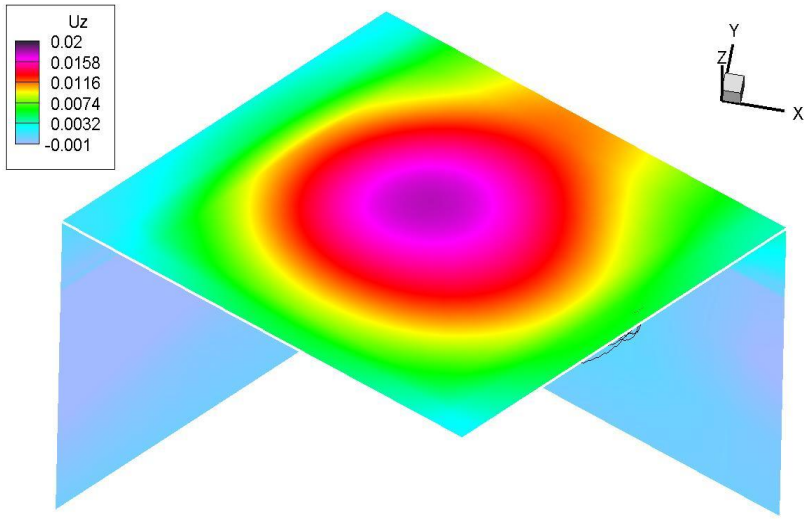


Figure 7. 84 U_z distribution on the ground on Feb 28, 1998 (unit: m)

CHAPTER 8 SEISMIC MODELLING

8.1 Introduction

Time-lapse seismic modelling based on the results of reservoir simulation intends to examine how closely it matches the real time-lapse seismic. With proper rock physics models, synthetic seismic experiments can illustrate how the reservoir parameters influence seismic responses, which may take in many different forms. The modelling is able to demonstrate how seismic data is modified with calendar time progression and how the modifications relate to recovery.

There are two sophistications involved in the procedure of seismic modelling, i.e., rock physics and wave propagation mechanisms. The former is the connection between reservoir seismic properties (elasticity, anelasticity and density) and reservoir engineering properties (saturation, pressure, temperature etc.). It may be so complicated to defy any mathematical solutions. For practical purposes, it must be simplified either empirically or mathematically. My M. Sc. thesis gives a detailed presentation of how to make such simplifications (2001). The rock physics handbook (Mavko et al., 1998) provides a series of references for lab measurements and theoretical formulae. In the next section a concise relationship will be introduced for our seismic modelling. The latter refers to wave propagation theories that can be very complicated and intractable beyond the scope of this thesis. Margrave and Manning (2004) gave a brief summary of how the complexities reduce to mathematically manageable formulae on certain assumptions. Among the simplest and most operable is the convolution model, in which the seismic traces result from convolving the wavelet with reflectivity

series. It omits multiples, mode conversions and energy loss, which can be removed from seismic data by modern seismic processing technologies (after Lindseth, 1979). It is therefore used for seismic modelling in this thesis.

8.2 Rock physics models

Rock physics models link the reservoir parameters to the elastic moduli and the density. In this study the key models were employed as follows:

1) Given the molecular weight or specific gravity of gas, the bulk modulus and density at any pressure and temperature can be calculated using empirical formulae (Batzle and Wang, 1992). Two gases of steam and methane may occur with molecular weight 18 and 16, respectively, during the process of heavy oil recovery. Given API or density at standard conditions, the bulk modulus and density of oil can be calculated at any pressure and temperature using empirical formulae (Batzle and Wang, 1992). Heavy oil and light oil are the two components in the oil phase and their densities are assumed to be 1.0 and 0.7, respectively. Given the salinity of water, the bulk modulus and density of brine can be calculated at any pressure and temperature using empirical formulae (Batzle and Wang, 1992). The salinity of brine in the area is assumed to be 0.36%.

2) The mixture of fluids has the bulk modulus averaged harmonically over three phases due to the assumption that low seismic frequencies provide enough time for fluids to equilibrate pressures among different phases.

3) The dry bulk and shear moduli will change with effective pressure. Lewis (1990) measured the bulk and shear moduli of sands at a variety of pressures and proposed a set of equations to relate them. The following equations are a modified version (after Lewis, 1990):

$$\text{Bulk Modulus: } dK_d/d\sigma = a\sigma^{b-1}Pa^{1-b}/F(e)$$

$$\text{Shear Modulus: } d\mu_d/d\sigma = c\sigma^{d-1}Pa^{1-d}/F(e)$$

where, σ is mean effective stress; Pa is atmospheric pressure; a , b , c and d are constants; $F(e) = 0.3 + 0.7e^2$; e is void ratio; K_d and μ_d are the dry bulk and shear moduli, respectively

4) The dry bulk and shear moduli will change with temperature. The simple relation between the dry moduli and temperature can be linearized as follows (Zhang, 2001):

$$dK_d/dT = -0.0155$$

$$d\mu_d/dT = -0.0065$$

5) For fluid-saturated sands, the effect of fluid on the bulk modulus is estimated using Gassmann's equation. The fluid effect is assumed to exert no influence on the shear modulus.

The dry bulk and shear moduli of oil sands before recovery were extracted from the velocity model (see the next section) using Gassmann's equation. The velocity distribution at the time of the first monitor seismic survey was then calculated using the results of reservoir simulation (the previous section) and the above rock physics models.

8.3 Seismic modelling

The formations from the surface to the reservoir top were divided into five layers and each layer was assumed to have a constant velocity and density, blocked from well logs. As stated in the section on Reservoir Characterization, the reservoir is a body of oil sands with tight rock inclusions. The reservoir layer was assumed to have two rock types, oil sands and tight rocks. It is believed that the significant contrast of acoustic impedance between these two types of rocks generates strong reflections within the reservoir. The reservoir does not have a strong acoustic impedance contrast with the overlying and underlying formations and its top and bottom cannot be delineated with the consistent and easily-picked reflections. At 550m, the top of Devonian occurs with a supposition of the velocity of 4630 m/s and the density of 2.43g/cc.

The velocities above the reservoir were assumed to be unaltered during recovery. The velocity of the tight rocks within the reservoir may undergo some changes, but, considering no fluid substitution, it was also assumed to be constant. The velocity of the oil sands was changing and the variations were computed using the procedure described in the previous section.

With the HRS module of AVO application, the normal-incidence synthetic seismograms with the wavelet extracted from the monitor survey seismic data were generated for the baseline and monitor surveys, as shown in Figures 8.1 & 8.2. The cross section is along well 226 (see Figure 8.3), where two fracture zones crossed over with two sink points leaking the injected steam. As in Figure 8.2 at these two locations, the top Devonian reflections are sagged considerably and the traces in the reservoir and below are disturbed, when compared with those in Figure 8.1.

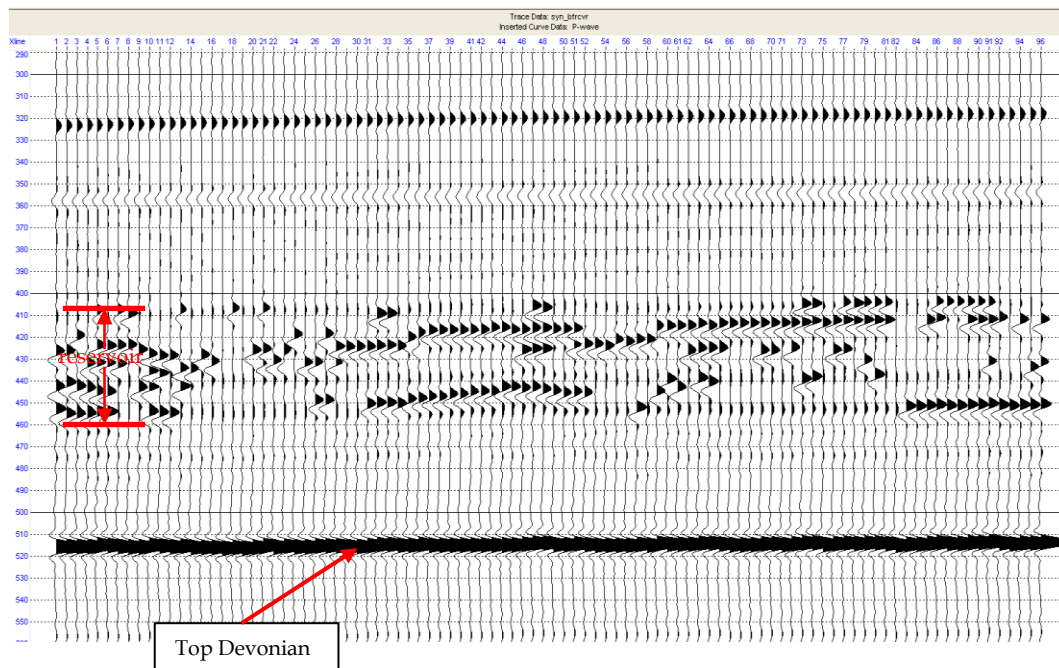


Figure 8. 1 Cross section of the synthetic baseline seismic along well 226

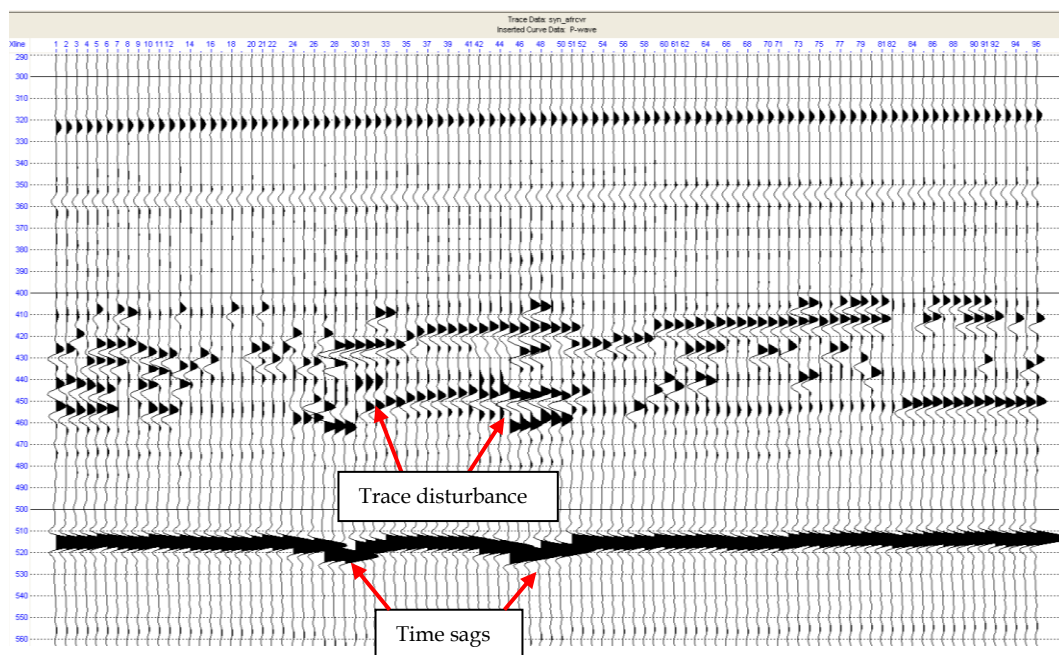


Figure 8. 2 Cross section of the synthetic monitor seismic along well 226

The map of the time structure of the top Devonian resembles those of the real seismic data in Figures 5.10 & 5.11 (it is noted that the map should be rotated counter clockwise at an angle so that they can coincide with the real ones; the same as below). If the amplitude attenuation were included in the modelling, the anomaly would look like that in Figures 8.3 & 5.11. It can be observed that the time delay happened chiefly along the two fracture zones and existed obscurely along the five well bores.

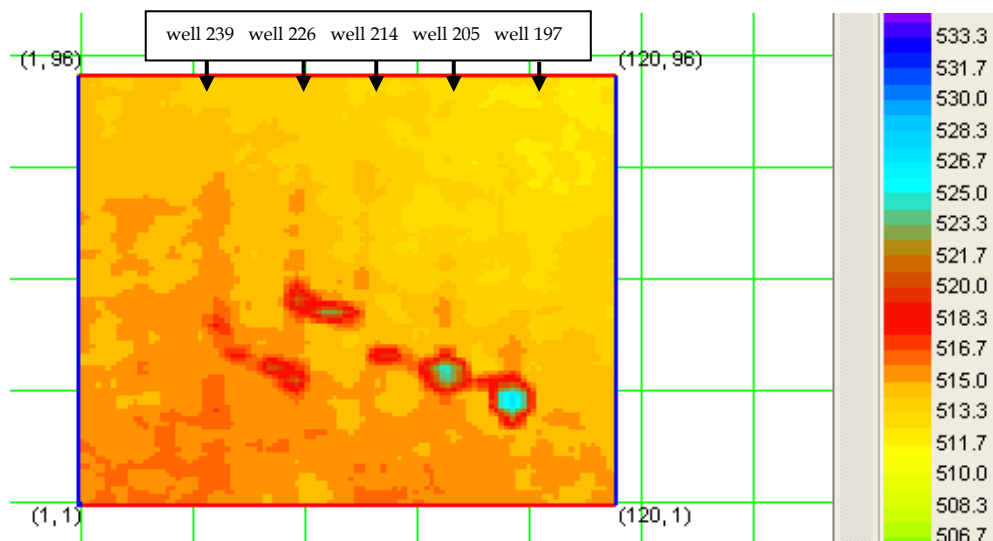


Figure 8. 3 Time map of the top Devonian sliced from the synthetic monitor survey (1998)

(counter-clockwise rotation needed for the correct orientation, the same below)

When cross correlating trace by trace the synthetics of baseline and monitor surveys on the window of 400-500 ms, the maximum cross correlation coefficients and corresponding time shift (negative) outline the two fracture zones of low values, as in Figures 8.4-5. If the noise were added to the synthetics, the two attributes would not be able to delineate the well bores clearly.

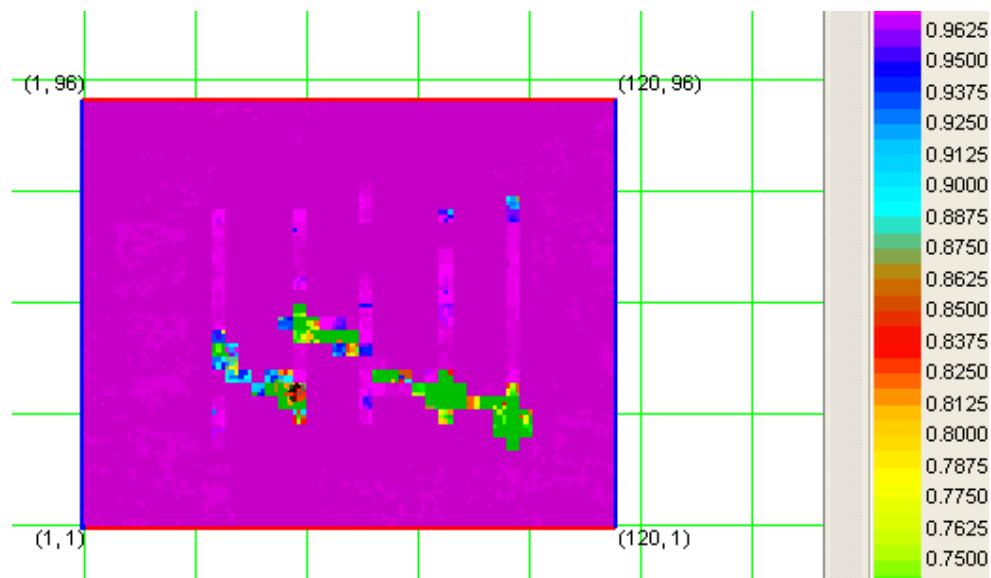


Figure 8. 4 Cross correlation coefficient between the synthetic baseline and monitor surveys on the window of 400-500ms.

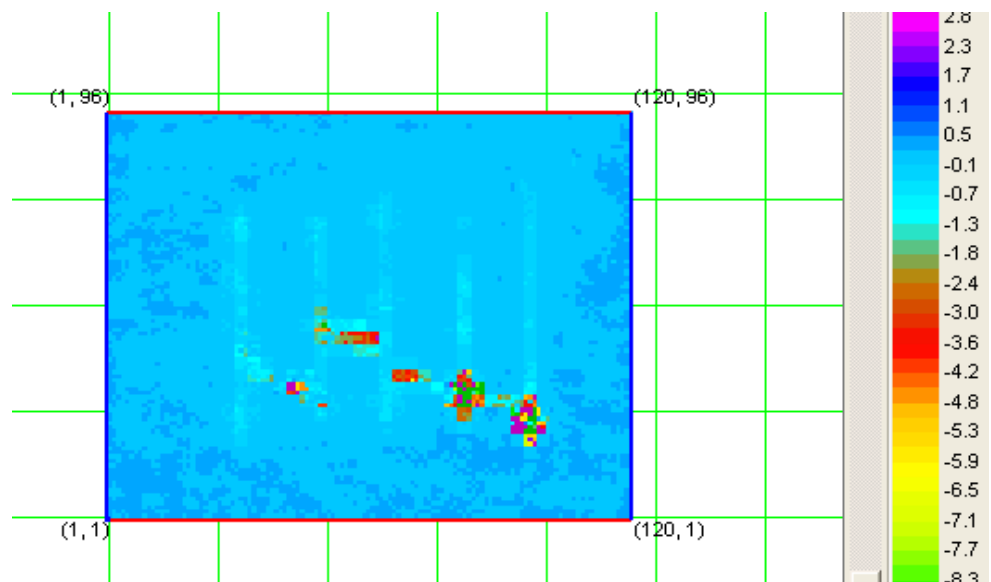


Figure 8. 5 Cross correlation time shift between the synthetic baseline and monitor surveys on the window of 400-500ms.

The synthetic difference volume was used to create the amplitude map in Figure 8.6. The RMS amplitude map on the window of 430-450 indicates the existence of the fracture zones once again. However, it also displays the strong anomalies along the five well bores. They are similar to those in Figures 5.6.

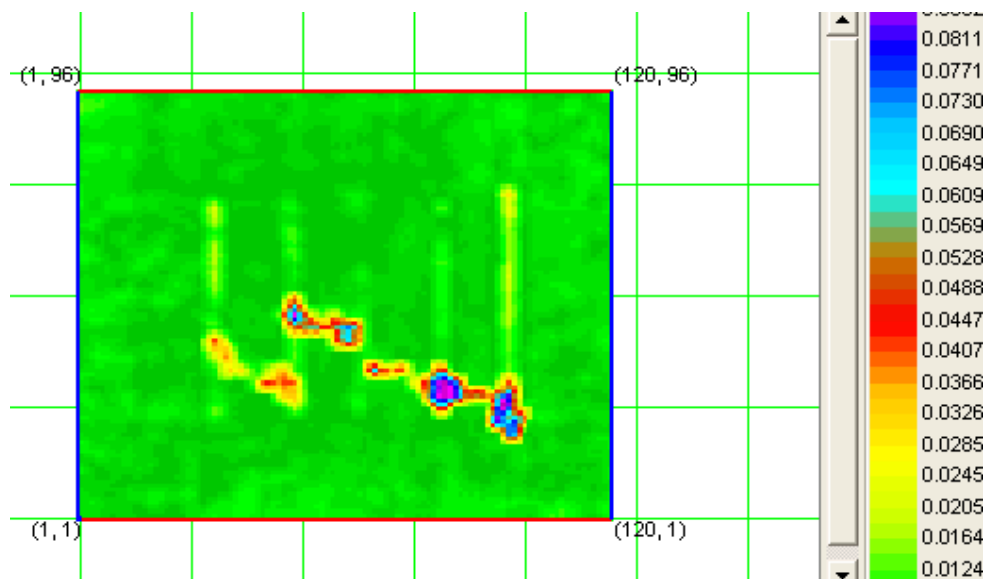


Figure 8. 6 RMS amplitude map sliced from the synthetic difference volume on the window of 430-450ms

In summary, the time-lapse synthetics is capable of re-generating the anomalies and pictures derived from the real time-lapse seismic data. The attributes involved in the process include time sag, cross correlation, and amplitude. The close match would consolidate our confidence to use the reservoir simulation results for enhancing recovery efficiency.

CHAPTER 9 CONCLUSIONS

The time-lapse seismic surveys are an essential tool to calibrate, or even rectify, reservoir simulation results. In the area studied, in order to explain the fluid paths observed by time-lapse seismic, it was postulated that the two zones of fractures were developed under injection, and they cut the five wellbores obliquely and formed the conduit system that controlled the fluid flow during the course of recovery. This is uncovered by the seismic data, and could not be predicted by the initial reservoir simulation in chapter 4. The reservoir simulation parameters were then adjusted correspondingly, and the updated reservoir simulation re-created the different scenario. The subsequent time-lapse seismic synthetics demonstrates the closeness to the time-lapse seismic surveys, which further consolidates our confidence in the reservoir simulation results.

The remedy one could recommend based on the knowledge of the fluid flow pattern is to seal the well sections that are intersected by the zones of fractures so that the draining network would not be confined mainly within them and the leakage upwards and downwards would not happen in the operation. However, this is only possible after the fractures have been identified, as their positions can't be predicted a priori. Besides, the injection pressure should not be so high, in which case the steam and hot water would have enough time to permeate into the virgin blocks instead of opening new shear fractures.

There are a few other contributions on the road to improved reservoir simulation. The distribution of tight strings that are scattered with the reservoir has been quantified using 3-D seismic data. It is beneficial to well trajectory

design and perforation section selection. Their lateral extension may locally affect the vertical permeability, an important parameter for choosing recovery methods.

Cross correlation is a key step to achieve time-lapse seismic data cross equalization, after which comparison can be made in different fashions for potential changes leading to the unmasking of the fluid flow pattern. Conventionally, cross correlation operates only in the time direction ignoring 3D dimensionality of geological objects. This may be partly responsible for that we could not align seismic events to a considerable accuracy. 3D cross correlation that operates in 3 dimensions avoids the disadvantage and the seismic event alignment can be enhanced to a certain degree.

Wavelet transform is a new approach to extracting potential changes in reservoirs. It decomposes the embedded wavelet into a series of sub-wavelets of different dominant frequencies, which have different maximum tuning thicknesses. Not knowing the thickness of fluid invaded zones a priori, scanning is necessary to find the highest amplitude, which will delineate the path of fluid movement. Our example indicates that the sub-wavelet of lower dominant frequency is needed to portray the flow pattern. It also proves to be better than the conventional time-lapse seismic methodology.

REFERENCES

Aziz, Khalid and Antonin Settari, 2002, Petroleum reservoir engineering, Calgary: Blitzprint Ltd.

Batzle, Michael and Zhijing Wang, 1992, Seismic properties of pore fluids, *Geophysics*, 57(11), 1396-1408.

Britton, Michael W., William L. Martin , Robert J. Leibrecht, and Richard A. Harmon, 1983, The Street Ranch pilot test of fracture-assisted steamflood technology, *JPT*, 35(3), 511-522.

Cant, Doug and G. G. Stockmal, 1989, Stratigraphy of the Alberta foreland basin; an interpretation in terms of Cordilleran tectonics, in *The Geology of Stratigraphic Sequences* ed. by A. D. Miall, Springer: New York.

Carlson, Mike, 2003, Practical reservoir simulation: using, assessing, and developing results, Tulsa: PennWell Books.

Chadwick, R. A., R. Arts, and O. Eiken, 2005, 4D seismic quantification of a growing CO₂ plume at Sleipner, North Sea, *Petroleum Geology of Northwest Europe: Proceedings of the 6th petroleum geology Conference*, 6, 1385-1399.

Colorado School of Mines, 1997, Reservoir characterization project, , in *Time-lapse Seismic in Reservoir Management* ed. by Ian Jack, 9.92-124.

Daubechies I., 1992, Ten Lectures on Wavelets, Society for Industrial and Applied Mathematics (SIAM), Philadelphia.

Davis, Thomas L., 2005, 4-D seismic monitoring of a fractured reservoir, Weyburn Field, Saskatchewan, *The Mountain Geologist*, 42(2), 45-52.

Deighan, Andrew J., and Doyle R. Watts, Groud-roll suppression using the wavelet transform, *Geophysics*, 62(6), 1896-1903.

Donobo, D. L., 1993, Nonlinear wavelet methods for recovering signals, images and densities from indirect and noisy data, *Proceedings of Synposia in Applied Mathematics*, 47, 173-205.

Dubrule, Olivier, 2003, *Geostatistics for seismic data integration in earth models*, SEG course notes.

Eastwood, J. E., 1996, Discriminant analysis for reservoir monitoring, CSEG Annual Convention, Expanded Abstracts.

Eastwood, J. E., 1996, Case history: Drilling 46 wells based on seismic monitoring at Cold Lake, CSEG Annual Convention, Expanded Abstracts.

Eastwood, John, David Johnston, Xuri Huang, Ken Craft, and Ricky Workman, 1998, Processing for robust time-lapse seismic analysis: Gulf of Mexico example, Lena Field, 68th Annual Int. Mtg., SEG Expanded Abstracts, 20-23.

Gabor, D., 1946, Theory of communication, *J. I.E.E.E.* v. 93, 429-441.

Gabriels, P., A. Horvei, K. Koster, A. Onstein, and R. Staples, 1999, Time-Lapse Seismic Monitoring of the Draugen field: 69th Annual Int. Mtg., SEG Expanded Abstracts, 2035-2037.

Goldhammer, Robert K., , 2003, Cyclic sedimentation, in Encyclopedia of Sediments and Sedimentary Rocks ed. By Middleton, G.V. et al., Science

Gosselin, O., S. I. Aanonsen, I. Aavatsmark, A. Cominelli, R. Gonard, M. Kolasinski, F. Ferdinandi, L. Kovacic, and K. Neylon, 2004, History matching using time-lapse seismic, JPT, 56(4), 66-67.

Goupillaud, Pierre L, A. Grossmann and Jean Morlet, 1985, A simplified view of the cycle-octave and voice representations of seismic signals, Geophysics, 50(2), 311.

Greaves, Robert J. and Terrance J. Fulp, 1987, Three-dimensional seismic monitoring of an enhanced oil recovery process, Geophysics, 52(9), 1175-1187.

Hall John S., Peter Mozley, J. Matthew Davis, and Nicole Delude Roy, Environments of formation and controls on spatial distribution of calcite cementation in Plio-Pleistocene fluvial deposits, New Mexico, U.S.A., Journal of Sedimentary Research, 74, 643-653.

Hirsche, Keith, M. Batzle, R. Knight, Z. Wang, L. Mewhort, R. Davis and G. Sedgwick, 1997, in Time-lapse Seismic in Reservoir Management ed. by Ian Jack, 9.126-138.

Hosung Shin, J. Carlos Santamarina and Joseph A. Cartwright, 2008, Contraction-driven shear failure in compacting uncemented sediments, Geology, 36(12), 931-934.

Huang, Xuri, Laurent Meister, and Rick Workman, 1997, Production history matching with time lapse seismic data, 67th Annual Int. Mtg., SEG Expanded Abstracts, 862-865.

Huang, Xuri, Laurent Meister, and Rick Workman, 1998, Improvement on the quantitative seismic history matching, 68th Annual Int. Mtg., SEG Expanded Abstracts, 36-39.

Huang, Xuri, Thaddeus Charles Jones, and Albert Berni, 1999, Reprocessing of time-lapse seismic data improves seismic history matching, 69th Annual Int. Mtg., SEG Expanded Abstracts, 1703-1706.

Huang, Xuri, L. Bentley, and C. Laflamme, 2001, Seismic history matching guided by attribute zonation, 71th Annual Int. Mtg., SEG Expanded Abstracts, 1568-1571.

Hubans, C., M. Rapin, J.F. Otlé, M. Manin, S.D. Harker, G Richardson, and R. Cooper, 2003, 4D using legacy seismic data on the Alwyn North Oil Field, *Petroleum Geoscience*, 9(1), 15-24.

Isaaks, E. H., and R. M. Srivastava, 1989, *Applied geostatistics*, Oxford University Press: Oxford.

Jack, Ian, 1998, Time-lapse seismic in reservoir management, SEG course notes.

Jenkins, S. D., M. W. Waite and M. F. Bee, 1997, Time-lapse monitoring of the Duri steamflood: A pilot and case study, *The Leading Edge*, 16, 1267-1274.

Johnston, D. H., 1997, Time-lapse seismic analysis of the North Sea Fulmar Field, in Time-lapse Seismic in Reservoir Management ed. by Ian Jack, 9.68-89.

Kenter, C. J., A. C. Van Den Beukel, P. J. Hatchell, K. P. Maron, M. M. Molenaar, and J. G. F. Stammeijer, 2004, Geomechanics and 4D: Evaluation of reservoir characteristics from timeshifts in the overburden, 6th N. AMER. ROCK MECH. SYMP. [GULF ROCKS 2004] (Houston, TX, 6/5-10/2004) PROC. pap. no.ARMA/NARMS 04-627, 2004.

Kloosterman, H. J., R. S. Kelly, J. Stammeijer, M. Hartung, J. van Waarde, and C. Chajacki, 2003, Successful application of time-lapse seismic data in Shell Expro's Gannet Fields, Central North Sea, UKCS, Petroleum Geoscience, 9(1), 25-34.

Koster, K., P. Gabriels, M. Hartung, J. Verbeek, G. Deinum, and R. Staples, 2000, Time-lapse surveys in the North Sea and their business impact, The Leading Edge, 19(3), 286-293.

Lee, Jungwon, 2000, Noise reduction in the wavelet domain, from <http://scien.stanford.edu/class/ee368/projects2000/project8/project.htm>.

Lewis, Martin D., 1990, A laboratory study of the effect of stress state on the elastic moduli of sand, Ph. D. dissertation, University of Texas at Austin.

Lindseth, R. O., 1979, Synthetic sonic logs - a process for stratigraphic interpretation, Geophysics, 44, 3-26.

Leckie, D. A. and D. G. Smith, 1992, Regional setting, evolution, and depositional cycles of the western Canada Foreland Basin, in R. W. Macqueen and D. A. Leckie, eds., *Foreland basins and fold belts: AAPG memoir 55*, 9-46.

Mallat, S., and W. L. Hwang, 1992, Singularity detection and processing with wavelets, *IEEE Trans Inform Theory*, 38, 617-643.

Margrave, Gary F., and Peter M. Manning, 2004, Seismic modelling: An essential interpreter's tool, CSEG Annual Convention, Expanded Abstracts.

Marfurt, Kurt, 2003, 3D seismic attributes for prospect identification and reservoir characterization, SEG Continuing Education Course.

Mavko, G., Mukerji, T. and J. Dvorkin, 1998, *The rock physics handbook*, Cambridge: Cambridge University Press.

Miao, X., and S. P. Cheadle, 1998, Noise attenuation with wavelet transforms: 68th Annual Int. Mtg., SEG Expanded Abstracts, 1072-1075.

Mukerji, Tapan, Gary Mavko, Daniel Mujica, and Nathalie Lucet, Scale-dependent seismic velocity in heterogeneous media, *Geophysics*, 60, 1222-1233.

Nguyen, M. Q., and J. Mars, 1999, Noise attenuation with wavelet transforms: 68th Annual Int. Mtg, SEG Expanded Abstracts, 1228-1230.

Nur, Amos, Carol Tosaya and Dung Vo-Thanh, 1984, Seismic monitoring of thermal enhanced oil recovery processes: 54th Annual Int. Mtg., SEG Expanded Abstracts, 337-340.

Pan, P. P. and de Bremaecker, J. C., 1970, Direct location of oil and gas by the seismic reflection method, *Geophysical Prospecting*, 18, 712-727.

Potocki, D. and I. E. Hutcheon, 1992, Lithology and diagenesis of sandstones in the Western Canada Foreland Basin: in R. W. Macqueen and D. A. Leckie, eds., *Foreland basins and fold belts: AAPG memoir 55*, 229-257.

Rickett, James and David E. Lumley, 1998, A cross-equalization processing flow for off-the-shelf 4D seismic data: 68th Annual Int. Mtg., SEG Expanded Abstracts, 16-19.

Robinson, Enders A. and Sven Treitel, 1980, *Geophysical signal analysis*, Prentice Hall: Englewood Cliffs.

Scorer, J, N. Fuller, J. Malcolm, and J. Bruner, 2005, The MacCulloch Field; improving reservoir characterization through time-lapse analysis, *Petroleum Geology of Northwest Europe: Proceedings of the 6th petroleum geology Conference*, 6, 1517-1531.

Selesnick, Ivan W., 2007, Wavelet transforms-A quick study, *Physics Today*, October 2007, (1-11).

Serra, Oberto, 1986, *Fundamentals of well-log interpretation; 2, The interpretation of logging data*, Elsevier:Amsterdam.

Settari, A., and D. W. Walters, 2000, Reservoir geomechanics; new approach to reservoir engineering analysis and a powerful tool for reservoir management *Proceedings - World Petroleum Congress*, vol.16, Vol. 2, pp.206-208.

Settari, A, and F. M. Mourits, 1998, A coupled reservoir and geomechanical simulation system, *SPE Journal*, 3(3), 219-226.

Settari, A, and J. M. Raisbeck, 1981, Analysis and numerical modeling of hydraulic fracturing during cyclic steam stimulation in oil sands *JPT*, 33(11), 2201-2212.

Sheriff, Robert E., and Lloyd P. Geldart, 1995, *Exploration Seismology*, Cambridge: Univ of Cambridge Press.

Smith R. J., and K. R. Perepelecta, 2004, Steam conformance along horizontal wells at Cold Lake, *JCPT*, 43(11), 56-61.

Sonneland, L., Veire, H.H., Raymond, B., Signer, C., Pedersen, L., Ryan, S. and Sayers, C., 1997, Seismic reservoir monitoring on Gullfaks, *The Leading Edge*, 16(9), 1247-1252.

Spetzler, Jesper, Ziqiu Xue, Hideki Saito and Osamu Nishizawa, 2008, Case story: time-lapse seismic crosswell monitoring of CO₂ injected in an onshore sandstone aquifer, *Geophysical Journal International*, 172(1), 214-225.

Surdam, R. C., and J. R. Boles, 1979, Diagenesis of volcanic sandstones , in *Special Publication - Society of Economic Paleontologists and Mineralogists*, ed. by Scholle, P A, and P. R. Schluger, 26, 227-242,

Trad, D. O., and J. M. Travassos, 2000, Wavelet filtering of magnetotelluric data, *Geophysics*, 65, 482-491.

Vail, P. R., R. G. Todd and J. B. Sangree, 1977, Seismic stratigraphy and global changes of sea level, Part 5: Chronostratigraphic significance of seismic reflections, in *Seismic Stratigraphy – Applications to Hydrocarbon Exploration* ed. By Charles E. Payton, 99-166, AAPG Special Publication.

Vedanti, Nimisha and Mrinal K. Sen, 2009, Seismic inversion tracks in situ combustion: a case study from Balol oilfield, India, *Geophysics*, 74(4), B103-B112.

Waal, Hans De and Rodney Calvert, 2003, Overview of global 4D seismic implementation strategy, *Petroleum Geoscience*, 9(1), 1-6.

Waite, M. W. and Rusdinadar Sigit, 1997, Seismic monitoring of the Duri steamflood: Application to reservoir management, *The Leading Edge*, 16, 1275-1278.

Walker, Greg, Peter Allan, Robert Trythall, Ronnie Parr, Marcus Marsh, Roar Kjelstadli, Olav Barkved, Daniel Johnson, and Scott Lane, 2006, Three case studies of progress in quantitative seismic-engineering integration, *The Leading Edge*, 25(9), 1161-1166.

Walters, D. W., and A. Settari, 2002, Coupled geomechanical and reservoir modelling investigating poroelastic effects of cyclic steam stimulation in the Cold Lake reservoir, *SPE Reservoir Evaluation Eng.*, 5(6), 507-516.

Widess, M. B., 1973, How thin is a thin bed? *Geophysics*, 38, 1176-1180.

Zhang, J. J., 2001, Time-lapse seismic surveys: Rock physics basis, M. Sc. thesis, University of Calgary.

Zhang, R., and D.O. Trad, 2002, Noise attenuation: A hybrid approach based on wavelet transform, CSEG Annual Convention, Expanded Abstracts.

APPENDIX 1 MISMATCH INDICES

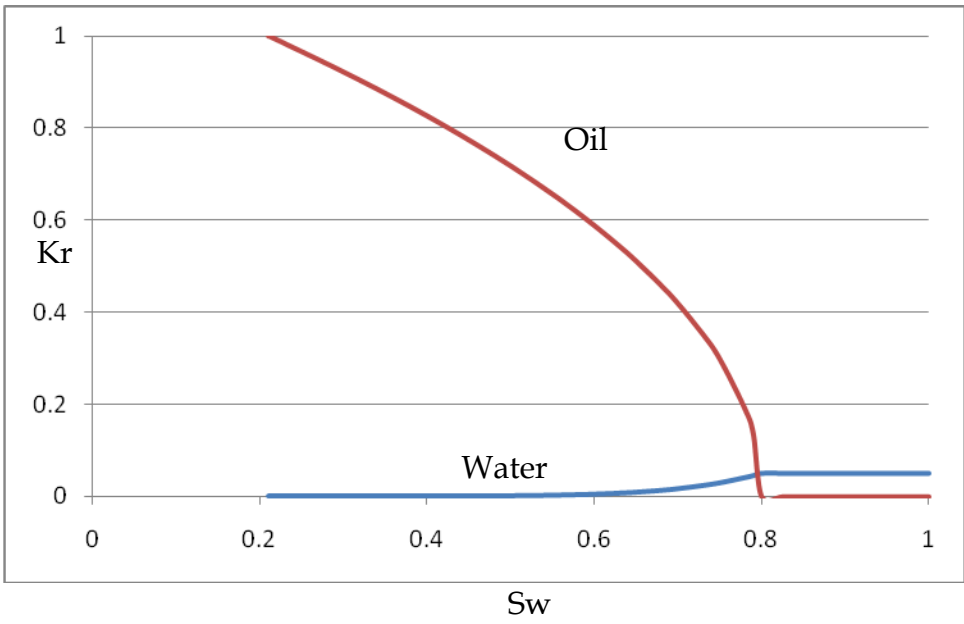
Slope: acquired by linear regression analysis ($y=ax$) of two quantities. The closer to one it is, the better the quantities match each other.

Distance: average perpendicular distance from the point to the straight line ($y=x$) on the cross plot. The smaller it is, the better the quantities match each other.

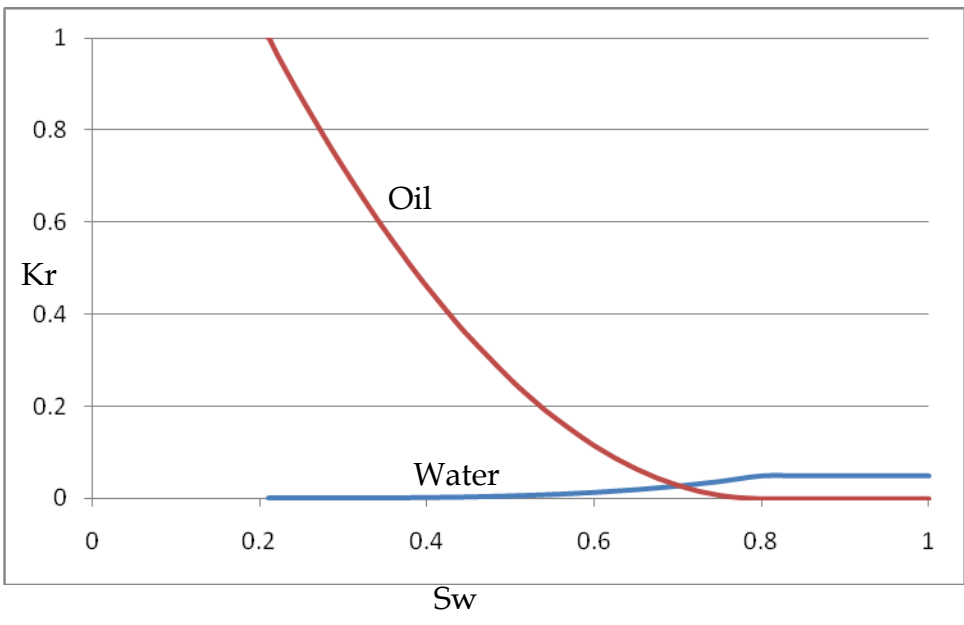
Mean percentage: defined as $M = \frac{1}{n} \sum_{i=1}^n \left| \frac{X_i - Y_i}{X_i} \right|$. The smaller it is, the better the quantities match each other.

STD percentage: defined as $S = \sqrt{\frac{1}{n} \left[\sum_{i=1}^n \left(\left| \frac{X_i - Y_i}{X_i} \right| - M \right)^2 \right]}$. The smaller it is, the better the quantities match each other.

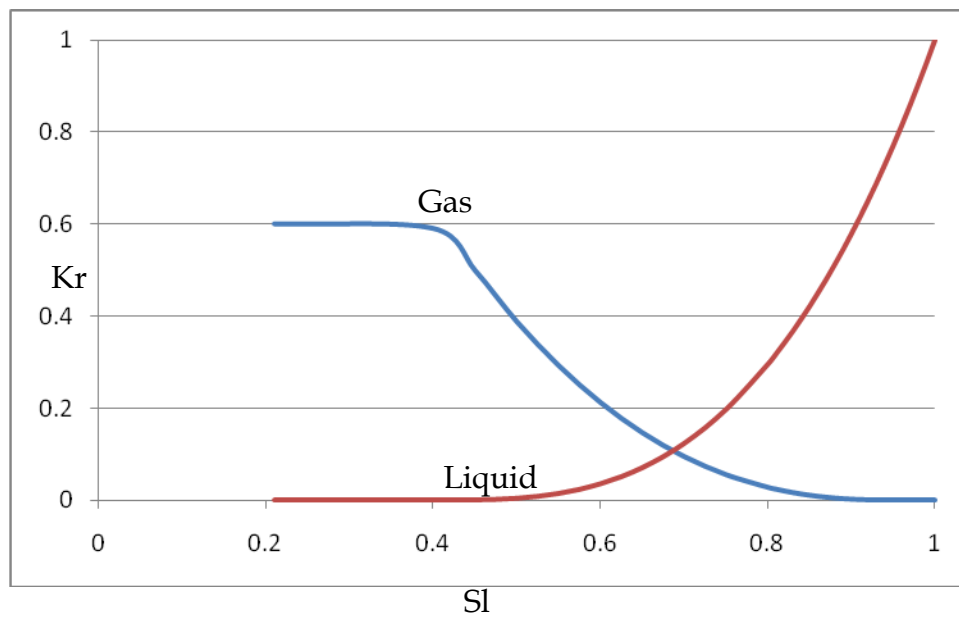
APPENDIX 2 RELATIVE PERMEABILITY CURVE



Drainage Oil-Water relative permeability curve



Imbibition Oil-Water relative permeability curve



Liquid-Gas relative permeability curve